

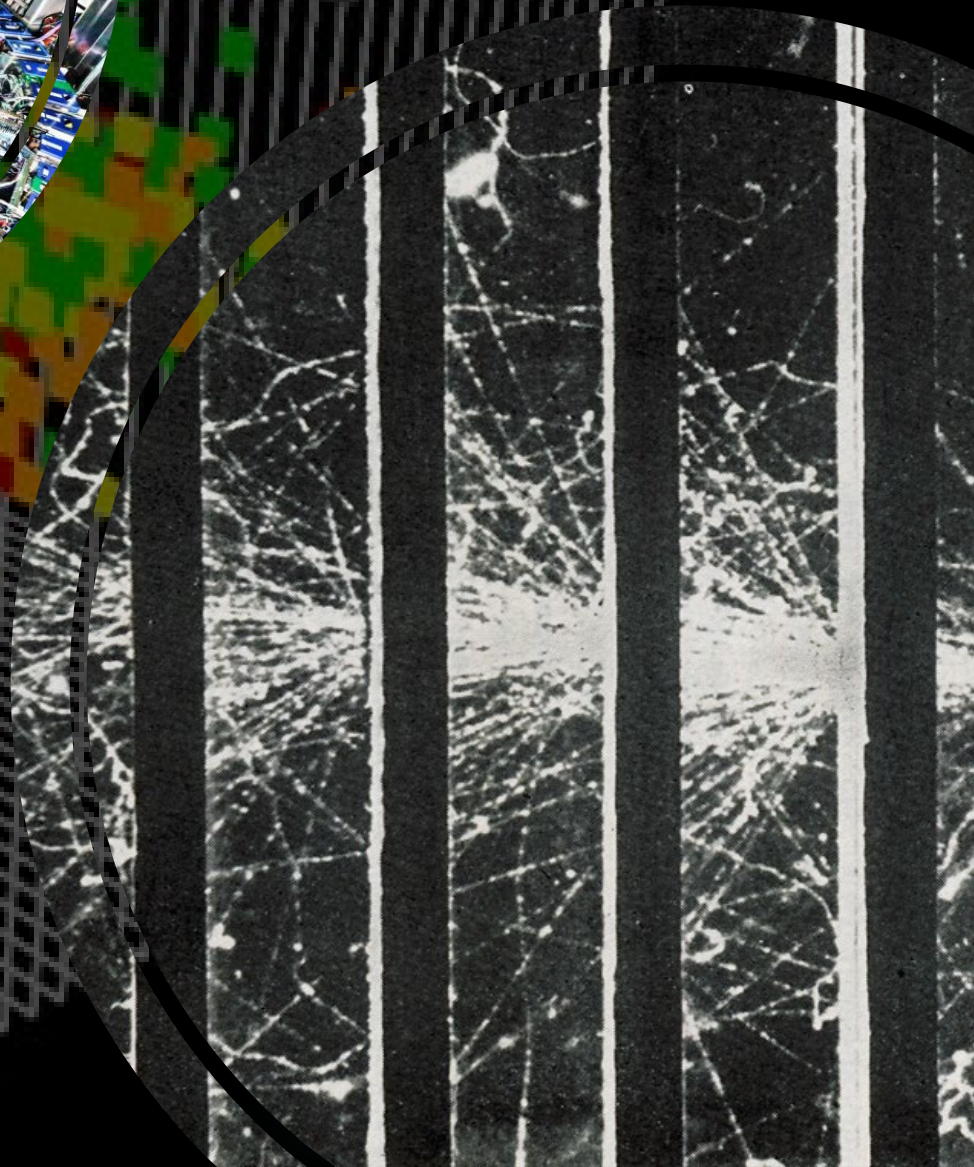


Calorimeters for high energy colliders

SARAH ENO

13,14 AUGUST 2020

2020 HADRON COLLIDER PHYSICS SUMMER SCHOOL



Calorimeter Bibliography

Some of my go-to references:

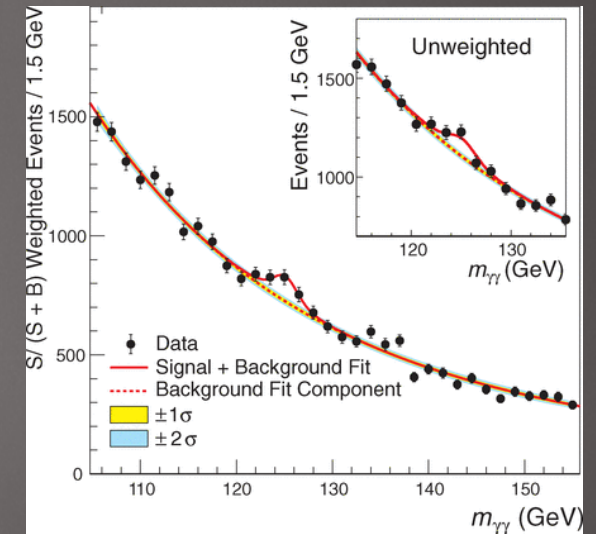
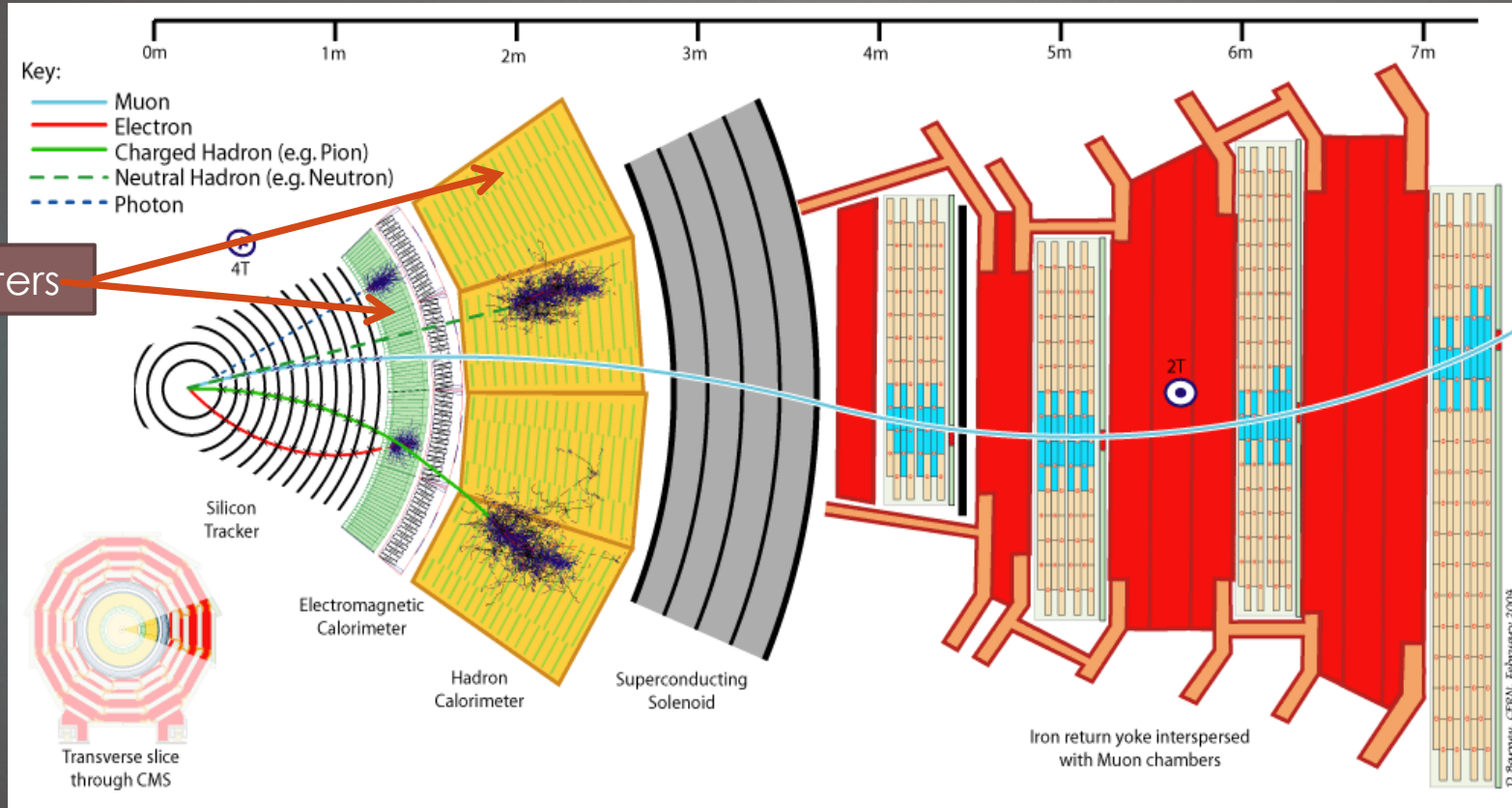
- My own recent work: <https://arxiv.org/abs/2008.00338>
- Electromagnetic calorimetry (<https://www.sciencedirect.com/science/article/pii/S0168900211005572>)
- Theoretical studies of hadronic calorimetry for high luminosity, high energy colliders; (<https://www.sciencedirect.com/science/article/pii/0168900289910619>)
- Passage of Particles through Matter; (<http://pdg.lbl.gov/2019/reviews/rpp2018-rev-passage-particles-matter.pdf>)
- Dual-Readout Calorimetry; (<https://arxiv.org/abs/1712.05494>)
- Particle Flow Calorimetry and the PandoraPFA Algorithm; (<https://arxiv.org/abs/0907.3577>)
- Particle-flow reconstruction and global event description with the CMS Detector (<https://arxiv.org/abs/1706.04965>)
- Recent results of the technological prototypes of the CALICE highly granular calorimeters (<https://arxiv.org/abs/1904.02825>)
- Exploring the structure of hadronic showers and hadronic energy reconstruction with highly granular calorimeters (<https://pos.sissa.it/367/152>)
- New Developments in Calorimetric Particle Detection (<https://arxiv.org/pdf/1807.03853.pdf>)
- Hadron Calorimetry (<https://www.sciencedirect.com/science/article/pii/S0168900211019851>)
- Particle Detectors at Accelerators (<http://pdg.lbl.gov/2019/reviews/rpp2019-rev-particle-detectors-accel.pdf>)
- And others noted at the bottom of (most) slides

Refresher on basics

Calorimeters

Calorimeters are the only source of information on the momenta of neutral particles such as (unconverted) photons, neutrons, and neutral kaons. They are used in particle identification, to distinguish electrons from charged pions.

calorimeters



Calorimeters

In addition, used to measure momenta of charged particles in crowded environments, inside high energy **jets**, where tracking-finding algorithms can be inefficient, and to infer (through momentum balance) the momenta of neutrinos and neutrino-like particles (**missing transverse energy and missing energy**).

Also, at very high momentum, the calorimeter resolution can be better than the tracker resolution.

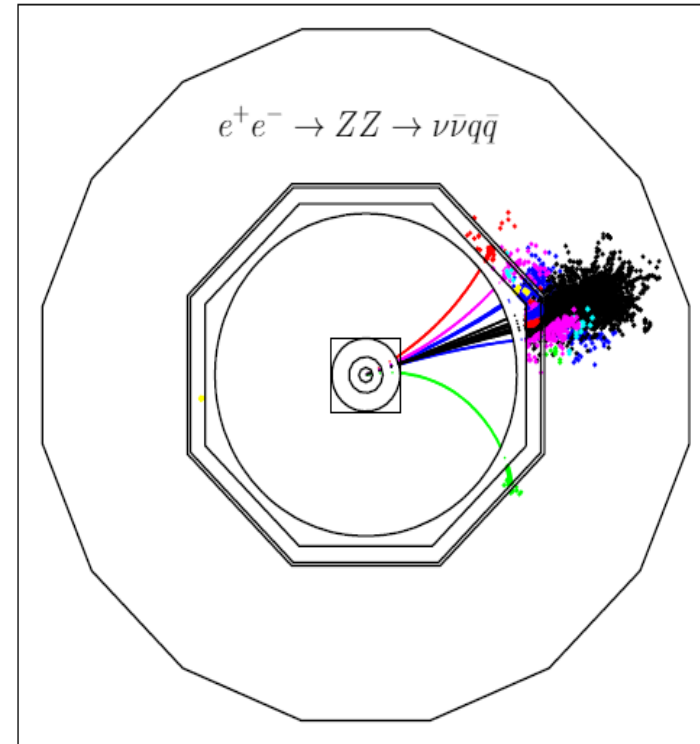
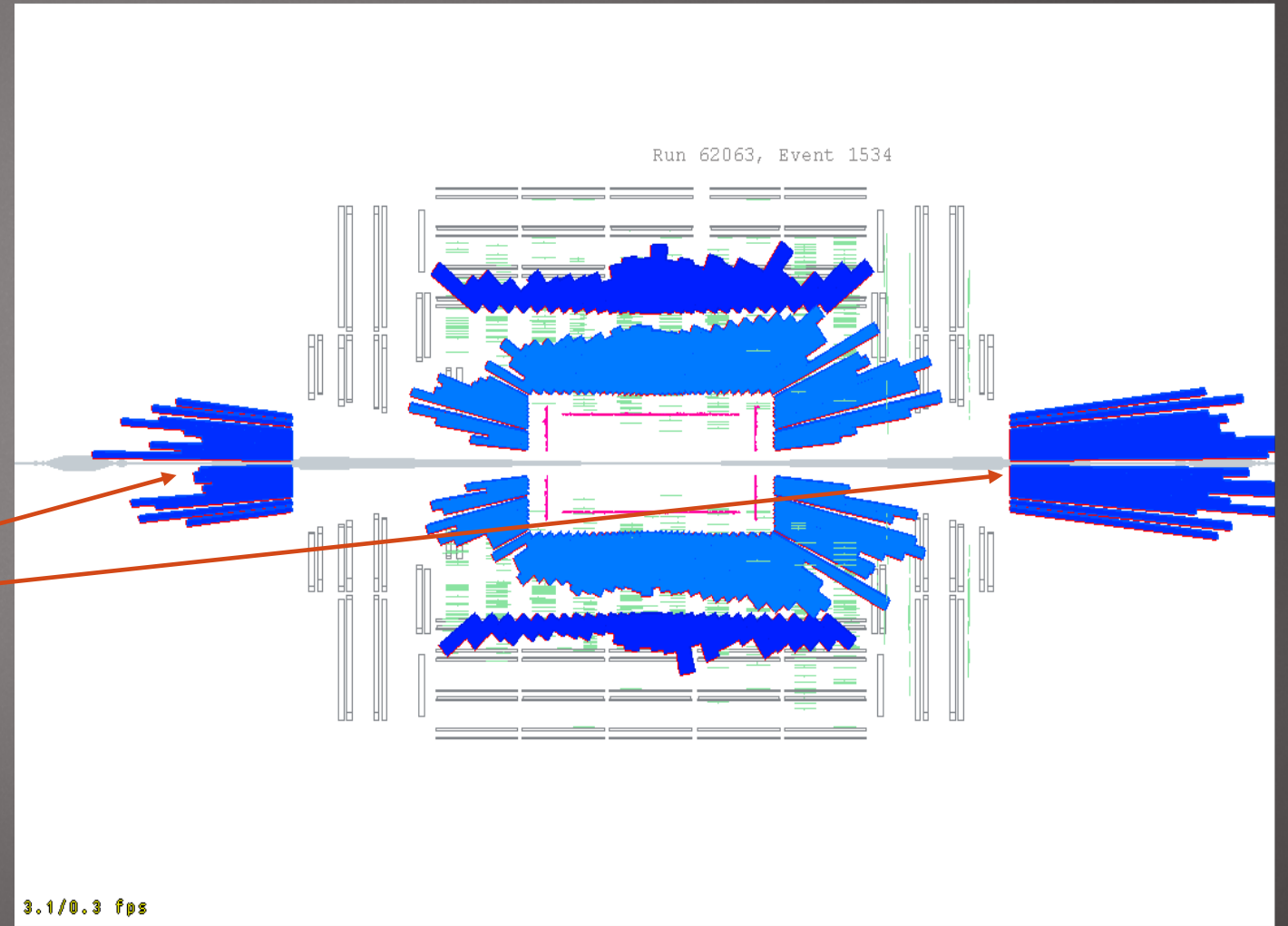


Figure 14: An example of a $Z \rightarrow d\bar{d}$ decay with $E_Z = 1$ TeV produced in a simulated $e^+e^- \rightarrow ZZ \rightarrow \nu\bar{\nu}d\bar{d}$ interaction in the ILD detector concept.

Calorimeters

And provide a measurement of charged particles in the forward region, at large pseudorapidity η , where the limited $\int \vec{B} \cdot d\vec{l}$ limits tracker-based momenta measurement

Hadron
Forward
Calorimeters

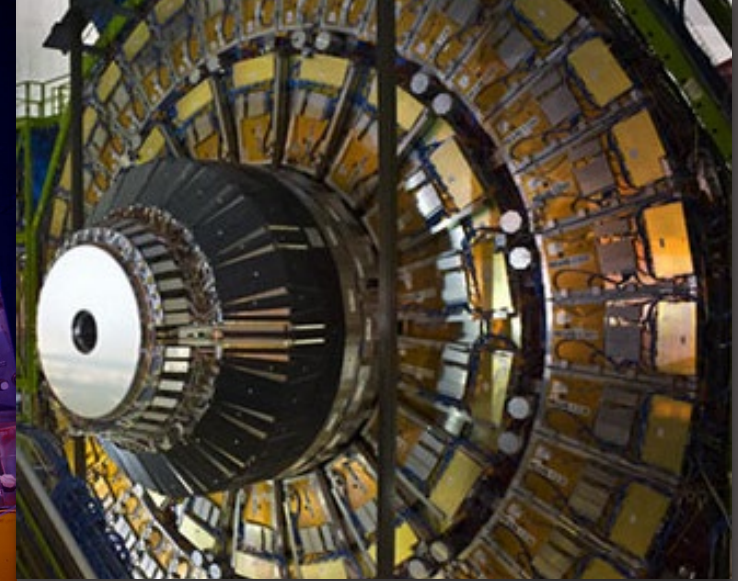
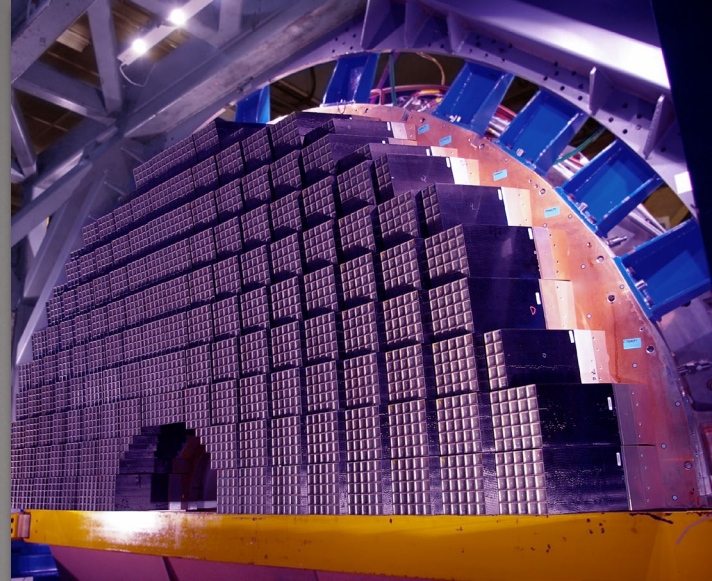


Calorimeter Types

Traditionally divided into

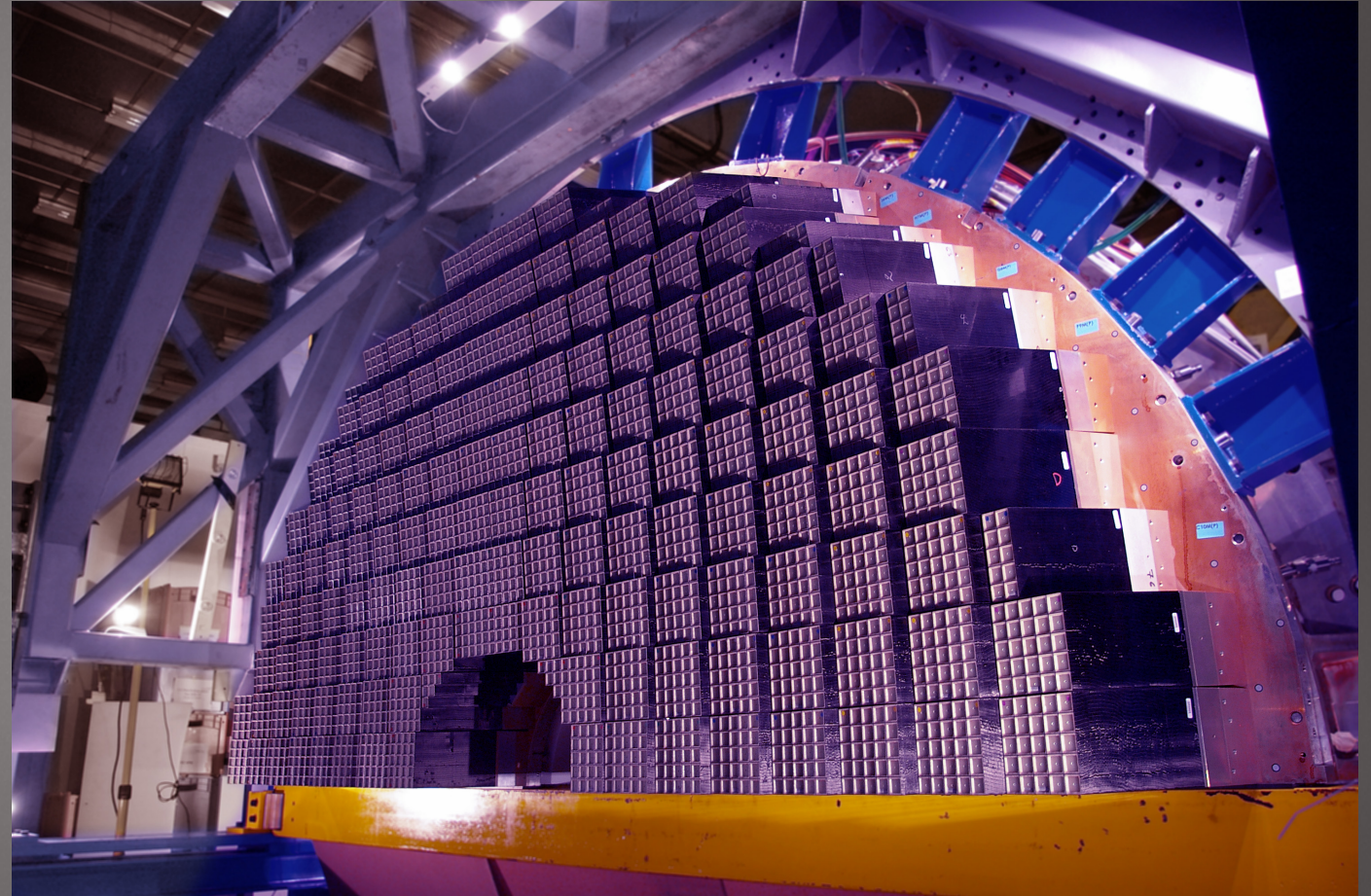
- “electromagnetic” or “**ECAL**” (front) versus “hadronic” or “**HCAL**” (back but really should be front+back) calorimeters
- “**homogeneous**” (entire detector generates detectable signal) versus “**sampling**” (only a small fraction generates signal) calorimeters containing **active** and **passive** material.
- “**high granularity**” (particle flow) versus “**dual readout** (different methodologies for improving hadron resolutions)

(although most contain aspects from several of these characterizations)



Homogenous

Mostly scintillating crystal calorimeters. Charged particles transversing the media create signal throughout its entire volume. For crystals, usually scintillation light (excitations of the crystal due to its electromagnetic interactions with charged particles de-excite by emitting detectable light. Called “ionizing energy” although mostly excitations, not ionization)



Sampling

Layers of

- passive material like lead, steel, brass, tungsten, Uranium, etc
- A signal-producing material (active) producing signals based on “ionization” (e.g. liquid noble, gas, silicon) or “excitations” (e.g. plastic scintillator, crystal scintillators) or Cherenkov radiation (e.g. quartz, many crystals)



Some current calorimeters

10

CMS

- Barrel (and current endcap)
 - Homogeneous PbWO₄ tungstate crystal electromagnetic calorimeter
 - a sampling hadronic calorimeter (scintillator and brass) (I work on this)
- Future Endcap “hgcal”
 - Silicon-(Cu/CuW/Pb) sampling particle flow EM calorimeter
 - (Silicon/scintillator)-steel sampling particle flow HAD calorimeter (I work on this)
- Far forward
 - a steel-quartz Cherenkov calorimeter

ATLAS

- Liquid argon-lead for barrel EM and for entire endcap calorimeter
- Scintillator-steel barrel sampling calorimeter

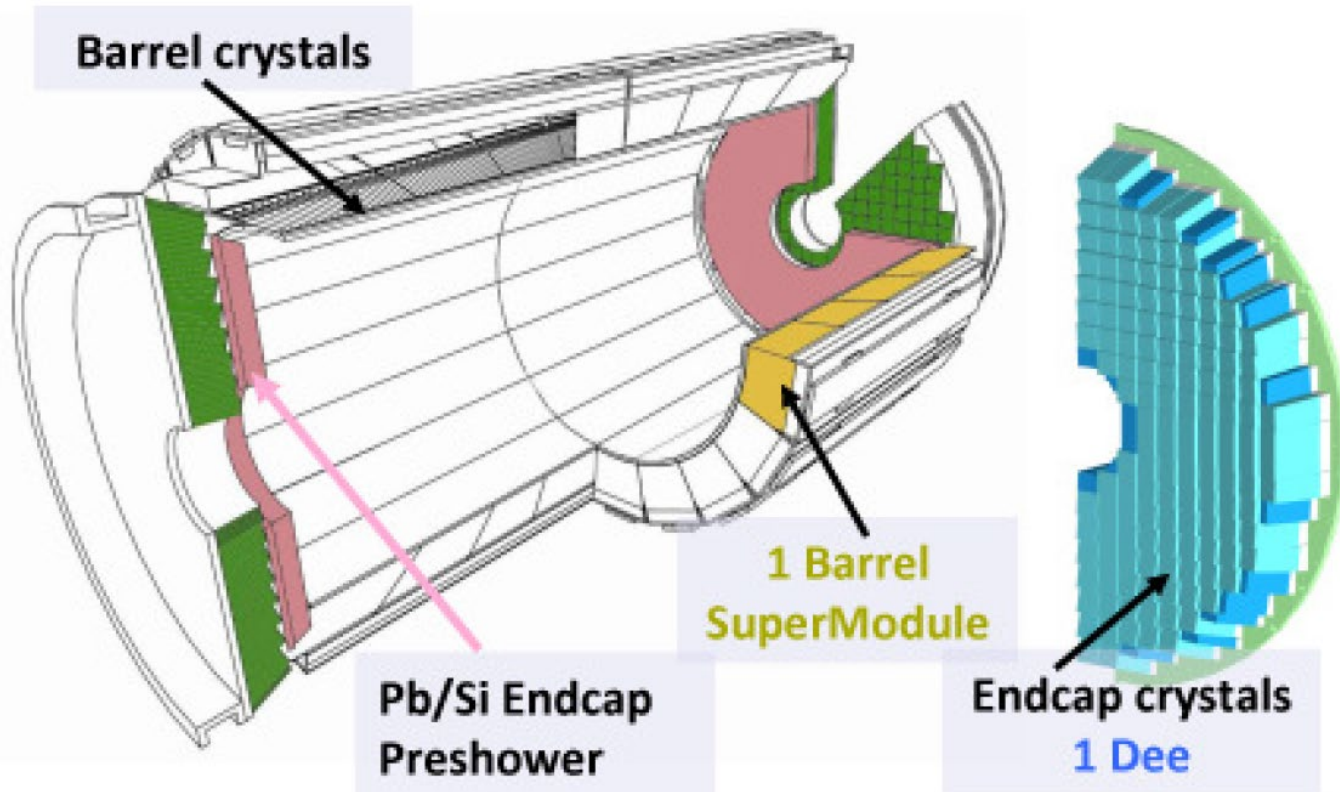
SCEPCAL (work-in-progress by Tully, Lucchini, with some minor contributions by me and my student Yihui Lai <https://arxiv.org/abs/2008.00338>)

- Dual-readout PbWO₄ crystal ecal and spaghetti-type dual readout brass-quartz-plastic scintillator hcal

(another warning: I know way too much about plastic scintillator)

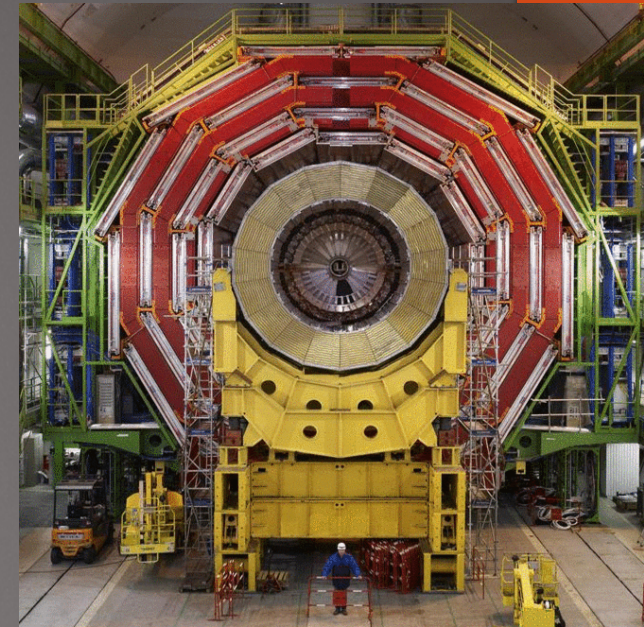
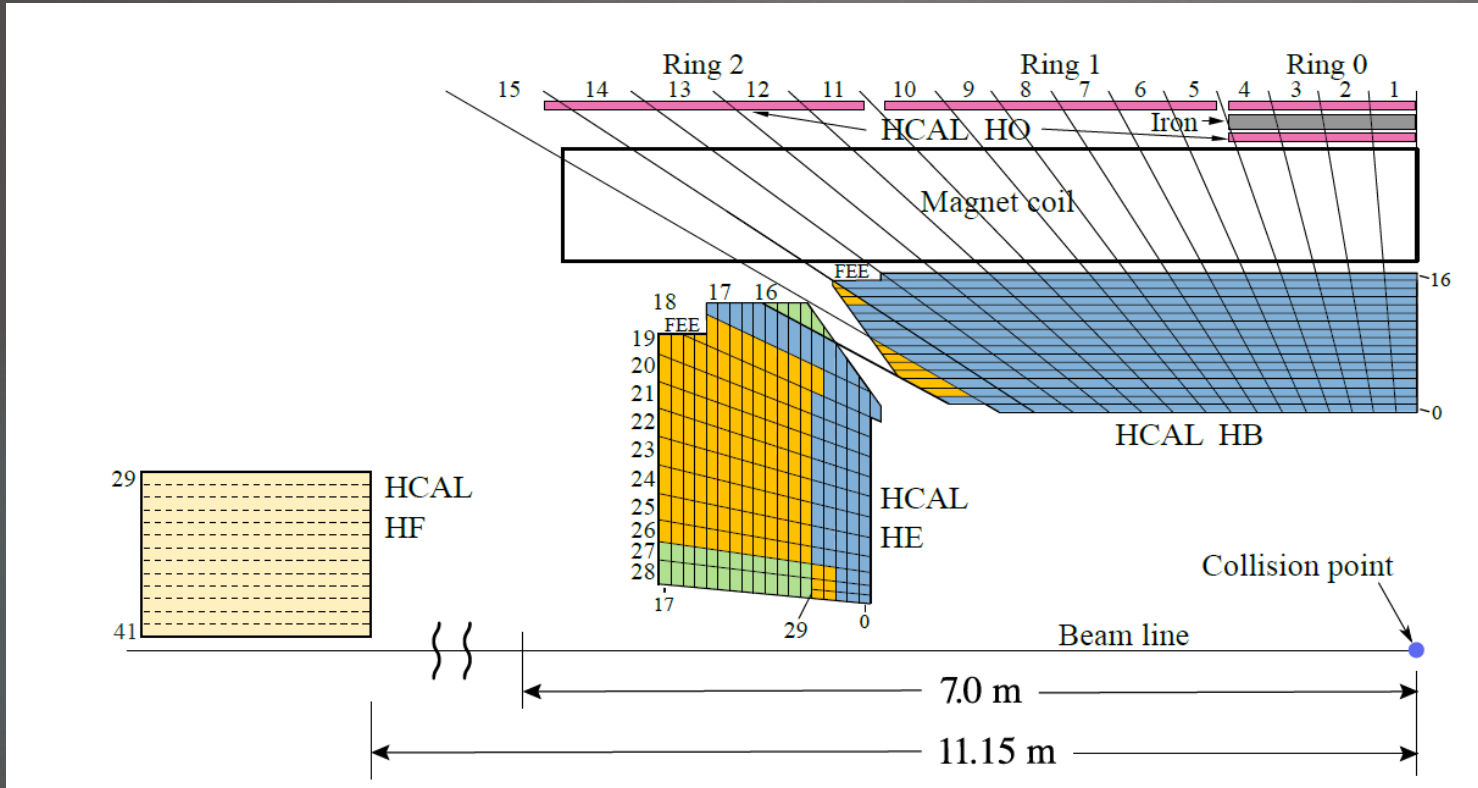
CMS barrel ECAL

11



State of the art resolution for electrons/photons

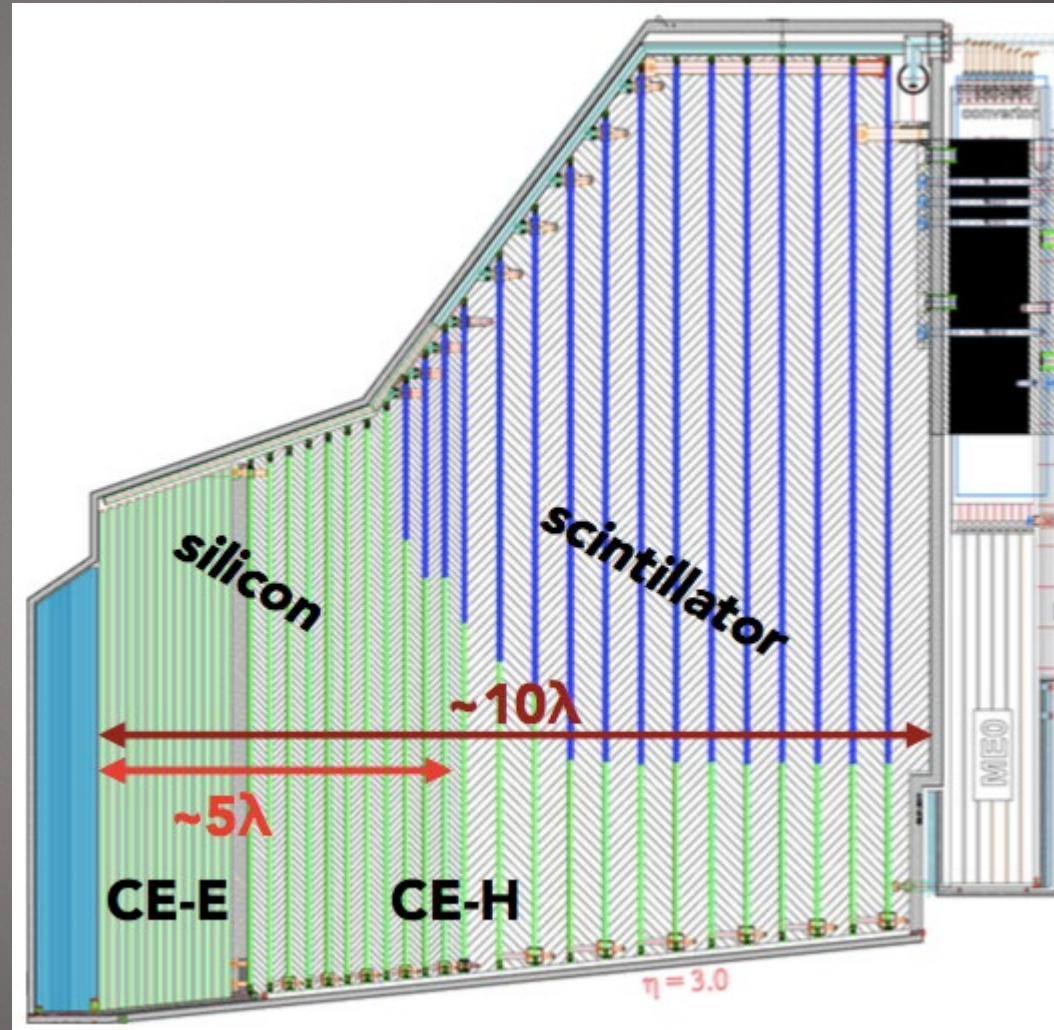
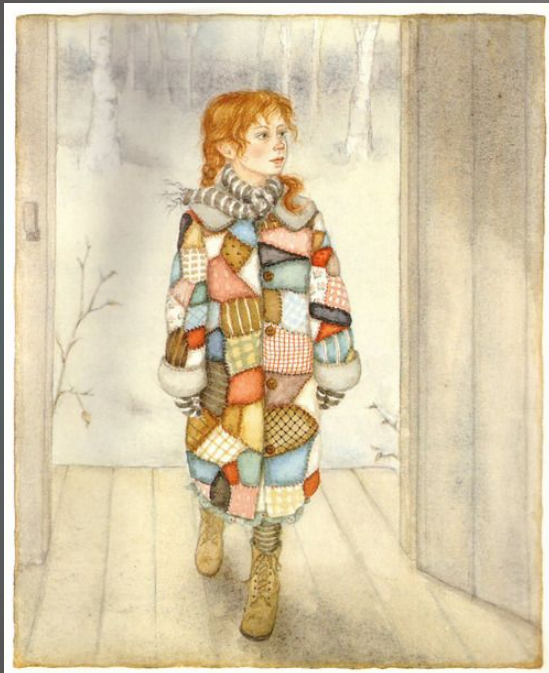
CMS HCAL



Cheap!

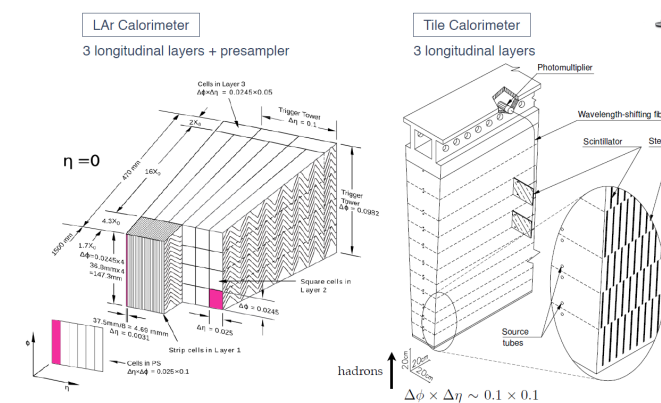
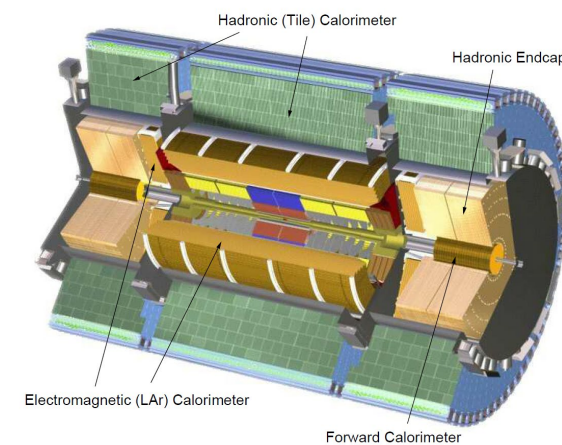
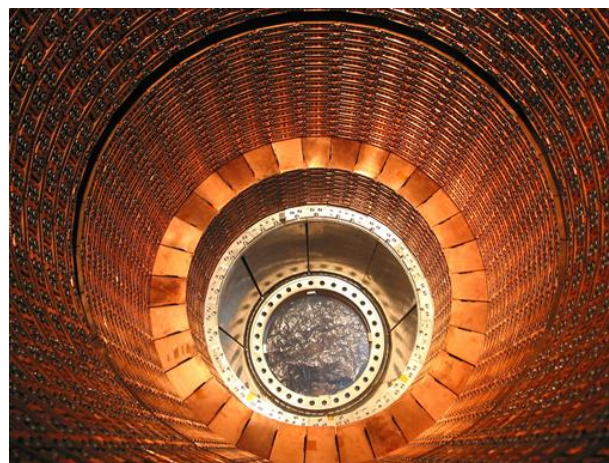
CMS HGCAL

First “high granularity” or “particle flow” calorimeter



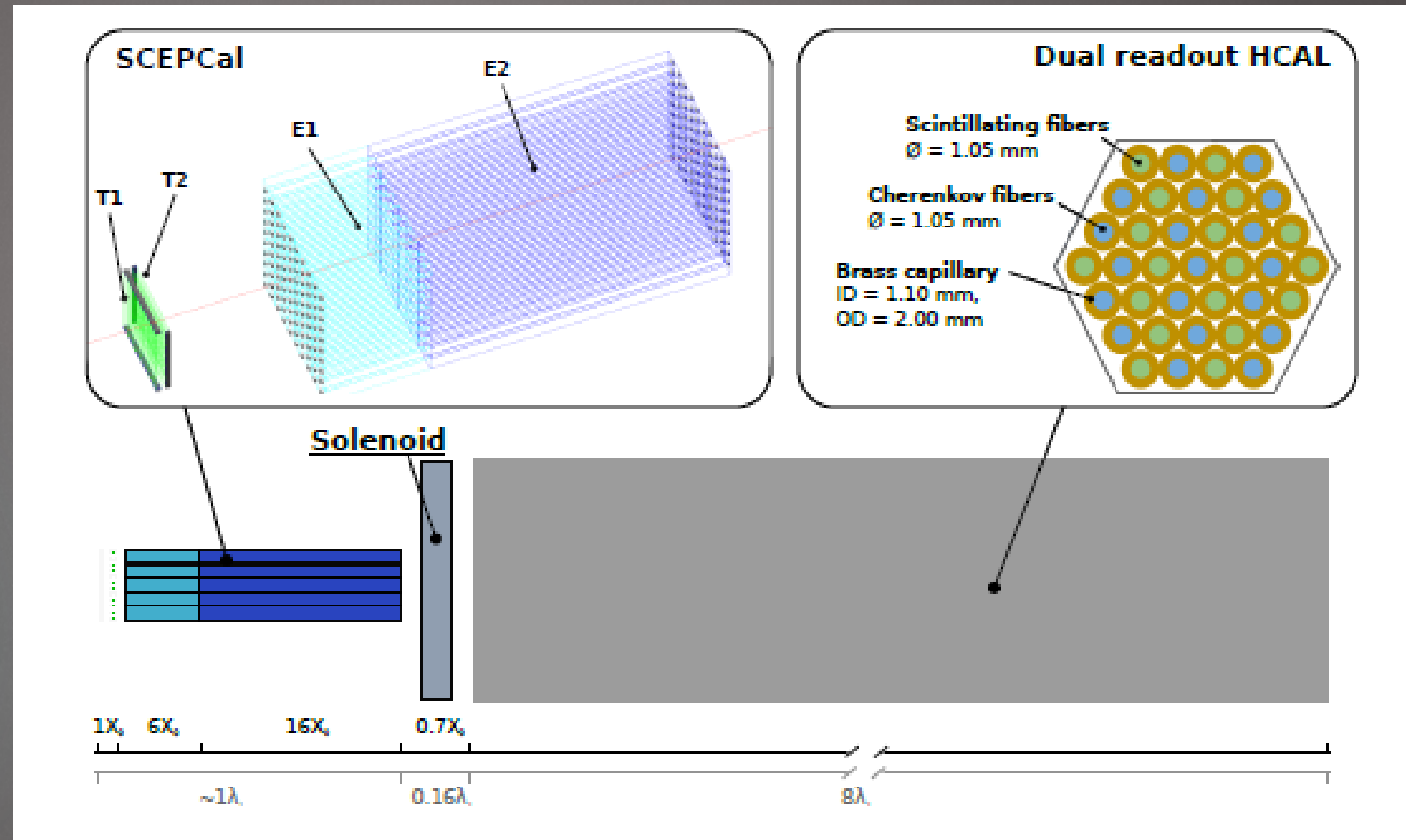
ATLAS

- ▶ Same technology for ECAL and most of HCAL leads to improved hadron resolution (will discuss)
- ▶ The gold standard in rad hard
- ▶ Very stable calibration



SCEPCAL+ IDEA

Proposed dual-readout calorimeter



Needs/challenges

- Precise energy scale and excellent resolution
- Handle a wide range of particle momenta (MeV to 100's of GeV)
- Calibration with minimal dependence on particle type (measure all kinds of particles)
- High collision rate
- Pileup
- Fierce radiation environments
- Insensitive to beam backgrounds (halo, etc)

COST!

LHCC-G_165

Table 1: Summary of CORE costs for the CMS Phase II Upgrade.

CORE cost estimate	MCHF (2014)	Further Details in Table
Pixel Detector	23	8
Outer tracker	89	8
Tracking System	112	
EB electronics	10	9
HB scintillators	1	9
Endcap HGC+BHE	64	10
Calorimeters	75	
DT and CSC electronics	10	11
Muon stations: GE11, GE21, RE31 and RE41	10	11
Muon extension ME0	5	11
Muon Systems	25	
Beam Monitors and Luminosity	4	12
Hardware trigger	7	13
HLT	11	14
DAQ	6	14
Trigger and DAQ	24	
Infrastructure, Systems and Support, Installation	25	15
Total	265	

Resolution

$$\frac{\sigma}{E} = \frac{s}{\sqrt{E}} \oplus \frac{b}{E} \oplus c$$

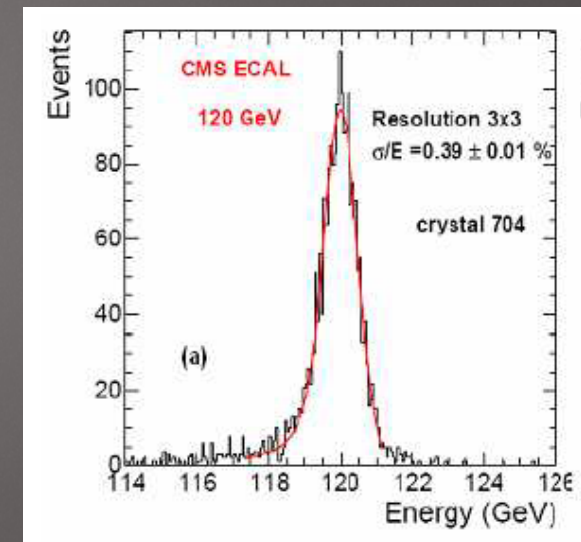
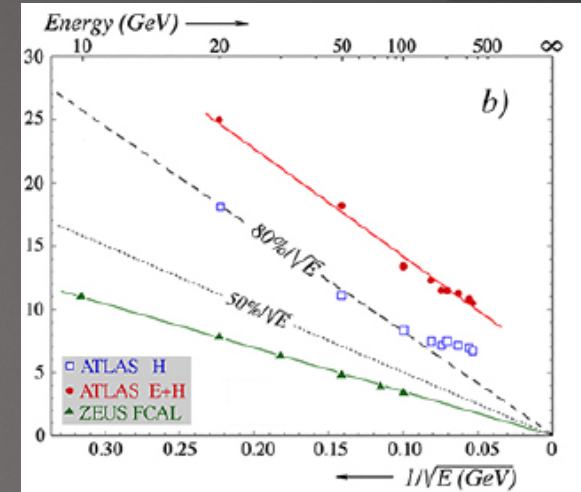
- “s” is the stochastic or “sampling” term, related to statistic fluctuations in the signal (sampling fraction for sampling calorimeters, photostatistics for homogeneous)
- “b” is the “noise” term, related to electronics noise, pileup, etc
- “c” is the “constant” term, related to imperfections, non-uniformities, channel-by-channel calibration uncertainties, leakage, dead material

Another parameterization by Wigmans, which works better for hadron energy measurements:

$$\frac{\sigma}{E} = \frac{S}{\sqrt{E}} \oplus a_2 \left[\left(\frac{E}{E_0} \right)^{l-1} \right] \approx \frac{s}{E} + a_2$$

$$a_2 = \left| 1 - \frac{h}{e} \right|$$

As you can see from these parameterizations, resolution improves with energy



Beware of tails

Often not gaussian. Quoted resolutions are often from a gaussian fit near the peak

CMS ECAL: clustering effects

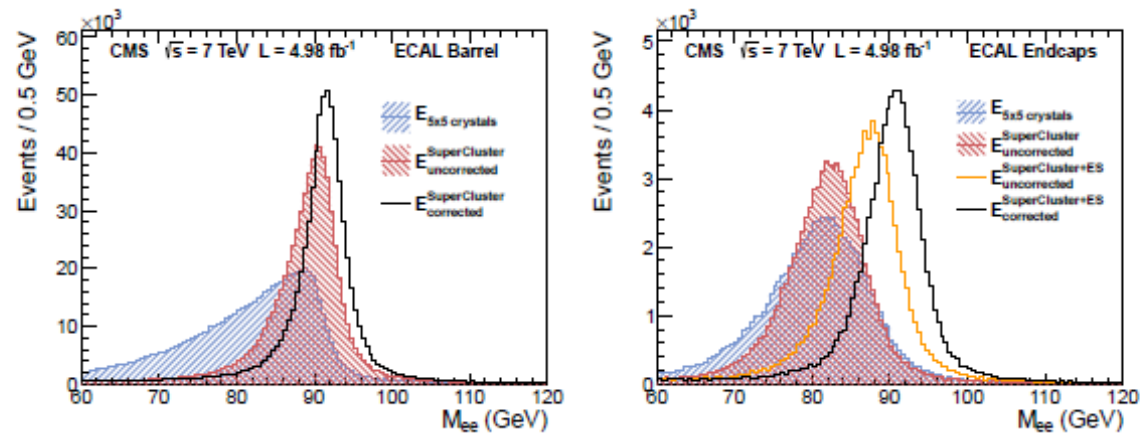


Figure 10: Reconstructed dielectron invariant mass for electrons from $Z \rightarrow e^+e^-$ events, applying a fixed-matrix clustering of 5x5 crystals, applying the supercluster reconstruction to recover radiated energy, and applying the supercluster energy corrections. For the EE the effect of adding the preshower detector energy is shown.

Can create problems for missing transverse and missing energy measurements

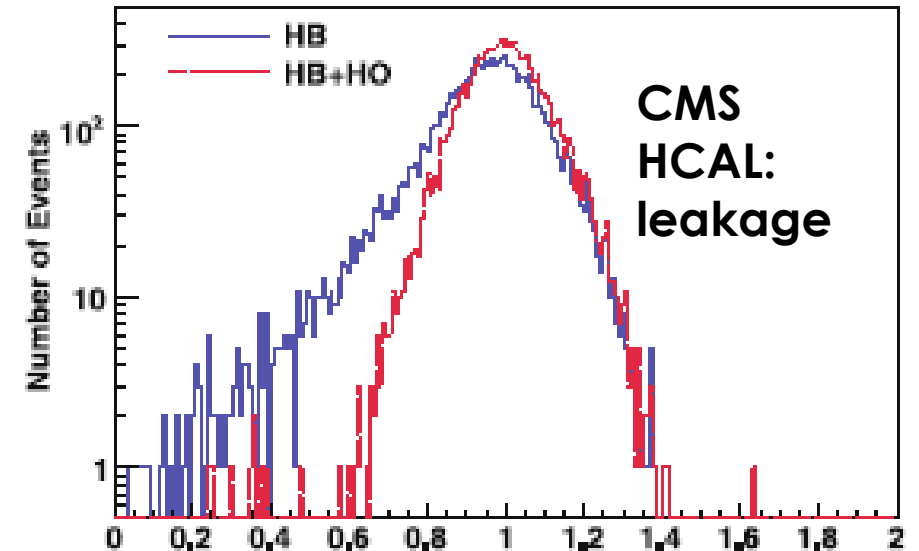


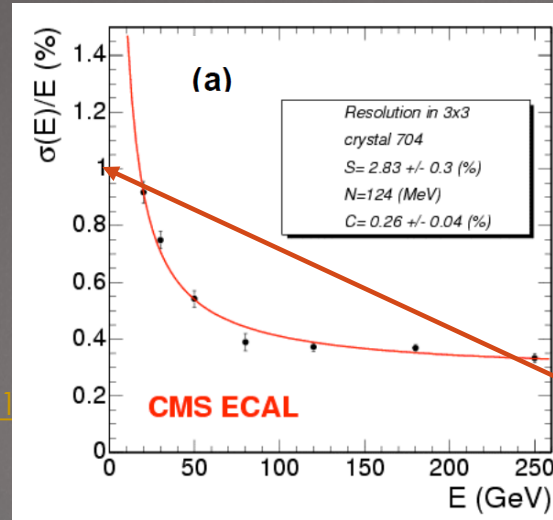
Fig. 3.3 The histograms are for the HB alone *solid (blue)*, and for the HB+HO *dashed (red)* with the optimal scale factor for the HO. The signal distributions are scaled such that 300 GeV/c is unity

EM/tracker versus HCAL

Photon resolution (CMS)

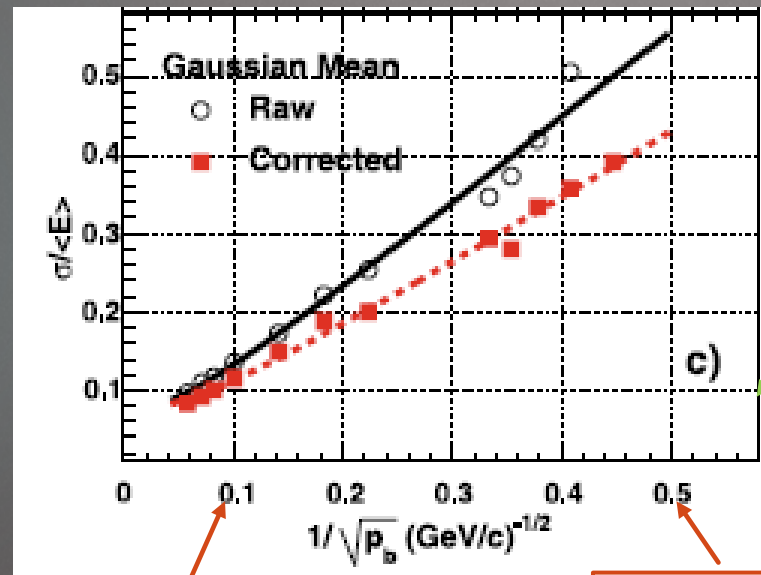
$$\frac{\sigma}{E} = \frac{2.8\%}{\sqrt{E \text{ (GeV)}}} \oplus \frac{12\%}{E \text{ (GeV)}} \oplus 0.3\%$$

Energy resolution of the barrel of the CMS electromagnetic calorimeter
<https://iopscience.iop.org/article/10.1088/1751-8121/2/04/P04004>



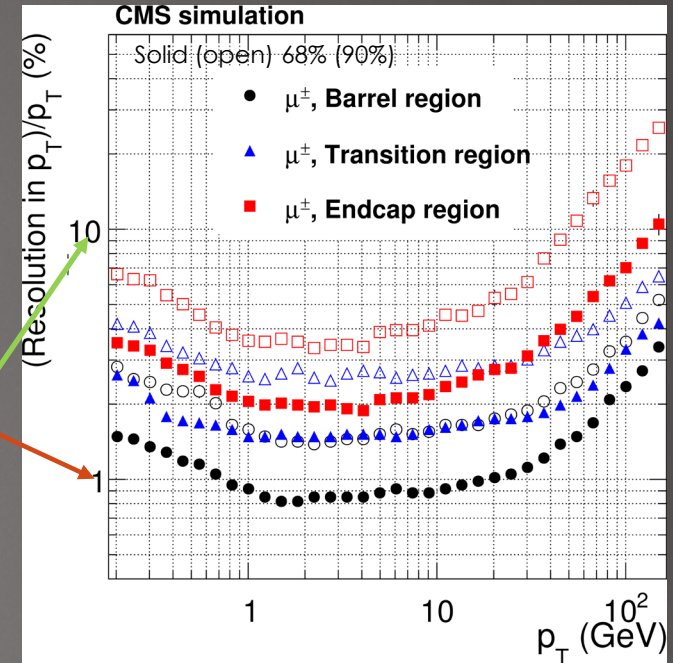
Charged pion resolution (CMS)

The CMS barrel calorimeter...
<https://link.springer.com/article/10.1140/epjc/s10052-009-0959-5>



100 GeV 4 GeV

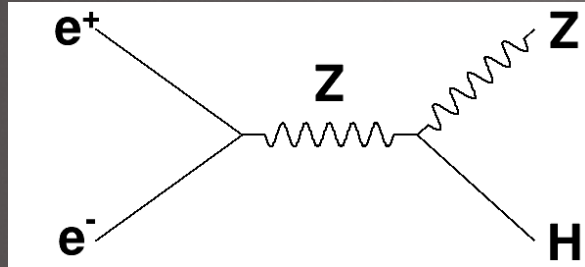
Tracker resolution, CMS



Description and performance of track... CMS tracker
<https://arxiv.org/abs/1405.6569>

Ultimate collider calorimeter: future

e^+e^-



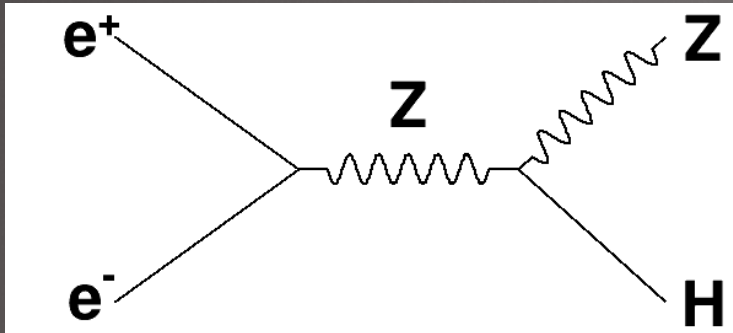
Higgs can be identified independent of decay mode using the “missing mass “ or “boson recoil mass” method, where you identify the Z and use its 3-momentum as the 3-momentum of the recoil particle and the center-of-mass collision energy minus the visible energy as the energy, requiring that to be consistent with the Higgs mass. Mass peak can distinguish ZH from WW, ZZ.

CEPC CTDR V2

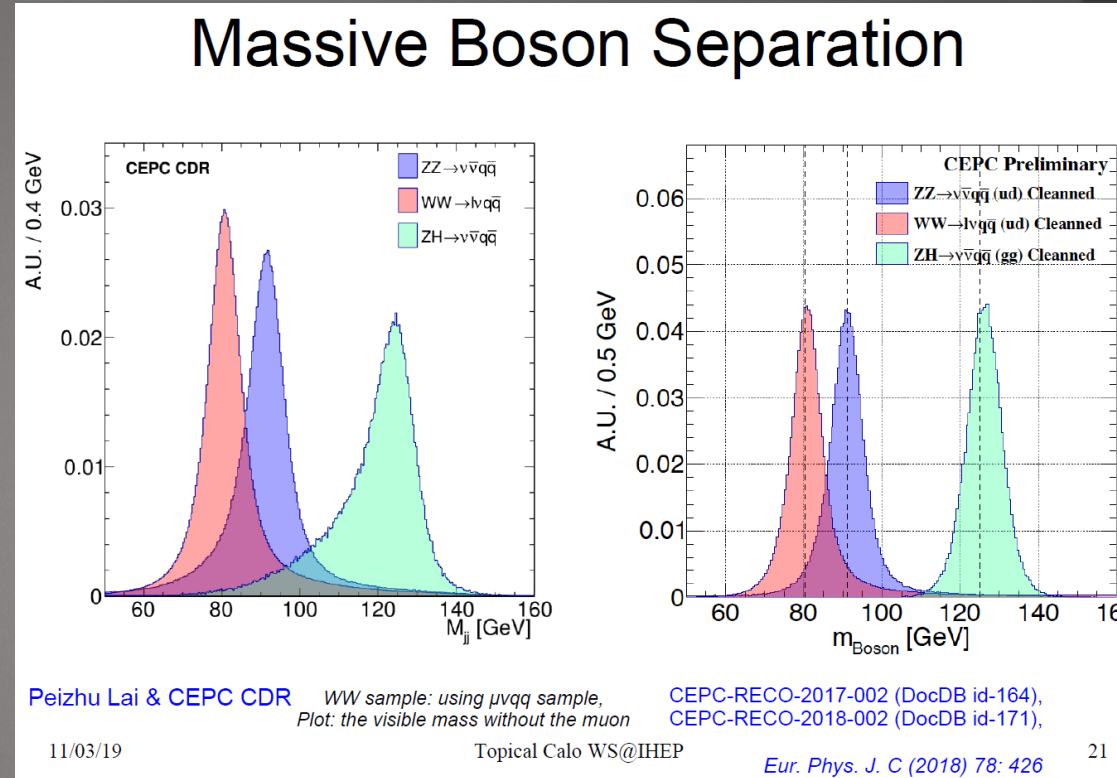
Process	Cross section	Events in 5.6 ab^{-1}
Higgs boson production, cross section in fb		
$e^+e^- \rightarrow ZH$	196.2	1.10×10^6
$e^+e^- \rightarrow \nu_e \bar{\nu}_e H$	6.19	3.47×10^4
$e^+e^- \rightarrow e^+e^- H$	0.28	1.57×10^3
Total	203.7	1.14×10^6
Background processes, cross section in pb		
$e^+e^- \rightarrow e^+e^- (\gamma)$ (Bhabha)	930	5.2×10^9
$e^+e^- \rightarrow q\bar{q} (\gamma)$	54.1	3.0×10^8
$e^+e^- \rightarrow \mu^+\mu^- (\gamma)$ [or $\tau^+\tau^- (\gamma)$]	5.3	3.0×10^7
$e^+e^- \rightarrow WW$	16.7	9.4×10^7
$e^+e^- \rightarrow ZZ$	1.1	6.2×10^6
$e^+e^- \rightarrow e^+e^- Z$	4.54	2.5×10^7
$e^+e^- \rightarrow e^+\nu W^- / e^-\bar{\nu} W^+$	5.09	2.6×10^7

Table 11.2: Cross sections of Higgs boson production and other SM processes at $\sqrt{s} = 240 \text{ GeV}$ and numbers of events expected in 5.6 ab^{-1} . Note that there are interferences between the same final states from different processes after the W or Z boson decays. Their treatments are explained in the text. With the exception of the Bhabha scattering process, the cross sections are calculated using the Whizard program [14]. The Bhabha scattering cross section is calculated using the BABAYAGA event generator [15] requiring final-state particles to have $|\cos \theta| < 0.99$. Photons, if any, must have $E_\gamma > 0.1 \text{ GeV}$ and $|\cos \theta_{e\pm\gamma}| < 0.99$.

Separate EWK bosons



Physics process	Measurands	Detector subsystem	Performance requirement
$ZH, Z \rightarrow e^+e^-, \mu^+\mu^-$ $H \rightarrow \mu^+\mu^-$	$m_H, \sigma(ZH)$ $BR(H \rightarrow \mu^+\mu^-)$	Tracker	$\Delta(1/p_T) = 2 \times 10^{-5} \oplus \frac{0.001}{p(\text{GeV}) \sin^{3/2} \theta}$
$H \rightarrow b\bar{b}/c\bar{c}/gg$	$BR(H \rightarrow b\bar{b}/c\bar{c}/gg)$	Vertex	$\sigma_{r\phi} = 5 \oplus \frac{10}{p(\text{GeV}) \times \sin^{3/2} \theta} (\mu\text{m})$
$H \rightarrow q\bar{q}, WW^*, ZZ^*$	$BR(H \rightarrow q\bar{q}, WW^*, ZZ^*)$	ECAL HCAL	$\sigma_E^{\text{jet}}/E = 3 \sim 4\%$ at 100 GeV
$H \rightarrow \gamma\gamma$	$BR(H \rightarrow \gamma\gamma)$	ECAL	$\frac{\Delta E}{E} = \frac{0.20}{\sqrt{E(\text{GeV})}} \oplus 0.01$

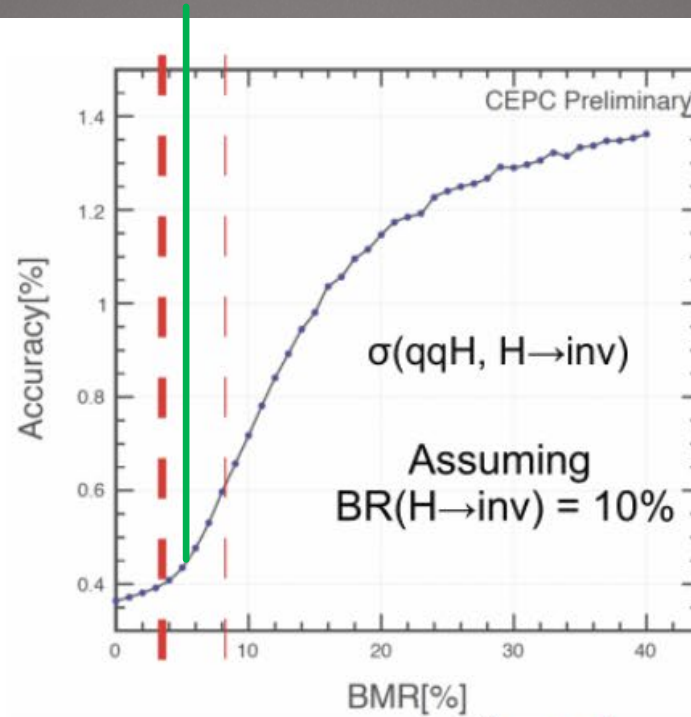
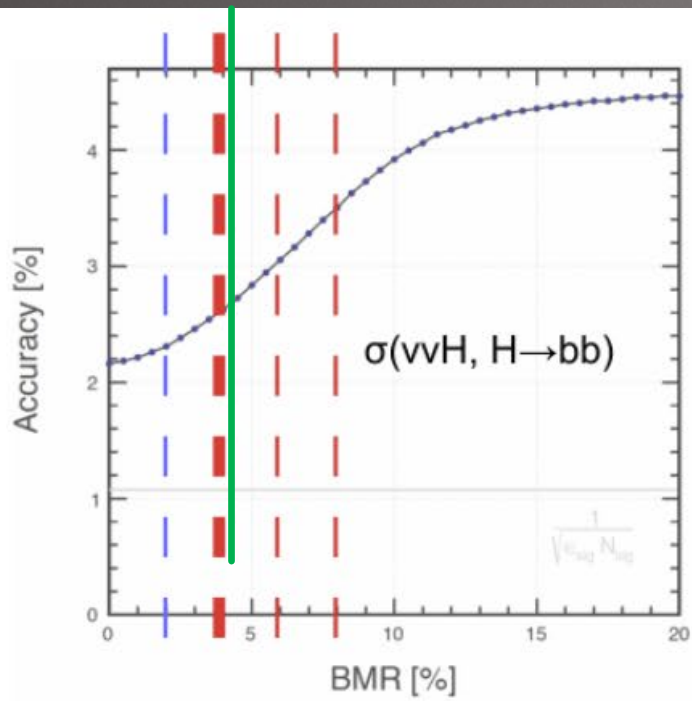


3-4% at 100 GeV corresponds to a sampling term of 30%

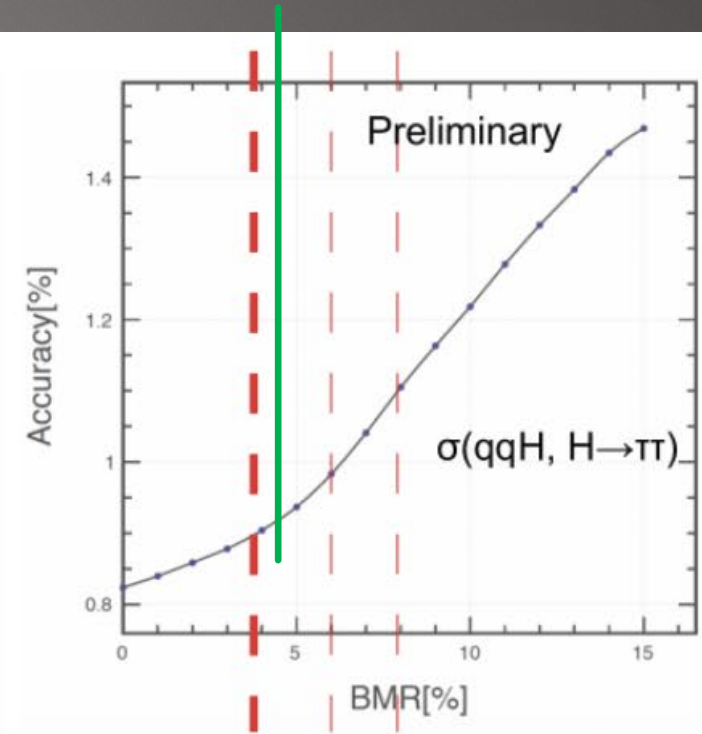
As we will discuss in detail, there are two approaches to achieving this resolution: using the calorimeter as little as possible (PFA high granularity calorimetry) or developing a new kind of precision calorimeter (dual readout)

Jet resolution is essential to $e^+ e^-$ Higgs factory calorimetry

22



$$Accuracy = \frac{\sqrt{S+B}}{S}$$



3

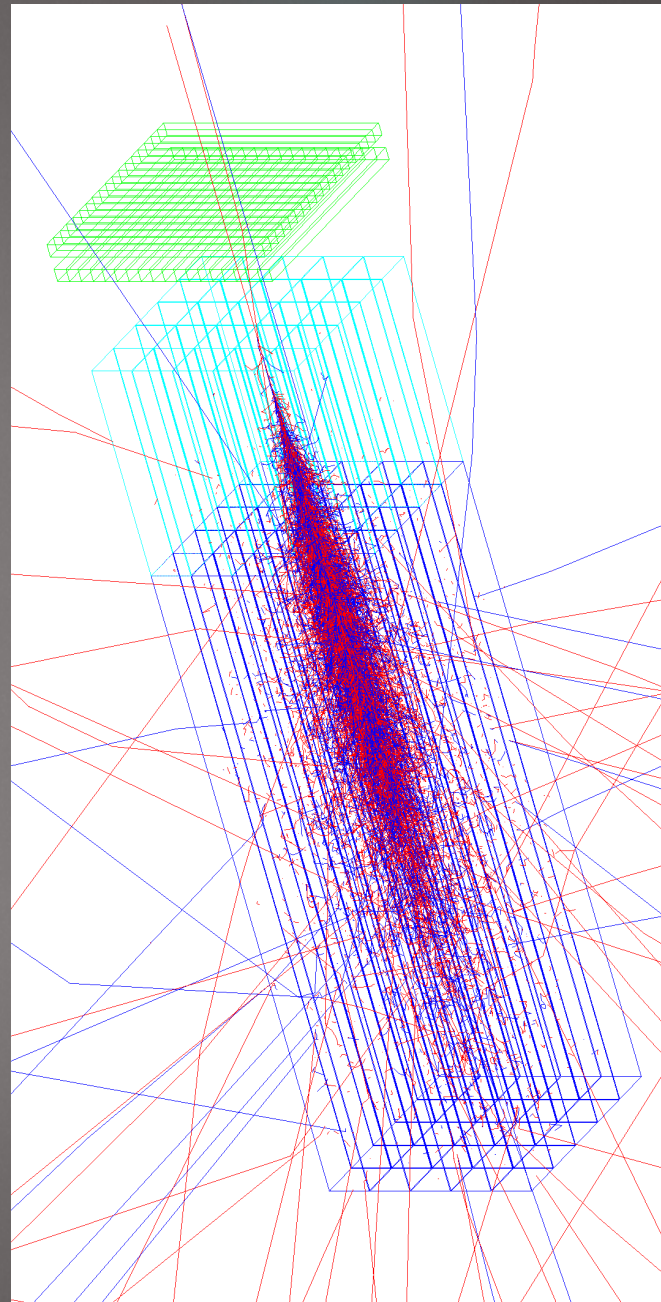


Electromagnetic calorimetry

What we call calorimetry when our goal is to measure electrons/positrons/photons

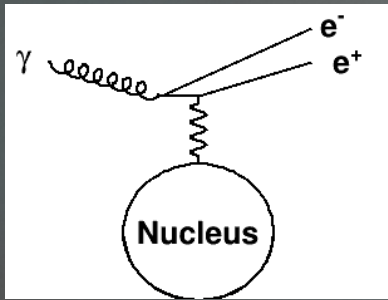
Electromagnetic shower

Particle interactions with matter convert a high energy incident particle to a large number of low energy particles which eventually “range out” and come to rest through “ionizing” interactions with the media. The initial kinetic energy converts to mostly heat, with a small amount to some sort of measurable signal.



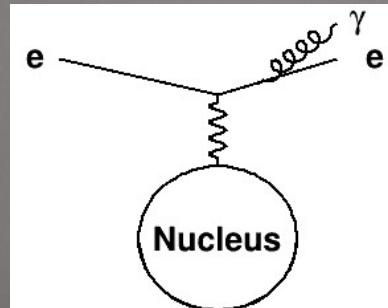
Production of new secondaries driven by two processes:

Pair production



$$-\frac{dE}{dx} \approx \frac{E}{X_0}$$

Bremsstrahlung



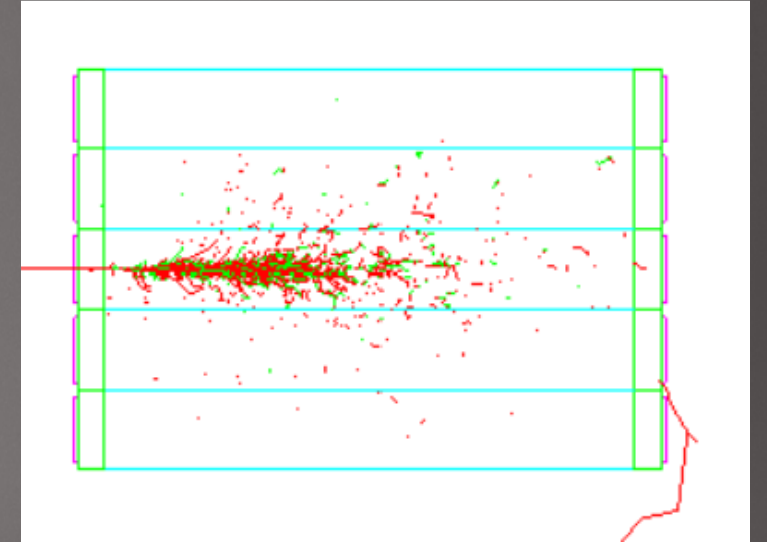
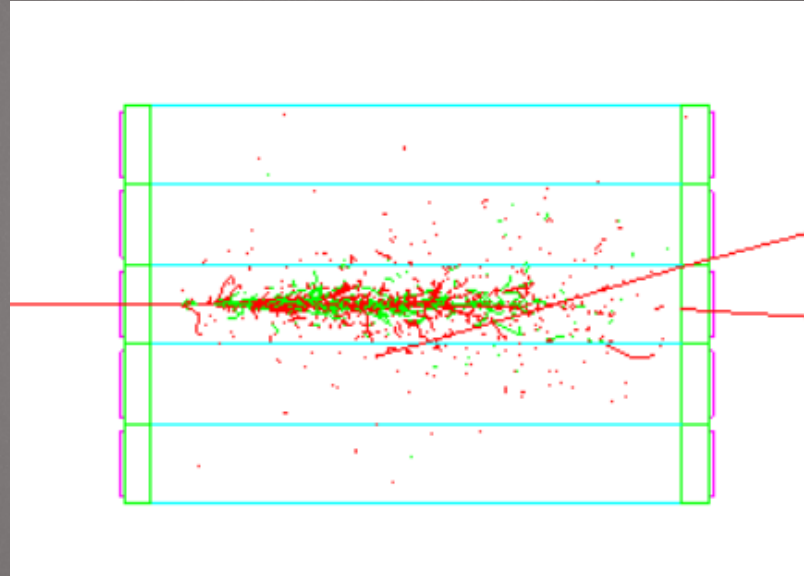
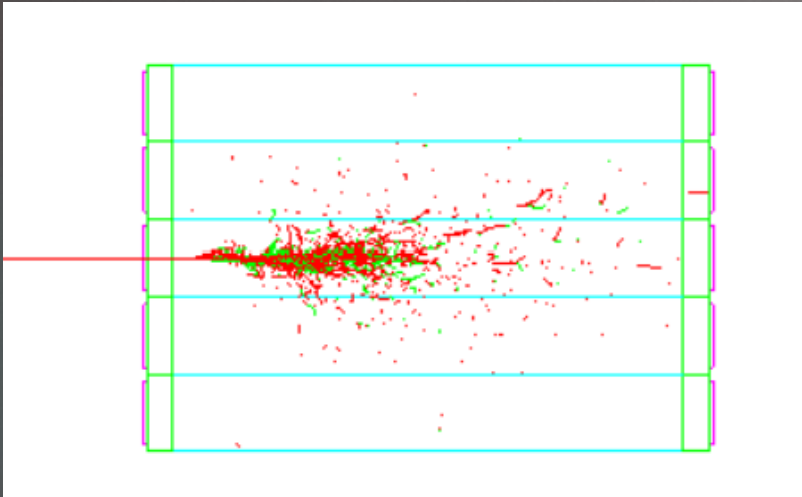
$$L_{pair} = \frac{9}{7}X_0$$

$$X_0 = \frac{716.4A}{Z(Z+1)\ln(287/\sqrt{Z})} \text{ gcm}^{-2}$$

Note units on X_0 . Multiply by density to get a length.

showers

25



Quite uniform showers

GEANT4 visualization tool

bremstrahlung

k is photon E $\frac{d\sigma}{dk} = \frac{A}{X_0 N_A k} \left(\frac{4}{3} - \frac{4}{3}y + y^2 \right) .$ (34.29)

This cross section (times k) is shown by the top curve in Fig. 34.12.

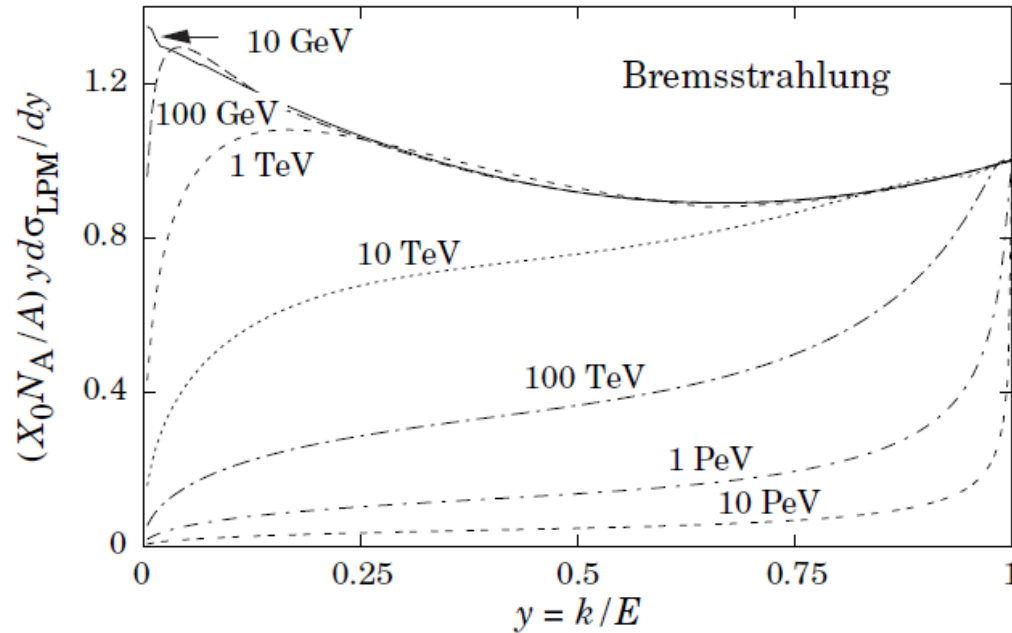
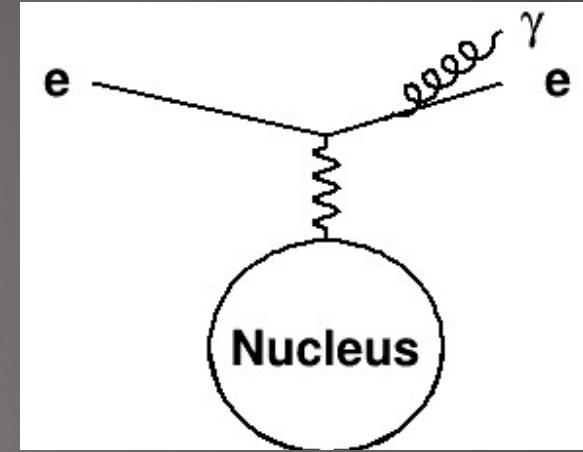


Figure 34.12: The normalized bremsstrahlung cross section $k d\sigma_{LPM}/dk$ in lead versus the fractional photon energy $y = k/E$. The vertical axis has units of photons per radiation length.



$$P_{a||v} = \frac{q^2 a^2 \left(\frac{E}{mc^2}\right)^6}{6\pi\epsilon_0 c^3}$$

$$P_{a\perp v} = \frac{q^2 a^2 \left(\frac{E}{mc^2}\right)^4}{6\pi\epsilon_0 c^3}$$

Except at very high energies, only electrons have significant brem.

Other processes

What actually makes the detector signal

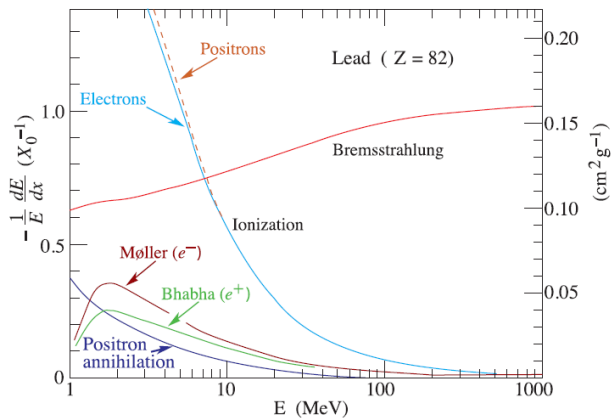


Figure 34.11: Fractional energy loss per radiation length in lead as a function of electron or positron energy. Electron (positron) scattering is considered as ionization when the energy loss per collision is below 0.255 MeV, and as Møller (Bhabha) scattering when it is above. Adapted from Fig. 3.2 from Messel and Crawford, *Electron-Photon Shower Distribution Function Tables for Lead, Copper, and Air Absorbers*, Pergamon Press, 1970. Messel and Crawford use $X_0(\text{Pb}) = 5.82 \text{ g/cm}^2$, but we have modified the figures to reflect the value given in the Table of Atomic and Nuclear Properties of Materials ($X_0(\text{Pb}) = 6.37 \text{ g/cm}^2$).

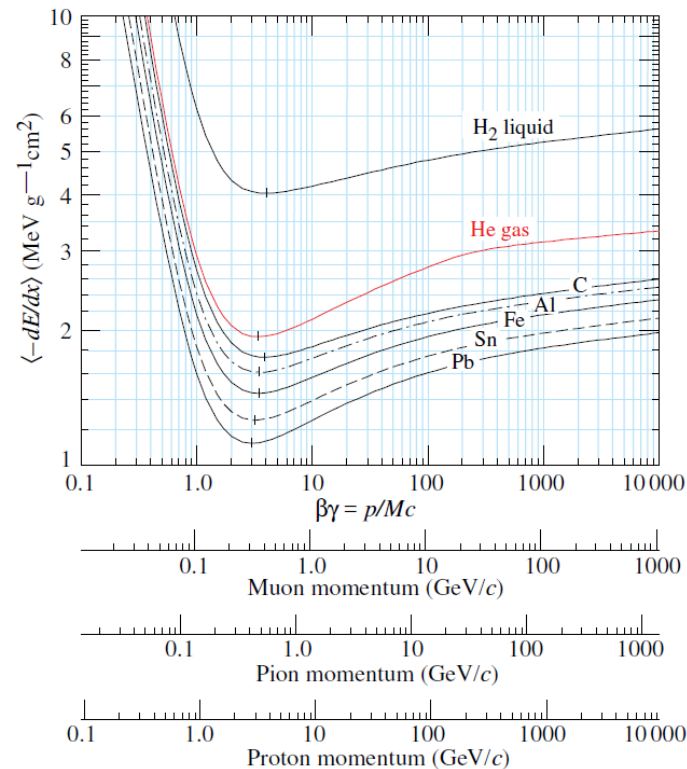


Figure 34.2: Mean energy loss rate in liquid (bubble chamber) hydrogen, gaseous helium, carbon, aluminum, iron, tin, and lead. Radiative effects, relevant for muons and pions, are not included. These become significant for muons in iron for $\beta\gamma \gtrsim 1000$, and at lower momenta for muons in higher- Z absorbers. See Fig. 34.23.

After taking out the density, and ignoring hydrogen, approximately independent of Z .

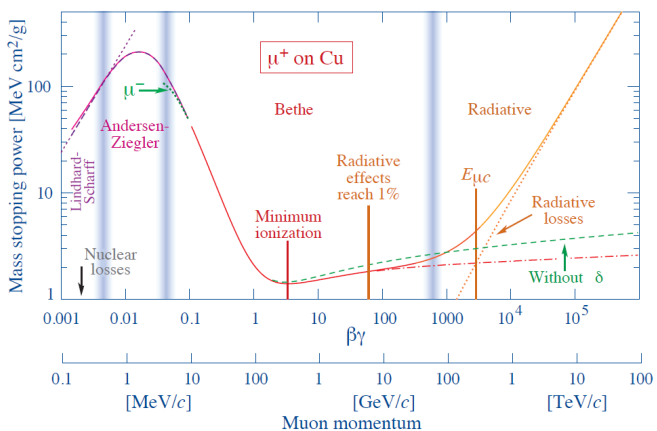


Figure 34.1: Mass stopping power ($= \langle -dE/dx \rangle$) for positive muons in copper as a function of $\beta\gamma = p/Mc$ over nine orders of magnitude in momentum (12 orders of magnitude in kinetic energy). Solid curves indicate the total stopping power. Data below the break at $\beta\gamma \approx 0.1$ are taken from ICRU 49 [4] assuming only β dependence, and data at higher energies are from [5]. Vertical bands indicate boundaries between different approximations discussed in the text. The short dotted lines labeled “ μ^- ” illustrate the “Barkas effect”, the dependence of stopping power on projectile charge at very low energies [6]. dE/dx in the radiative region is not simply a function of β .

Shower profile

Al: 13
Fe: 26
Pb: 82

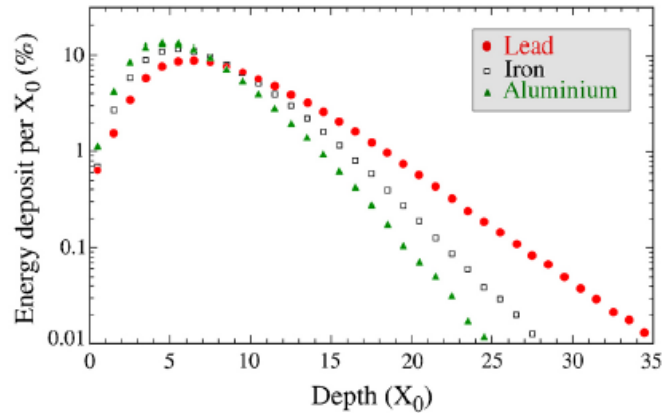


Figure 2: Energy deposit as a function of depth, expressed in radiation lengths, for 10 GeV electron showers developing in aluminium, iron and lead. Results of EGS4 calculations [5].

If you look more carefully, the shower profile does not only depend on X_0 .

The early shower is electron dominated, the later photon

Phenomenological parameterization of the position of shower max and of the shower shape

$$t_{max} = \ln\left(\frac{E_0}{E_c}\right) + c_i$$

$$\frac{dE}{dt} = C t^\alpha e^{-\beta t} \quad (9)$$

where t is the depth in the material in units of X_0 , and C , α and β are parameters to be determined empirically.

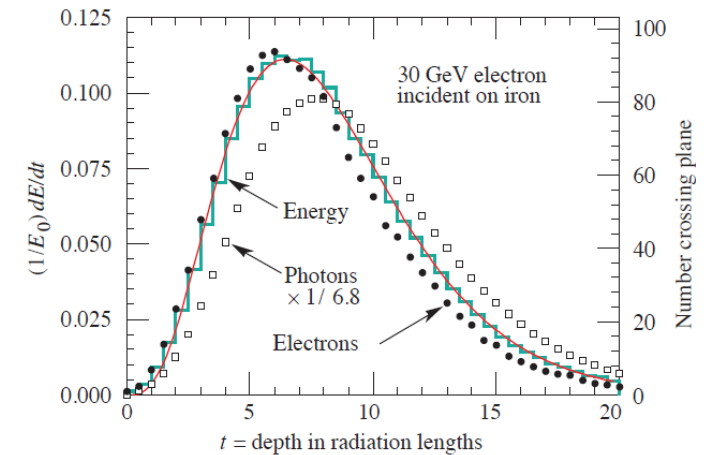


Figure 34.20: An EGS4 simulation of a 30 GeV electron-induced cascade in iron. The histogram shows fractional energy deposition per radiation length, and the curve is a gamma-function fit to the distribution. Circles indicate the number of electrons with total energy greater than 1.5 MeV crossing planes at $X_0/2$ intervals (scale on right) and the squares the number of photons with $E \geq 1.5$ MeV crossing the planes (scaled down to have same area as the electron distribution).

Critical energy

Energy loss in an X_0

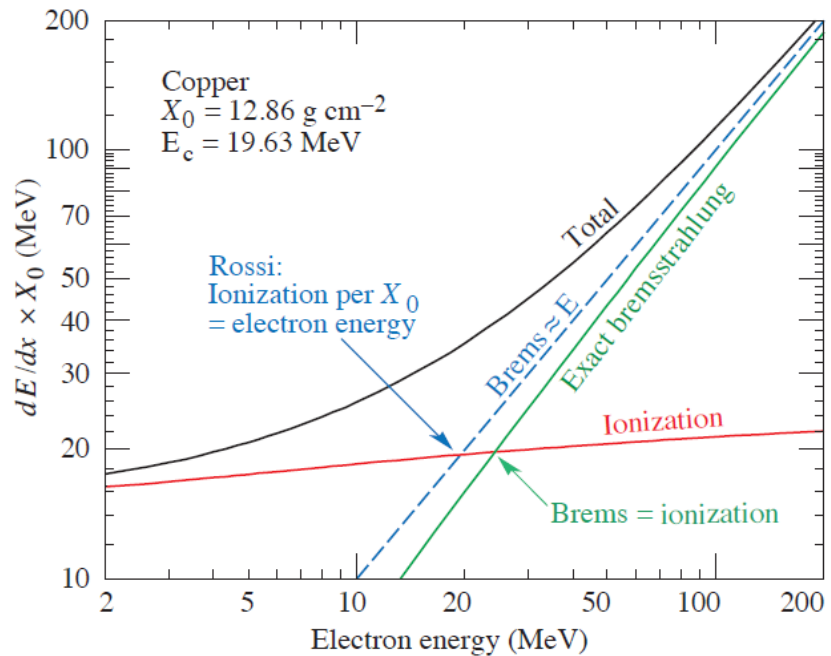


Figure 34.13: Two definitions of the critical energy E_c .

The critical energy, E_c , may be defined as the energy for which, in a given material, the rates of energy loss through ionization and bremsstrahlung are equal. For all but the lightest elements ($Z \leq 12$), the critical energy is given to an adequate approximation by the expression:

$$E_c = \frac{550}{Z} \text{ MeV} \quad (7)$$

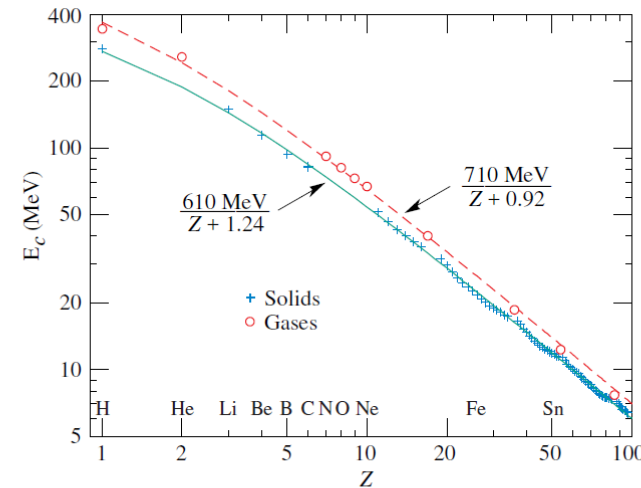


Figure 34.14: Electron critical energy for the chemical elements, using Rossi's definition [2]. The fits shown are for solids and liquids (solid line) and gases (dashed line). The rms deviation is 2.2% for the solids and 4.0% for the gases.

For higher Z materials, brem continues to be important down to lower energies

Importance of low energy particles

30

Fe: 26
Cu: 29
Pb: 82
U : 92

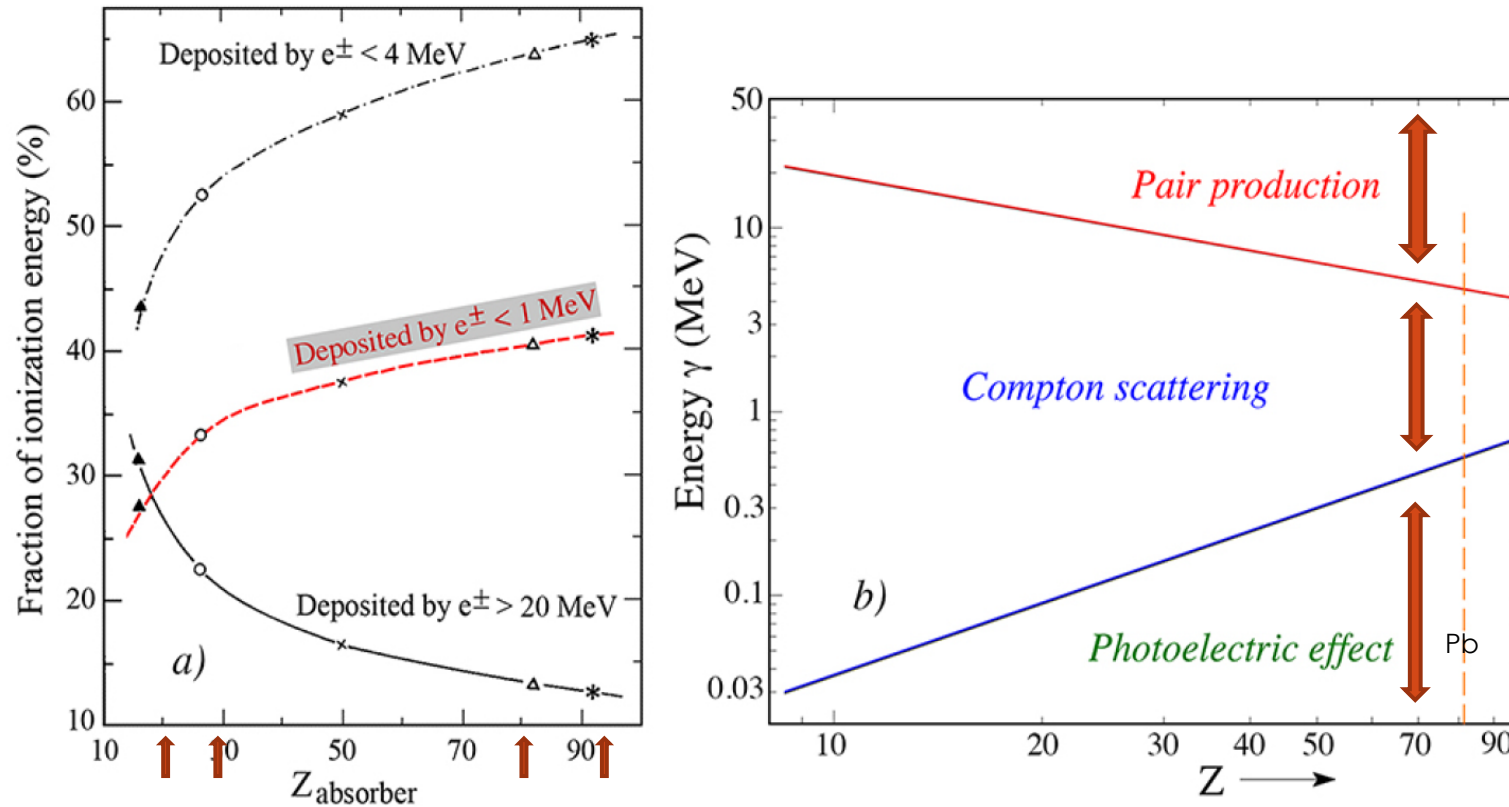


Figure 1: The composition of em showers. Shown are the percentages of the energy of 10 GeV electromagnetic showers deposited through shower particles with energies below 1 MeV (the dashed curve), below 4 MeV (the dash-dotted curve) or above 20 MeV (the solid curve), as a function of the Z of the absorber material (a). The energy domains in which photoelectric effect, Compton scattering and pair production are the most likely processes through which γ s are absorbed, as a function of the Z value of the absorber material (b). Results of EGS4 simulations [5].

A good ECAL

31

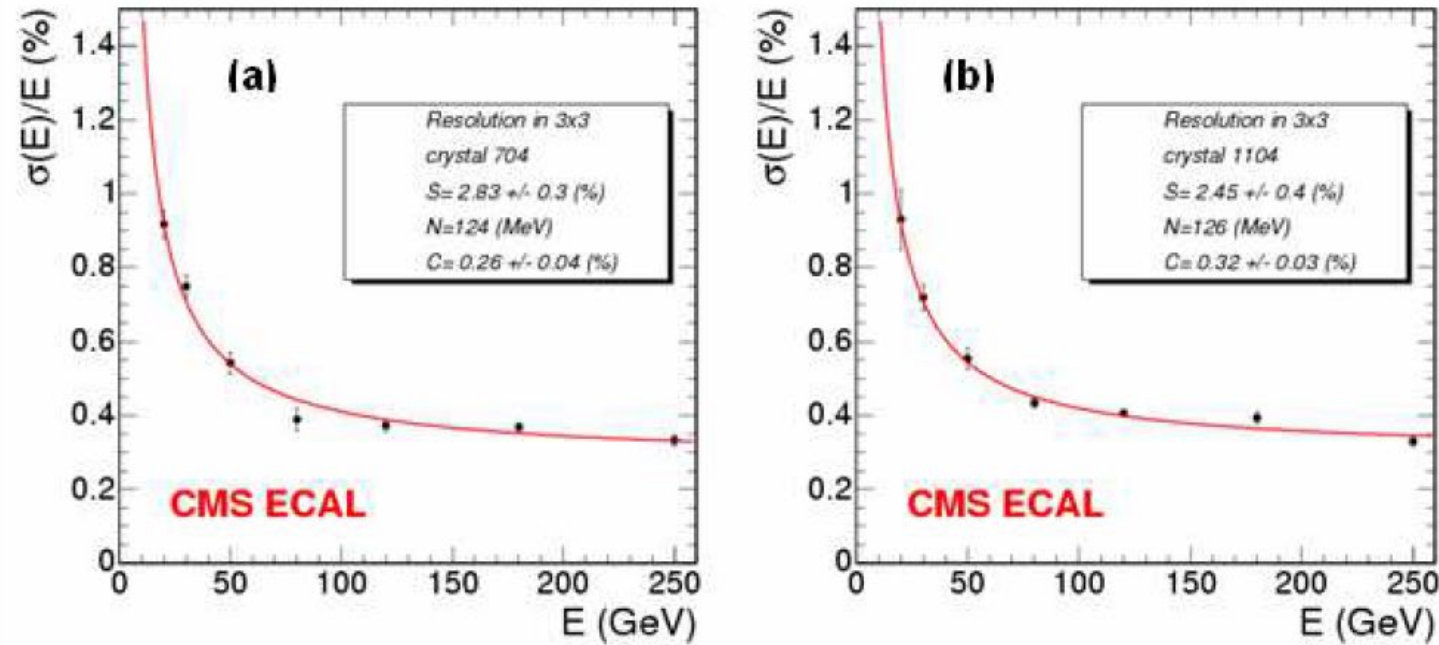


Figure 5. Resolution as a function of the energy for the 3×3 array of crystals centred a) on crystal 704 and b) on crystal 1104, with beam hodoscope cuts of 4×4 mm².

$$\frac{3\%}{\sqrt{E}} \oplus 1\%$$

Hadronic calorimetry

What we call calorimetry when our goal is to measure hadrons

Again a shower, but...

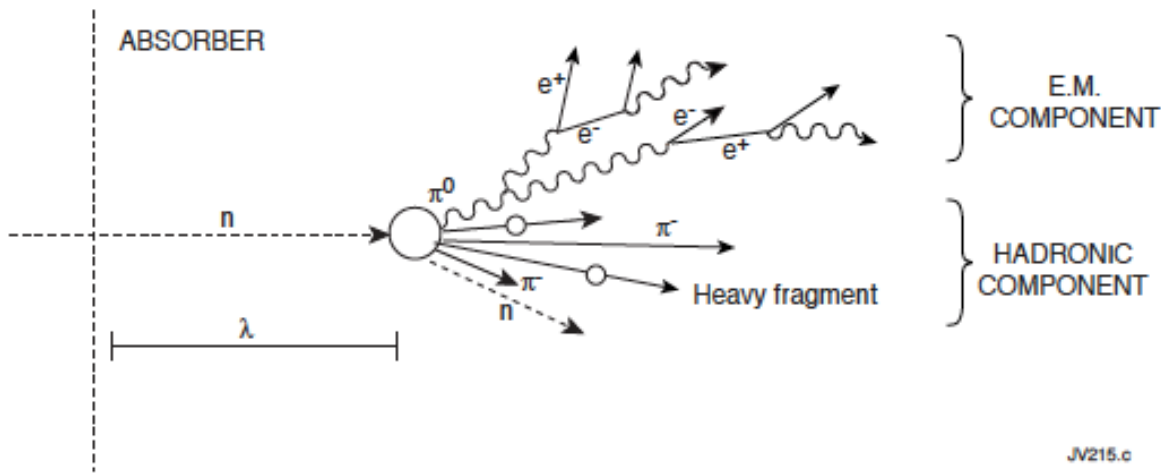


Fig. 9: Schematic of development of hadronic showers.

Look at all the different types of products: charged pions, neutral pions (to photons), ion fragments...

Multiplicity and exclusive proton-nucleon cross sections

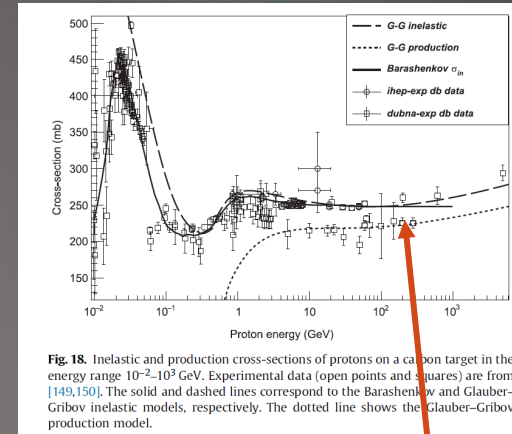


Fig. 18. Inelastic and production cross-sections of protons on a carbon target in the energy range 10^{-2} - 10^3 GeV. Experimental data (open points and squares) are from [149,150]. The solid and dashed lines correspond to the Barashenkov and Glauber-Gribov inelastic models, respectively. The dotted line shows the Glauber-Gribov production model.

At high energy, it is essentially a geometric cross section, and the cross section is small

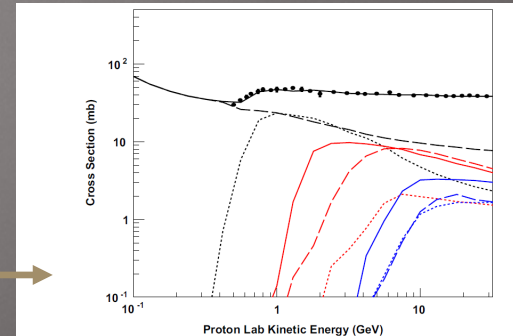


Fig. 2. Total and final state multiplicity cross-sections for n -body final states of the $p-p$ reaction. Black curves represent the total (solid), two-body (dashed) and three-body (dotted) cross-sections. Red curves represent the four-body (solid), five-body (dashed) and six-body (dotted) cross-sections. Blue curves represent the seven-body (solid), eight-body (dashed) and nine-body (dotted) cross-sections. Filled circles represent a subset of the $p-p$ total cross-section data [17]. (For interpretation of the references to color in this figure caption, the reader is referred to the web version of this paper.)

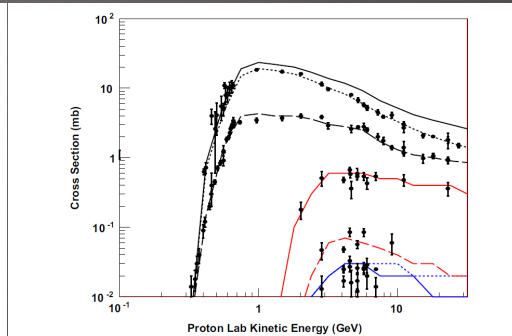
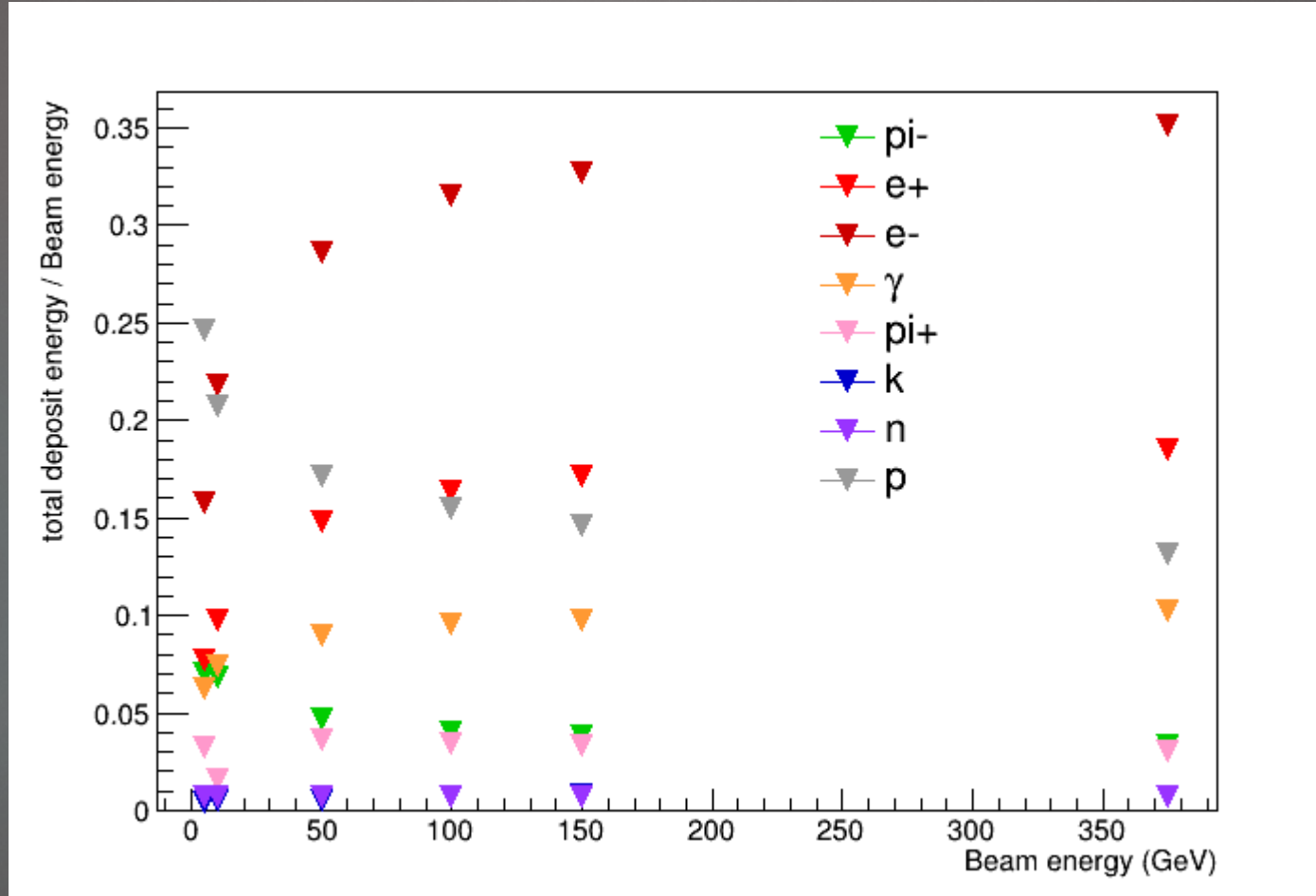


Fig. 3. Exclusive and summed three-body final state cross-sections for $p-p$ scattering. Black curves represent the total three-body final state (solid), the $p-p-p \pi^+$ (dotted), and the $p-p-p \pi^0$ (dashed) cross-sections. The solid red curve represents $p-p-p \Lambda K^+$ which has been multiplied by a factor of 10 for clarity. The dashed red curve represents $p-p-p \Sigma^+ K^+$. The blue curves represent the $p-p-p \Sigma^0 K^+$ (solid) and $p-p-p \Sigma^+ K^0$ (dashed) cross-sections. Filled circles represent experimental data. (For interpretation of the references to color in this figure caption, the reader is referred to the web version of this paper.)

Energy deposition in PbWO_4 by species for incident pion

Interaction length

35

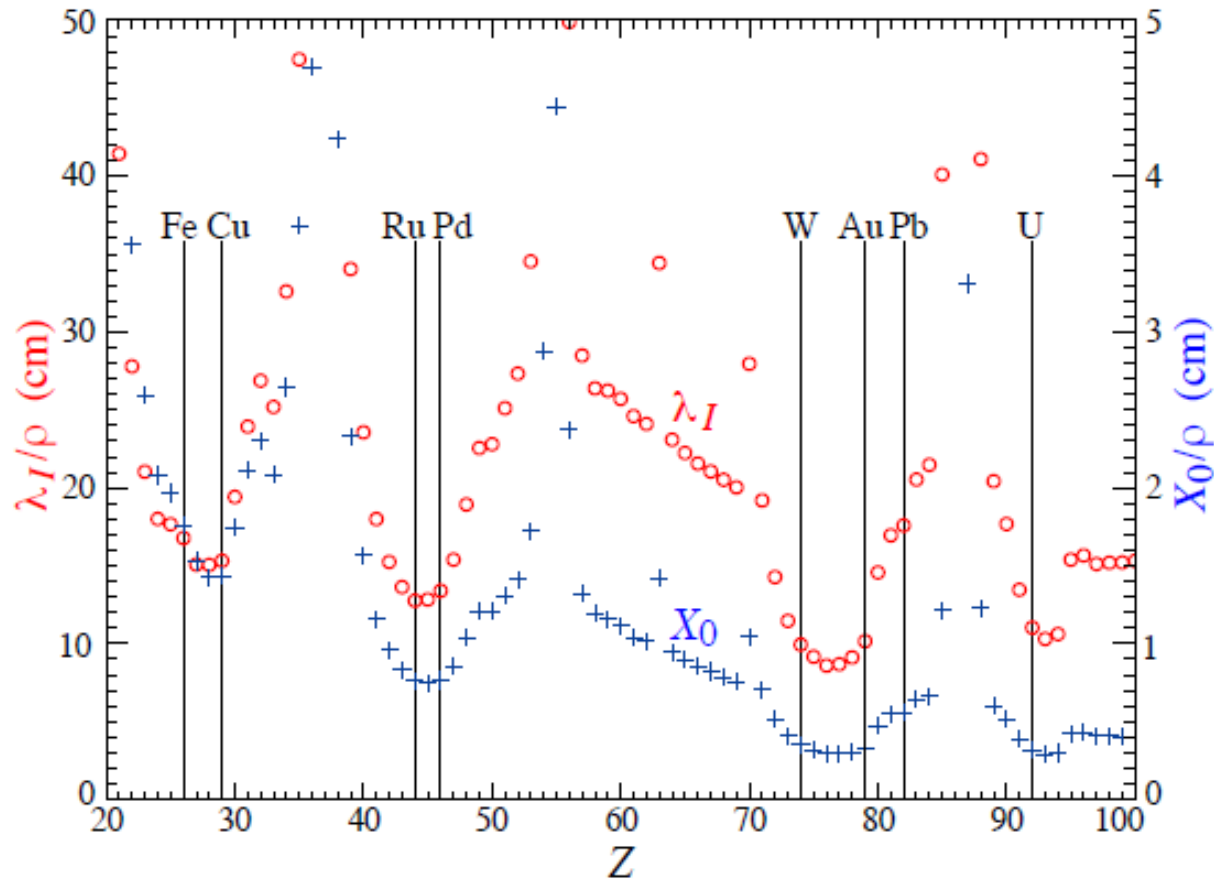


Figure 34.21: Nuclear interaction length λ_I/ρ (circles) and radiation length X_0/ρ (+'s) in cm for the chemical elements with $Z > 20$ and $\lambda_I < 50$ cm.

Again characterized by a characteristic length scale. However, since the cross section is much smaller (basically need a physical impact), the characteristic length scales are much bigger (note different y scales on left and right)

Again a shower, but...

36

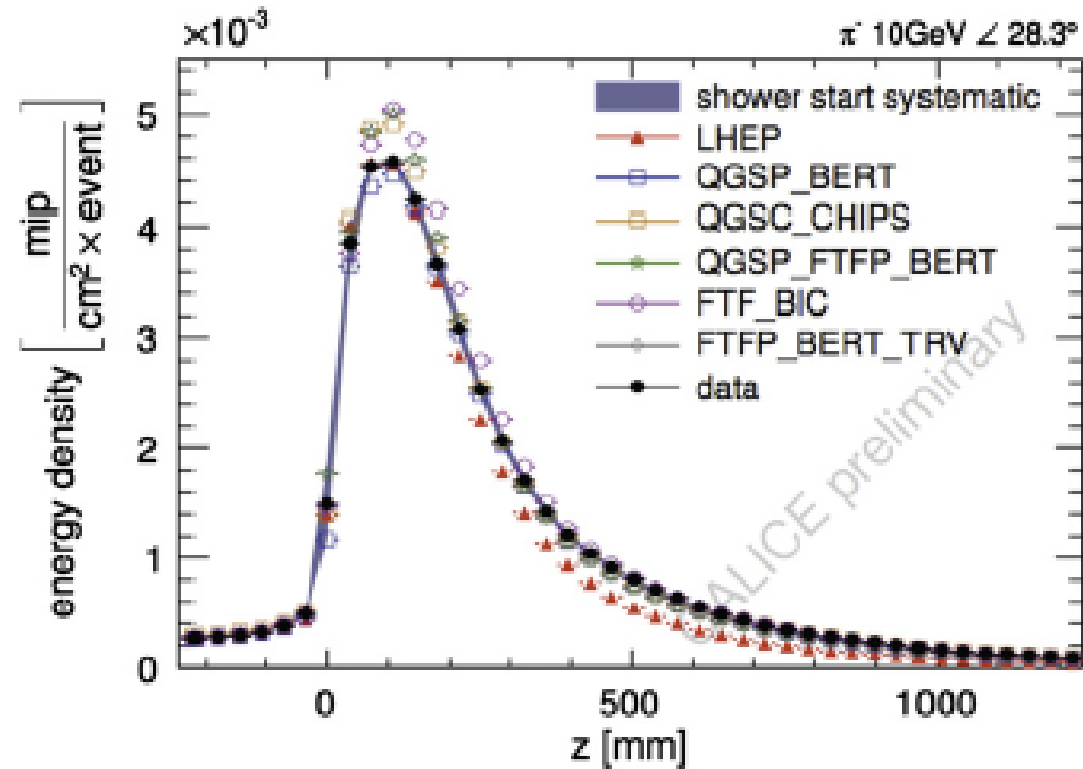


Fig. 19. The longitudinal shower profile measurement with 10 GeV π^- s is contrasted against several physics lists. See Ref. [45] for details.

Lots of variability

37

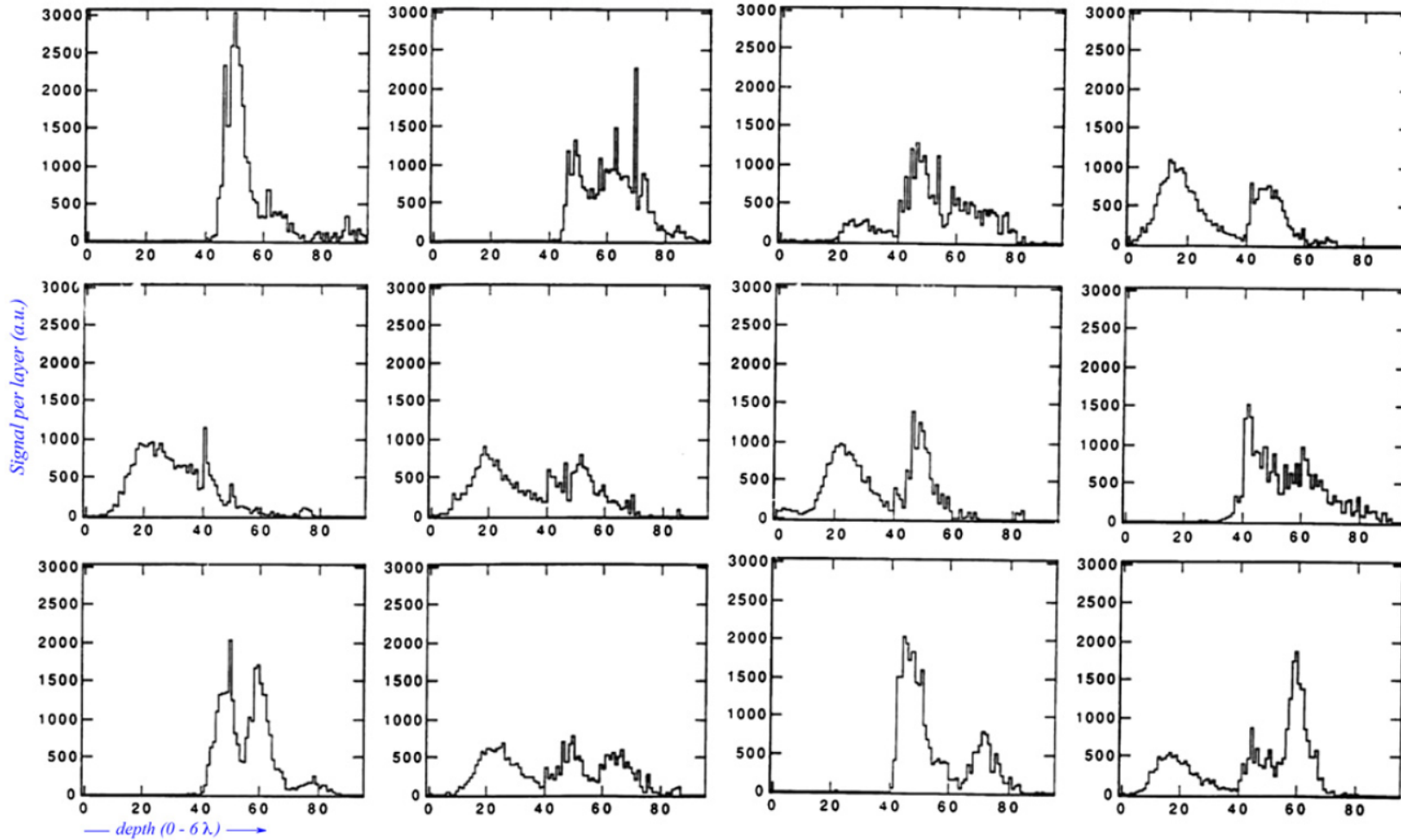
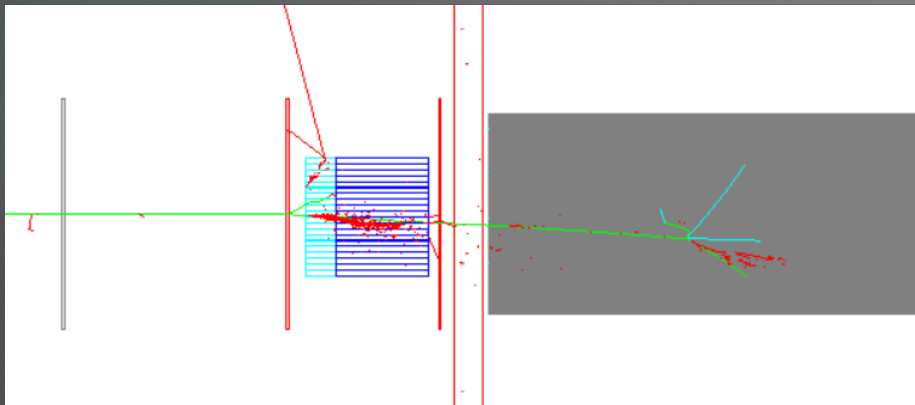
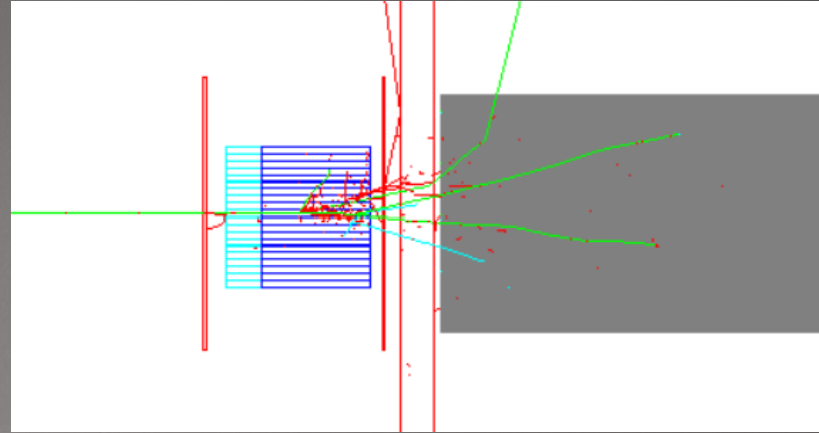
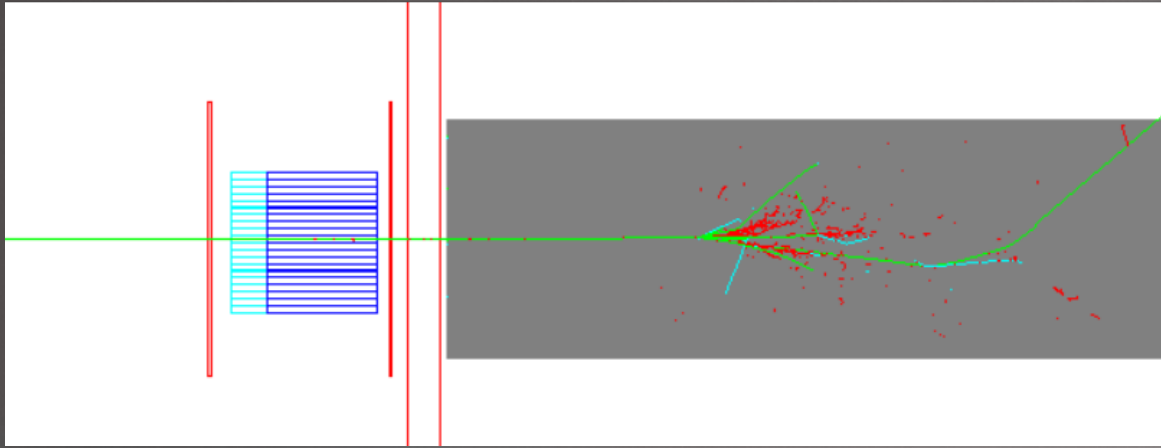


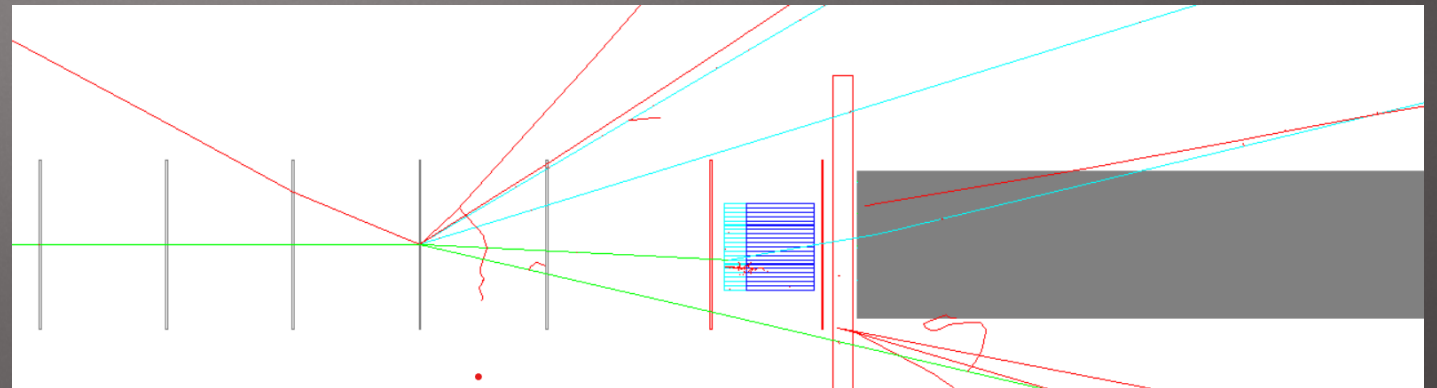
Fig. 22. Longitudinal energy deposit profiles for 270 GeV π^- showers in a lead/iron/plastic-scintillator calorimeter [13]. Shown are the longitudinal profiles for 12 randomly chosen events. For each event, the horizontal scale spans a total depth of six nuclear interaction lengths.

Lots of variability

38



Sometimes the shower starts earlier than you would like



GEANT4 visualization tools

Lots of variability

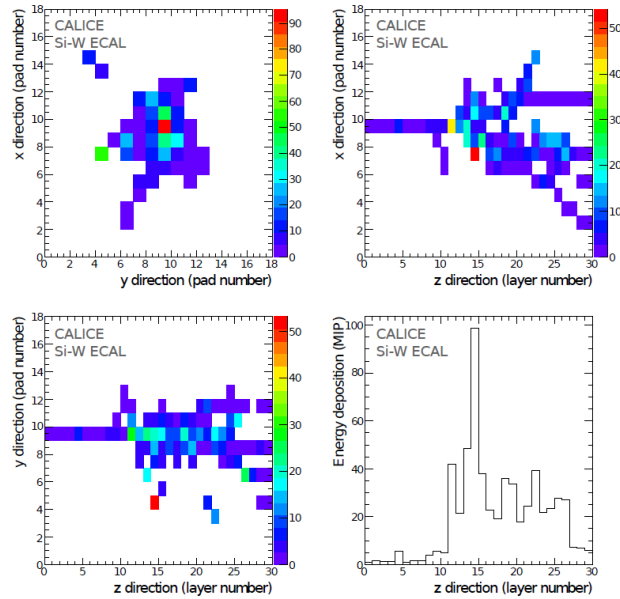


Figure 3: A hadronic interaction of a π^- with an incident kinetic energy of 10 GeV in the Si-W ECAL. Top left: projection in the x-y plane of the reconstructed energy. Top right: projection on the x-z plane of the reconstructed energy. Bottom left: projection on the y-z plane of the reconstructed energy. Bottom right: the reconstructed energy in each layer of the Si-W ECAL. The energy unit is in MIPs.

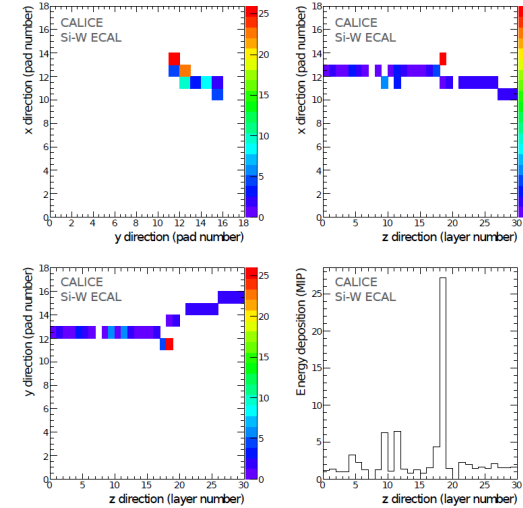


Figure 4: A hadronic interaction of a π^- with an incident kinetic energy of 2 GeV in the Si-W ECAL. Top left: projection in the x-y plane of the reconstructed energy. Top right: projection on the x-z plane of the reconstructed energy. Bottom left: projection on the y-z plane of the reconstructed energy. Bottom right: the reconstructed energy in each layer of the Si-W ECAL. The energy unit is in MIPs.

Testing hadronic interaction models using a highly granular silicon-tungsten calorimeter (arXiv:1411.7215)

Different responses

40

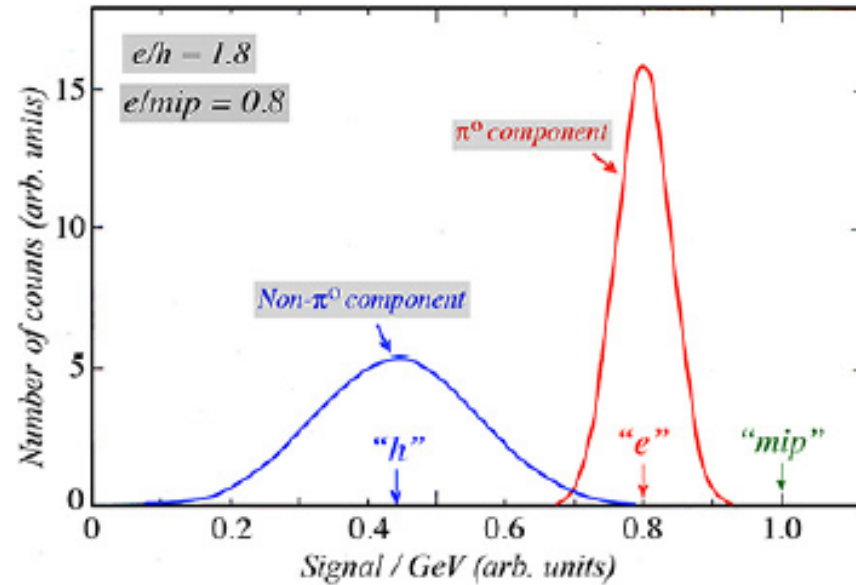


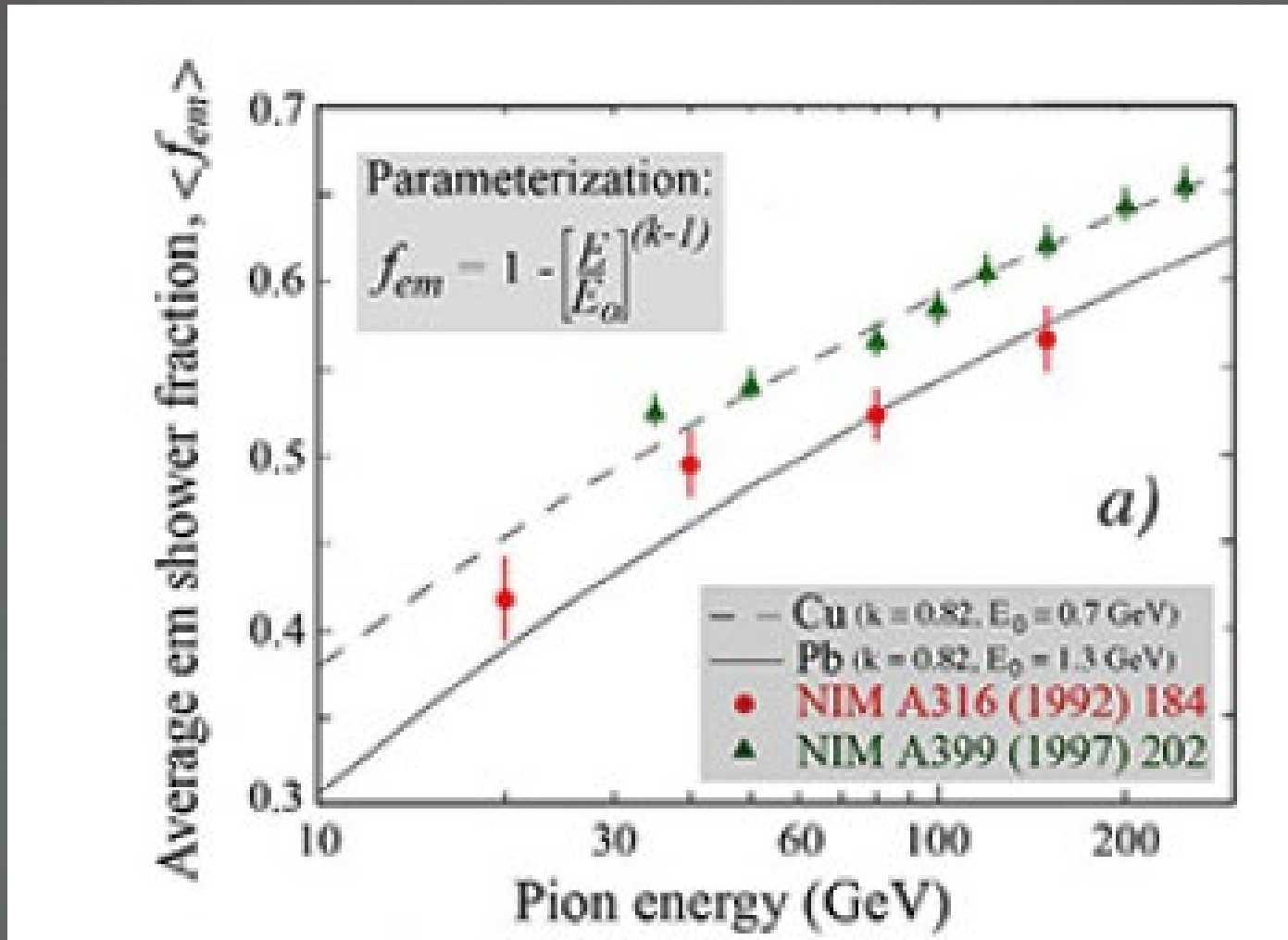
FIG. 2: Illustration of the meaning of the e/h and e/mip values of a (generic) calorimeter. Shown are distributions of the signal per unit deposited energy for the electromagnetic and non-em components of hadron showers. These distributions are normalized to the response for minimum ionizing particles (“ mip ”). The average values of the em and non-em distributions are the em response (“ e ”) and non-em response (“ h ”), respectively.

The signal depends on the particle type. To LO, though, there is a response to high energy muons, to the “EM” part of the shower generated by neutral pions, and the the “hadronic” rest of the shower.

The ratio of the response for the EM and HAD parts varies by material. It is 1.3 in the CMS HCAL and 2.4 in the CMS ECAL.

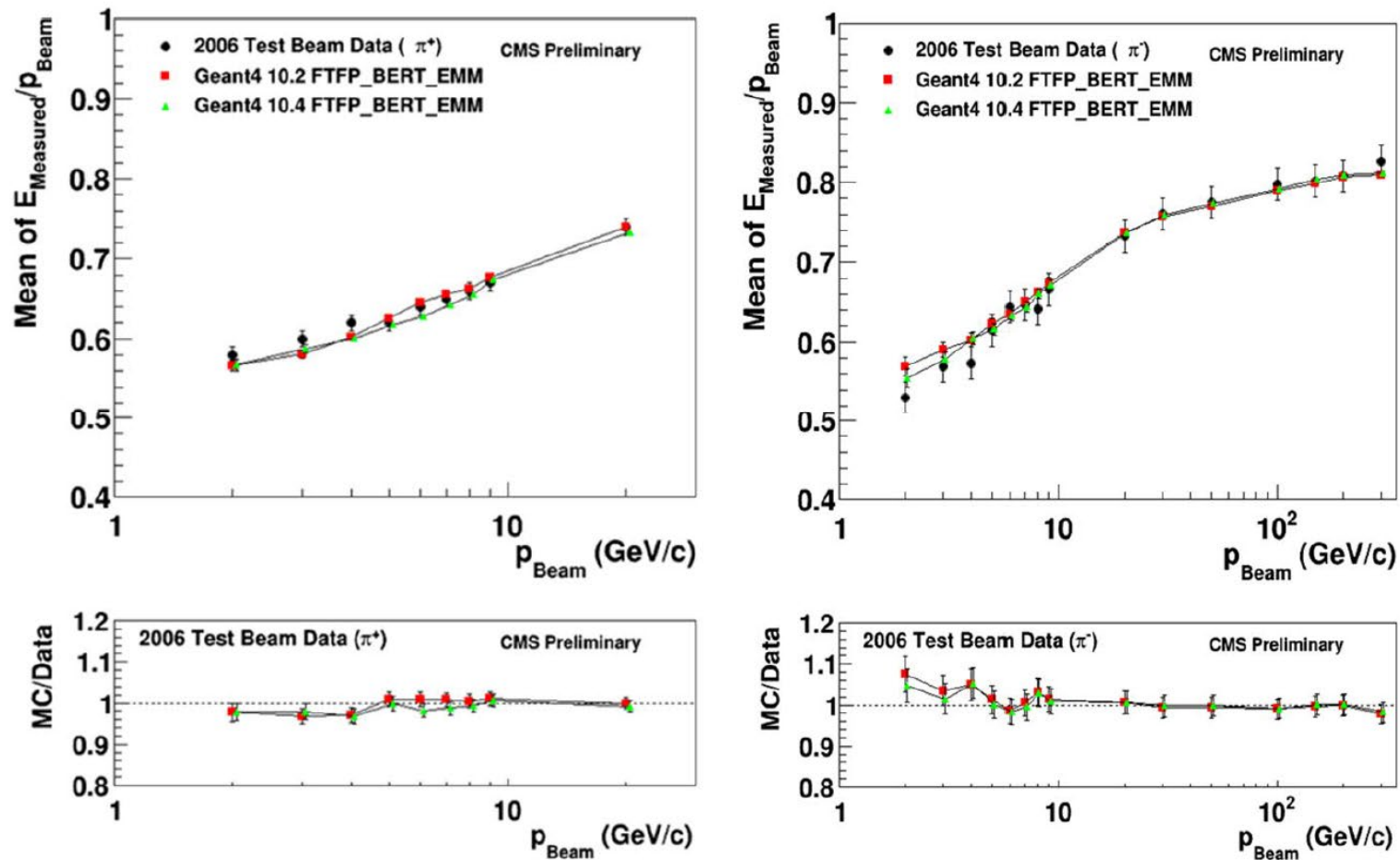
Fluctuations in the EM fraction of the shower are generally the dominate contribution to calorimeter resolution.

EM fraction versus pion energy



nonlinearity

42



Different for π^+ and π^- .

Fig. 1. Mean energy response of combined calorimeter for charged pion beams as a function of beam momenta.

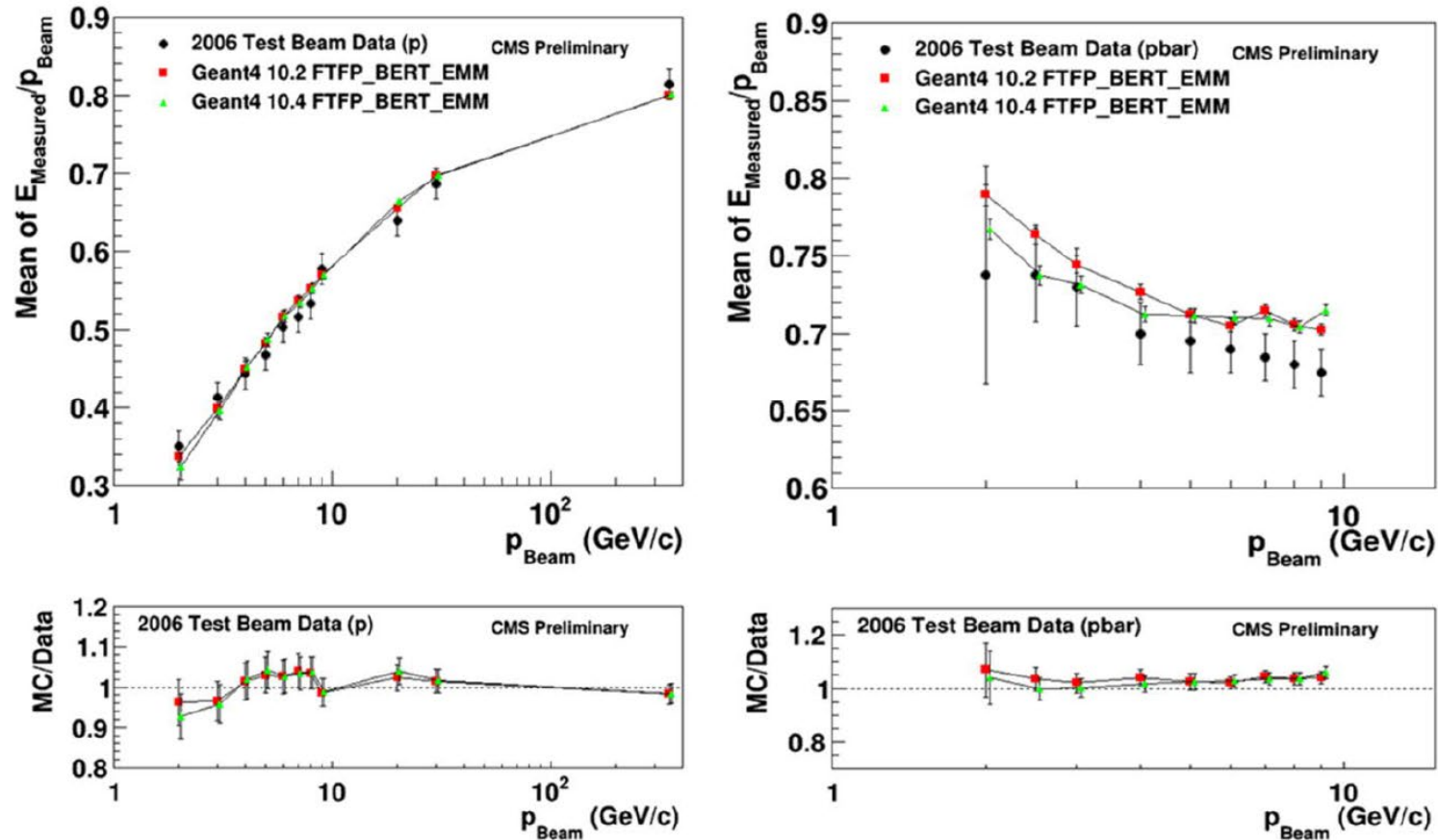


Fig. 2. Mean energy response of combined calorimeter for proton (left) and anti-proton (right) beams as a function of beam momenta.

Different for π and protons and for antiprotons

The resolution of a hadronic calorimeter is determined both by statistical (sampling) fluctuations and by shower composition fluctuations.

$$\frac{\sigma}{E} = \frac{a_1}{\sqrt{E}} \oplus a_2 \left[\left(\frac{E}{E_0} \right)^{l-1} \right]$$

Second term is due to EM fraction fluctuations, and a_2 is determined by e/h

Dual readout calorimeter (arXiv: 1712.05494)

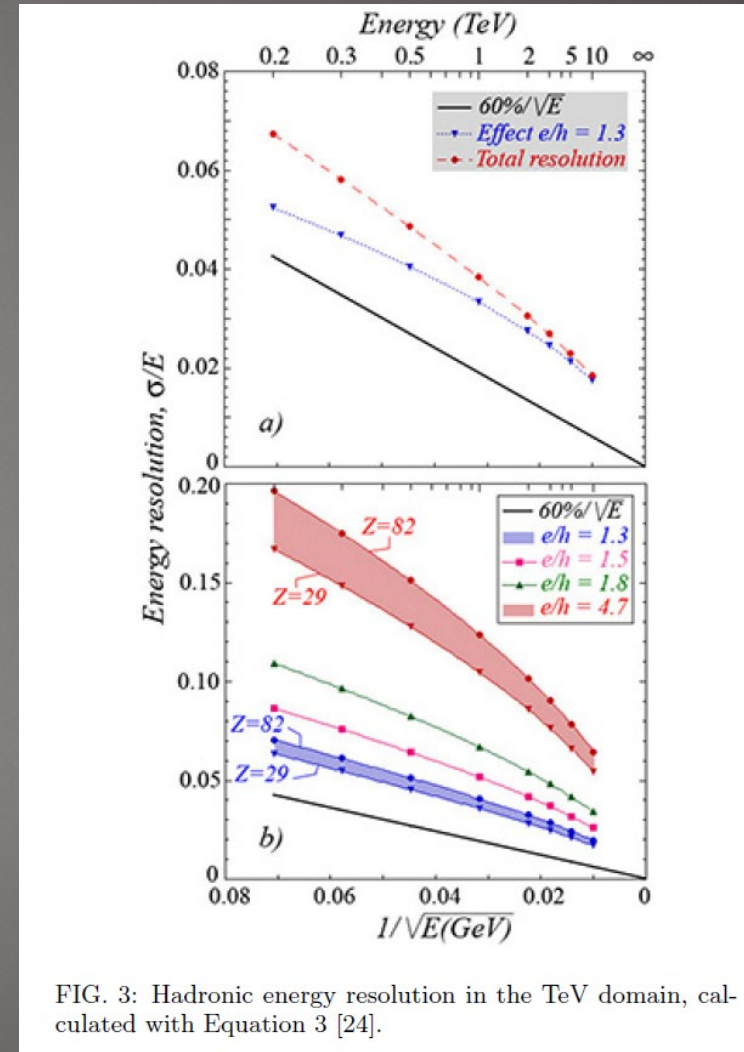
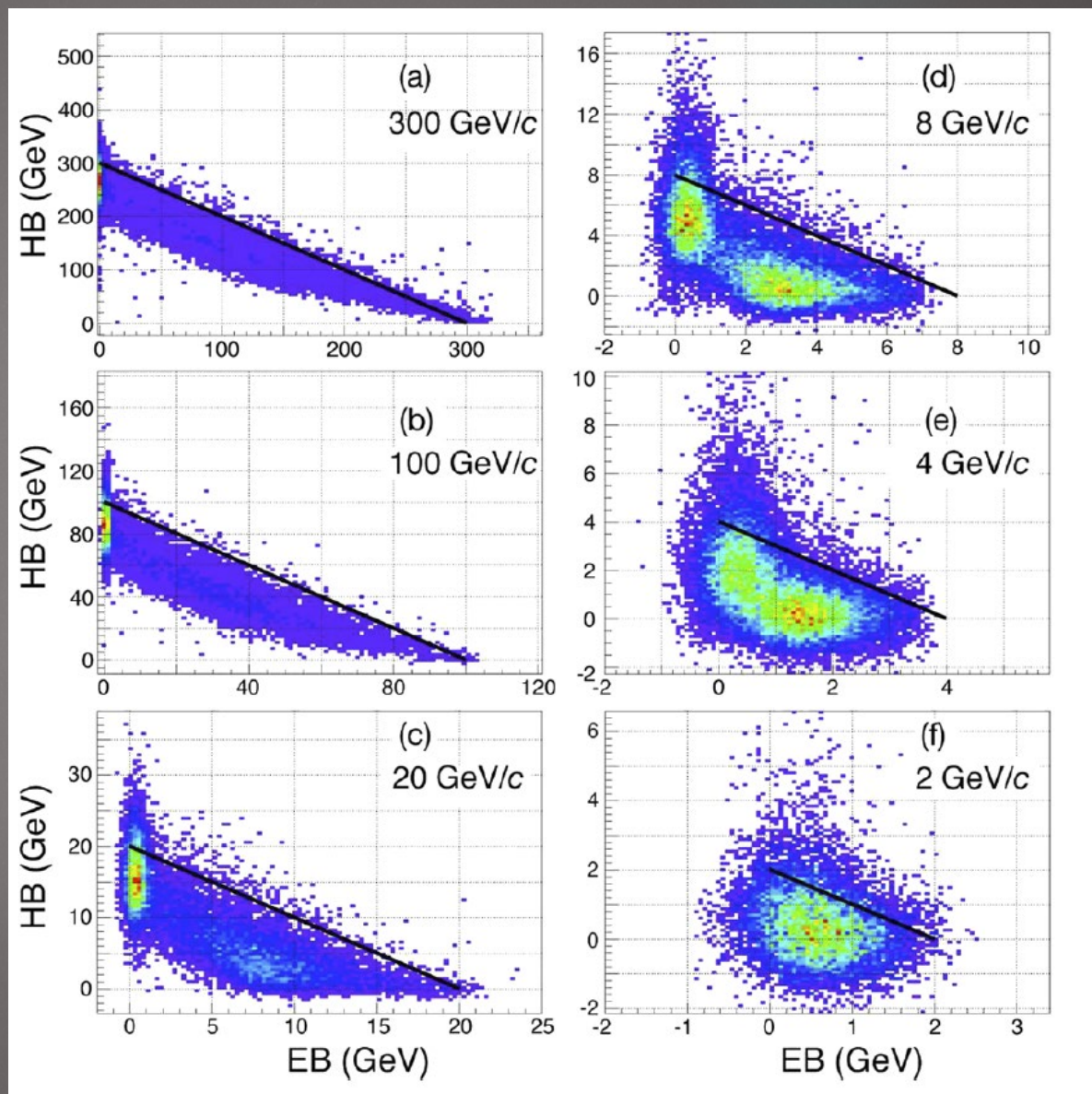


FIG. 3: Hadronic energy resolution in the TeV domain, calculated with Equation 3 [24].

e/h in CMS Ecal/Hcal

The hadronic energy resolution of the CMS calorimeter is degraded by the very different e/h of its ECAL and HCAL



A bad HCAL

$$\frac{\sigma}{E} = \frac{94\%}{\sqrt{E}} \oplus 4.4\%$$

$$\frac{\sigma}{E} = \frac{82\%}{\sqrt{E}} \oplus 4.5\%$$

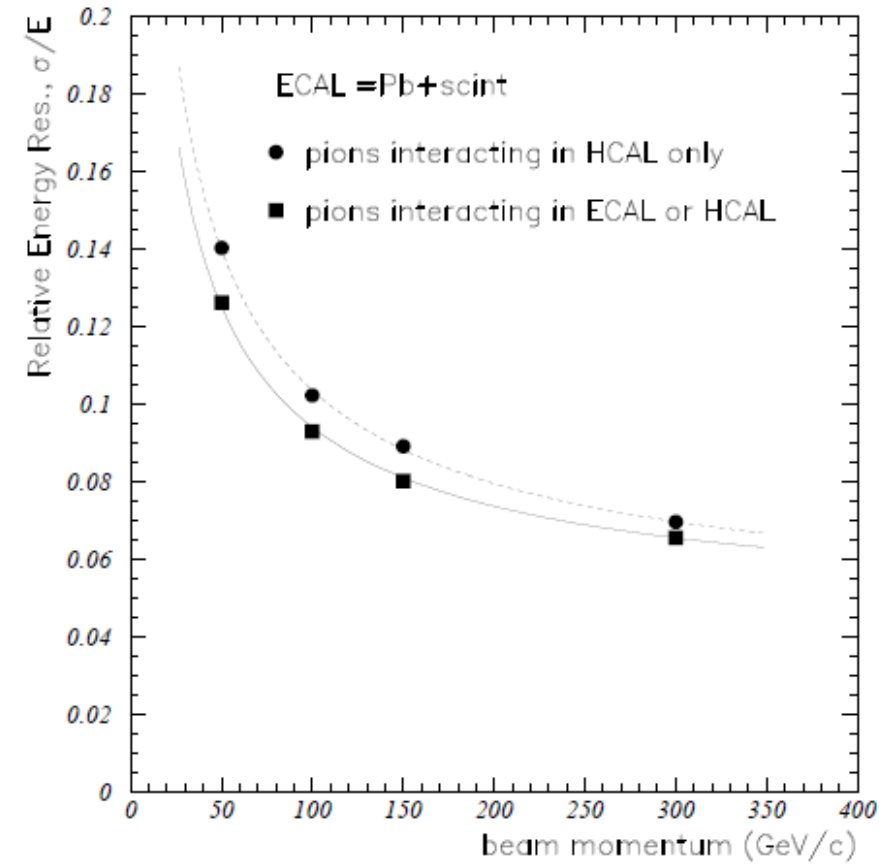
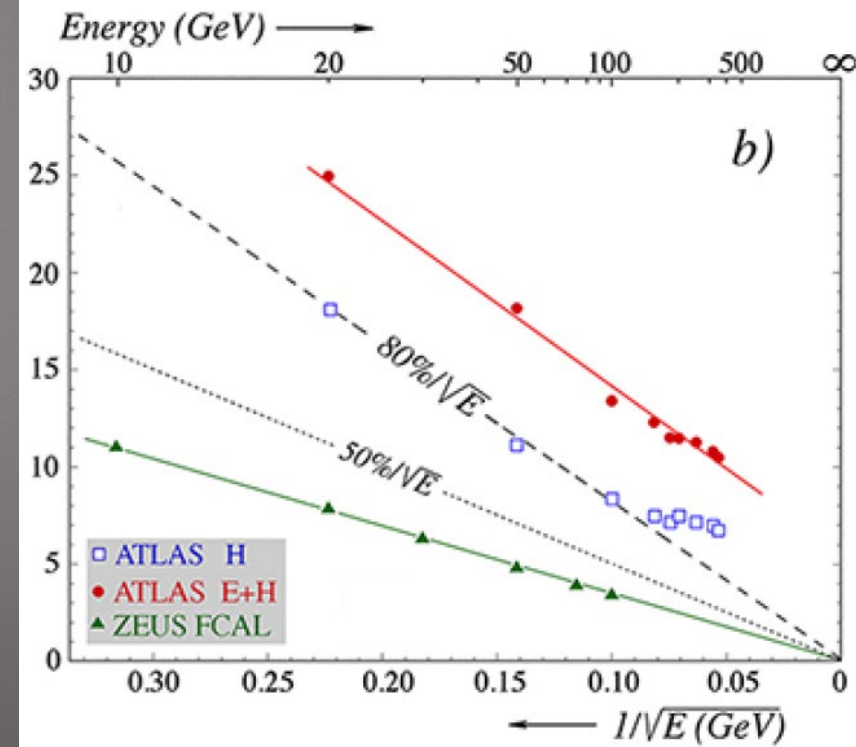


Fig. 21. H2(1995) data: fractional energy resolutions for "mip-in-ECAL" pions and "full pion sample". The statistical errors are smaller than the size of the symbols.

A good HCAL and another bad one

47

Figure 20b also shows another interesting phenomenon, namely that the ATLAS hadronic energy resolution was actually measured to be *better* when the hadronic calorimeter section (Tilecal) was used in stand-alone mode, rather than in combination with the LAr ECAL. The reason for this is the fact that these calorimeter sections have different e/h values. For the Tilecal, an e/h value of 1.336 ± 0013 has been reported [58], while the value for the Pb/LAr ECAL, which unlike the Tilecal is very insensitive to the neutrons produced in the shower development, is estimated at ~ 1.5 [5]. Typically, the energy deposited by showering hadrons and jets is shared between these compartments, and the large event-to-event fluctuations in this energy sharing translate into an additional contribution to the hadronic energy resolution. This contribution is absent when the showers develop entirely in the Tilecal, hence the better energy resolution.



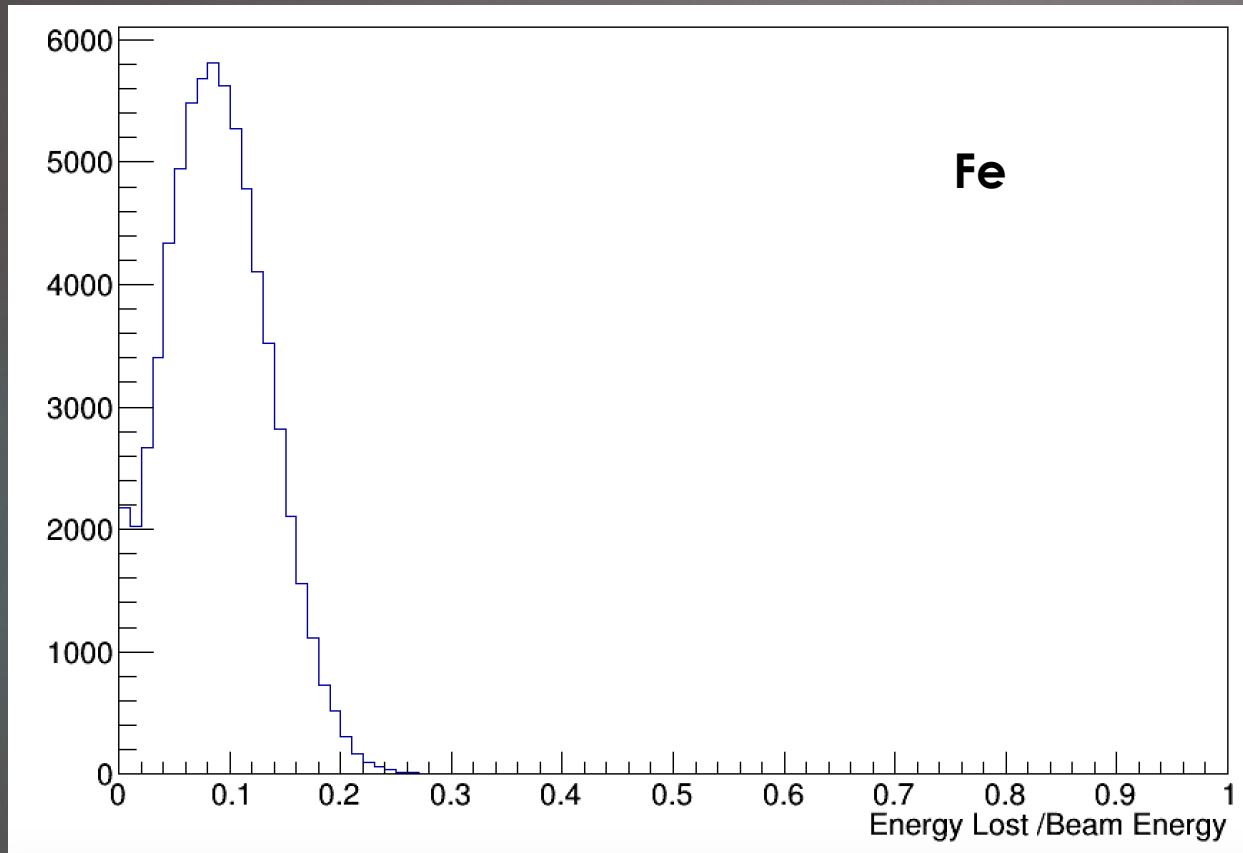
There can be several reasons why the response to hadrons is lower than that of electrons

- Losses to binding energy
- The interaction cross section for thermal neutrons is low. They can scatter out the front of the calorimeter or move so far away (in distance and time) from the initial hadron impact point as to be effectively lost
- Escaping neutrinos
- Escaping muons from charged pion decay
- Birks' law (scintillators or the equivalent in noble liquids) decreases light output for slow moving highly charged ions produced in hadronic showers relative to the relativistic electrons in EM showers
- Difference in response for very low energy and higher energy shower particles

Binding energy

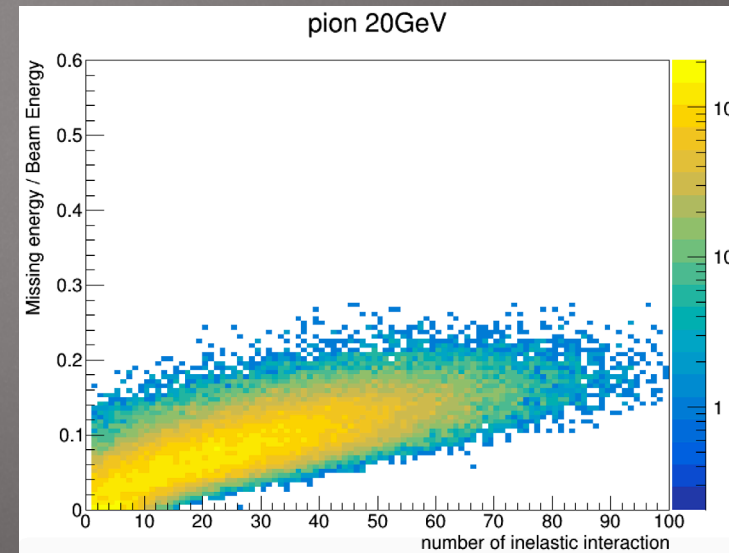
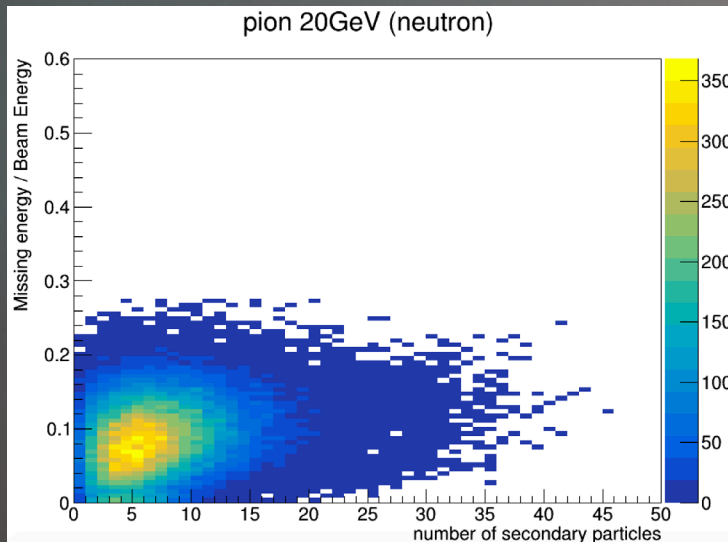
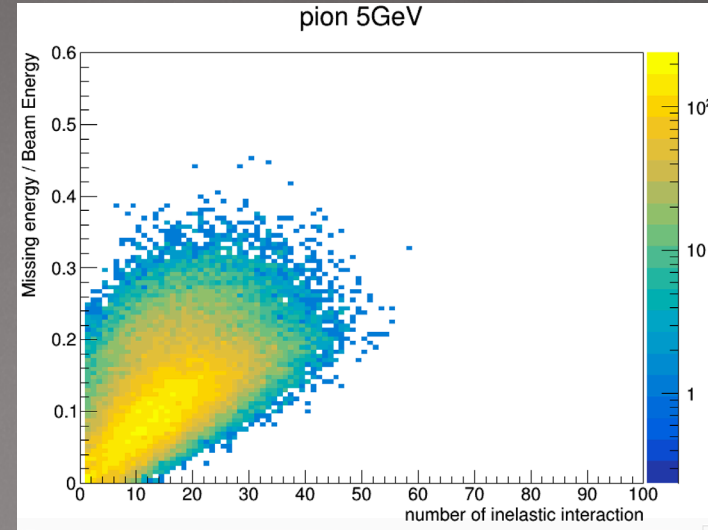
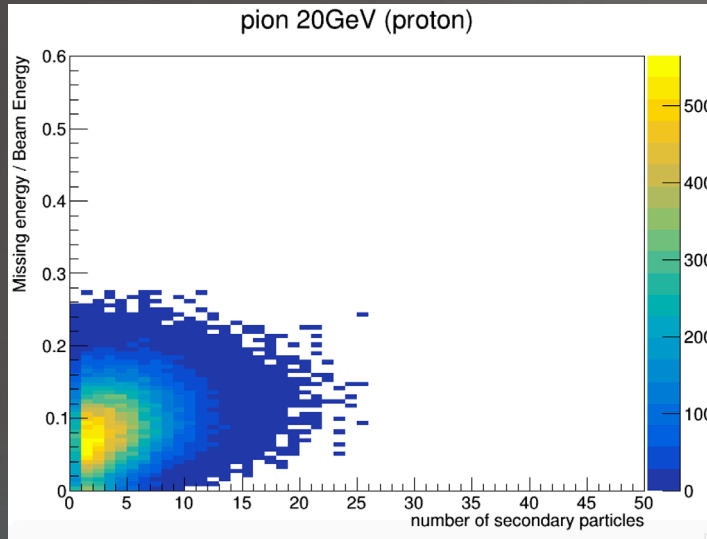
Loss per nuclear breakup

49



Cannot produce a detectable signal. Truly missing energy. But there are ways of estimating this (albeit on average, so a contribution to the resolution will come from fluctuations in this). Will discuss this later.

Missing energy

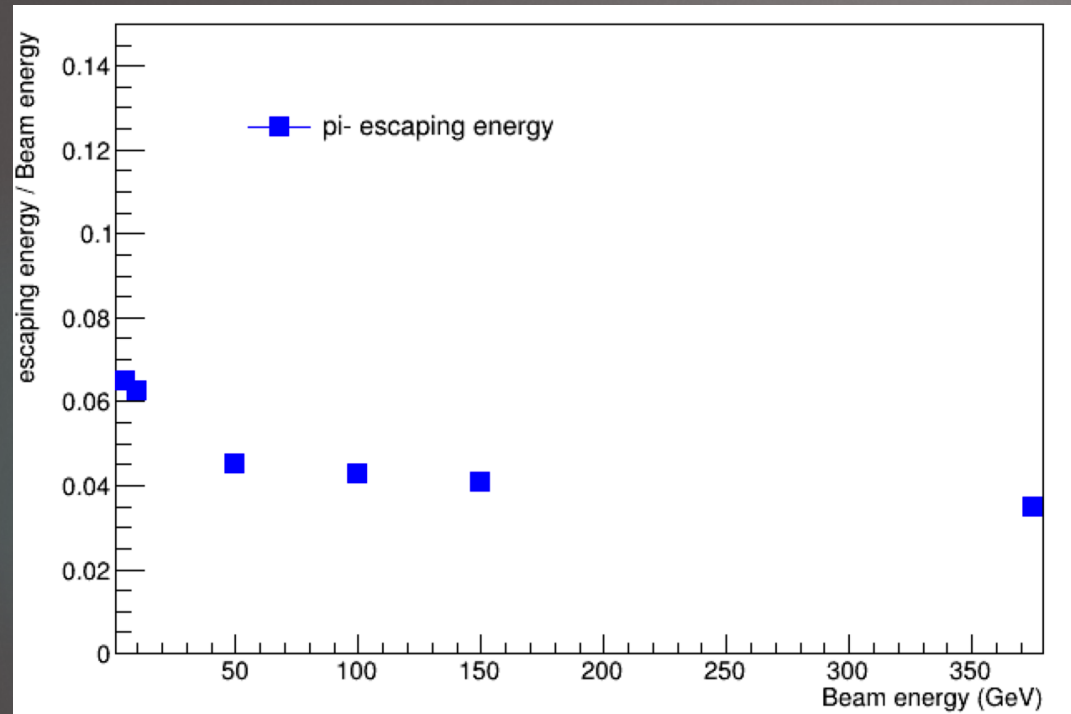


Can be many secondaries especially for the first collision

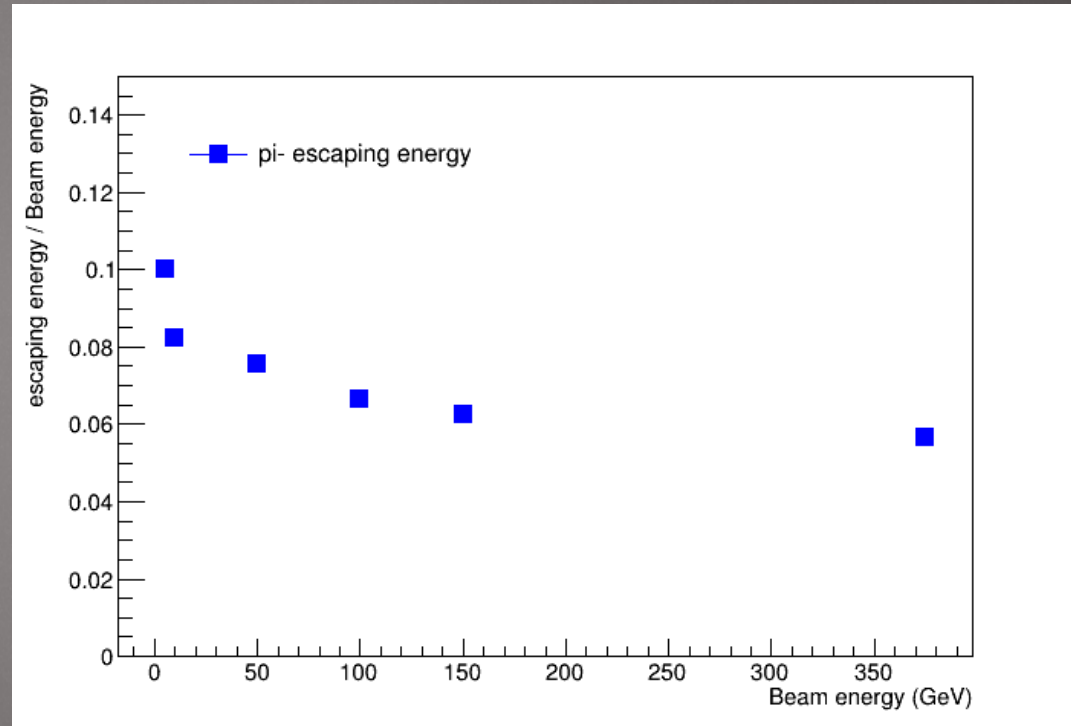
The total energy lost to binding energy is an irreducible resolution term

Escaping energy

Very large PbWO4 crystal

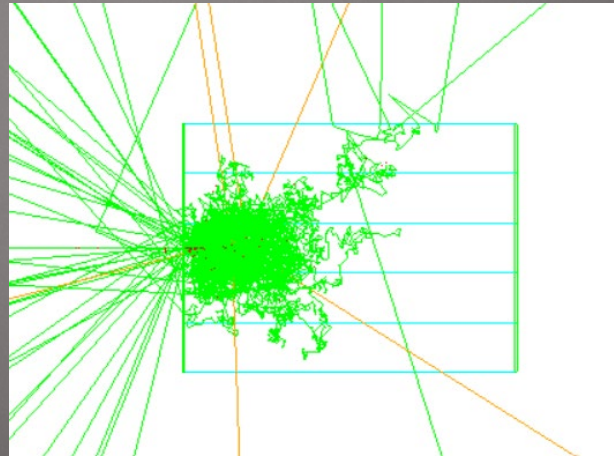
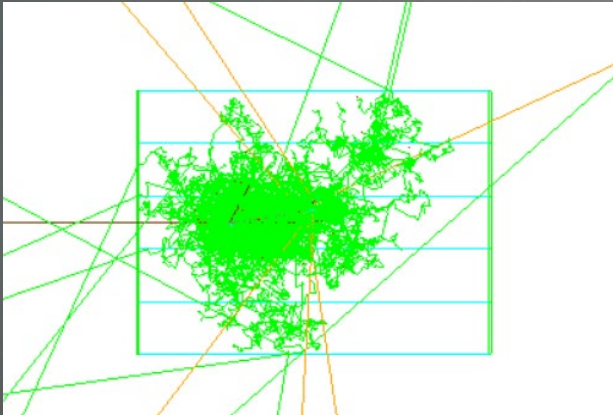
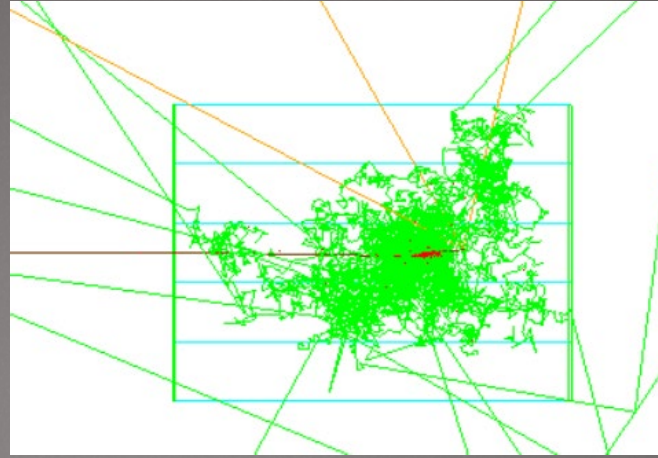
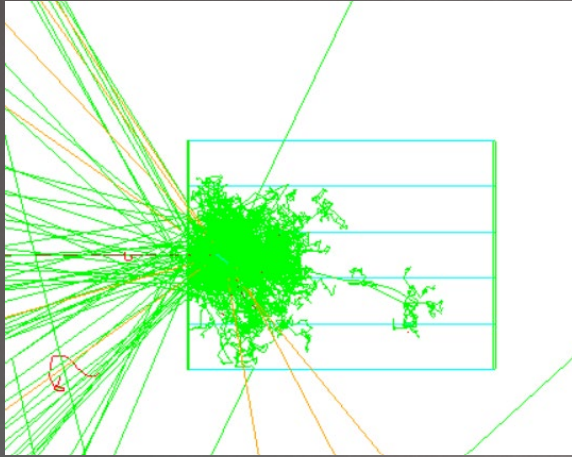


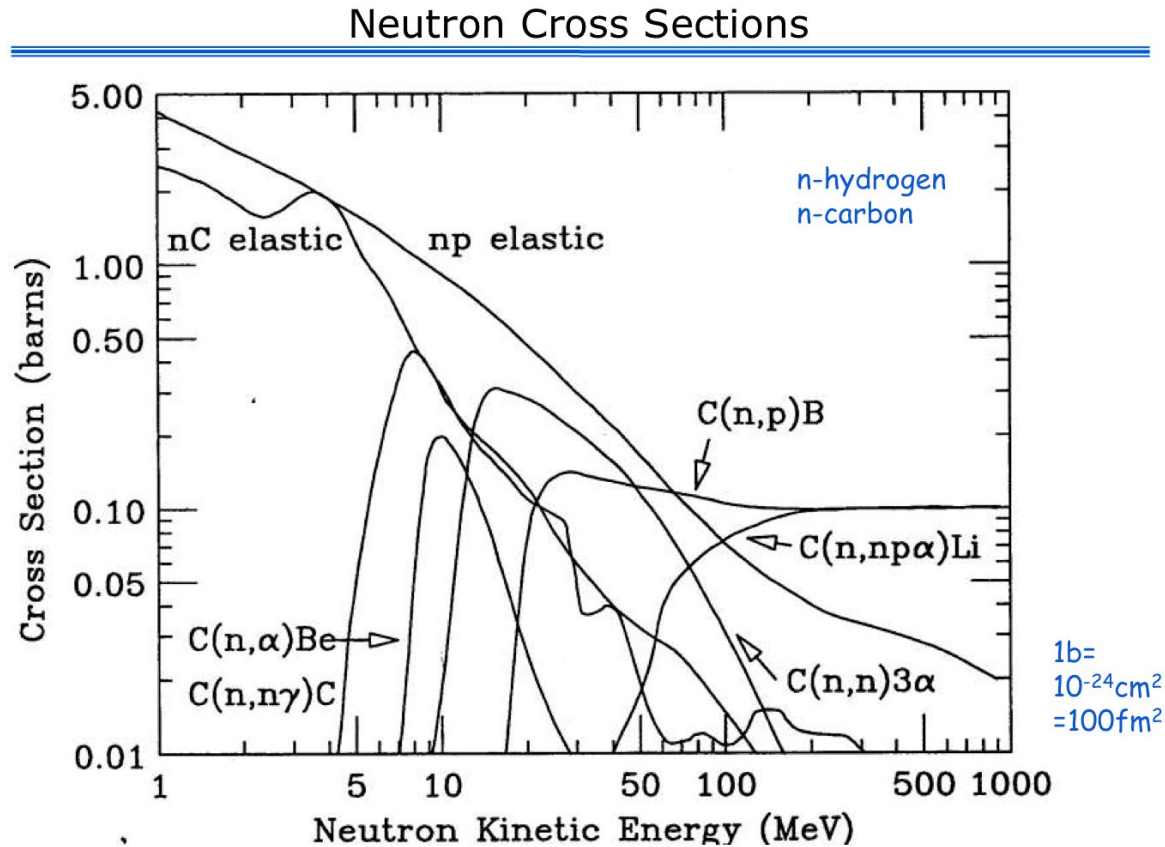
CMS HCAL-like



neutrons

52





Only way to get a signal is if they transfer all their energy to a proton. Really only effective for low energy neutrons on hydrogen. Off heavier materials, they just bounce off and continue on their way

neutrons

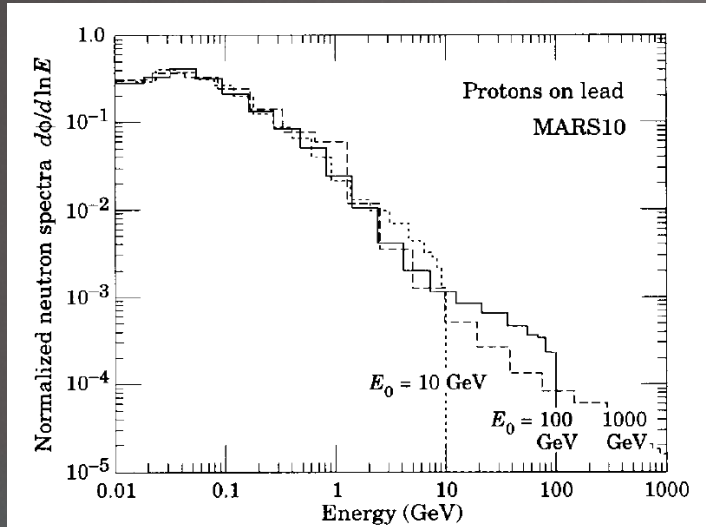


Fig. 2. MARS10 simulations of the neutron spectra in a lead beam stop for incident proton energies of 10, 100, and 1000 GeV. Spectra are for all of the neutrons in the cascade. They are normalized for relative agreement at low energies to emphasize the shape similarity below the beam energy cutoff.

Spectrum of produced neutrons roughly independent of incident particle energy (protons in this case)

Produced neutrons tend to be low energy

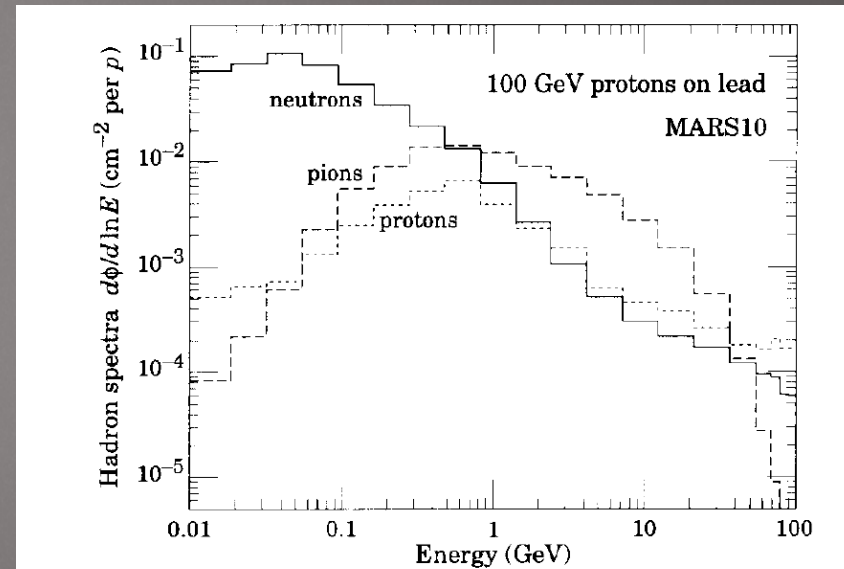


Fig. 3. MARS10 simulations of the neutron, proton, and pion spectra for 100 GeV incident protons on lead. At low energies the charged particles are removed by ionization loss. At high energies the neutrons and protons have similar spectra. The relative numbers, particularly of neutrons, will be different in a different material.

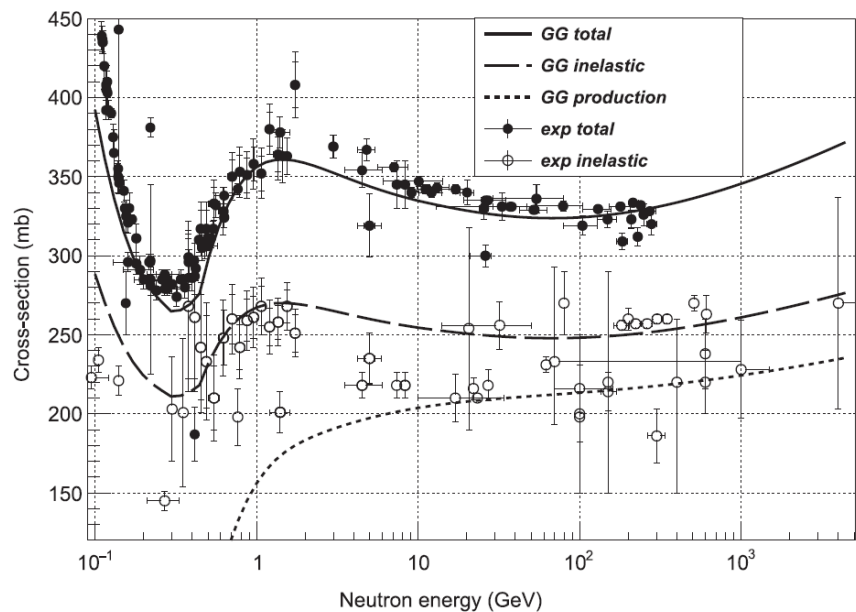


Fig. 17. Total, inelastic and production cross-sections of neutrons on a carbon target in the energy range 10^{-2} – 10^3 GeV. Experimental data (open and solid points) from [149,150], lines correspond to the Glauber–Gribov model.

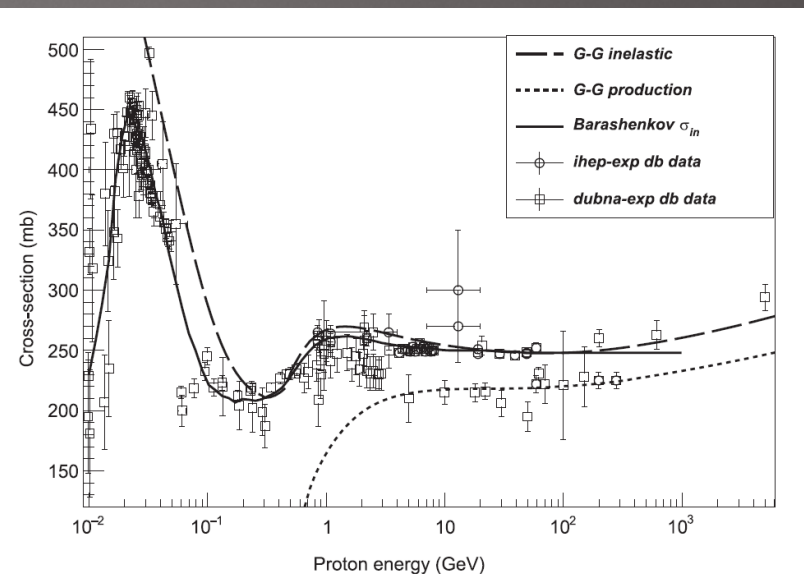


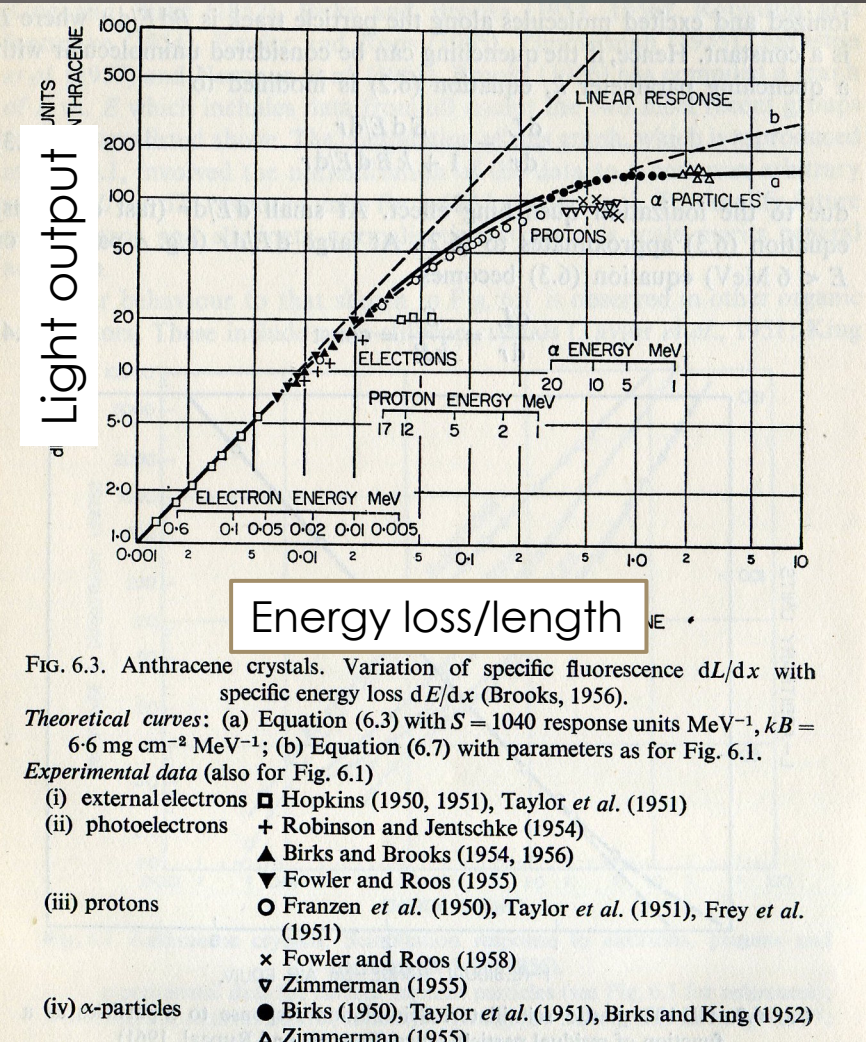
Fig. 18. Inelastic and production cross-sections of protons on a carbon target in the energy range 10^{-2} – 10^3 GeV. Experimental data (open points and squares) are from [149,150]. The solid and dashed lines correspond to the Barashenkov and Glauber–Gribov inelastic models, respectively. The dotted line shows the Glauber–Gribov production model.

Comparing neutron and proton cross sections, neutrons have a large elastic cross section. Inelastic cross sections are similar (geometrical “direct hit”)

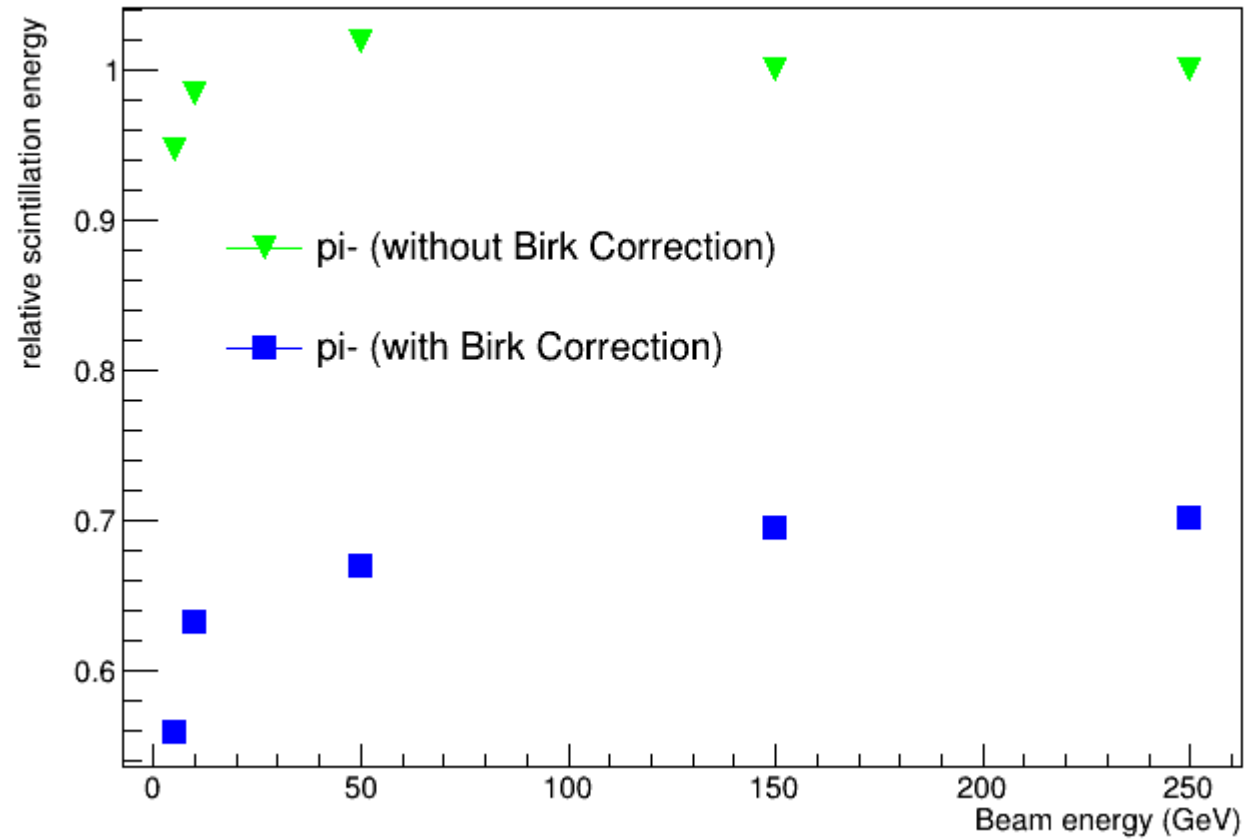
Birks' law

$$\frac{dL}{dx} = S \frac{dE/dx}{1 + k_B \cdot dE/dx}$$

L is the light yield
 S is the scintillation efficiency
 k_B is Birks' constant (0.126 mm/MeV for polystyrene)



A similar process occurs in noble liquids. If the ion density is too large, there is more recombination before the signal is collected on the electrode



MIP response

For very low energy hadrons, particle can be stopped via ionization losses before there is a hadronic interaction. This decreases the missing energy, increasing the response. These particles are not unimportant for jets

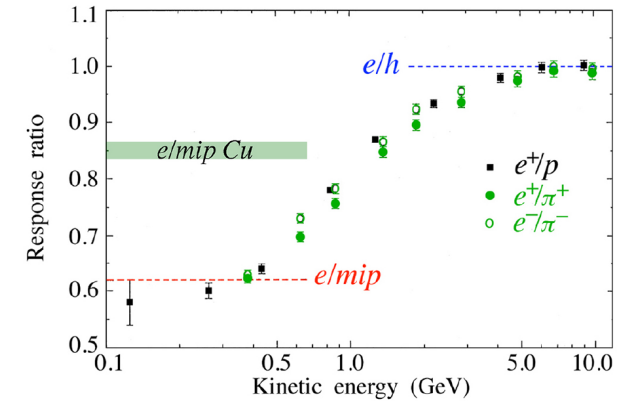


Figure 23: The ratio of the responses of the (compensating) ZEUS calorimeter to electrons and (low-energy) hadrons. This ratio equals 1.0 for energies above ~ 10 GeV. At low energies, the hadron response increases because of the absence of nuclear interactions, and the associated losses in nuclear binding energy. Data from [59].

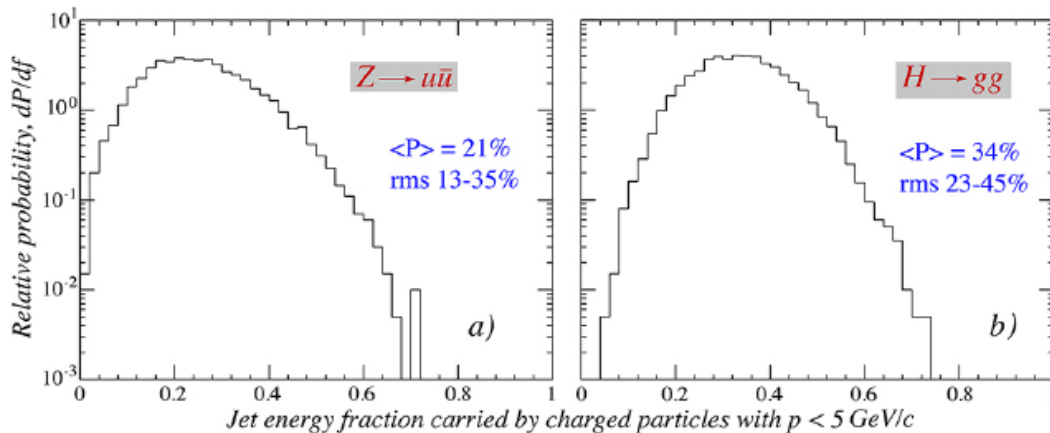


Figure 24: Distribution of the fraction of the energy released by hadronically decaying Z^0 (a) and H^0 (b) bosons at rest that is carried by charged final-state particles with a momentum less than 5 GeV/c [60].

Denominator gets larger at lower energy so ratio gets smaller

tails

- “punch through”
- Leakage
- Neutrinos in charged pion decays

Can also have high side tails. Will discuss some sources at the very end.

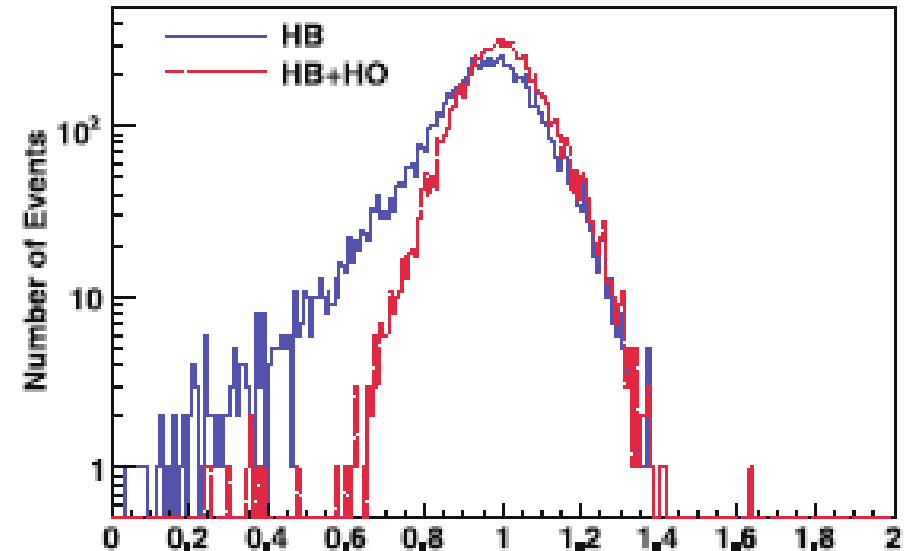


Fig. 3.3 The histograms are for the HB alone *solid (blue)*, and for the HB+HO *dashed (red)* with the optimal scale factor for the HO. The signal distributions are scaled such that 300 GeV/c is unity



Practical Modern calorimetry

Or how to design a good calorimeter

EM calorimeters

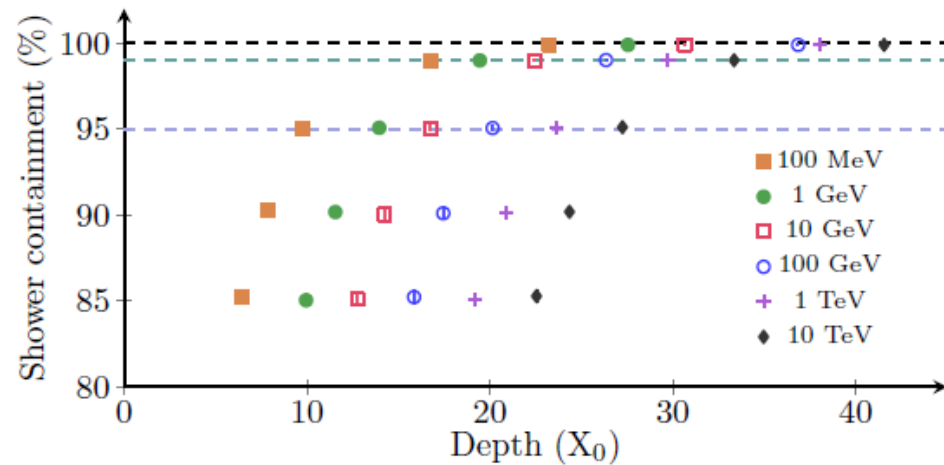
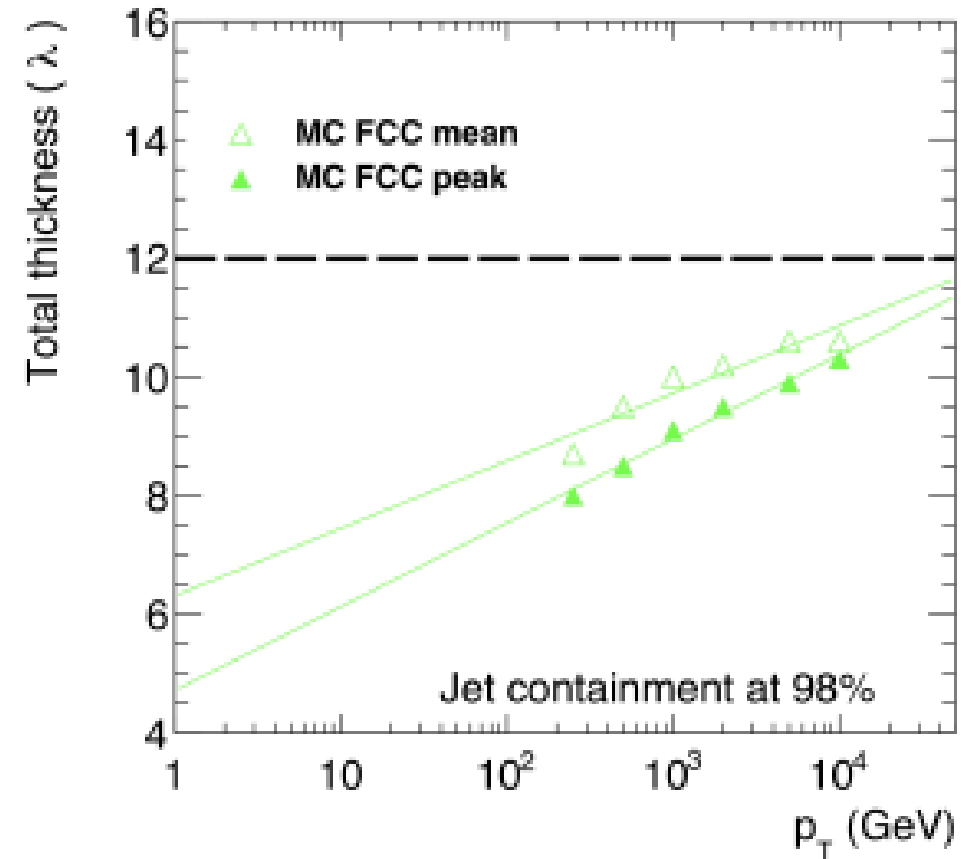


Figure 4: Dependence of the electron shower containment on the calorimeter depth expressed in the radiation lengths. The horizontal lines correspond to the shower containment of 95%, 99% and 100% respectively.

Hadron calorimeters



Compact transverse shower

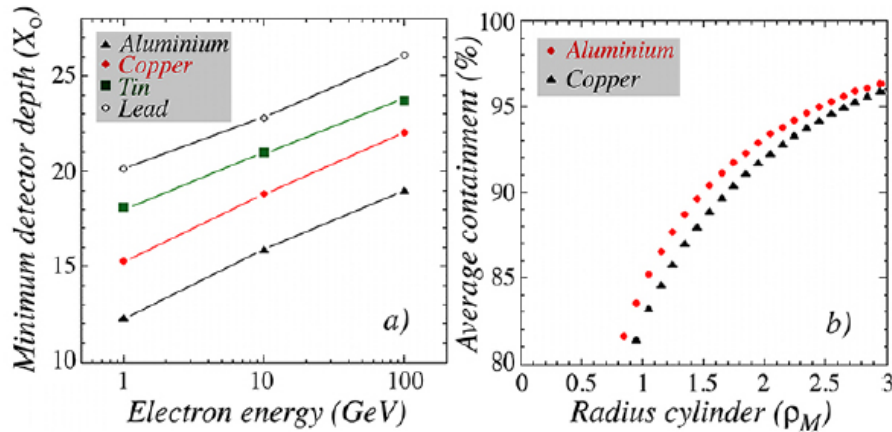


Figure 8: Size requirements for electromagnetic shower containment. The depth of a calorimeter needed to contain electron showers, on average, at the 99% level, as a function of the electron energy. Results are given for four different absorber media (a). Average lateral containment of electron-induced showers in a copper and an aluminium based calorimeter, as a function of the radius of an infinitely deep cylinder around the shower axis (b). From Reference [17].

Most calorimeters are sampling. Don't forget that the shower can spread in the sampling media, which is usually of lower Z

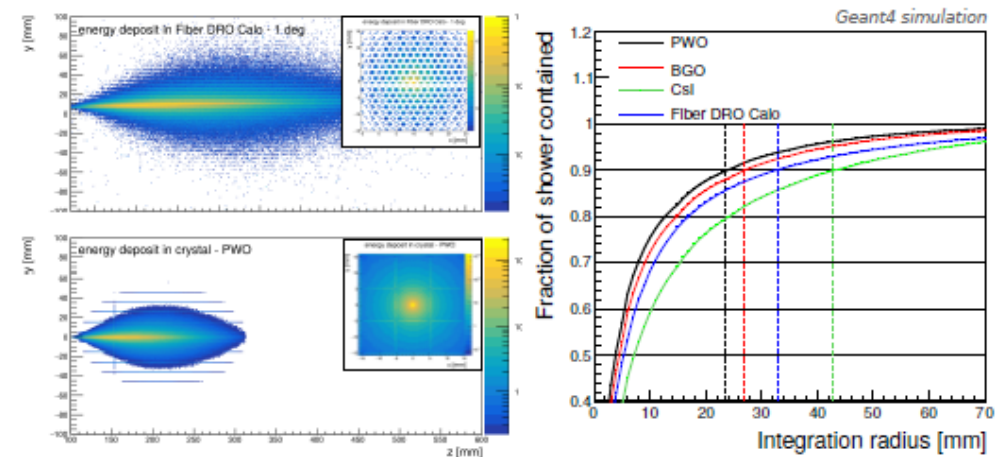
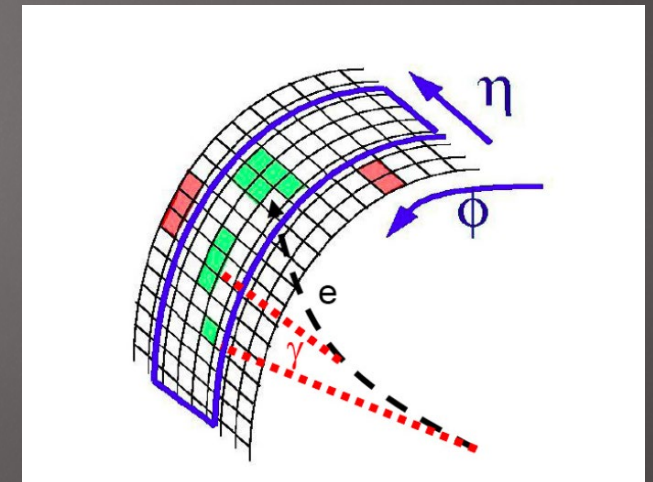
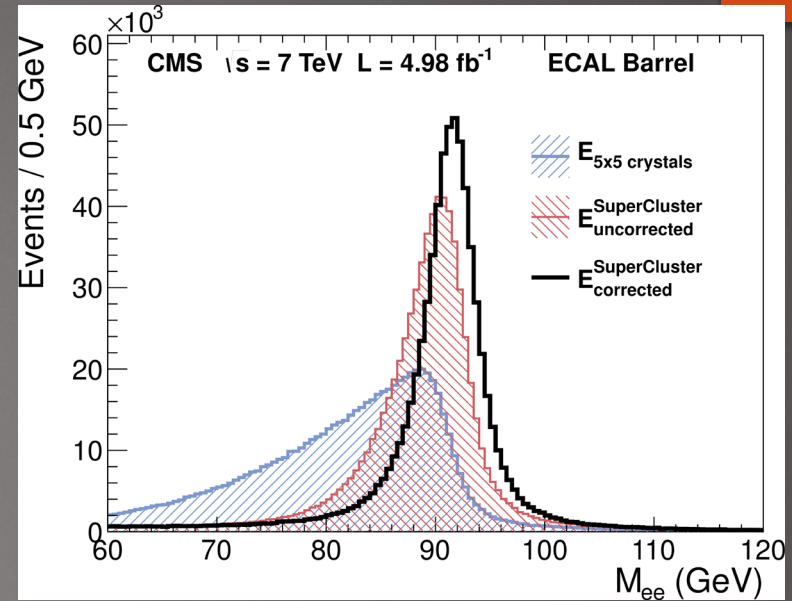
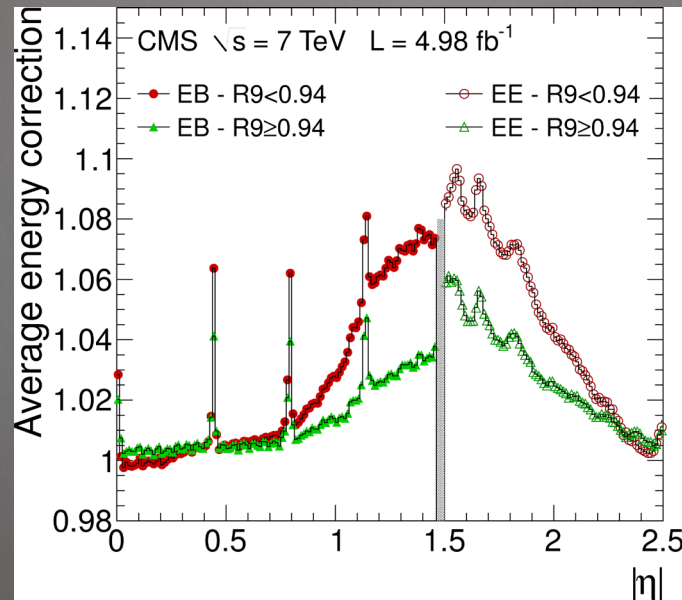
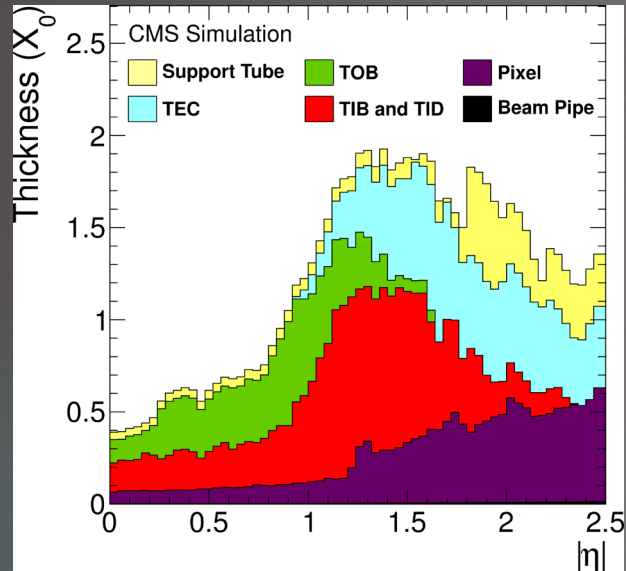


Figure 18. Left: longitudinal shower profile for 60 GeV electrons in a fiber DRO HCAL compared to that of a PbWO_4 -based SCEPCal (the inset in the plot shows the transverse shower profile). Right: comparison of Molière radii between homogeneous crystal calorimeters (PbWO_4 , BGO, CsI) and the fiber DRO HCAL.

Not stand alone devices

Don't want to start the shower before the calorimeter



Homogeneous calorimetry

64

Want to make the shower and make the signal from the same material. So far, done with light as the signal and an optically clear high Z material.

Table 1. Comparison of some of the key crystal properties for HEP applications. From left to right: crystal name, density, interaction length, radiation length, Molière radius, light yield relative to that of PbWO₄, scintillation decay time, photon time density and estimated cost for mass production.

Crystal	ρ [g/cm ³]	λ_I [cm]	X_0 [cm]	R_M [cm]	LY/LY ₀ [a.u.]	τ_D [ns]	Photon density [photons/ns]	Est. cost [\$/cm ² /X ₀]
PbWO ₄	8.3	20.9	0.89	2.00	1	10	0.10	7.1
BGO	7.1	22.7	1.12	2.23	70	300	0.23	7.8
BSO	6.8	23.4	1.15	2.33	14	100	0.14	–
CsI	4.5	39.3	1.86	3.57	550	1220	0.45	8.0



Particle Detectors at Accelerators (PDG)

New Developments in Calorimetric Particle Detection (<https://arxiv.org/pdf/1807.03853.pdf>)

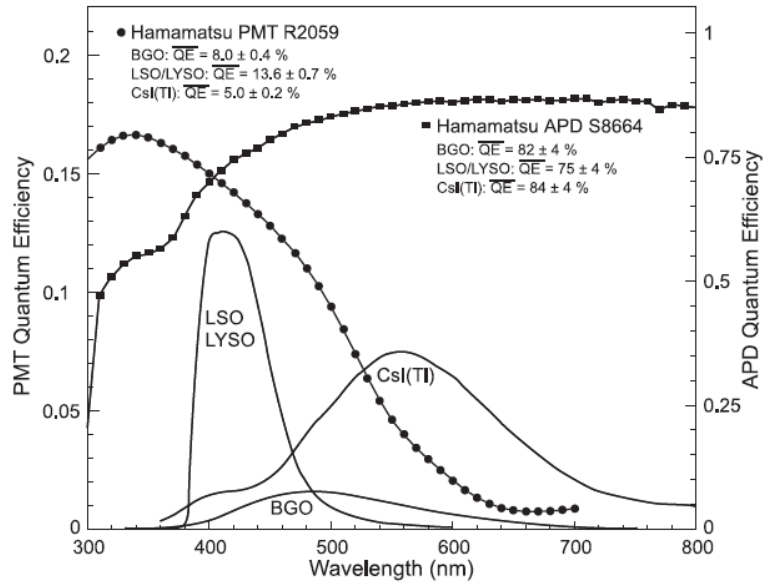


Figure 34.2: The quantum efficiencies of two photodetectors, a Hamamatsu R2059 PMT with bi-alkali cathode and a Hamamatsu S8664 avalanche photodiode (APD), are shown as a function of wavelength. Also shown in the figure are emission spectra of three crystal scintillators, BGO, LSO and CsI(Tl), and the numerical values of the emission weighted quantum efficiencies. The area under each emission spectrum is proportional to crystal's light yield.

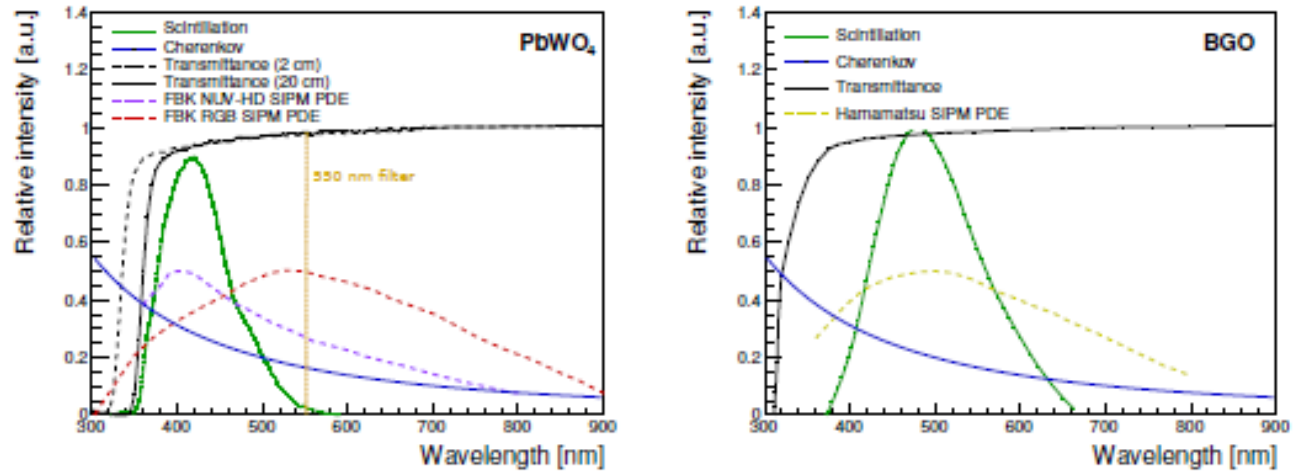


Figure 23. The transmission curves of the crystals (black) are compared with the wavelength spectrum for scintillation (green) and Cherenkov light (blue) and with the photon detection efficiency of commercially available SiPMs from FBK and Hamamatsu. A comparison of PbWO₄ (left) and BGO (right) crystals shows how different spectral regions of the Cherenkov light could be used for better separation from the scintillation component.

PMTs, SiPMs currently popular. PMTs have excellent linearity over a wide range but are expensive and need to be out of magnetic fields. SiPMs are somewhat nonlinear. Both have strong gain dependence on temperature.

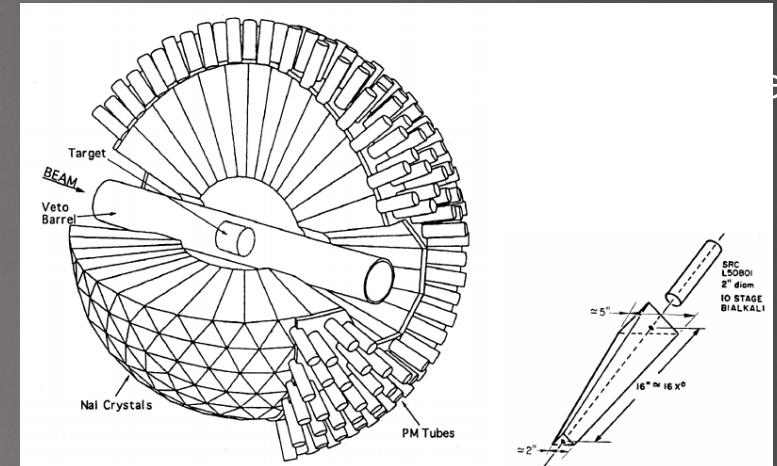
$$\langle n \rangle = \frac{T_{tot}}{L_{sig}} \quad (16)$$

The “intrinsic energy resolution” is then determined by fluctuations of n about the mean value. At first sight, one might expect the variance on n to be governed by Poisson statistics, thus for large n :

$$\frac{\sigma_E}{E_0} = \frac{\sqrt{n}}{n} = \sqrt{\frac{L_{sig}}{T_{tot}}} \quad (17)$$

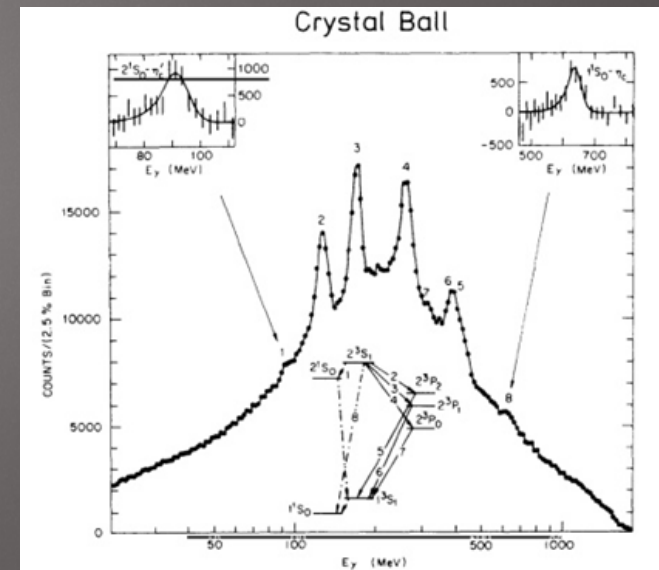
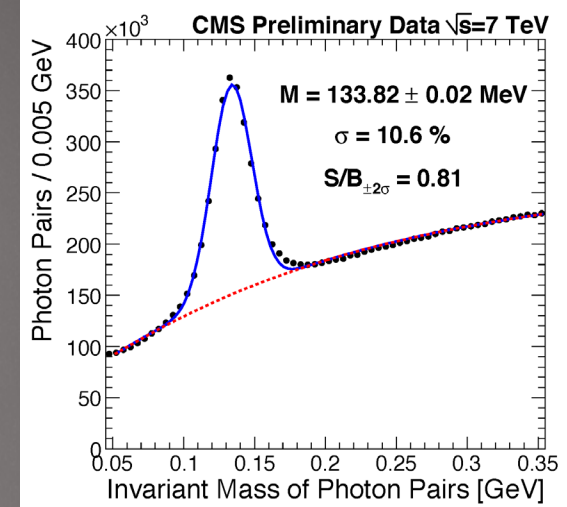
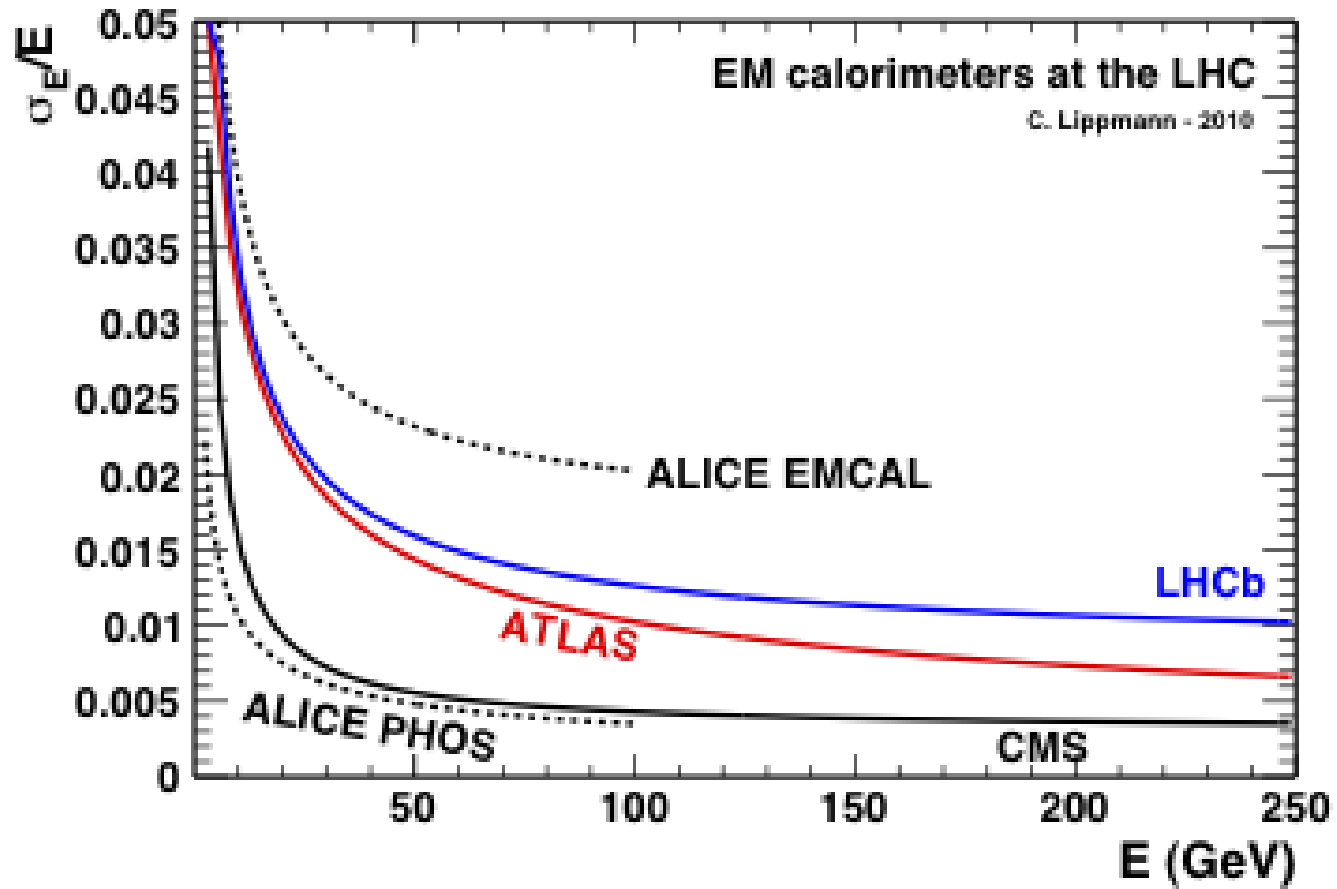
However, T_{tot} is constrained by the incident energy, thus fluctuations on n may be reduced. This is taken into account by introducing the “Fano factor”, F :

$$\frac{\sigma_E}{E_0} = \frac{\sqrt{Fn}}{n} = \sqrt{\frac{FL_{sig}}{T_{tot}}} \quad (18)$$



Advantages

67

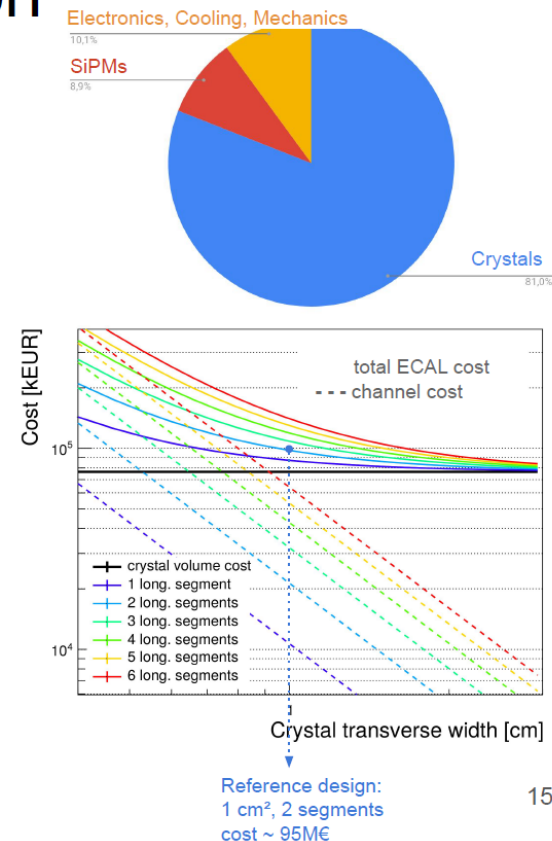


Disadvantage?

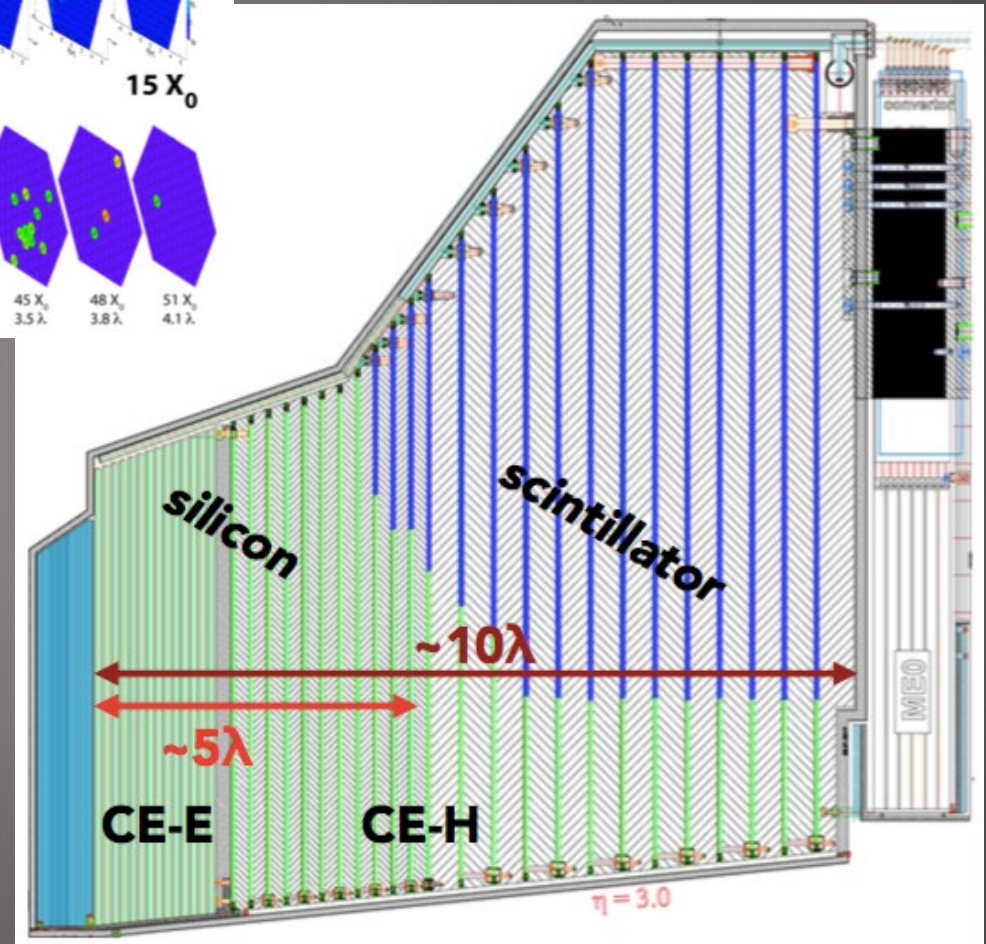
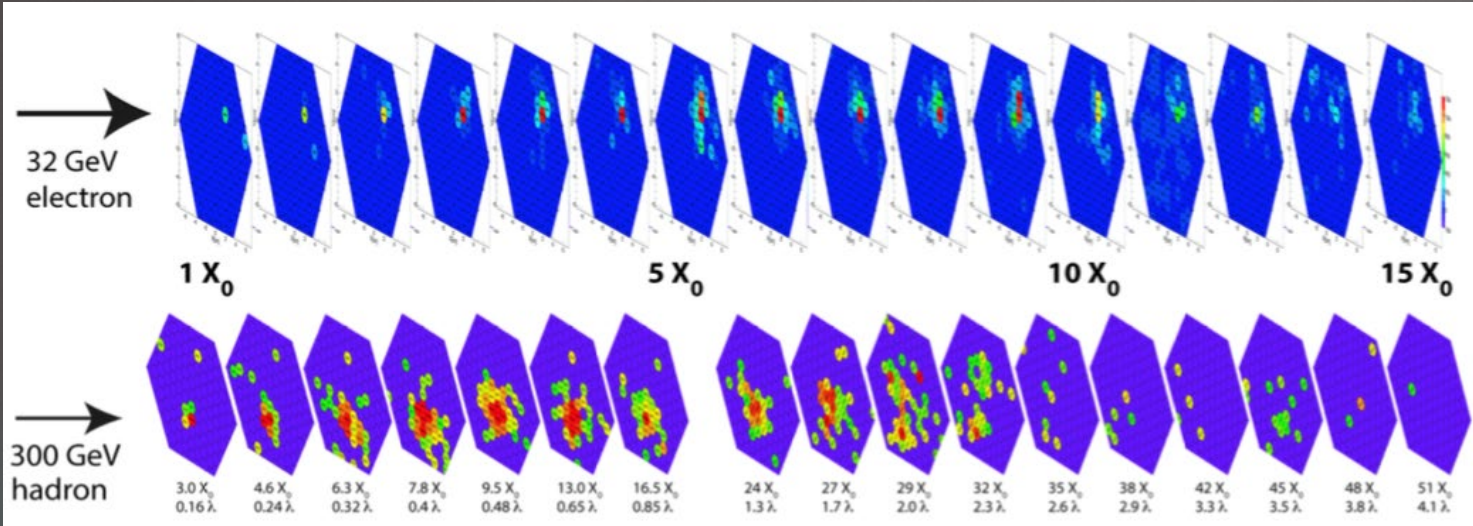
- Crystal costs used as reference
 - Quotes from crystal vendors
 - PWO: ~7€ /cc (for 10 m³, cut and polished)
 - LYSO: ~30€ /cc (for cut, polished and wrapped elements)

Cost-power drivers and optimization

- Channel count in SCEPCal is limited to ~2.5M
 - 625k channels/layer
- Cost drivers in ECAL layers (tot ~95M€):
 - ~81% crystals, 9% SiPMs, 10% (electronics+cooling+mechanics)
 - ~19% of cost scales with channel count
- Power budget driven by electronics: ~74 kW
 - 18.5 kW/layer
- Room for fine tuning of the segmentation and of the detector performance/cost optimization (see backup)



Sampling calorimetry



Sampling Fraction

70

Want to calculate ratio of energy in the passive+active to active
Can do this in MC or do a “poor man’s” calculation based on
nuclear interaction length

CMS HCAL: Brass 5cm/16.4 cm = 0.3 λ

Polystyrene: 0.37 cm/107 cm = 0.0035 λ

Sampling fraction: about 100

Typically measuring only 1 percent of the shower

Sampling fraction challenges

71

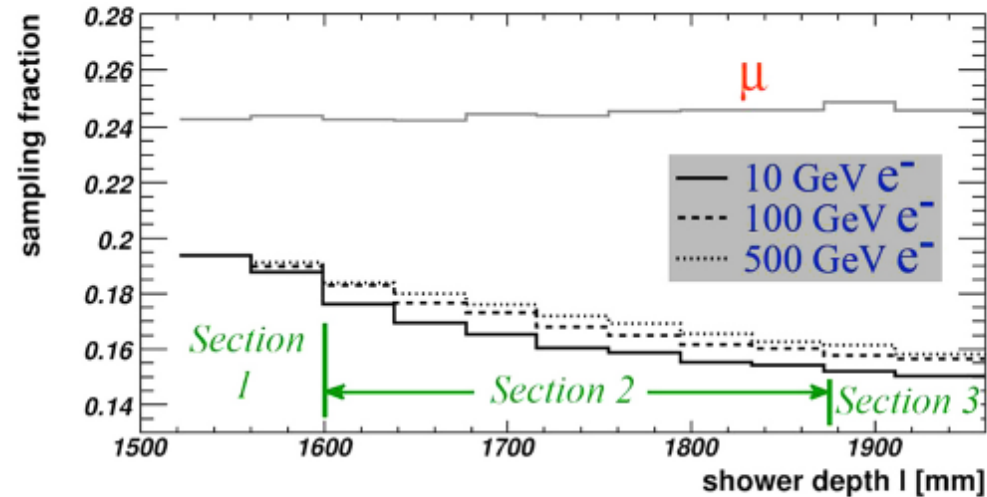


Figure 38: The evolution of the sampling fraction for electron showers of different energies in the three longitudinal segments of the ATLAS LAr calorimeter, at $\eta = 0$ [33].

3. The cross section for the photoelectric effect is extremely Z -dependent ($\propto Z^5$). This has very important consequences for sampling calorimeters that consist of high- Z absorber material and low- Z active layers. Low-energy γ s produced in the shower development will, for all practical purposes, **only** interact in the absorber material, and the photoelectrons produced in this process will only contribute to the signals if they are produced very close to a boundary layer. In practice, they are much less efficiently sampled than the high-energy electron/positron pairs produced in the early stages of the shower development. As a result, the sampling fraction in such calorimeters decreases as the shower develops in depth (see Figure 36). Also, the fact that $e/mip \neq 1$ in such calorimeters⁴ is the result of this phenomenon. Some consequences for calorimetry are discussed in Section 6.1.

Sampling EM calorimetry

$$(\sigma/E)_{\text{samp}} = \frac{a_{\text{samp}}}{\sqrt{E}}, \quad \text{with} \quad a_{\text{samp}} = 0.027 \sqrt{d/f_{\text{samp}}} \quad (2)$$

in which d represents the thickness of individual active sampling layers (in mm), and f_{samp} the sampling

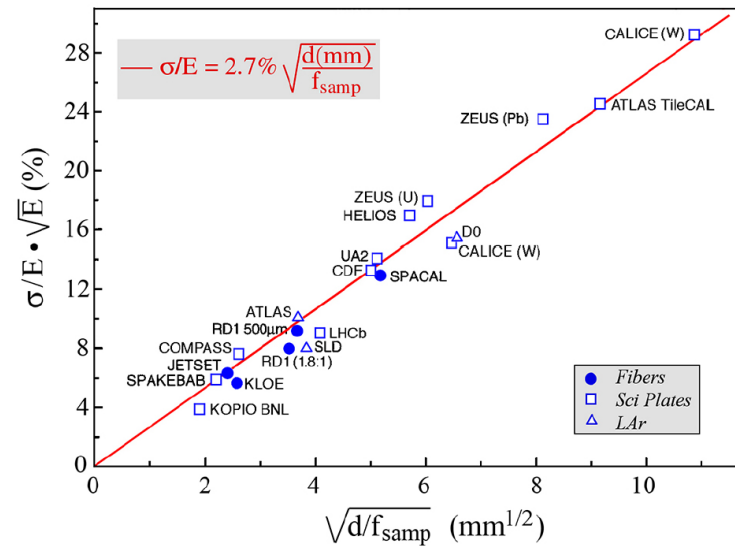


Figure 11: The em energy resolution of a variety of sampling calorimeters as a function of the parameter $(d/f_{\text{samp}})^{1/2}$, in which d is the thickness (in mm) of an active sampling layer (e.g., the diameter of a fiber or the thickness of a liquid-argon gap), and f_{samp} the sampling fraction for mips. The energy E is expressed in units of GeV [7].

Sampling term typically 10-12 % these days

The validity of Equation 2 is limited to calorimeters with plastic scintillator or liquid argon/krypton as active material. When the active layers are very thin (in terms of stopping power), as in calorimeters with gaseous or silicon readout, an additional factor contributes to the energy resolution: *pathlength fluctuations*. In

Liquid active material

73

Table 2

Properties of liquefied noble gases. W_i is the energy required to create an electron/ion pair. F is the Fano factor, relevant for detectors measuring ionization. T_{BP} is the boiling point at atmospheric pressure.

	Z	A	T_{BP} (K)	Density (g/cm ³)	X_0 (cm)	R_M (cm)	E_C (MeV)	dE/dx (min) (MeV/cm)	W_i (eV)	F
Argon	18	39.9	87.3	1.40	14.0	9.0	31.9	2.11	23.6	0.11
Krypton	36	83.8	119.9	2.42	4.7	5.9	16.5	3.28	18.4	0.06
Xenon	54	131.3	165.1	2.95	2.9	5.2	11.3	3.71	15.6	0.04

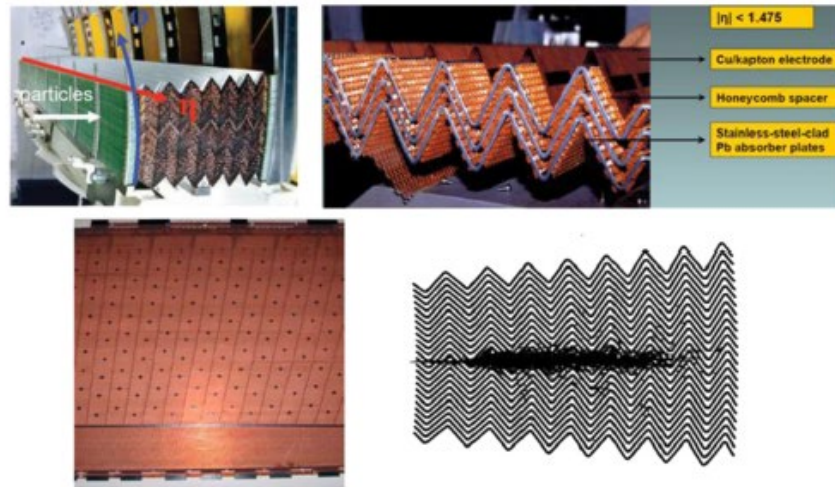


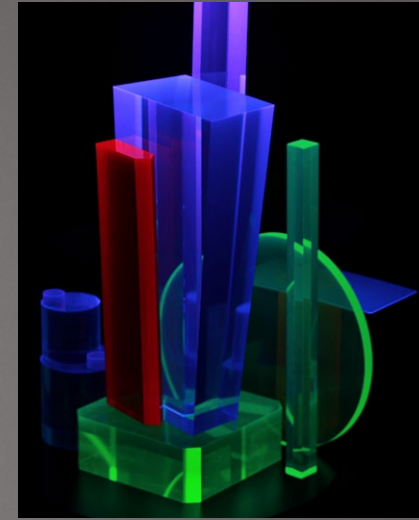
Fig. 17. A section of the Barrel accordion calorimeter (top left); a close-up showing the consecutive layers of absorber, liquid argon drift space, spacers and electrodes (top right); an electrode etched to form the readout cells (bottom left); a simulation of an electromagnetic shower as it propagates through the absorbers (bottom right).

- Stable calibration
- Radiation hard
- Needs expensive cryostat

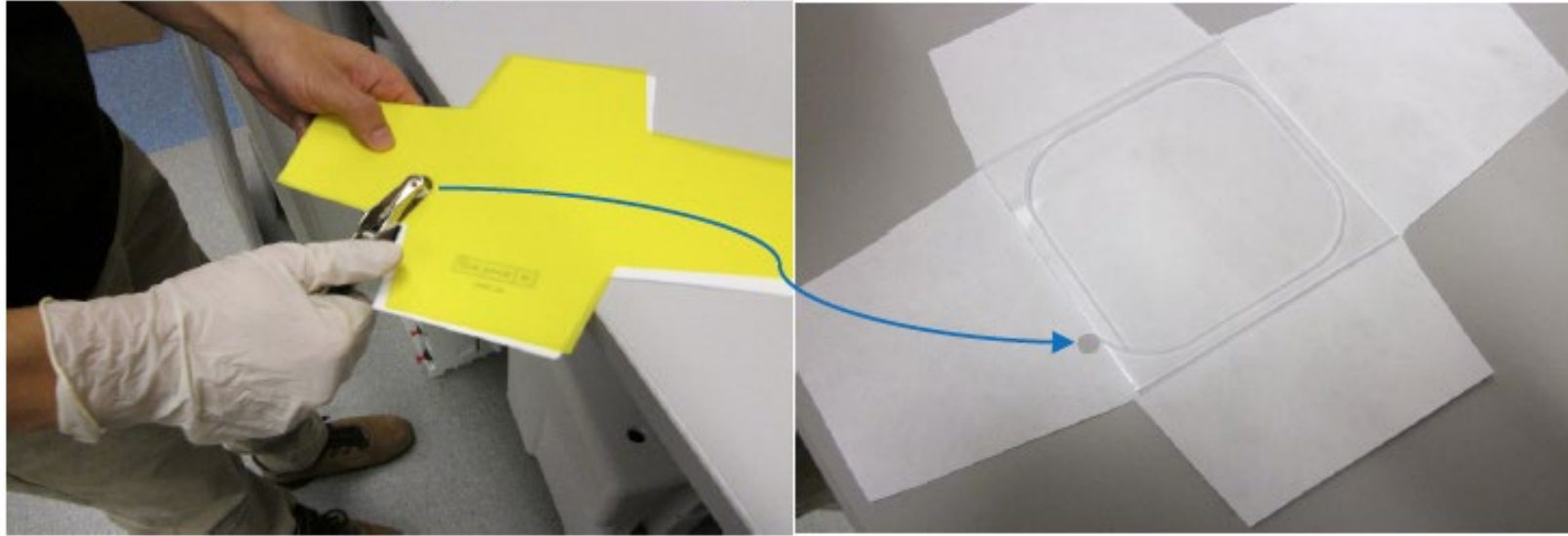
PLASTIC SCINTILLATOR

Plastic scintillator is used to detect particles, usually in the calorimeters, but sometimes in the trackers as well.

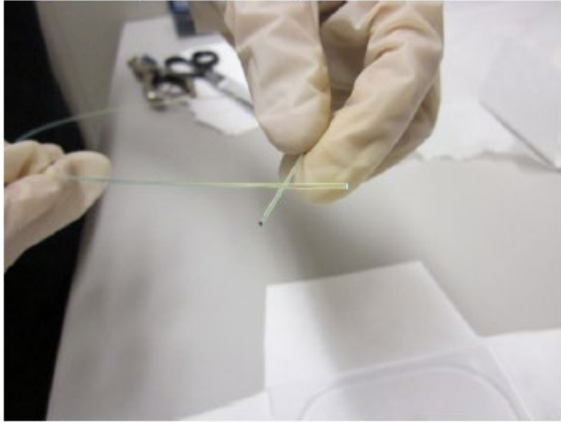
Produce visible light which can be detected by a photodetector (PMT, APD, HPD, Sipmm, etc.)



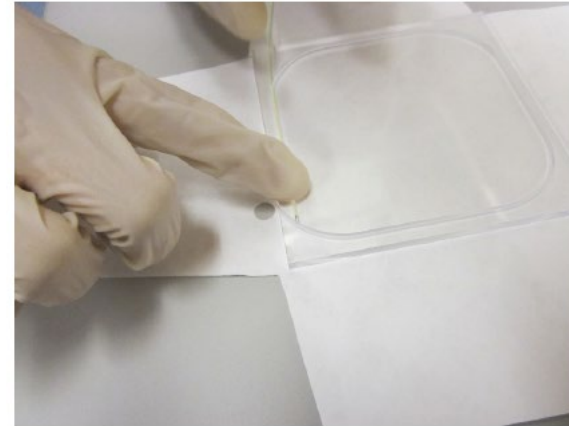
ii. Punch the hole for optical fiber according to the model:

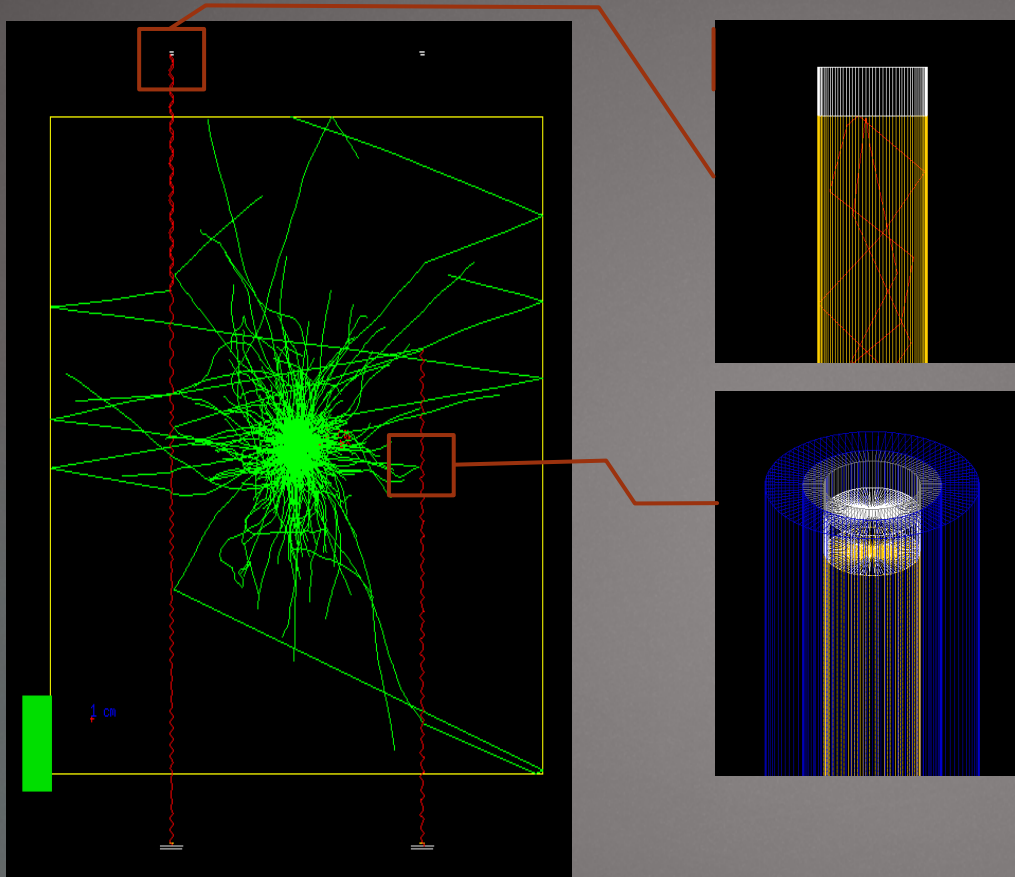


i. If the fiber is sputtered, identify the sputtered end and start from there:



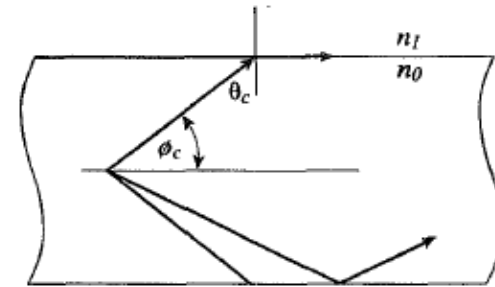
ii. With one hand holding the fiber, use finger to gently push the end into the groove. **Make sure not to block the exiting groove:**





Often used with wavelength shifting fibers, to trap the light.

$$\begin{aligned}
 F &= \frac{\Omega}{4\pi} = \frac{1}{4\pi} \int_{\phi=0}^{\phi=\phi_c} d\Omega = \frac{1}{4\pi} \int_0^{\phi_c} 2\pi \sin \phi \, d\phi \\
 &= \frac{1}{2}(1 - \cos \phi_c) = \frac{1}{2}(1 - \sin \theta_c) \\
 &= \frac{1}{2}(1 - n_1/n_0)
 \end{aligned}$$



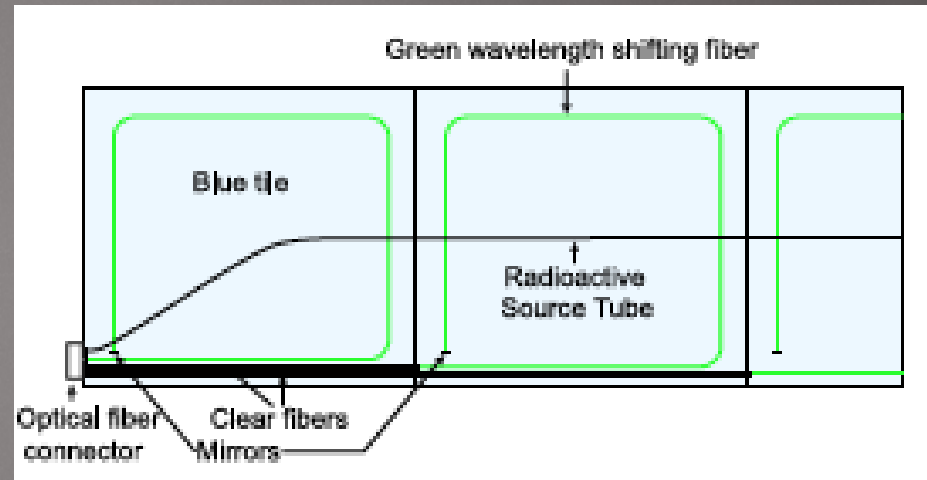
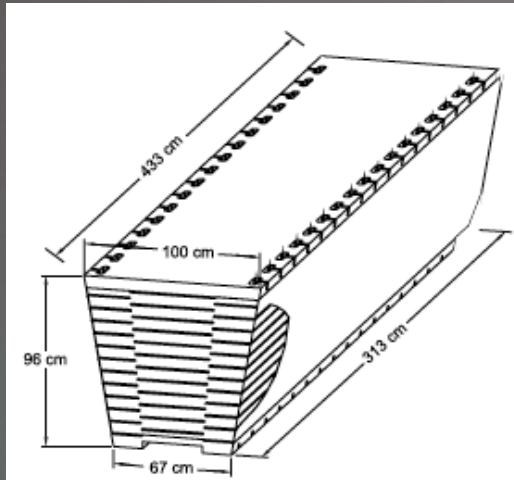
- air gap between fiber and tube
- WLS fibers can be sputtered on one end with Aluminum.

Hadron Barrel Calorimeter (HB)

77

1/17/17

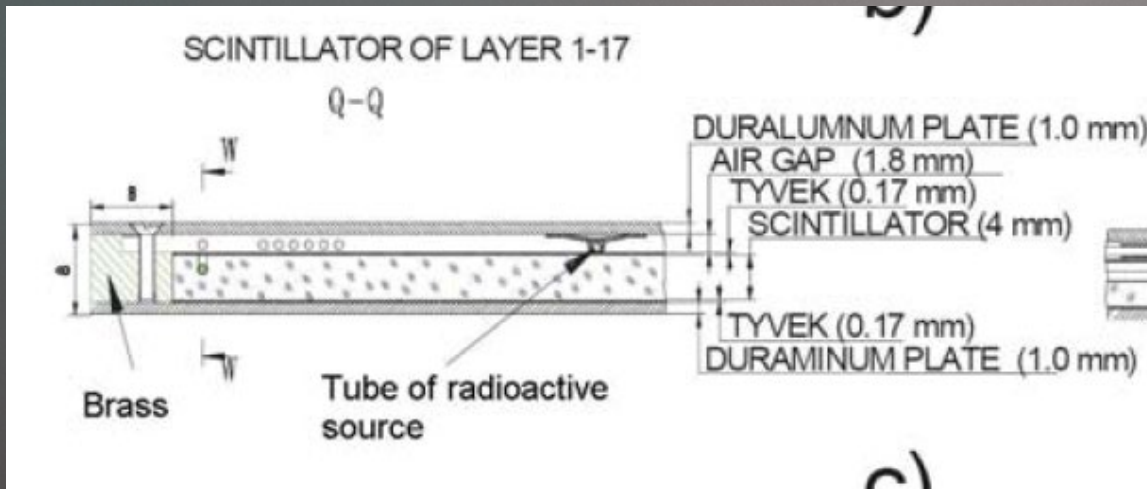
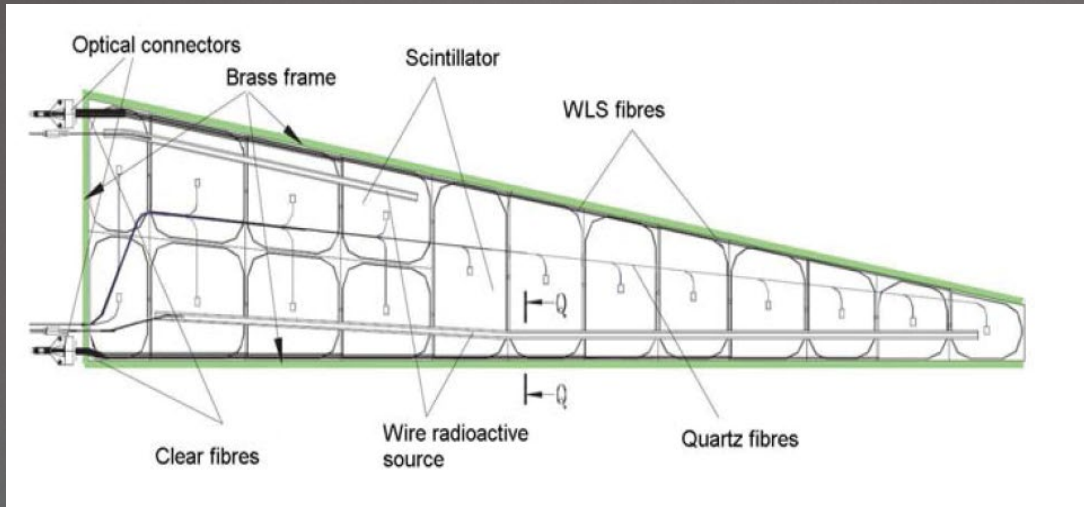
uses blue scintillator as the active material with blue-to-green wavelength shifting fiber to capture light and bring it to HPD



Layer 0: 9 mm BC-408
Layers 1-16: 3.7 mm SCSN-81
Both use 0.9 mm Y11 WLS fiber

For CMS design, a 10x10cm tile with a 3.7mm thickness of SCSN-81 (a blue scintillator by Kuraray) with 0.9mm Y11 blue to green WLS fiber (Kuraray) gives an average of 3 photoelectrons/mip.

Hadron Endcap (HE) tiles



Plastic Scintillator

79

Advantages:

- Long experience with this material
- Low cost
- Ease of construction
- Fast time response

Questions:

- Radiation hardness

What is plastic scintillator

80

1/17/17

- ▶ A **substrate** such as polyvinyltolulene (PVT), polystyrene (PS) or polymethylmethacrylate (PMMA)
- ▶ Two wavelength-shifting **dopants**, one with a concentration of about 1-2% (primary dopant), the other with a concentration of about 0.1% (secondary dopant)

Scintillation process

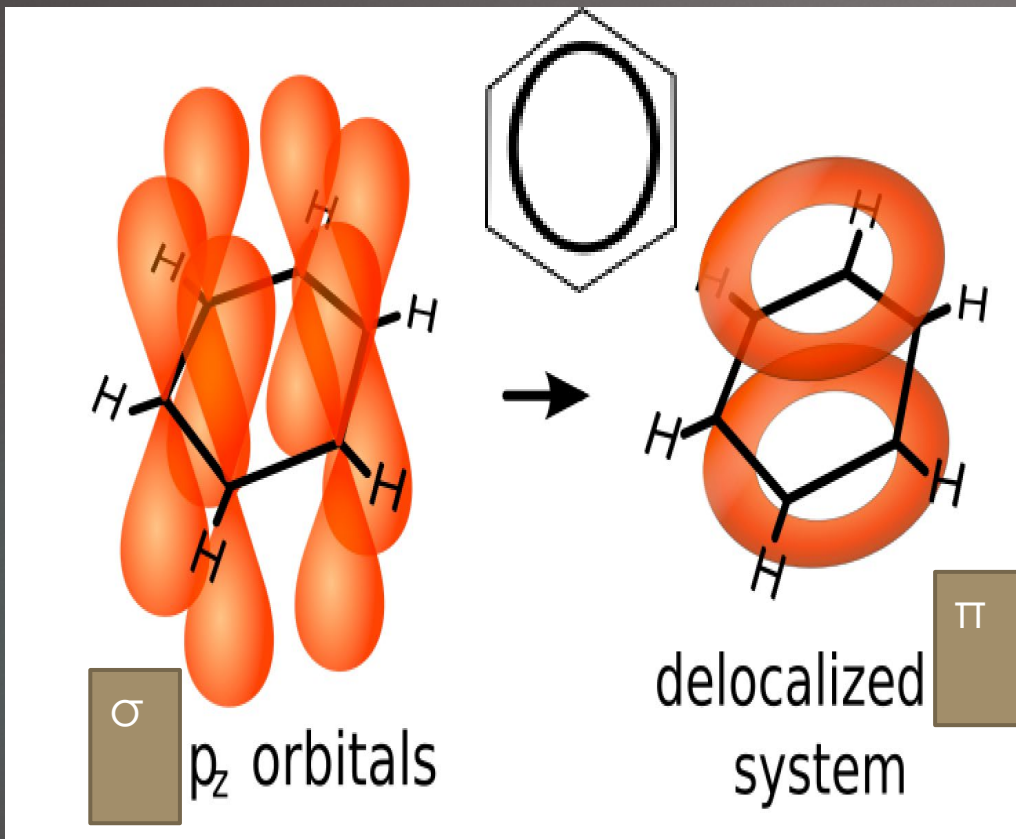
81

- Particle excites electrons in molecules in the substrate
- The initial excitation can be transferred to the primary dopant radiatively (in the deep UV) or through dipole-dipole interactions. The substrate can also de-excite in ways that do not lead to transfer to the dopant. These include transfer to another substrate molecule, quenching (becomes thermal energy) and inter-system crossing.
- Transfer to primary depends on concentration. Mostly radiative for low concentrations. Dipole-dipole increases with doping.
- Secondary dopant needed because the absorption length of the primary emission is typically $O(\text{cm})$ while detectors typically are large compared to this size. Also to match to photodetector

1/17/17

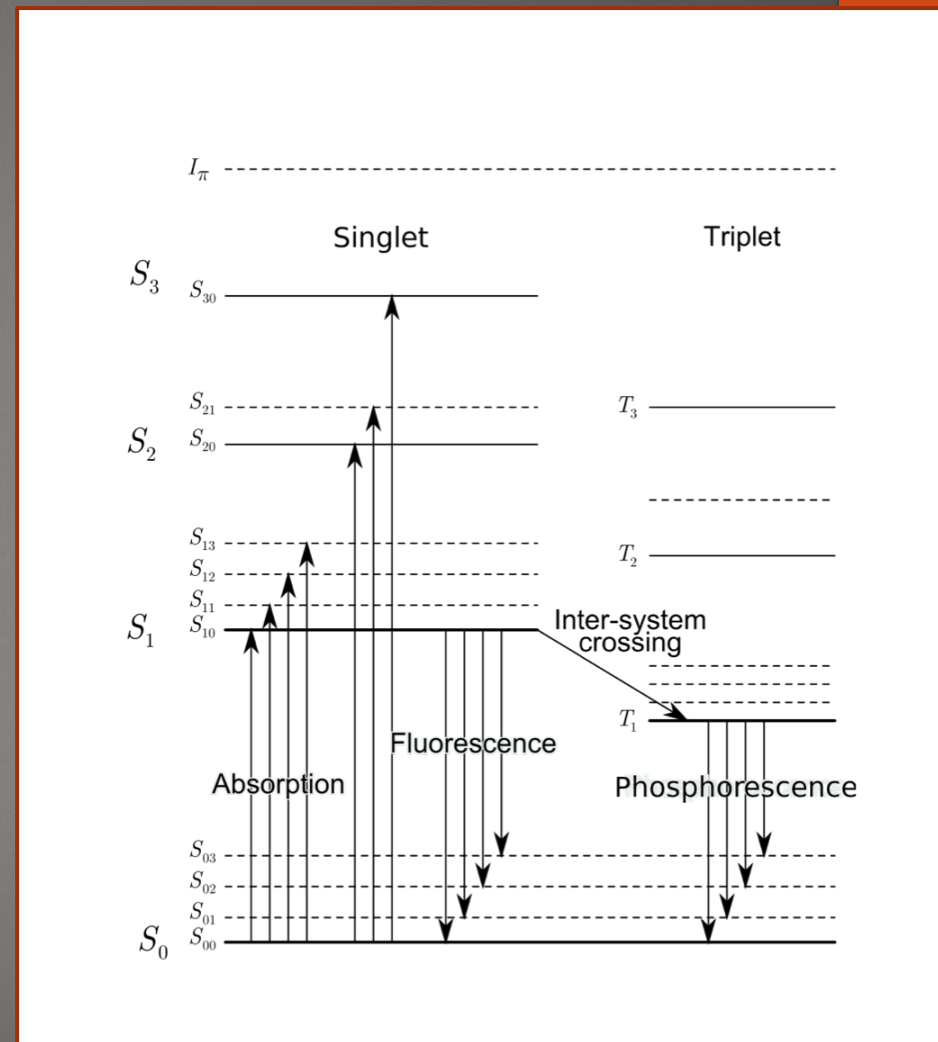
Of these, most of the physics and the problems/challenges of scintillator are in the substrate so let's talk about this first.

benzene



Three double bonds shared equally between 6 atoms

Picture from wikipedia.



Making polymers

83

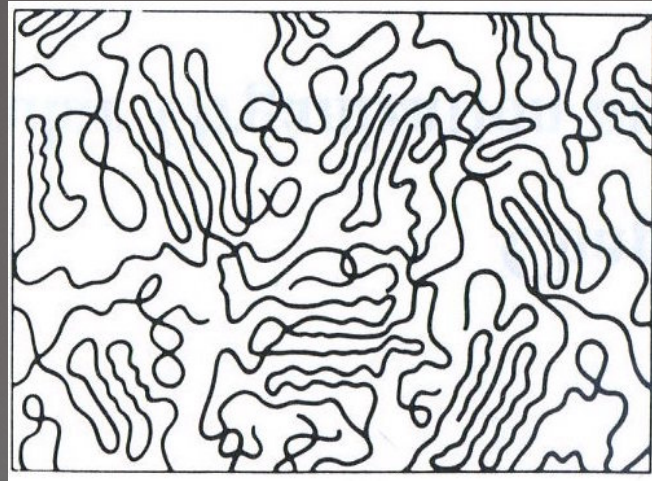
Styrene was first de inhibited through a column and then purified by vacuum distillation. Glass polymerization tubes were cleaned with nitric and sulfuric acids, rinsed with distilled water, and then treated for about 4 h with a 30% solution of dimethyldichlorosilane in chloroform. Finally, they were rinsed in turn with chloroform, methanol, and distilled water. This treatment builds a hydrophobic Langmuir layer on the walls of the tube which enables the removal of the plastic after polymerization. Appropriate dopants were then added to the polymerization tubes filled with purified styrene and the various solutions degassed with repeated freeze-pump-thaw cycles. The solutions were polymerized in a silicone oil bath at 110°C for 24 h, at 125°C for 48 h, and finally at 140°C for 12 h. The bath temperature was then ramped down to 90°C at a rate of 10°C/h. After removal from the oil bath, the tubes were quenched in liquid nitrogen for a fast release of the plastic rods. The rods were then cut and polished into discs of 2.2 cm diameter and 1 cm thick.

Form long strings of these monomers

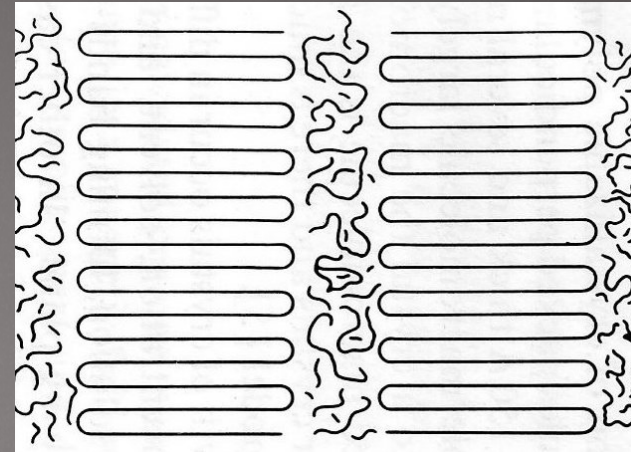
NIM A307 (1991) 35

Also see thesis, Ana Pla-Dalmau, NIU

polymers



Amorphous polymer



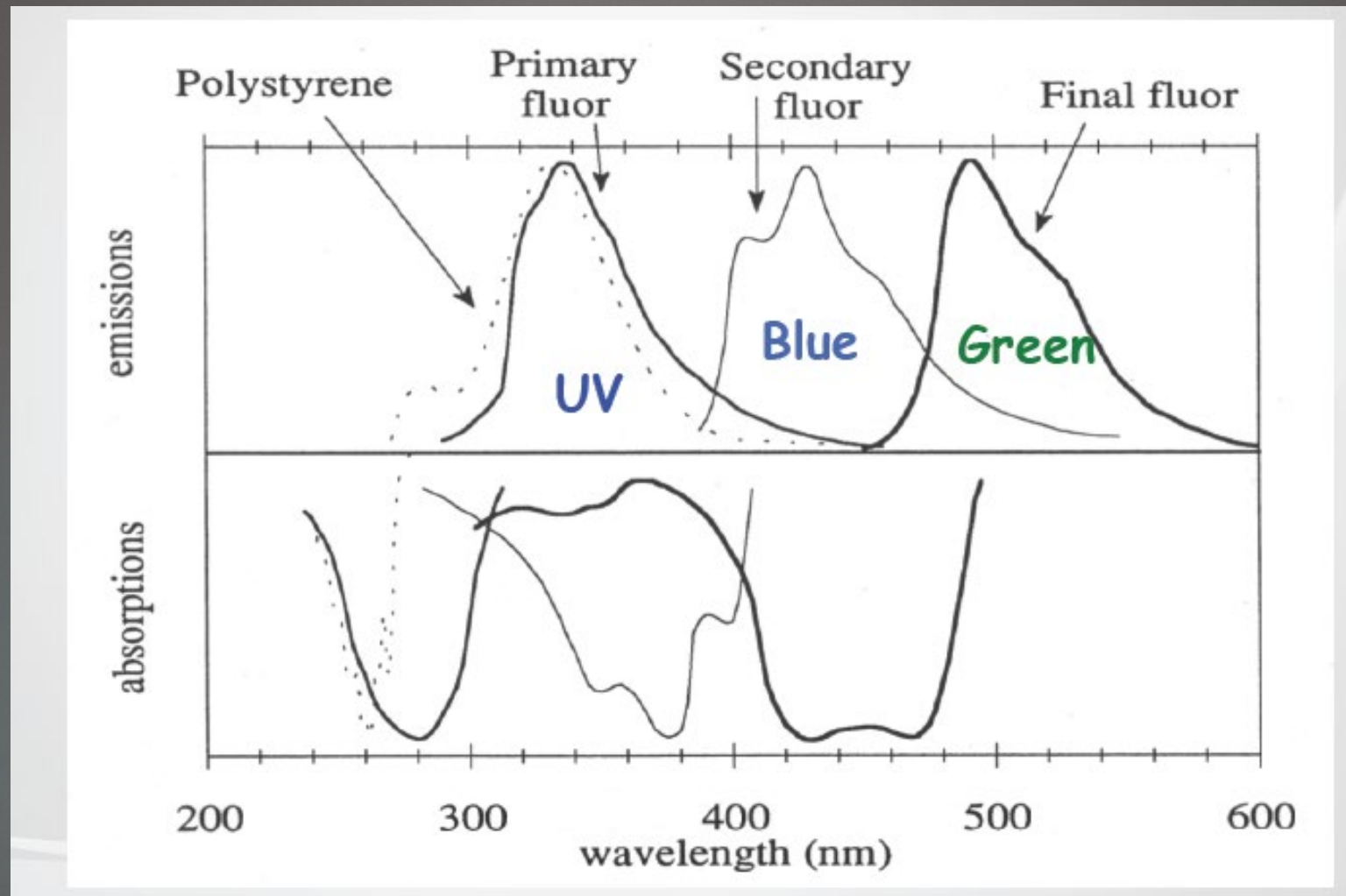
Crystalline polymer

Polymers can be created in “amorphous” arrangement or crystalline. Polystyrene is amorphous (unless specially prepared so that the phenyl groups are in the same substitution position throughout the polymer chain)

Behavior depends on molecule “weight”, related to the length of the molecule.

fluors

85



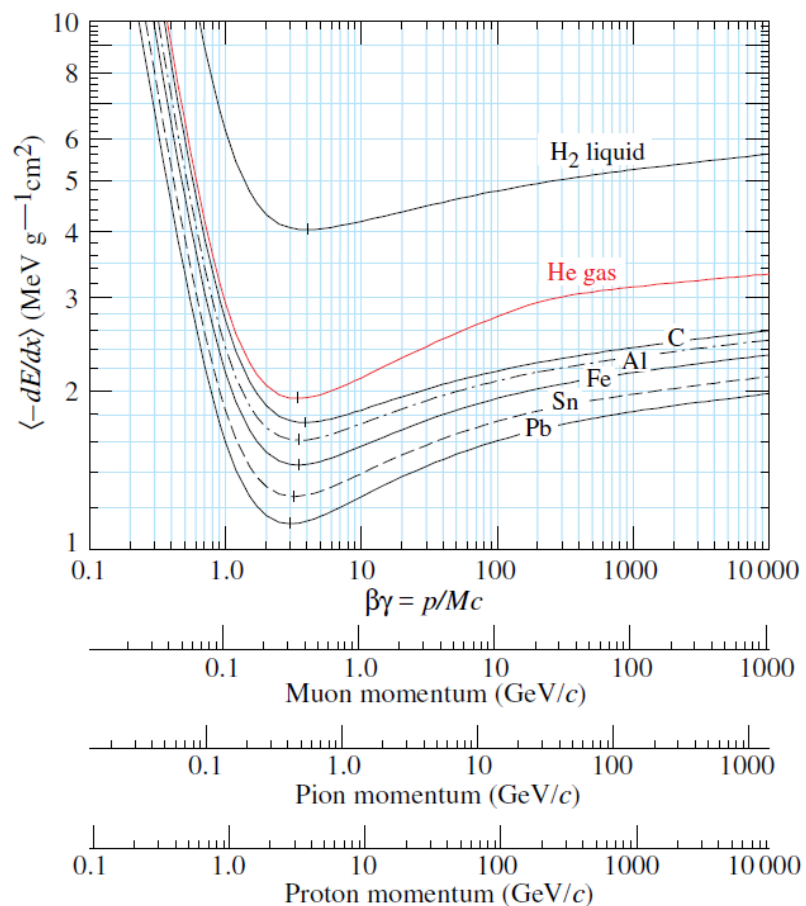


Figure 34.2: Mean energy loss rate in liquid (bubble chamber) hydrogen, gaseous helium, carbon, aluminum, iron, tin, and lead. Radiative effects, relevant for muons and pions, are not included. These become significant for muons in iron for $\beta\gamma \gtrsim 1000$, and at lower momenta for muons in higher- Z absorbers. See Fig. 34.23.

Need to be careful when calculating energy deposition. Scintillator is hydrogen rich.

This also affects its interactions with neutrons.

Building a better calorimeter

Improved hadronic calorimetry

compensation

compensation

89

The response to the “hadronic” portion of a hadronic shower gives a lower response due to a variety of factors. Is there some way to boost it back up?

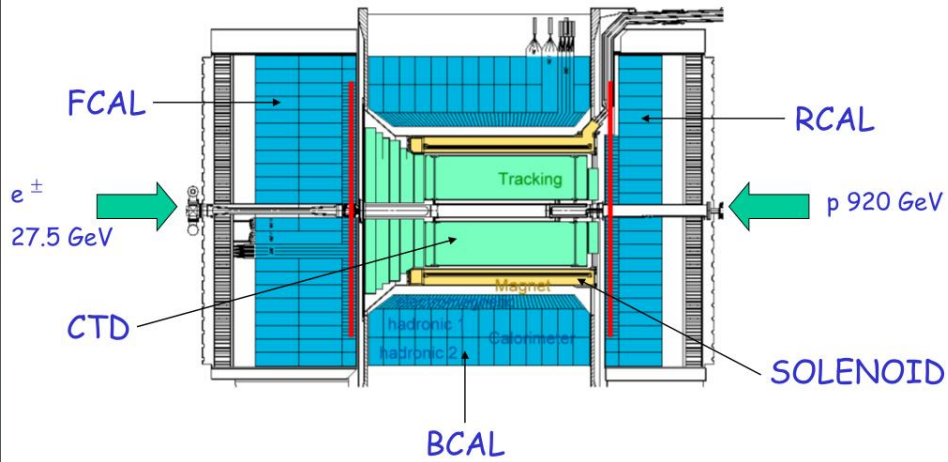
- Use uranium based calorimeter, using the released fission energy to boost the signal (Dzero, Zeus calorimeter). Turns out this was a red herring, although both did have good hadron resolution
- Use a detector with hydrogen to boost the signal from neutrons. Use a detector with high Z to suppress the EM response and increases neutron production. U has highest neutron production, but lead actually has the strongest correlation between neutron production and losses to binding energy. Sampling fraction needs to be low, which limits resolution. For a Pb/scintillator calorimeter, compensation occurs for a sampling fraction of 2% (too low for good EM resolution).

However

- Nevertheless tend to be nonlinear for particles with energies below 10 GeV, as these lose a lot of energy via ionization and e/mip is bad
- Recording neutrons requires long integration times, and also makes the showers broad

ZEUS

The ZEUS detector



EM calorimeter was Uranium and scintillator

Table 1
Composition of the EMC and HAC sections (normal incidence)

Section	Item	Material	Number	Thickness [mm]	X_0	λ
EMC	cover	steel	1	0.2	0.01	0.001
	front plate	Al	1	12.7	0.14	0.032
	scintillator	polystyrene	22	$22 \times 2.6 = 57.2$	0.14	0.072
	DU plate	U	21	$21 \times 3.3 = 69.3$	21.0	0.660
	cladding	steel	42	$42 \times 0.2 = 8.4$	0.48	0.050
	HES box	Al	2	$2 \times 1.0 = 2.0$	0.02	0.005
	shim	steel	1	0.2	0.01	0.001
	rear plate	Al	1	10.0	0.11	0.025
	Total		213.5	21.9	0.846	
HAC _I	front plate	steel	1	14.5	0.82	0.087
	scintillator	polystyrene	50	$50 \times 2.6 = 130.0$	0.31	0.164
	DU plate	U	49	$49 \times 3.3 = 161.7$	49.0	1.540
	cladding	steel	98	$98 \times 0.4 = 39.2$	2.23	0.234
	shim	Al	1	1.58	0.02	0.004
	Total		421.9	52.4	2.029	
HAC _{II}	interm. plate	steel	1	17.0	0.97	0.101
	scintillator	polystyrene	50	$50 \times 2.6 = 130.0$	0.31	0.164
	DU plate	U	49	$49 \times 3.3 = 161.7$	49.0	1.540
	cladding	steel	98	$98 \times 0.4 = 39.2$	2.23	0.234
	shim	Al	1	1.58	0.02	0.004
	Total		424.4	52.5	2.043	
T-beam	steel	1	30.0	1.71	0.179	
Total			1089.8	128.5	5.097	

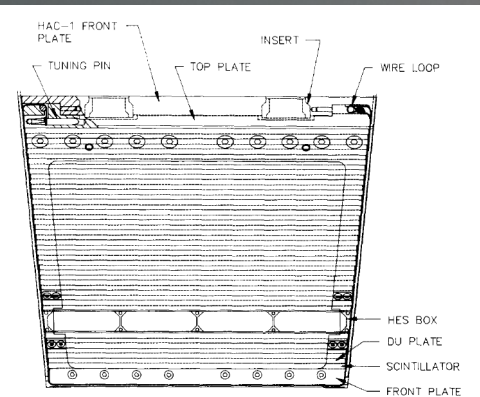


Fig. 9. Rear endview of the EMC section.

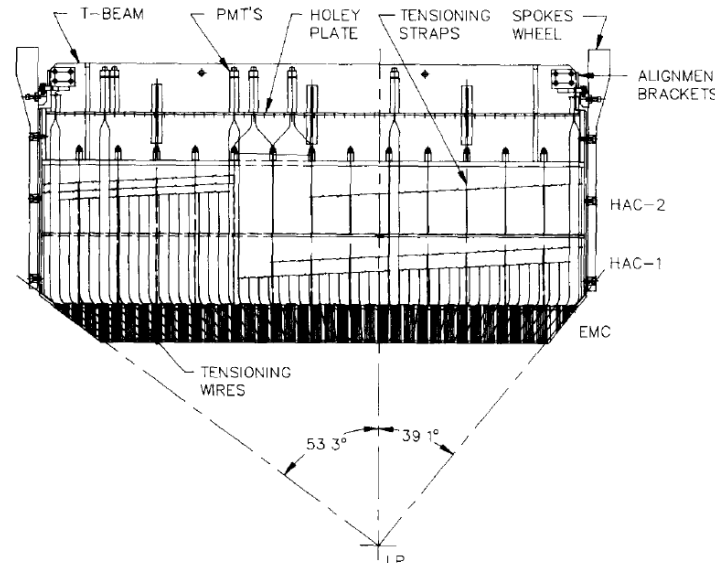


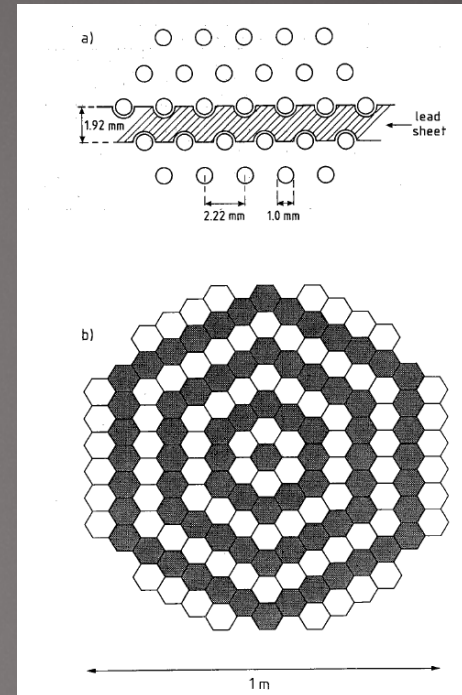
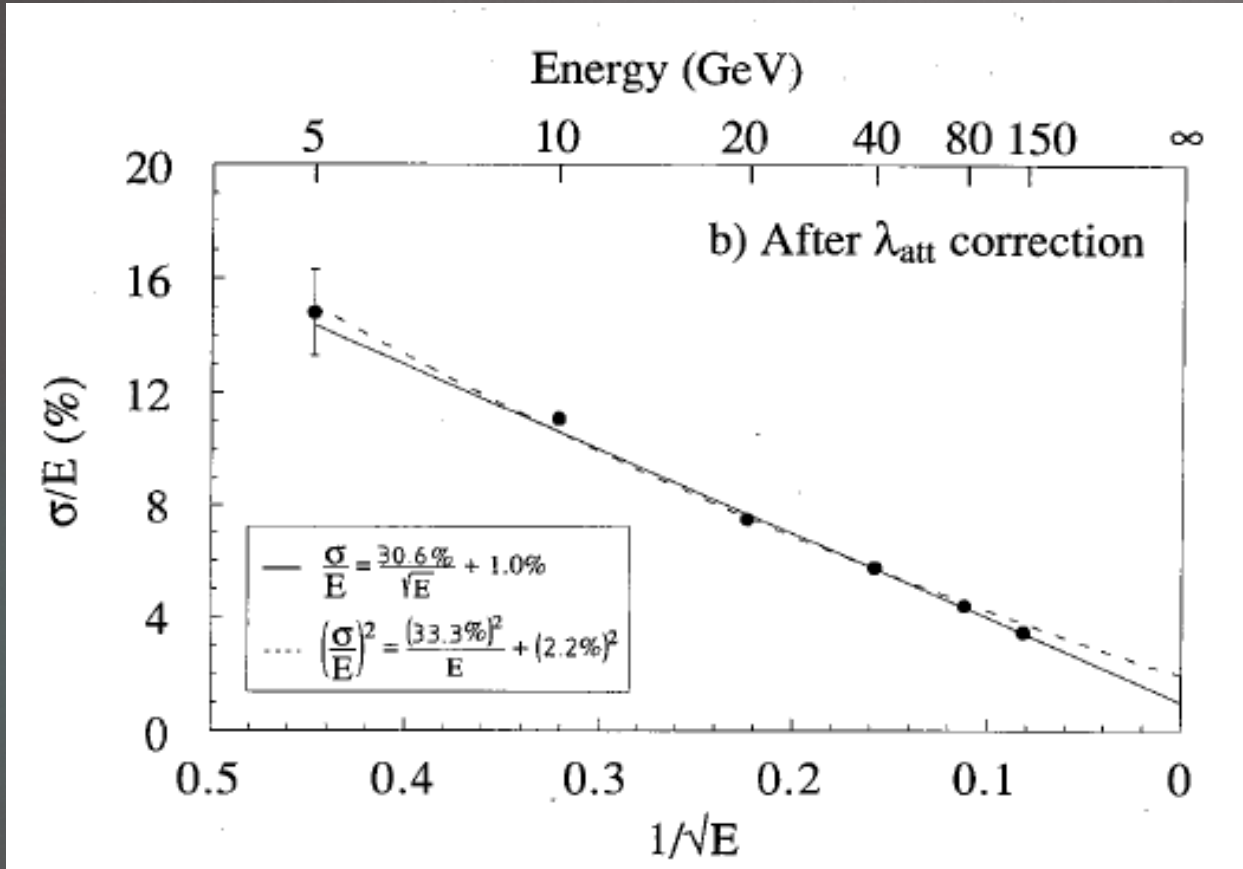
Fig. 4. Side view of a BCAL module mounted in the spokeswheels.

Another excellent calorimeter was the D0 U/liquid Argon calorimeter

spacal

Spaghetti calorimeter

91



Fibers parallel to incident particle direction uniformly sample the shower in depth, reducing response fluctuations due to shower starting position

Electron, pion, ... with a lead/scintillating-fiber calorimeter, CERN-PPE/91-85

Compensating calorimeters

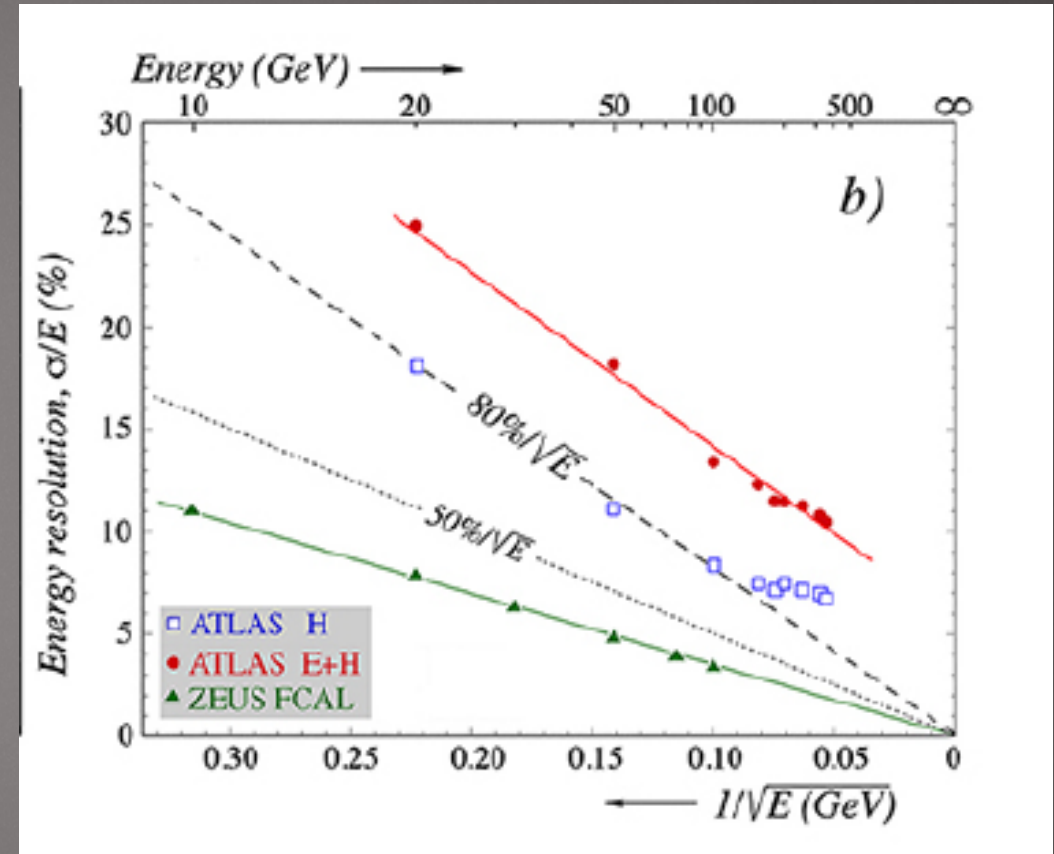
Table 34.9: Examples of near-compensating sampling hadron calorimeters. For our present purposes some calorimeter structure variation and “constant terms” in the fitted resolution have been ignored.

Calorimeter	Passive	Active	Resolution	$\langle e/h \rangle$	Reference
(Ake sson et al.)	U, U/Cu (3/5 m)	Scint (2.5mm)	$36\%/\sqrt{E}$	1.11	[238]
HELIOS	U (3 mm)	Scint (2.5 mm)	$34\%/\sqrt{E}$	1.016 ± 0.006	[239]
(Drews <i>et al.</i>)	Pb (10 mm)	Scint (2.5 mm)	$44\%/\sqrt{E}$	1.10 ± 0.01	[240, 241]
(Drews <i>et al.</i>)	U (3.2 mm)	Scint (3.0 mm)	$36\%/\sqrt{E}$	1.02 ± 0.01	[241]
WA80	U (3 mm)	Scint (3 mm)	$67\%/\sqrt{E}$	1.12	[242]
ZEUS FCAL	U (3.0/3.2 mm)	Scint (2,5/3.0 mm)	$35\%/\sqrt{E}$	0.97	[243, 244]
SPACAL	Pb (4× scint vol)	1 mm scint fibers	$30\%/\sqrt{E}$	1.15 ± 0.02	[245]
SICAPO	Fe/Pb	Si		$1.11-0.89^*$	[218]
DØ	U (6 mm) [†]	LAr (2 × 2.3)	$44\%/\sqrt{E}$	1.08	[246]

* SICAPO: Various Fe/Pb configurations, G10 plates next to Si detectors.

† DØ: 1 mm G10 between LAr gaps may help compensation.

Sampling terms of 30% for single particles. Up to the specs for jets for future calorimeters, but except in detail (low energy particle response, jet clustering artifacts, residual nonlinearity)



October 2018 Test Beam

300GeV pion

EE

Si-FH

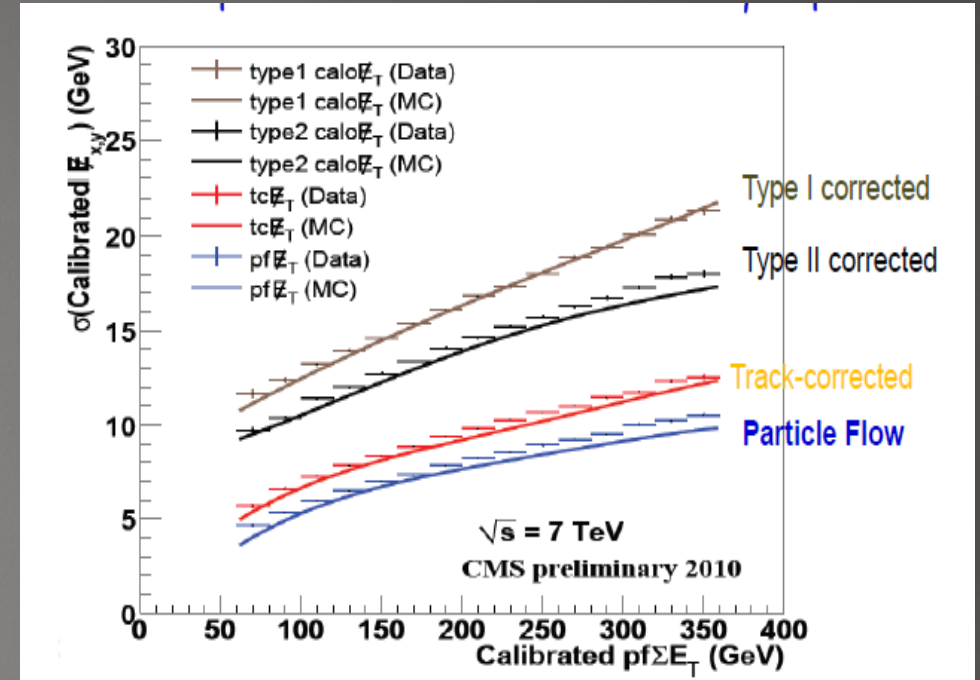
Scint-AHCAL



“Particle flow” or
“high granularity”
calorimetry

disclaimer

“Particle Flow” is a reconstruction technique that can be applied to any calorimeter. Invented at ALEPH and used extensively e.g. CMS. If your hadronic resolution is bad enough, it improves any calorimeter e.g. CMS. “The particle-flow (PF) algorithm is used to reconstruct and identify each individual particle, with an optimized combination of information from the various elements of the CMS detector.”



However, it works best with a calorimeter specifically designed for this kind of algorithm.

Basic idea

95

Since hadron calorimeter are challenging, use them as little as possible.

- Use tracker to measured charged particles
- Use EM calorimeter to measure photons
- Use HAD calorimeter only to measure neutral hadrons

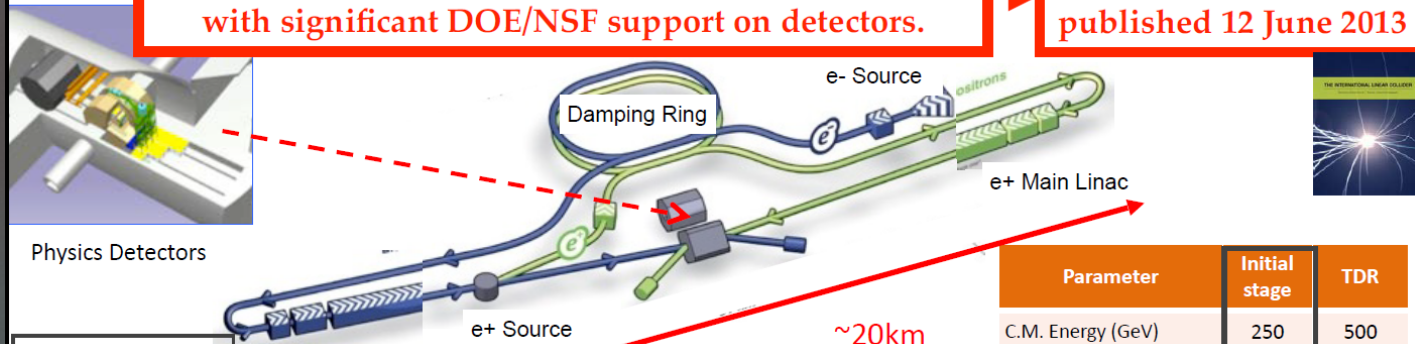
Of course, can improve things by combining the calorimeter and tracker information. Helps especially at high energy where the calorimeter works best

Originally developed for ILC

International Linear Collider (ILC)

Design from two decades of GDE-led dedicated R&D, with significant DOE/NSF support on detectors.

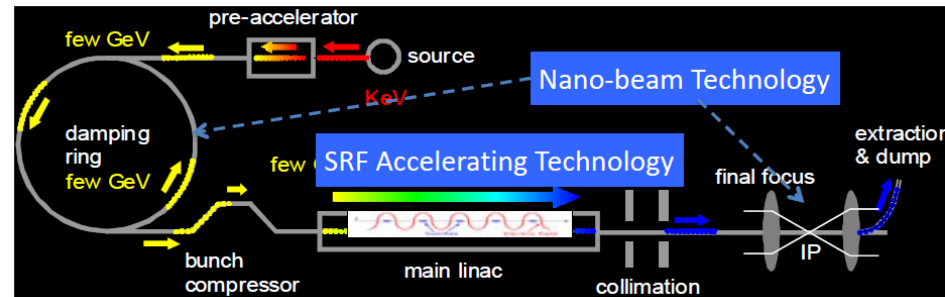
ILC TDR is 5-volumes, published 12 June 2013



Physics Detectors

arXiv:
1711.00568
1903.01629

Key Technologies



Polarized electrons ($\pm 80\%$) and positrons ($\pm 30\%$)

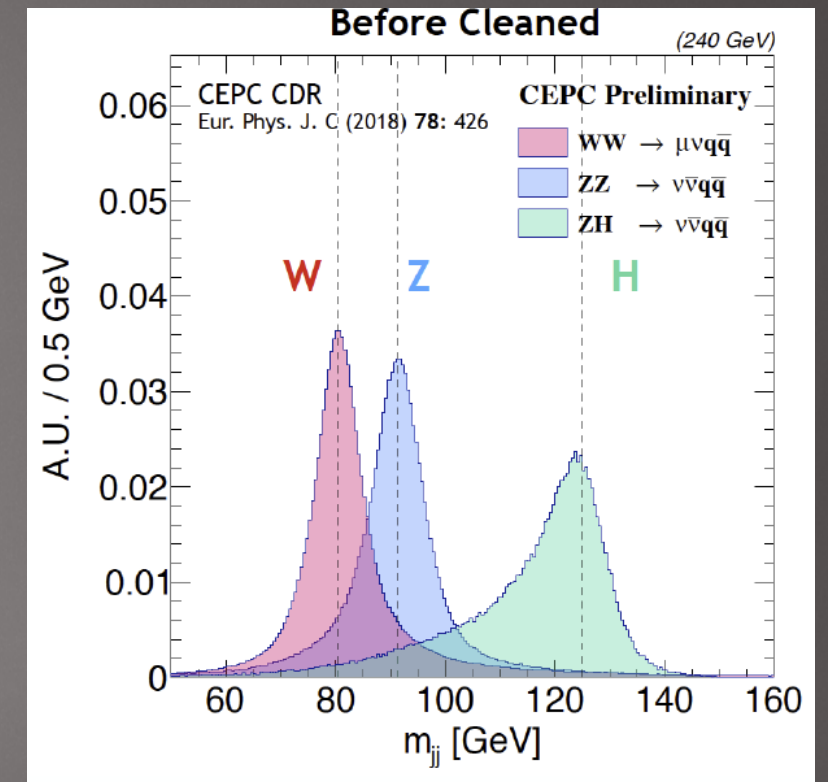
based on S. Michizono, 8 Nov 2017

The International Linear Collider

J. Brau - Virtual Workshop - 22 April 2020

5

Parameter	Initial stage	TDR
C.M. Energy (GeV)	250	500
Length (km)	20	31
Luminosity ($\times 10^{34}$)	1.35 (2.7, 5.4)	1.8
Repetition (Hz)	5 (10)	5
Beam Pulse Period (ms)	0.73	0.73
Beam Current (mA in pulse)	5.8	5.8
Beam size (y) at FF (nm)	7.7	5.9
SRF Cavity Gr (MV/m), Q_0	31.5, 1×10^{10}	31.5, 1×10^{10}
Site Power (MW)	129	163



Sampling term of 30%

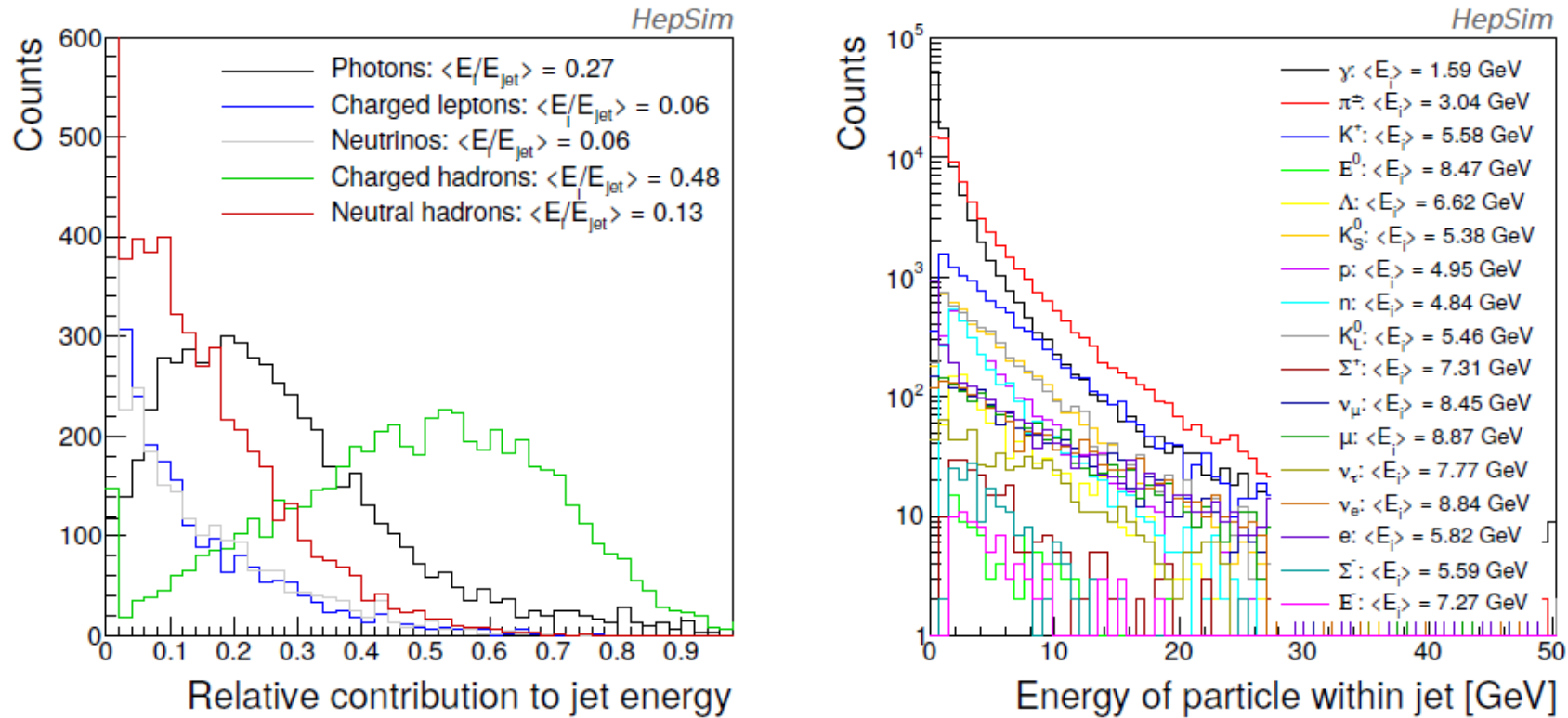
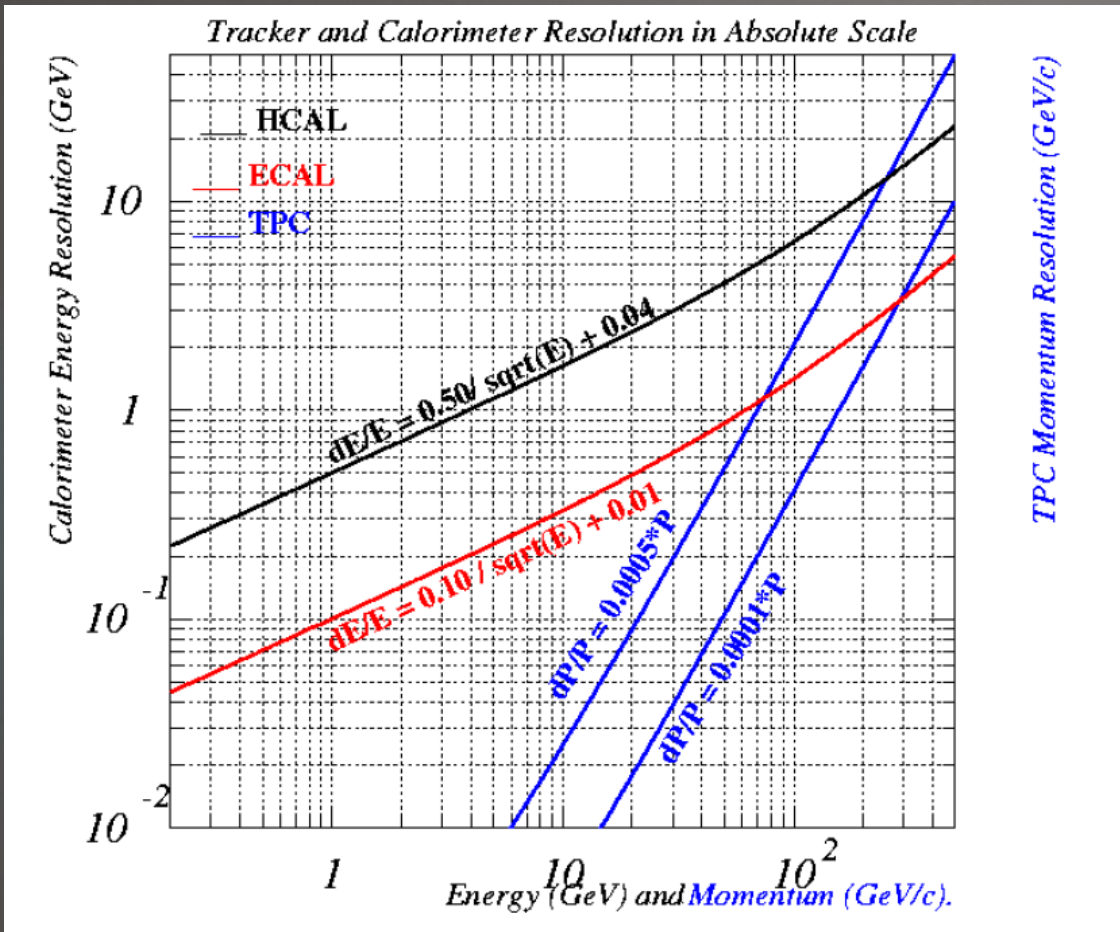
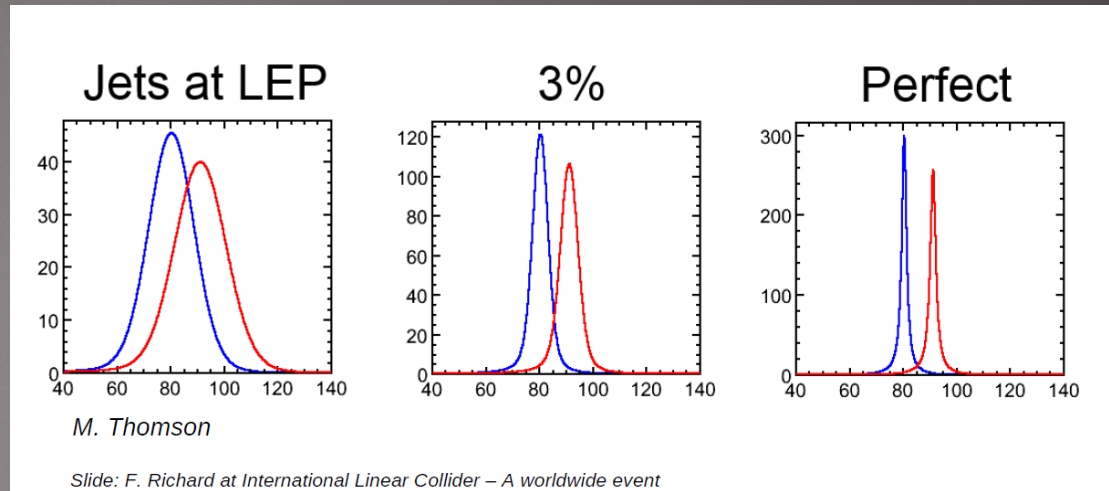


Figure 1. Left: relative contribution of different particles (photons, neutrinos, leptons, neutral hadrons, charged hadrons) to the jet energy. Right: energy distribution of different particle types clustered within jet.

Can live with a mediocre calorimeter



TPC Momentum Resolution (GeV/c)



Calorimeter resolution requirements not that stringent. 50% HAD and 10% EM stochastic terms

Jet resolution has 30% stochastic term.

But there is a challenge

99

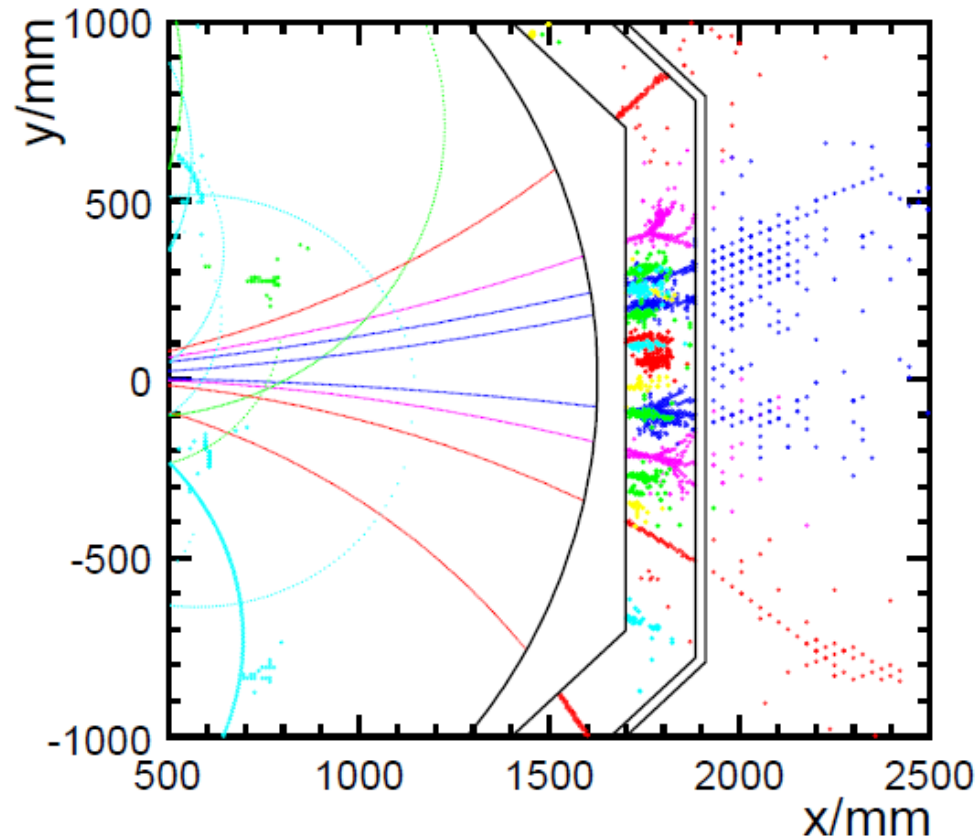


Figure 6: PandoraPFA reconstruction of a 100 GeV jet in the MOKKA simulation of the ILD detector. The different PFOs are shown by colour/grey-shade according to energy.

Unlike tracks, showers have finite lateral extent that can be larger than the separation between particles, it can be hard to “remove” the charged hadron energy.

CALICE: very high granularity can help resolve showers

n.b. This becomes much worse with higher energy jets

Pattern recognition in hadron calorimeter is hard

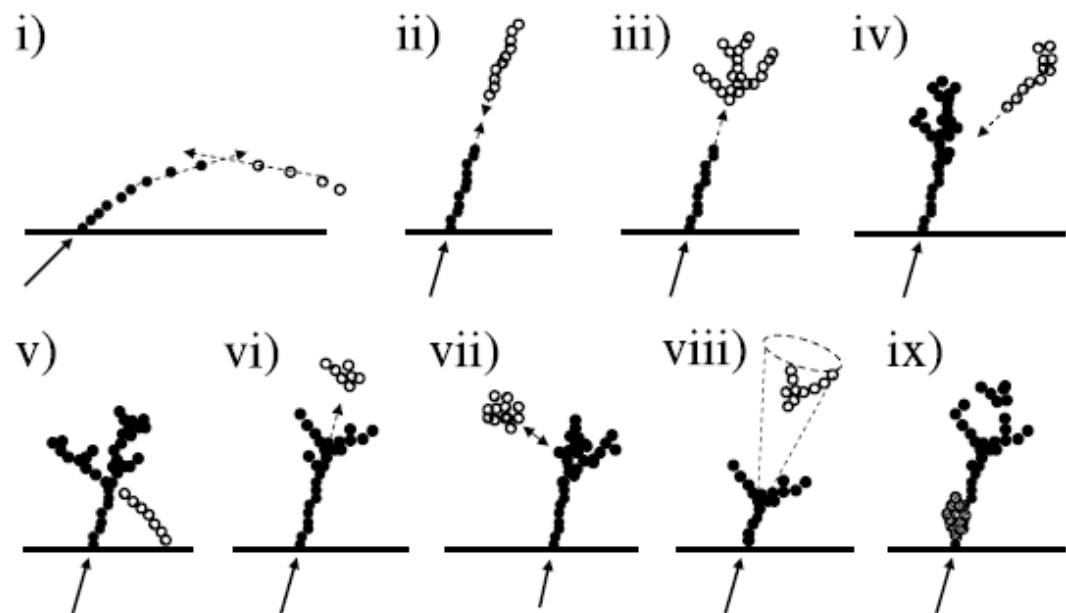


Figure 4: The main topological rules for cluster merging: i) looping track segments; ii) track segments with gaps; iii) track segments pointing to hadronic showers; iv) track-like neutral clusters pointing back to a hadronic shower; v) back-scattered tracks from hadronic showers; vi) neutral clusters which are close to a charged cluster; vii) a neutral cluster near to a charged cluster; viii) cone association; and ix) recovery of photons which overlap with a track segment. In each case the arrow indicates the track, the filled points represent the hits in the associated cluster and the open points represent the hits in the neutral cluster.

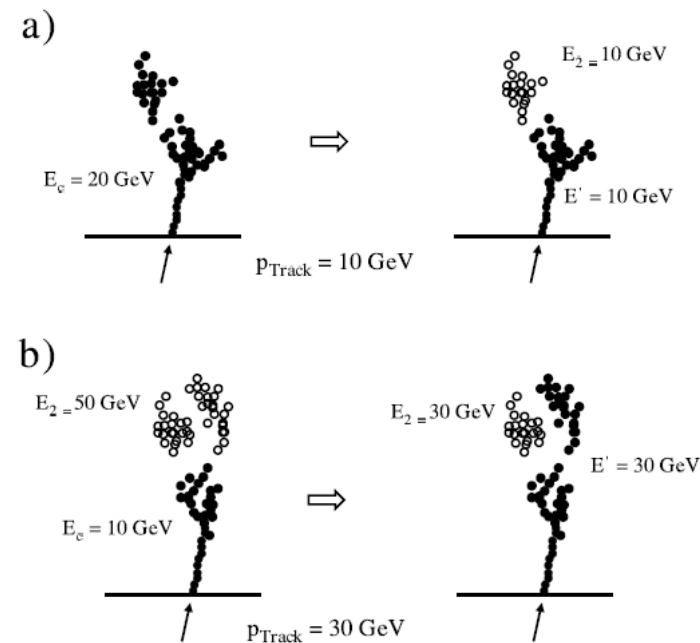


Figure 5: Schematic examples of the main reclustering strategies used in PandoraPFA. The arrows indicate the track, the filled points represent the hits in the associated charged cluster and the open points represent the hits in the neutral cluster. a) Here the charged cluster energy is initially significantly greater than the associated track momentum. The hits are reclustering using modified parameters for the clustering algorithm in the hope that a more consistent solution can be found. b) Here the cluster energy is significantly less than the associated track momentum. The topological association algorithms (vii) and (viii) have not added the neutral cluster as his would have resulted in a charged cluster with too much energy for the track momentum. The hits are reclustering in the hope that the neutral cluster naturally splits in such a way that the topological association algorithm will now make the correct association.

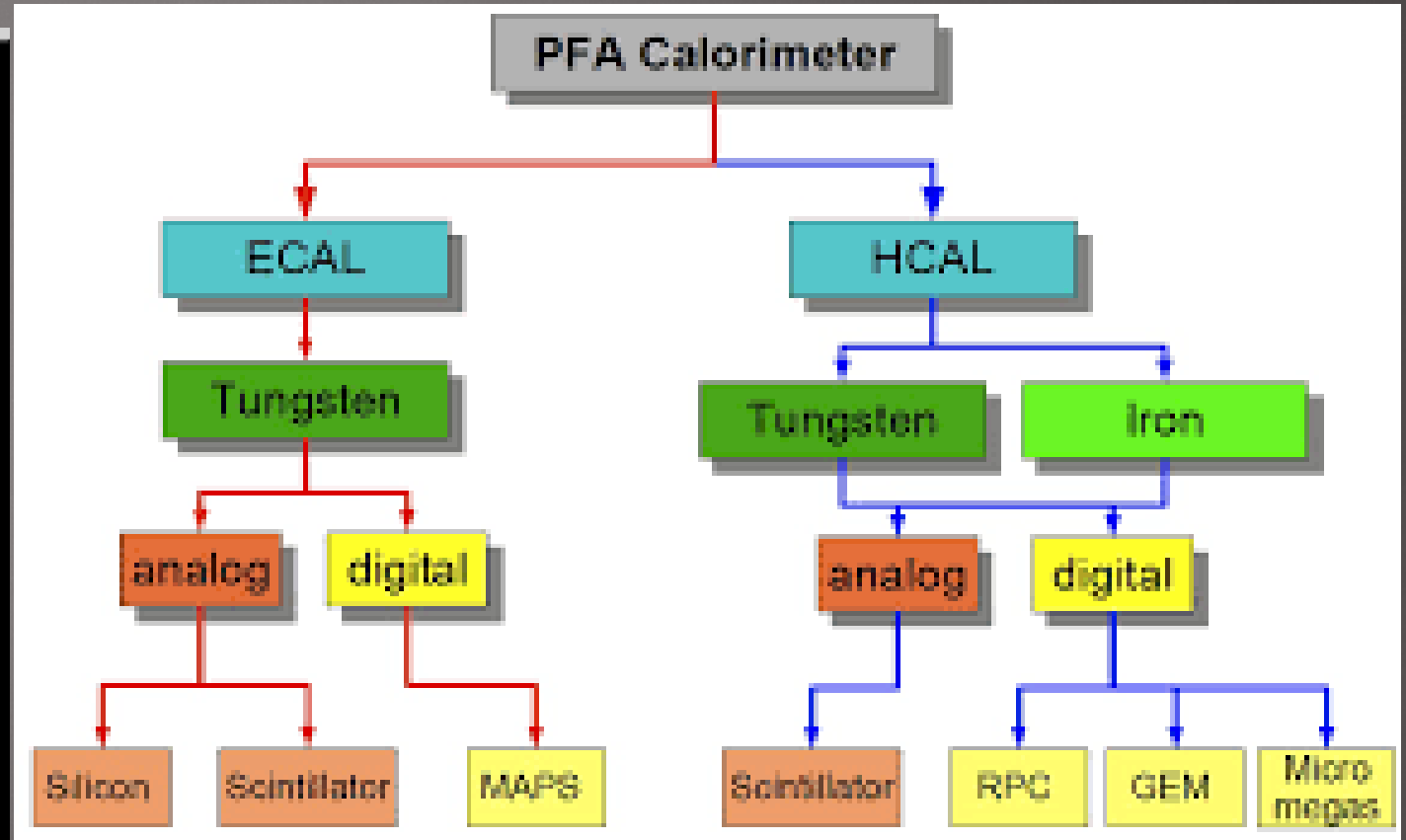
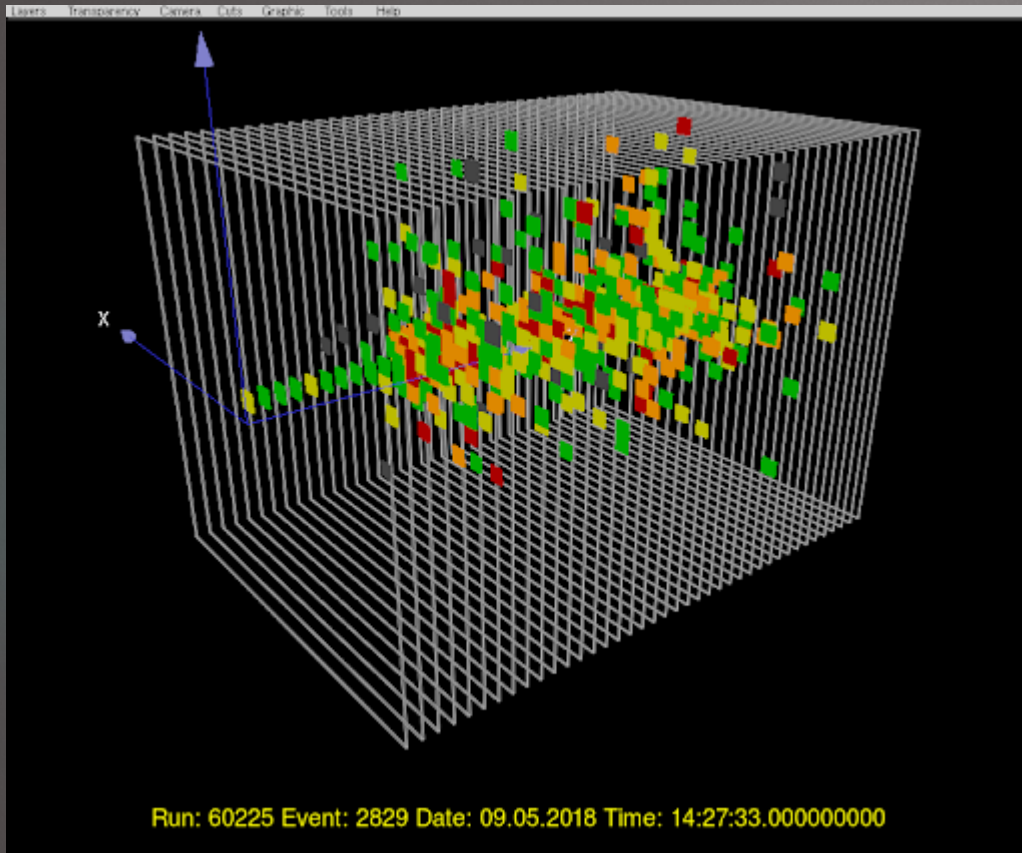
Very high granularity can help find links between main shower and splinter showers

Highly segmented calorimeters

101

CALICE

<https://twiki.cern.ch/twiki/bin/view/CALICE/WebHome>
Created in 2005



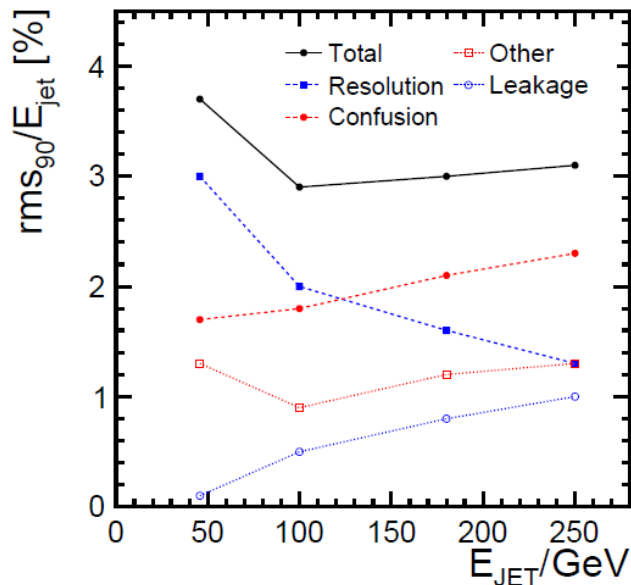
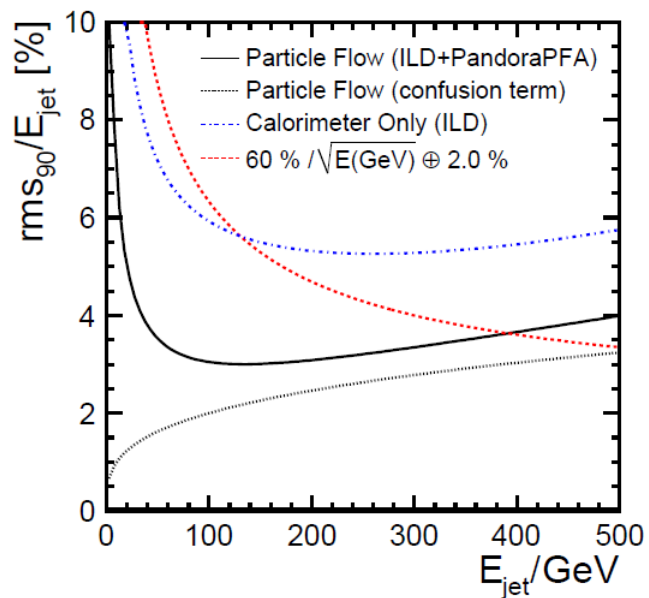
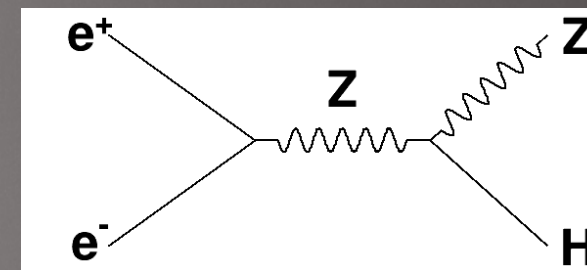


Figure 10: The empirical functional form of the jet energy resolution obtained from PFlow calorimetry (PandoraPFA and the ILD concept). The estimated contribution from the confusion term only is shown (dotted). The dot-dashed curve shows a parameterisation of the jet energy resolution obtained from the total calorimetric energy deposition in the ILD detector. In addition, the dashed curve, $60\% / \sqrt{E(\text{GeV})} \oplus 2.0\%$, is shown to give an indication of the resolution achievable using a traditional calorimetric approach.

Figure 9: The contributions to the PFlow jet energy resolution obtained with PandoraPFA as a function of energy. The total is (approximately) the quadrature sum of the components.

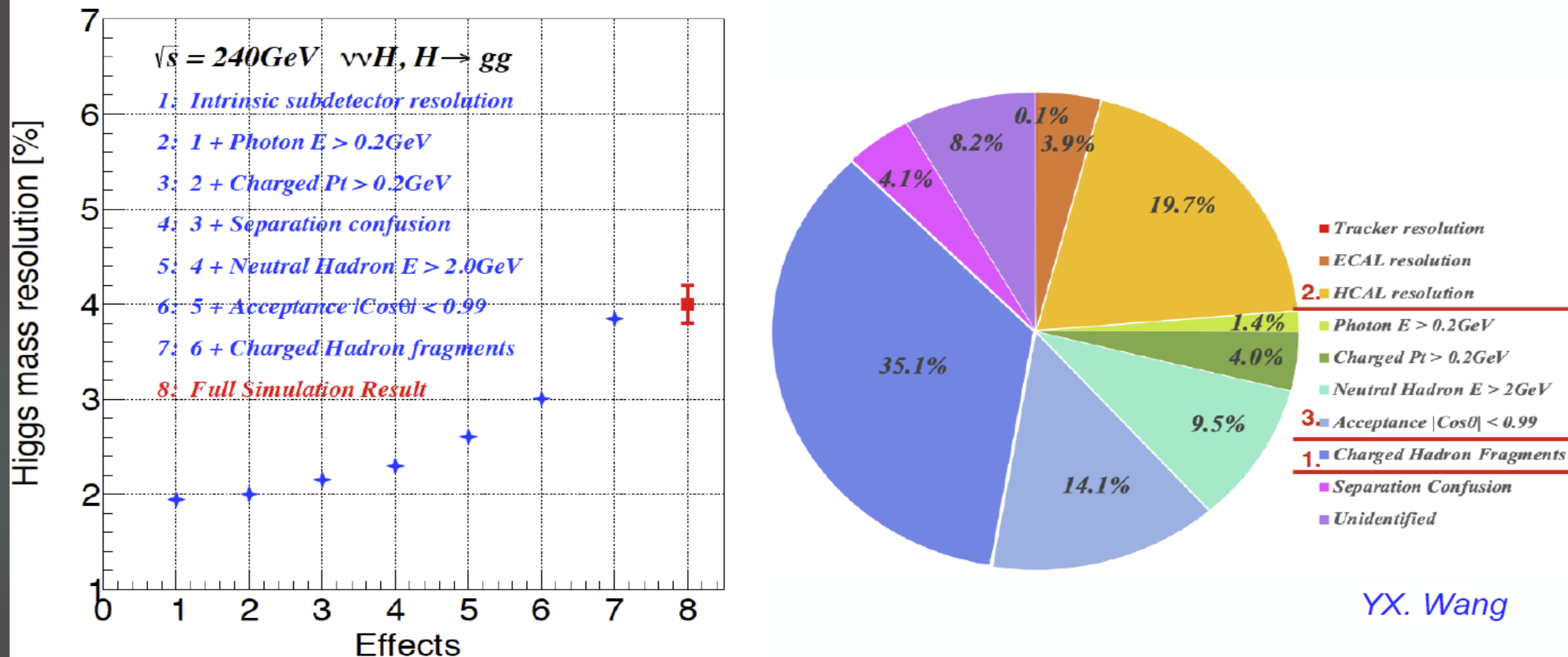


Shower separation is challenging for very high energy jets. The jets in ZH events are mostly less than 100 GeV, so PF should still work well for electron-positron Higgs factors. Di-Higgs at CLIC, etc more challenging

Contribution	Jet Energy Resolution $\text{rms}_{90}(E_j)/E_j$			
	$E_j=45 \text{ GeV}$	$E_j=100 \text{ GeV}$	$E_j=180 \text{ GeV}$	$E_j=250 \text{ GeV}$
Total	3.7%	2.9%	3.0%	3.1%
Resolution	3.0%	2.0%	1.6%	1.3%
Tracking	1.2%	0.7%	0.8%	0.8%
Leakage	0.1%	0.5%	0.8%	1.0%
Other	0.6%	0.5%	0.9%	1.0%
Confusion	1.7%	1.8%	2.1%	2.3%
i) Confusion (photons)	0.8%	1.0%	1.1%	1.3%
ii) Confusion (neutral hadrons)	0.9%	1.3%	1.7%	1.8%
iii) Confusion (charged hadrons)	1.2%	0.7%	0.5%	0.2%

Table 5: The PFlow jet energy resolution obtained with PandoraPFA broken down into contributions from: intrinsic calorimeter resolution, imperfect tracking, leakage and confusion. The different confusion terms correspond to: i) hits from photons which are lost in charged hadrons; ii) hits from neutral hadrons that are lost in charged hadron clusters; and iii) hits from charged hadrons that are reconstructed as a neutral hadron cluster.

PFA Fast simulation (Preliminary)



Fast simulation reproduces the full simulation results, factorize/quantifies different impacts
 Same cleaning condition as in the Full simulation applied
 Early phase of modeling/tuning

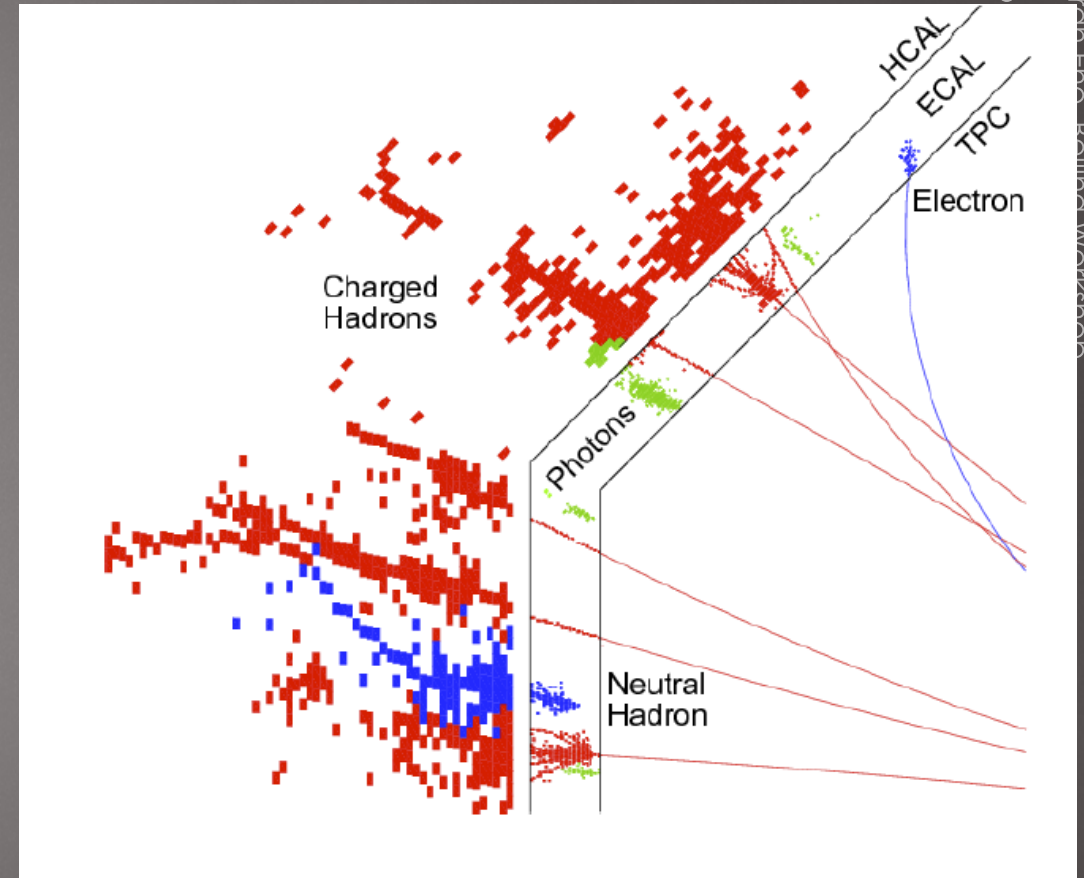
Hadron fragmentation

An interesting parameter is the ratio of the hadronic to electromagnetic interaction length.

Having deeper hadronic showers helps separation of gammas and neutral hadrons.

Material	Radiation length	Absorp. length	ratio
W	3.5 mm	99.5 mm	28
PbWO ₄	8.9 mm	240 mm	27

W:Cu	100:0	85:15	75:25
X ₀ (mm)	3.5	4.4	5.1



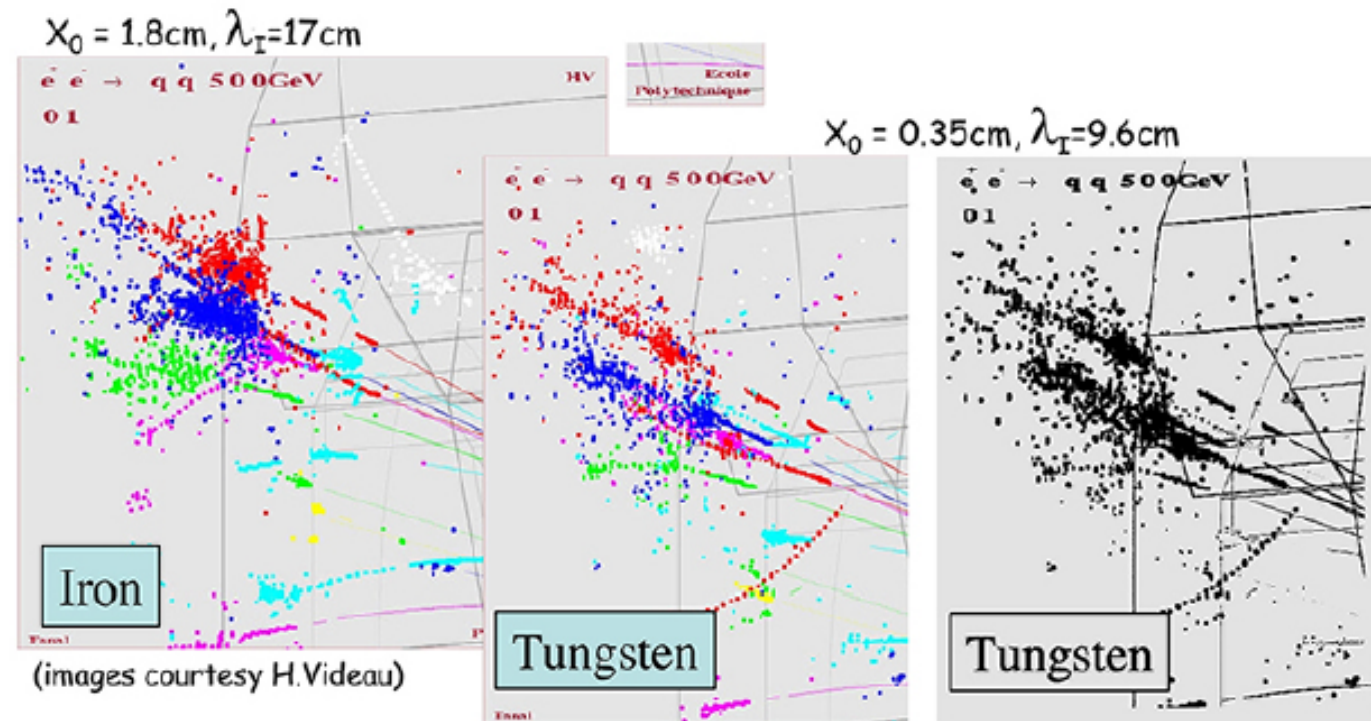


Figure 47: Simulated shower development of jet fragments in a calorimeter based on iron (left) or tungsten (center, right) as absorber material.

Cell size optimization

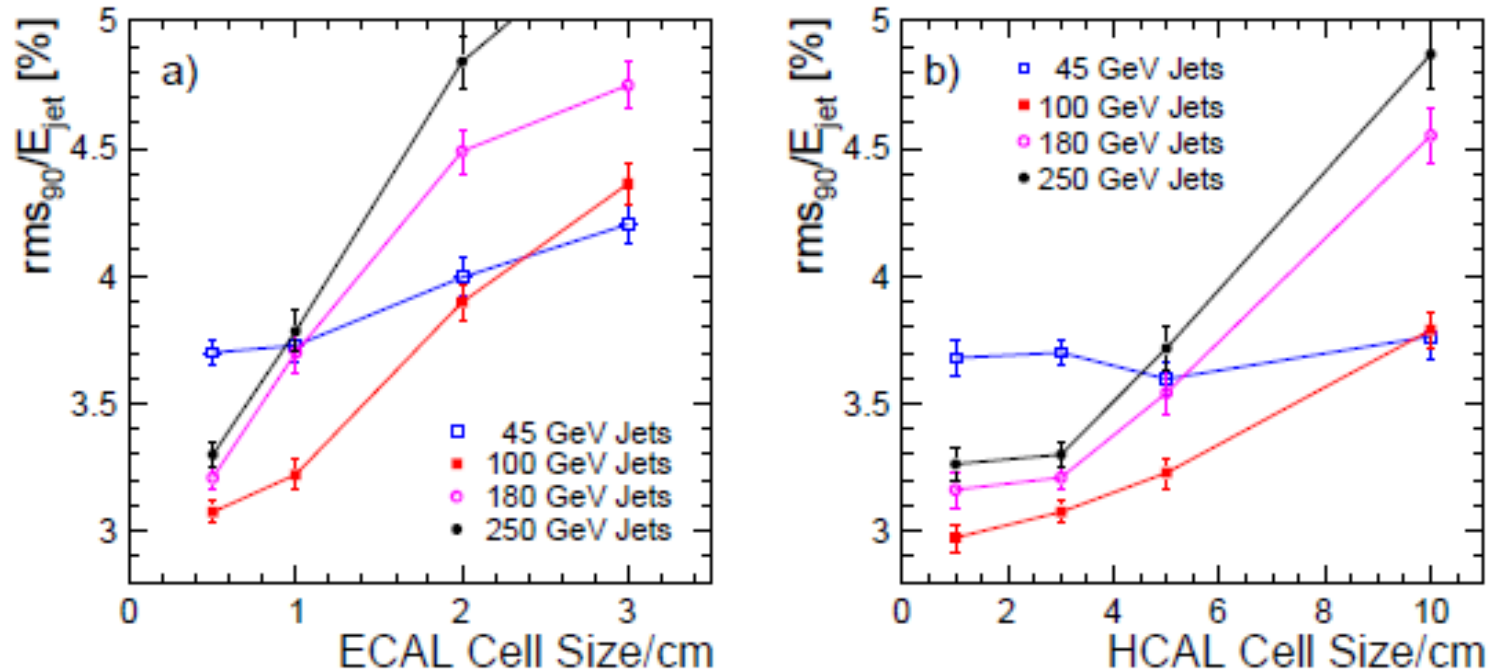
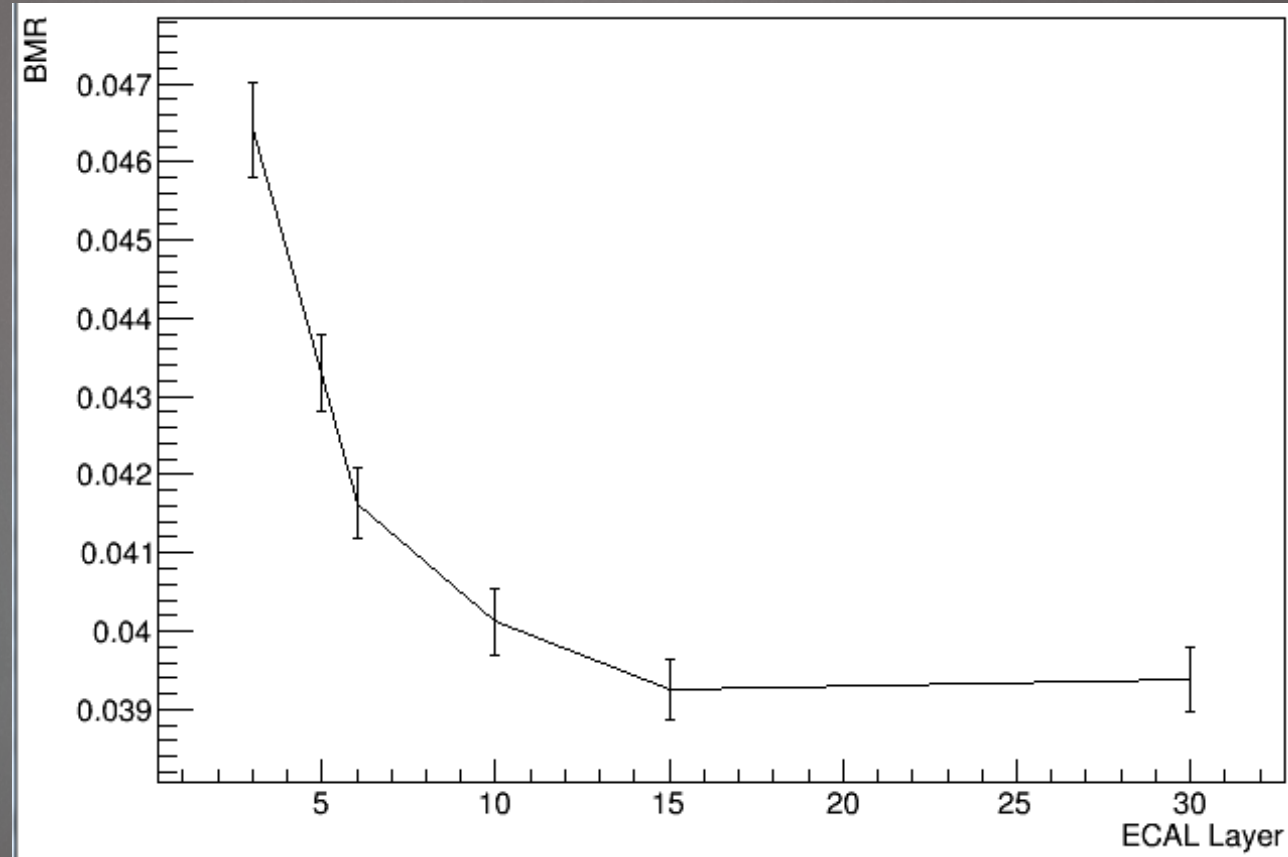


Figure 13: a) the dependence of the jet energy resolution (rms_{90}) on the ECAL transverse segmentation (Silicon pixel size) in the LDCPrime model. b) the dependence of the jet energy resolution (rms_{90}) on the HCAL transverse segmentation (scintillator tile size) in the LDCPrime model. The resolutions are obtained from $Z \rightarrow u\bar{u}, d\bar{d}, s\bar{s}$ decays at rest. The errors shown are statistical only.

Longitudinal segmentation

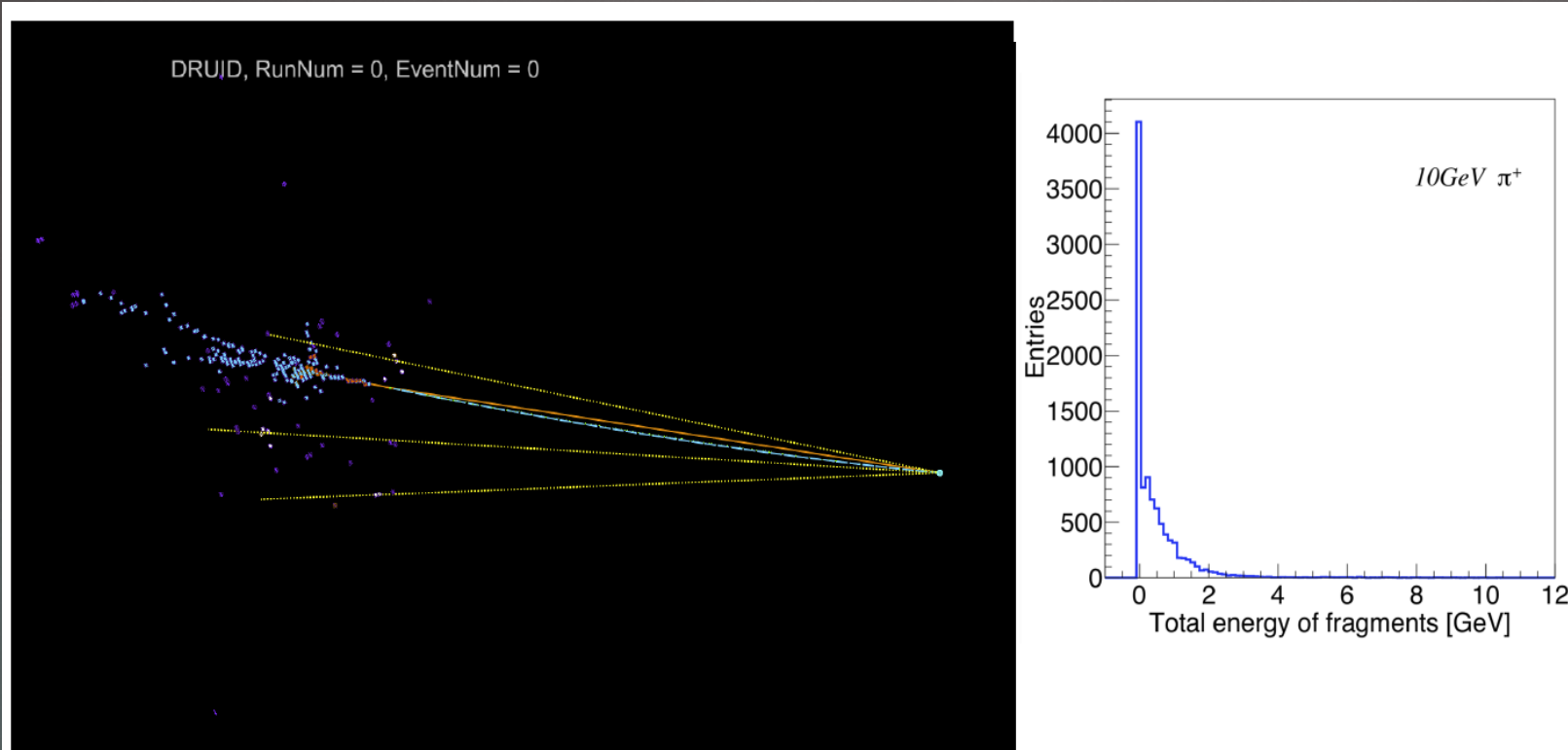
107

20% degradation going from 15 to 3 layers



Resolution drivers

108



Time/pattern recognition may help a lot, in identify the charged cluster fragmentations without arise the threshold for the neutral hadron significantly...

- Number 1 is hadronic splintering. Can timing help mitigate this splitting? Which would have better timing?
- Number 2 is hadronic resolution.
- Number 3 is acceptance. Impossible to improve?
- Neutral hadron energy threshold not negl. Any chance to go lower?

The CALICE Collaboration



Calorimeter R&D for the



... and beyond



~280 physicists/engineers from ~60 institutes
and 19 countries from 4 continents

- Integrated R&D effort
- Benefit/Accelerate detector development due to common approach
- Kicking since 2002

Technological solutions for a final detector II

SiW Ecal



Semi-conductor readout

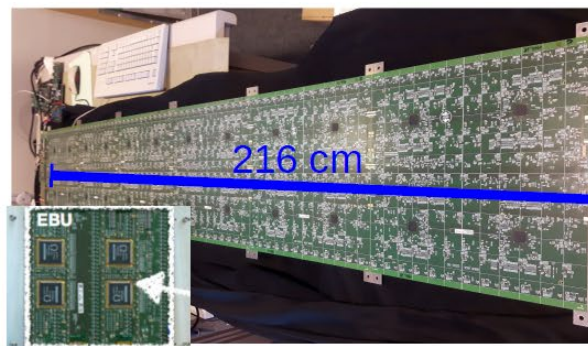
- Integrated front end electronic

No drawback for precision measurements *NIM A 654 (2011) 97*

- Small power consumption (Power pulsed electronics)
- Realistic dimensions
 - Structures of up to 3m
 - With compact external components

CEPC Xtal Calo Workshop – July 2020

Analogue Hcal and
Scintillator Ecal



Optical readout

Semi-digital Hcal



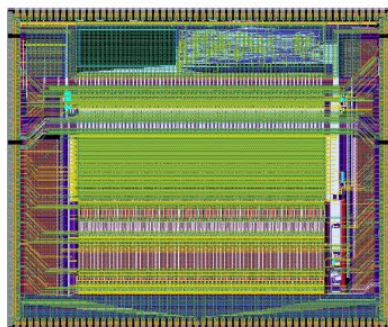
Gaseous readout

Calorimeters for PFA – Technological premises



Highly integrated front end electronics

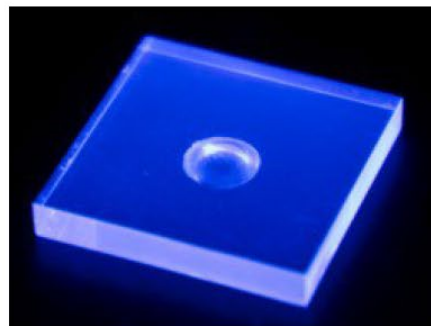
e.g. SKIROC (for SiW Ecal)



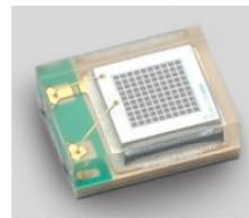
Size 7.5 mm x 8.7 mm, 64 channels

- Analogue measurement
- On-chip triggering
- Data buffering
- Digitisation
- ... all within one ASIC

Miniaturisation of r/o devices

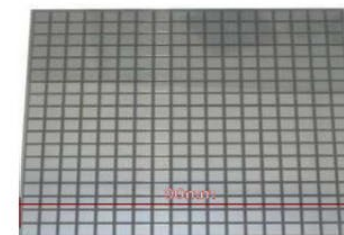


- Small scintillating tiles
- (Low noise) SiPMs



Large surface detectors

Si Wafer

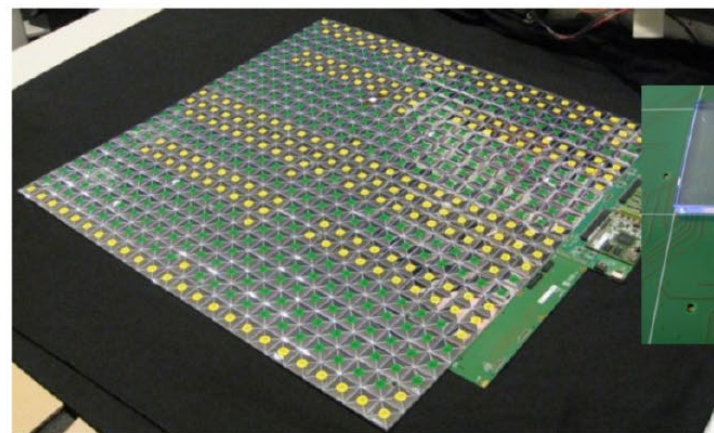
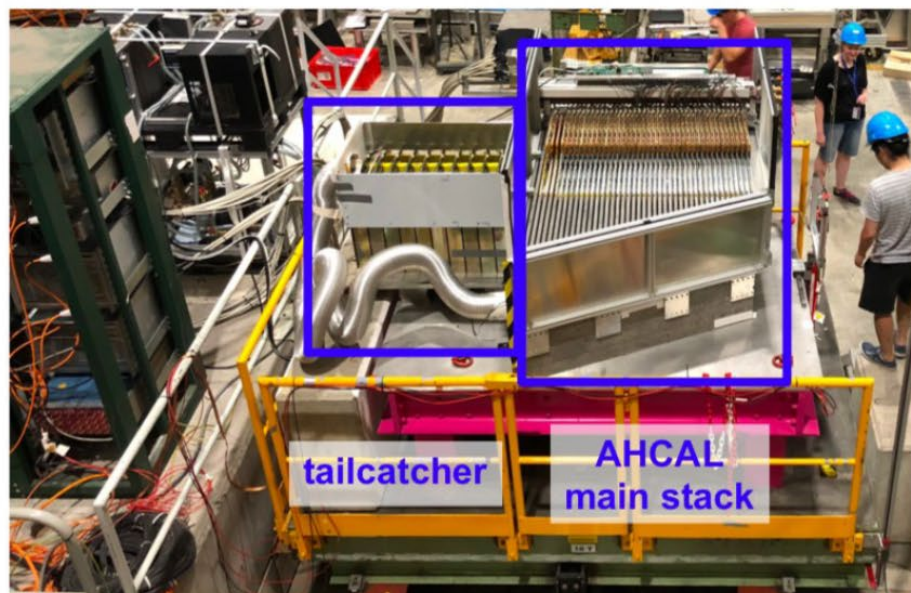


RPC layers



Many things that look familiar to you today were/are pioneered/driven by CALICE

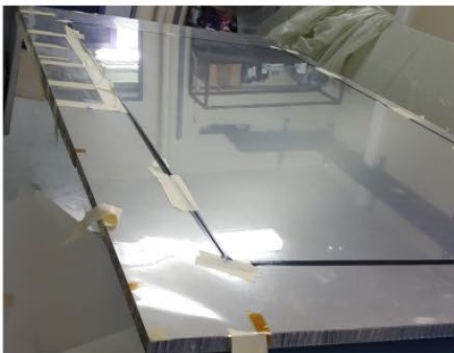
AHCAL Beam test setup



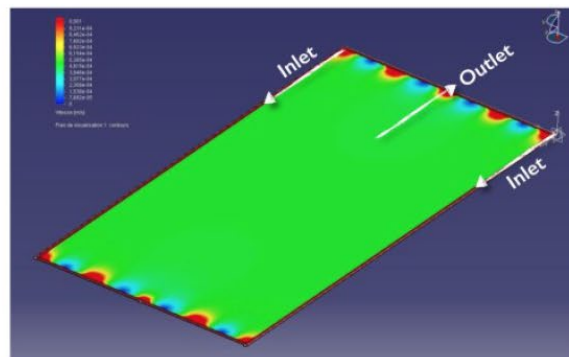
- AHCAL with 39 active layers of 72x72cm², 1.7cm steel absorber (4λ)
- Tail catcher: 12 layers with 5.4cm steel absorber (4λ)
- Commissioning and beam test in 2018, less than 0.1% dead channels
- Set-up of assembly and test infrastructure with contributions from Europe and Japan
 - Available to devices of similar purpose

Large gaseous layers

2 m² RPC assembled



Scalable gas distribution



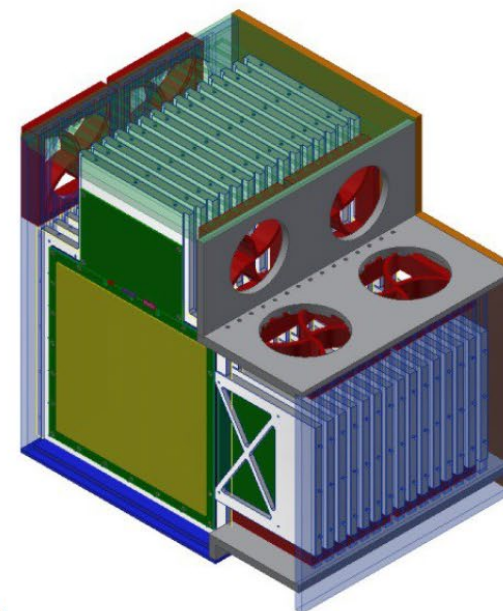
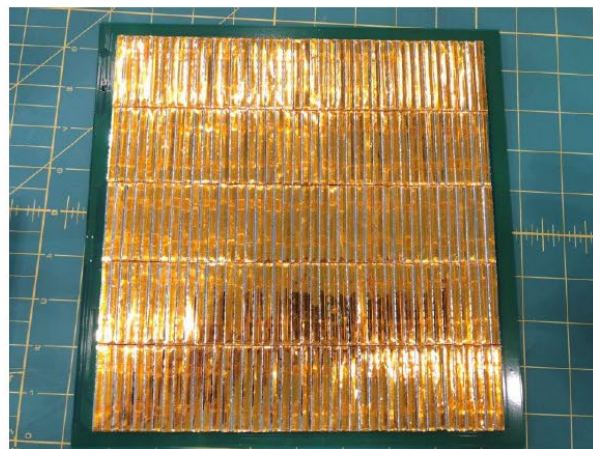
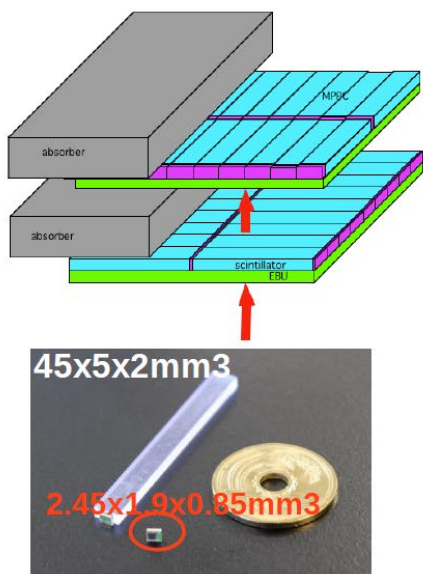
Mechanical structure

Industrial production of flat large absorber plates (3 m X 1 m) by roller leveling process + Electron Beam Welding
 ⇒ aplanarity less than 1mm.



Scintillator ECAL

ECAL with scintillator is option for electromagnetic calorimeters at CEPC and ILC

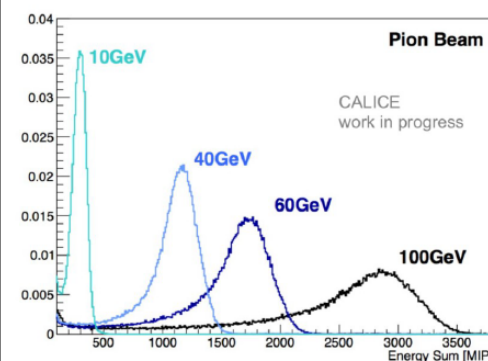
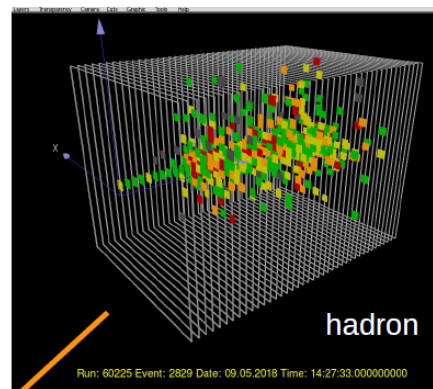
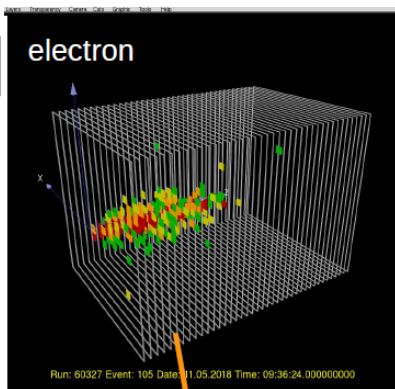
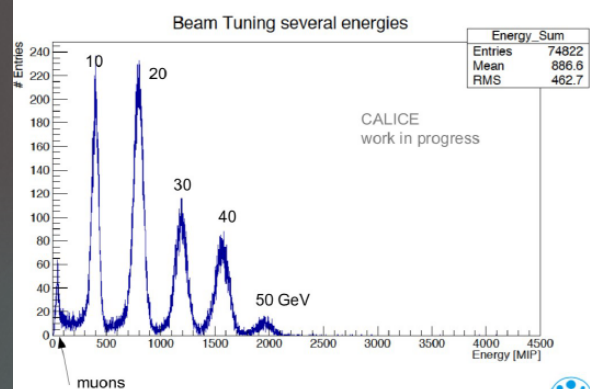


- R&D in CALICE since 2007 based on slightly modified AHCAL technology
 - Activity mainly driven by Chinese and Japanese groups with however with strong contributions by European groups on electronics and also mechanics
- Technological prototype with 32 layers under construction

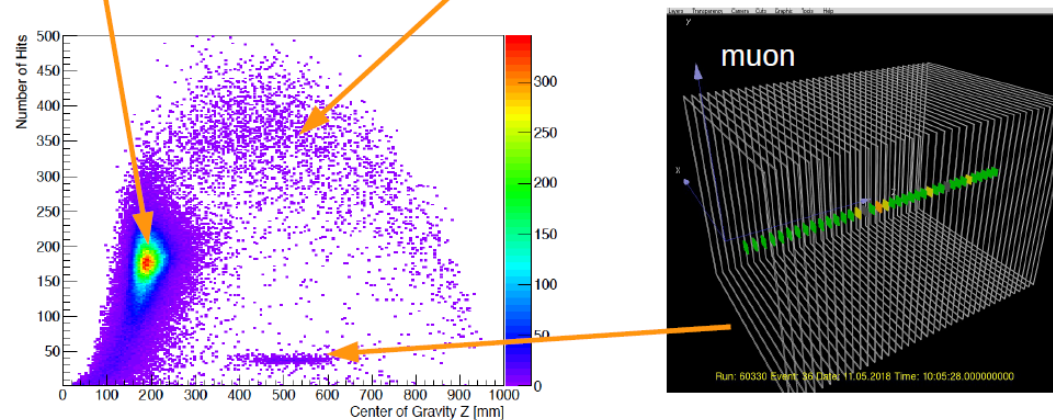
CEPC Xtal Calo Workshop – July 2020

20

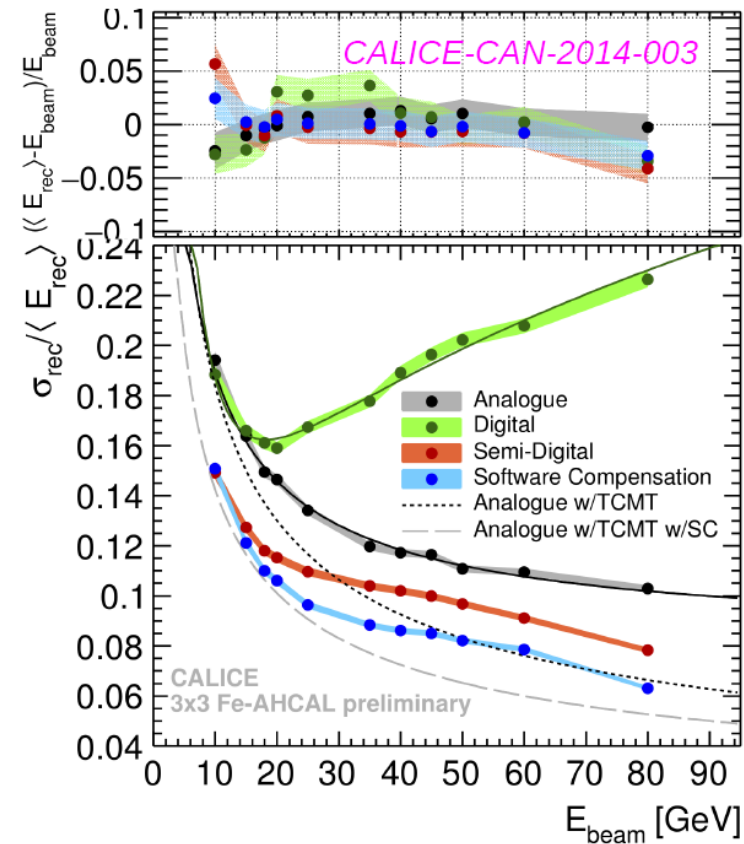
AHCAL Event Display



- Large scale techno, prototype can be successfully operated
- High granularity allows for efficient Particle Id
- Fine details of hadronic shower visible

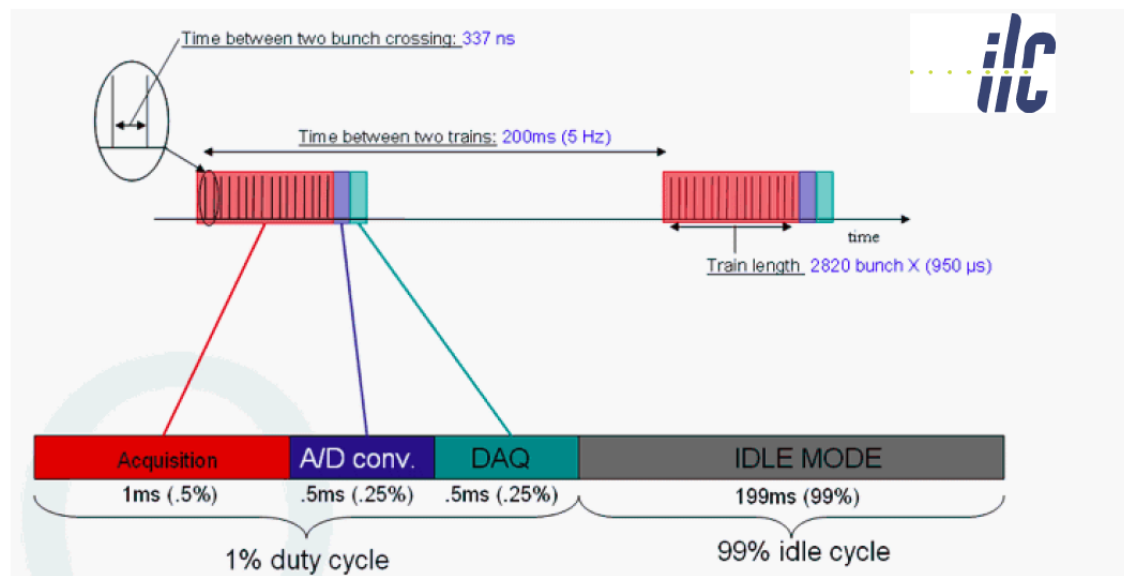


Systematic study with scintillating tiles



- Control of shower fluctuations improve resolution
 - Semi-digital or analogue with s/w compensation

Power pulsing



N.B. Final numbers may vary

- Electronics switched on during $> \sim 1\text{ms}$ of ILC bunch train and data acquisition
- Bias currents shut down between bunch trains

Mastering of technology is essential for operation of ILC detectors

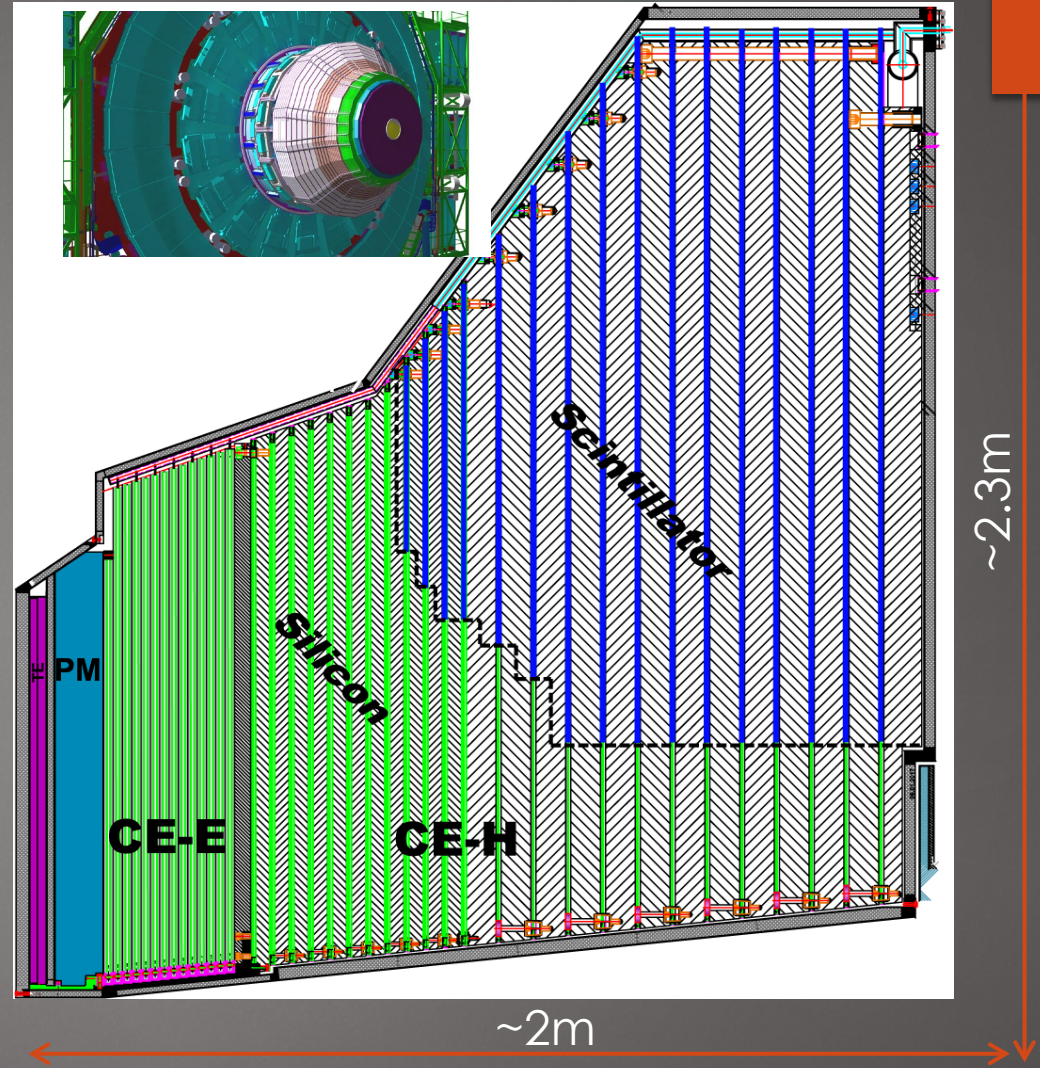
HGCAL

Active Elements:

- Hexagonal modules based on Si sensors in CE-E and high-radiation regions of CE-H
- “Cassettes”: multiple modules mounted on cooling plates with electronics and absorbers
- Scintillating tiles with SiPM readout in low-radiation regions of CE-H

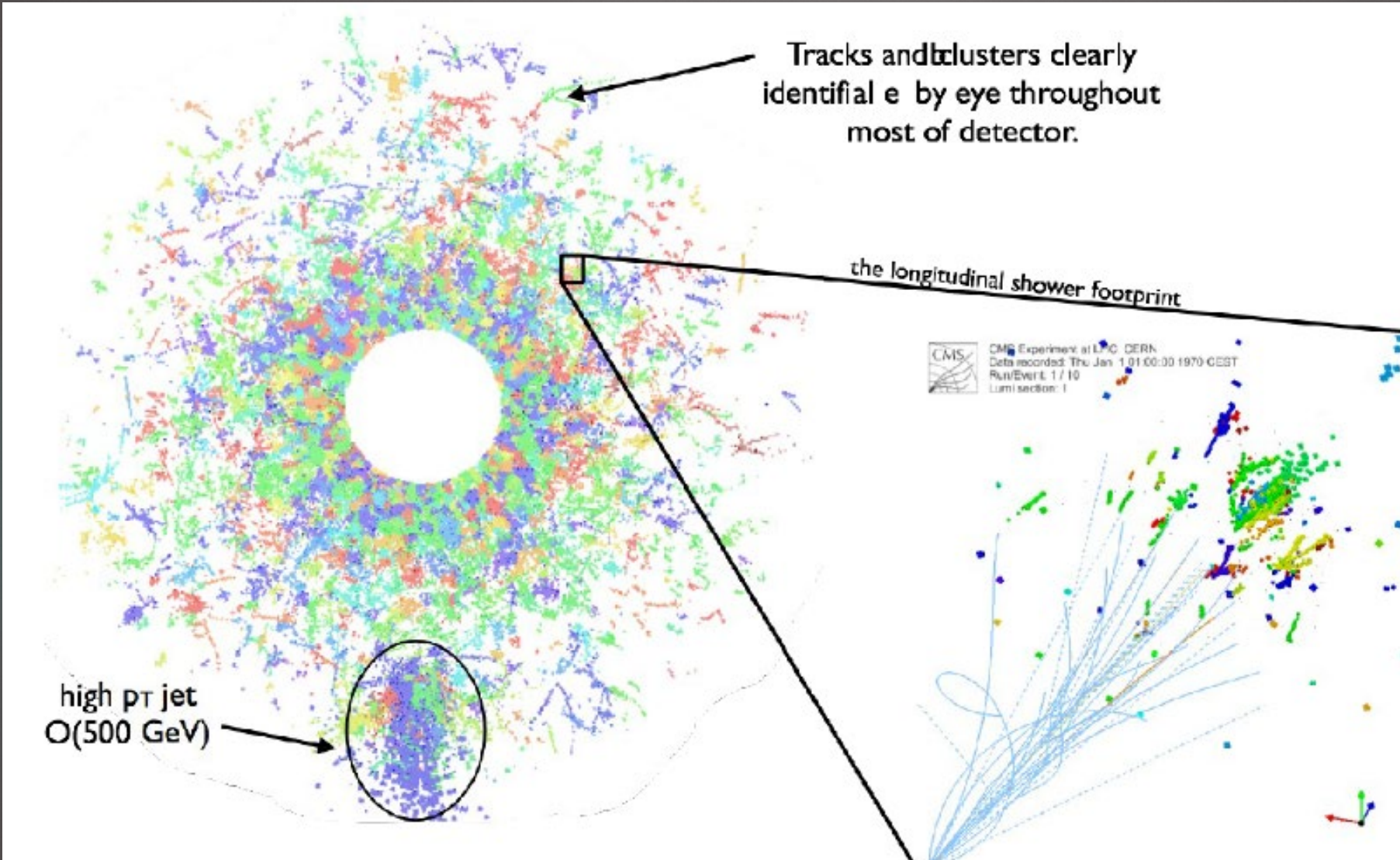
Key Parameters:

- CE covers $1.5 < \eta < 3.0$
- ~215 tonnes per endcap
- Full system maintained at -30°C
- ~600m² of silicon sensors
- ~500m² of scintillators
- 6M si channels, 0.5 or 1 cm² cell size
- ~27000 si modules
- Power at end of HL-LHC: ~110 kW per endcap



Electromagnetic calorimeter (**CE-E**): **Si**, Cu & CuW & Pb absorbers, 28 layers, $25 X_0$ & $\sim 1.3\lambda$

Hadronic calorimeter (**CE-H**): **Si** & **scintillator**, steel absorbers, 24 layers, $\sim 8.5\lambda$

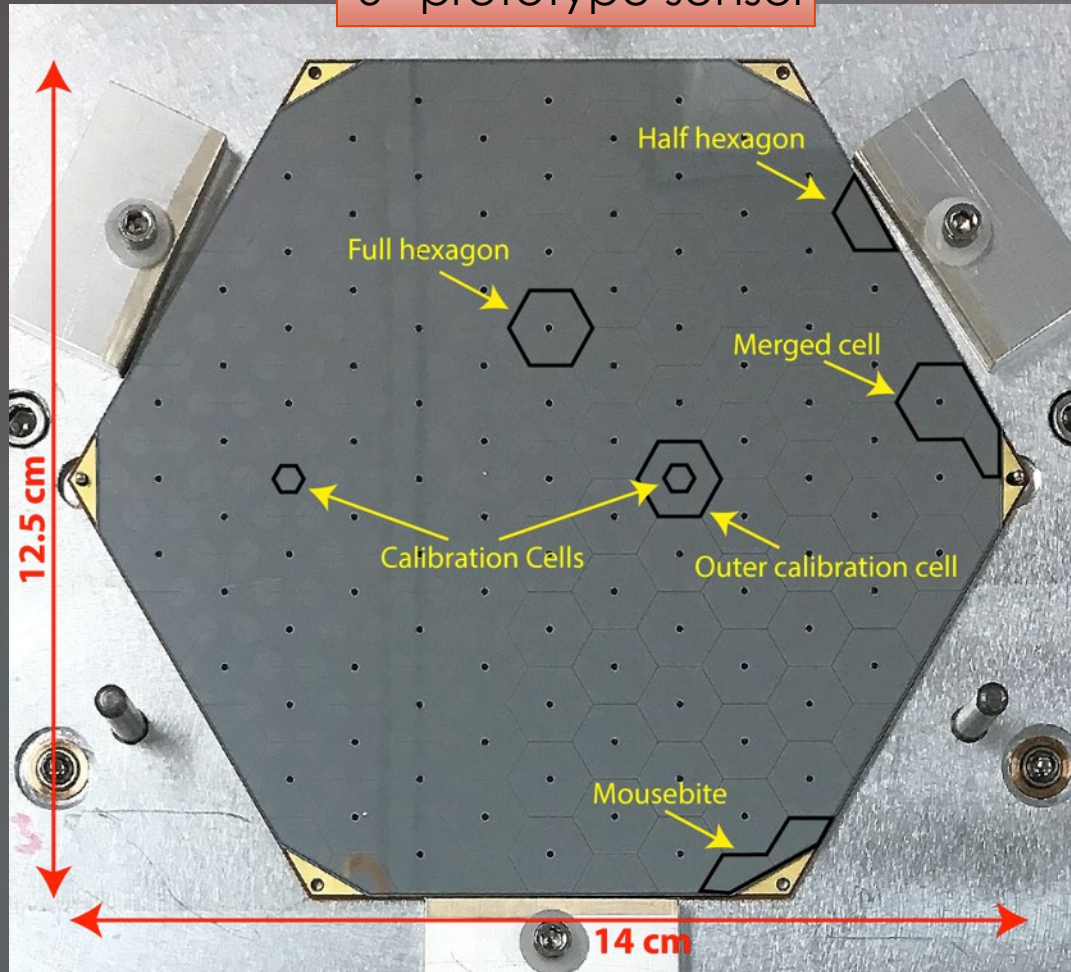


Simulation of 140 pileup events in CMS

Can remove through track matching energies from pileup

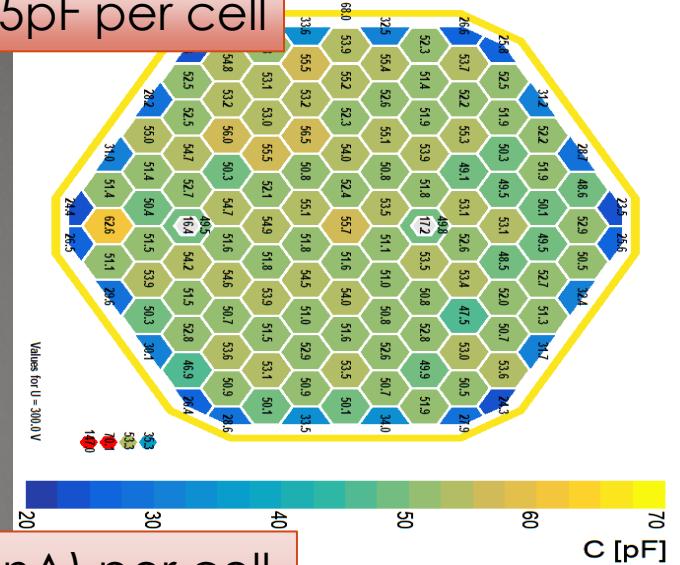
Hexagonal silicon sensors are divided (mostly) into hexagonal cells, with some special cells

6" prototype sensor

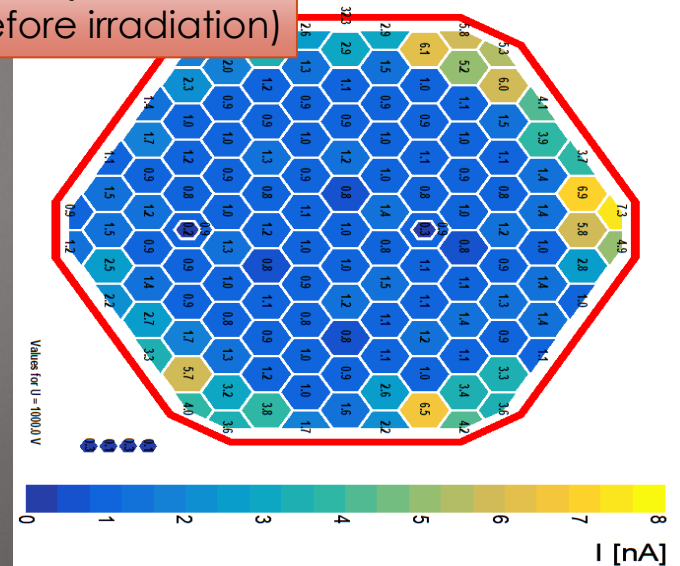


Prototype 6" and 8" sensors made by three producers

~55pF per cell

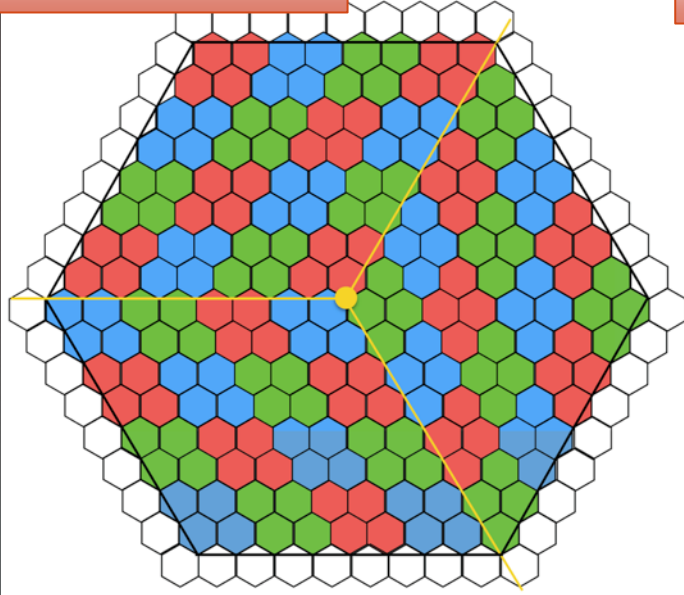


O(nA) per cell (before irradiation)

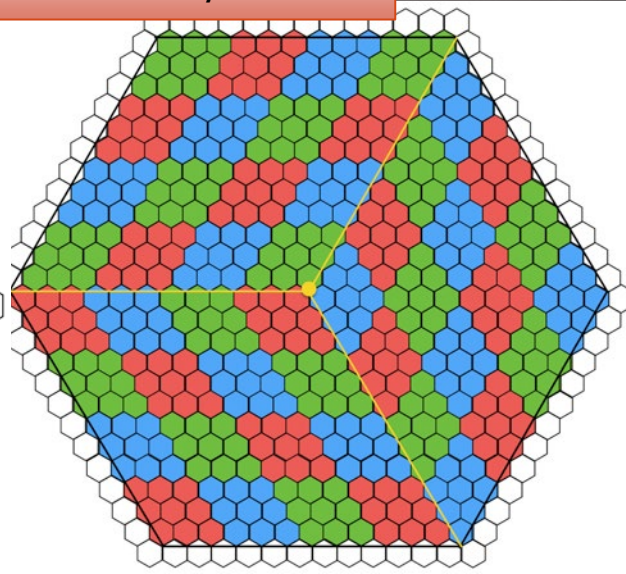


8" silicon sensors will be hexagonal, divided with 3-fold symmetry into hexagonal cells

192 cells/sensor



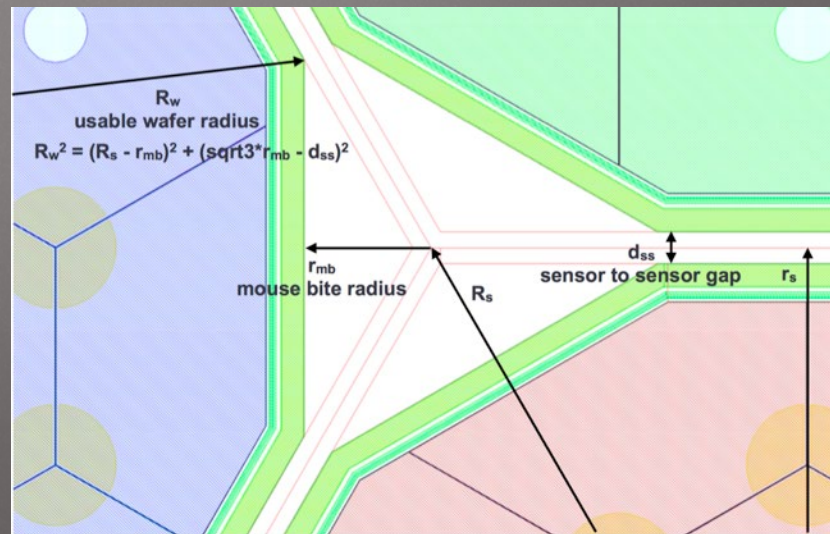
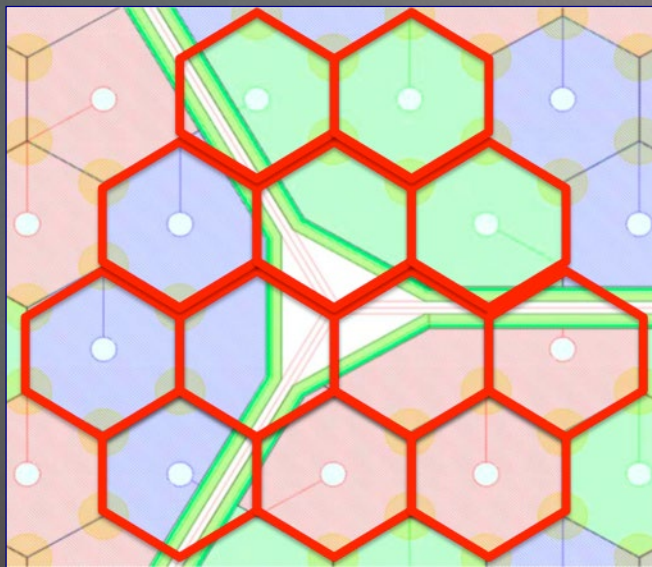
432 cells/sensor



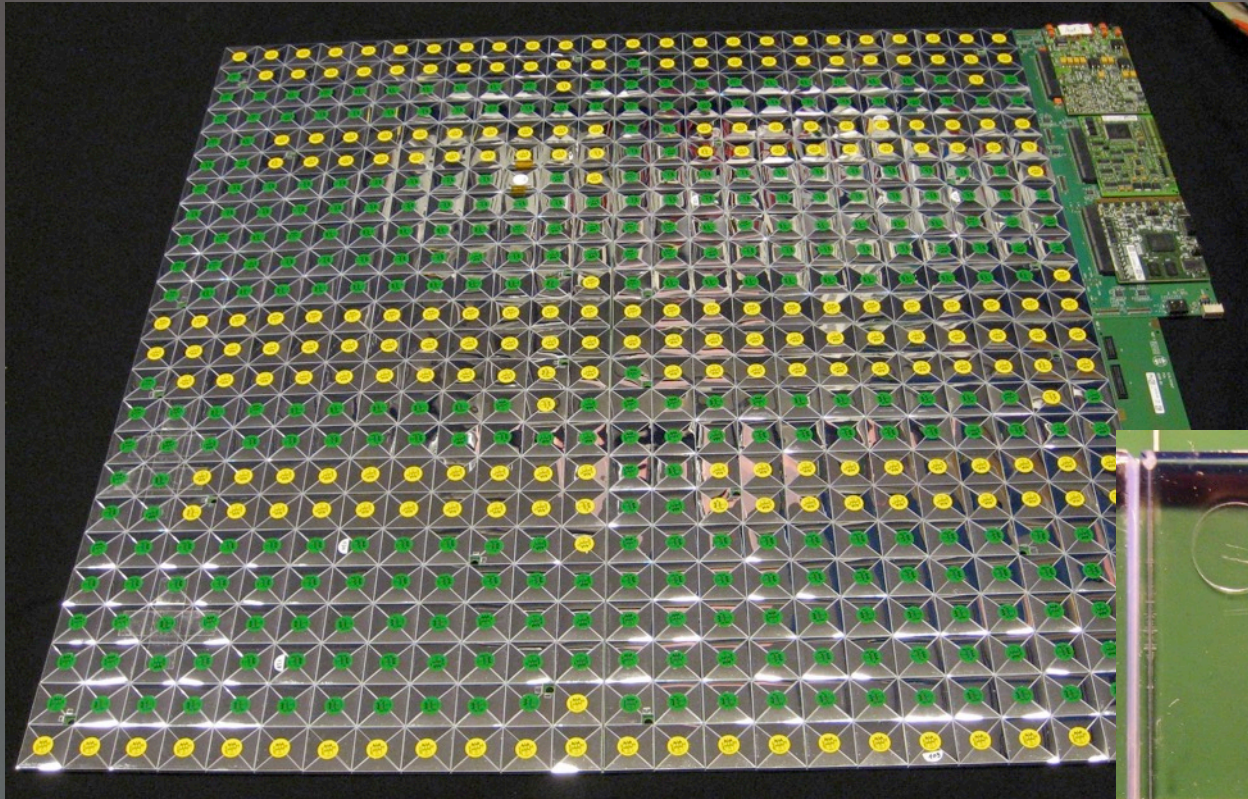
$\varnothing \sim 190\text{mm}$

All cells have $C \sim 65\text{pF}$

Coloured groupings of cells represent **trigger readout units**
 $\sim 4.5\text{cm}^2$ (half the area of a single crystal in the present ECAL endcap)



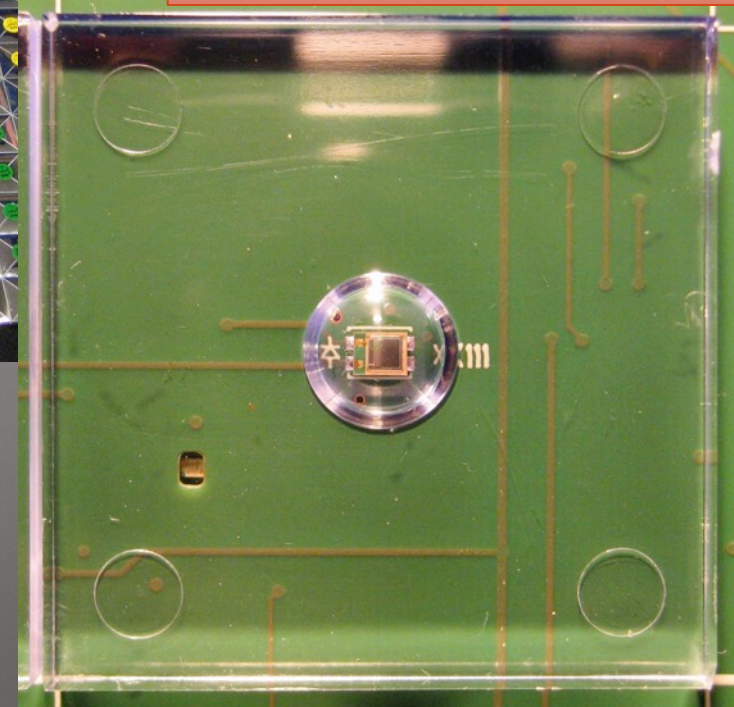
HGCAL will also include 500m² of scintillator tiles with on-tile SiPM readout



SiPMs already used successfully in e.g. CMS HCAL Phase 1 upgrade

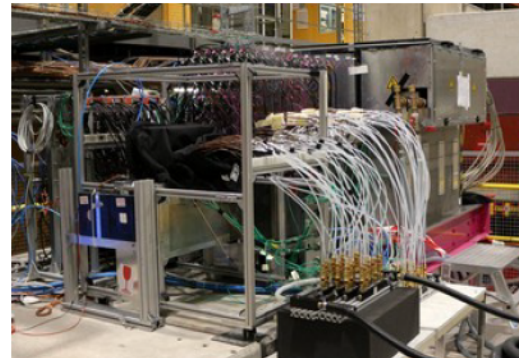
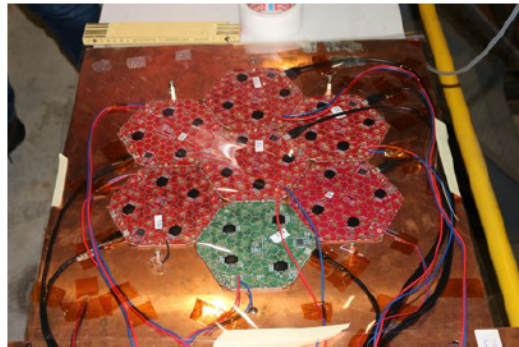
Tile boards or “megatiles” limited in size by CTE of different components

For first beam tests, modified CALICE AHCAL used for rear hadron calorimeter:
3x3cm² scintillator tiles + direct SiPM readout





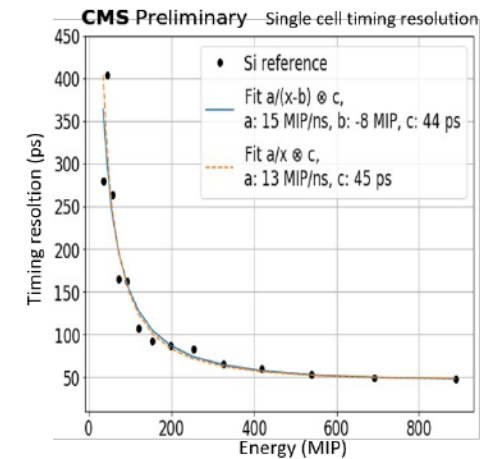
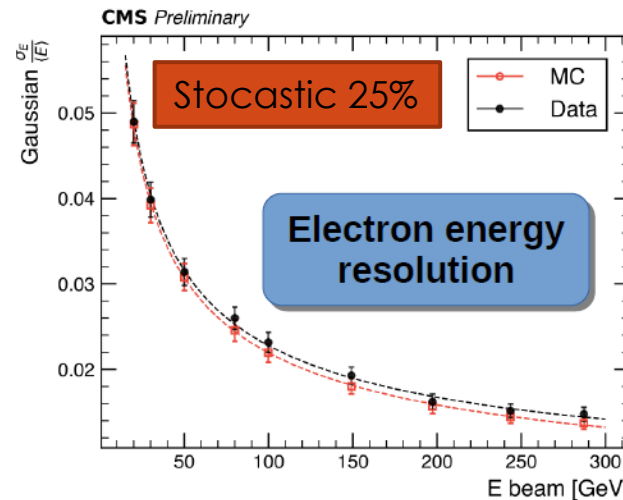
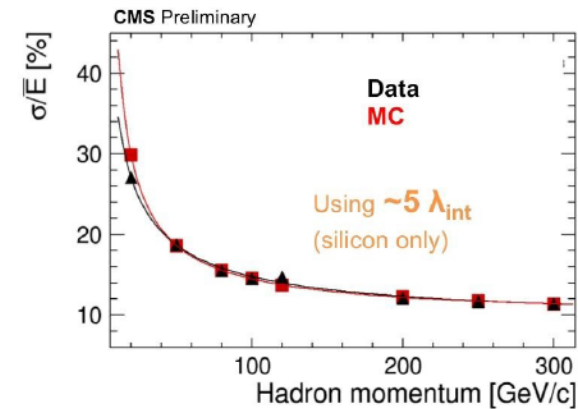
Test Beam Results



300 GeV pion starting showering in CE-H-Si



- 28 EM layers, 12 silicon HAD layers, 39 scintillator layers from CALICE AHCAL
- Measured electrons, pions, and muons with energies from 20 GeV to 300 GeV
- Papers under preparation/in final collaboration review



Dual readout

Instead of throwing calorimetry out as much as possible, we could improve it. Saw an attempt at this with compensation, but this required a high Z material (U or Pb, both with obvious engineering challenges) and a lowish sampling fraction, which limited the resolution.

Is there a better way?

Dual readout

125

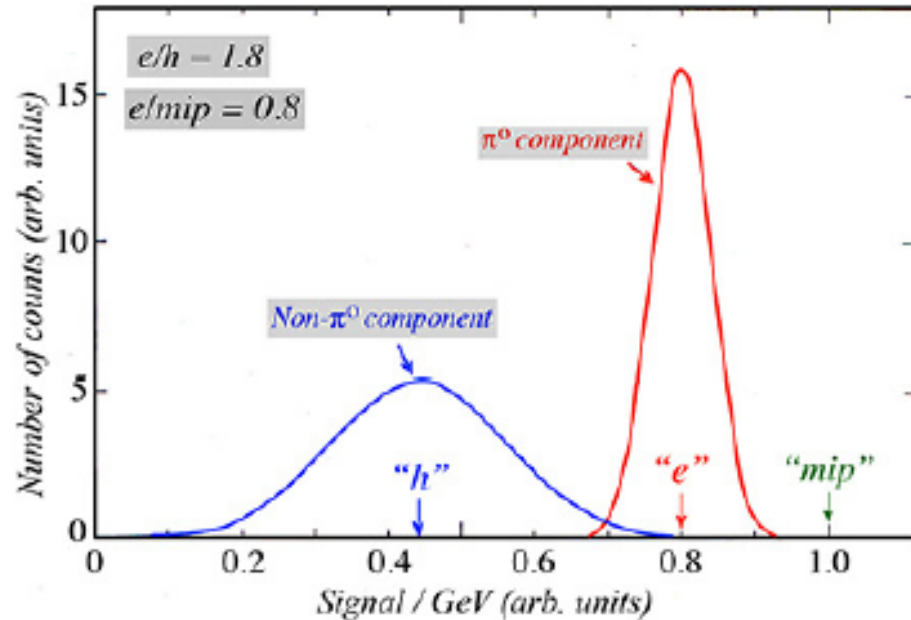


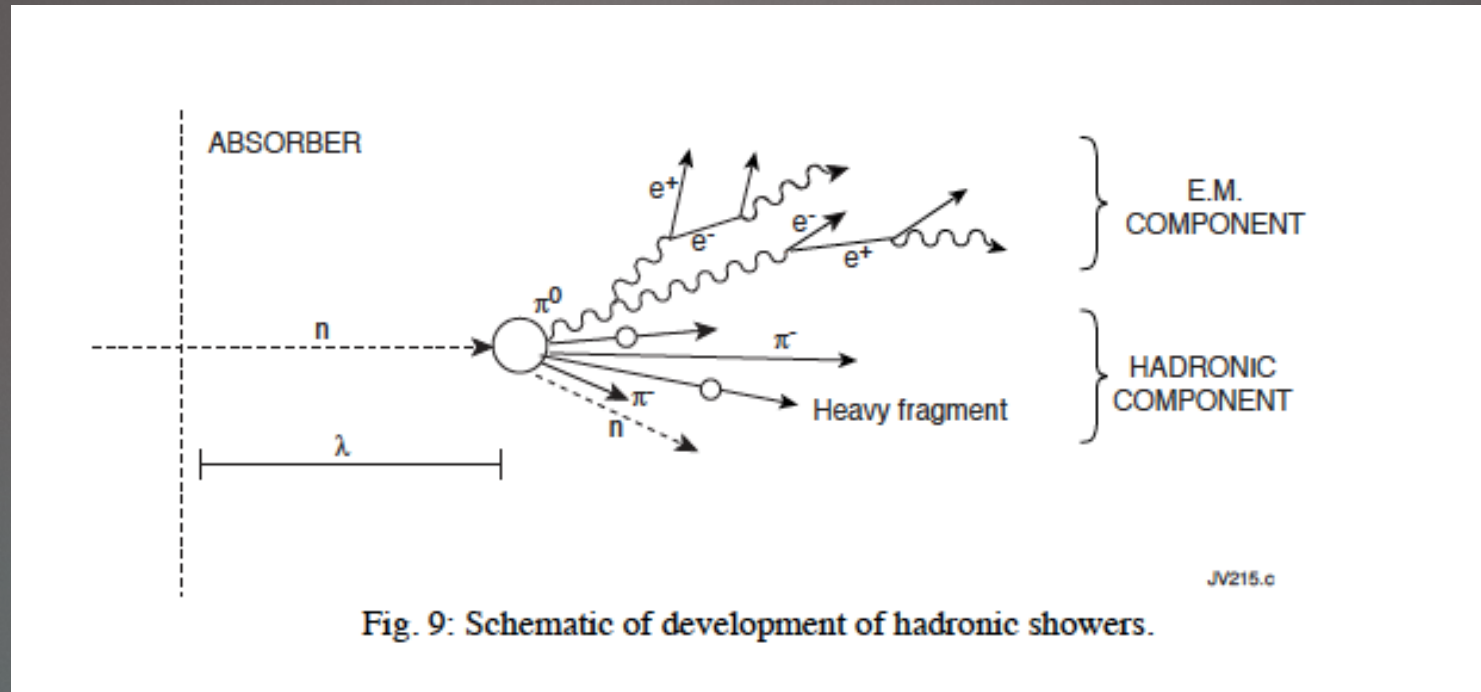
FIG. 2: Illustration of the meaning of the e/h and e/mip values of a (generic) calorimeter. Shown are distributions of the signal per unit deposited energy for the electromagnetic and non-em components of hadron showers. These distributions are normalized to the response for minimum ionizing particles (“mip”). The average values of the em and non-em distributions are the em response (“e”) and non-em response (“h”), respectively.

What if, instead of trying to boost the non-pizero component (compensation), we tried to separately identify it and apply a separate scale factor to that component of the readout?

Is this just a DREAM?

<http://www.phys.ttu.edu/~dream/links/links.html>

Cherenkov (Черенков)

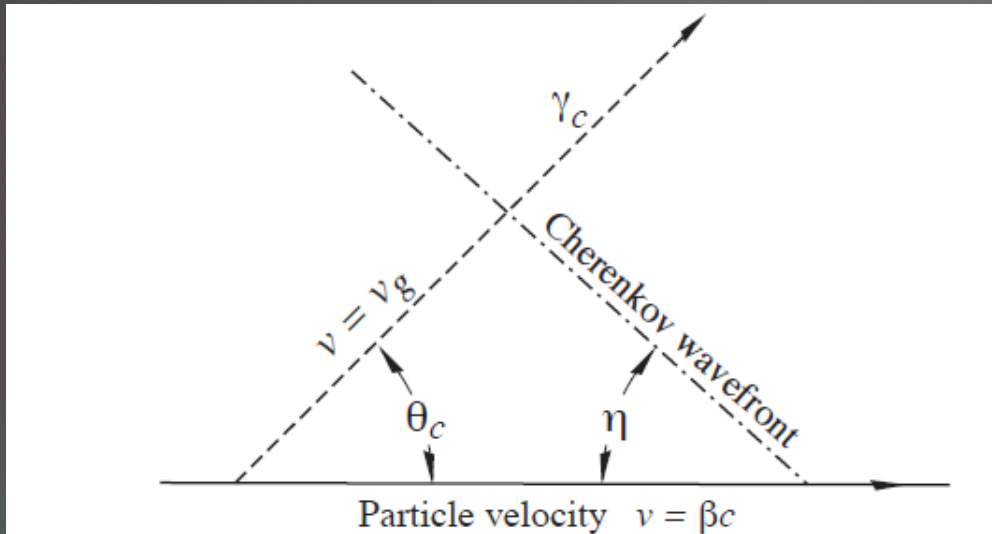


The nuclear part contains heavy slowly moving protons and ions while the pizero part of the shower contains many relativistic electrons.

Relativistic particles can Cherenkov radiation.

Cherenkov radiation

127



Can be identified by its

- Angle
- Wavelength
- timing

$$\frac{d^2 N}{dx d\lambda} = \frac{2\pi\alpha z^2}{\lambda^2} \left(1 - \frac{1}{\beta^2 n^2(\lambda)} \right)$$

Passage of particles through matter (pdg.lbl.gov)

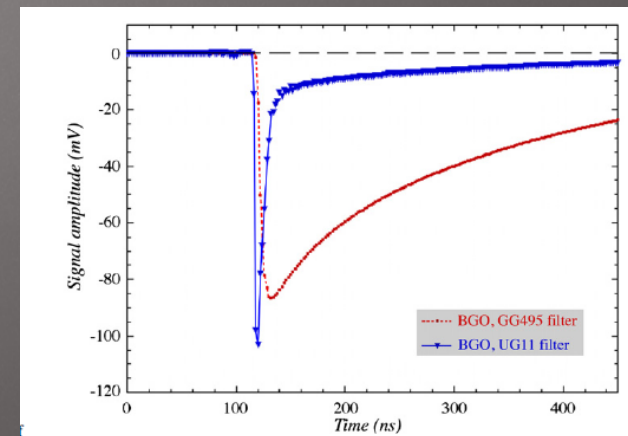
Can generate in

- Quartz
- Clear plastic fibers
- Crystals like BGO, PbWO4

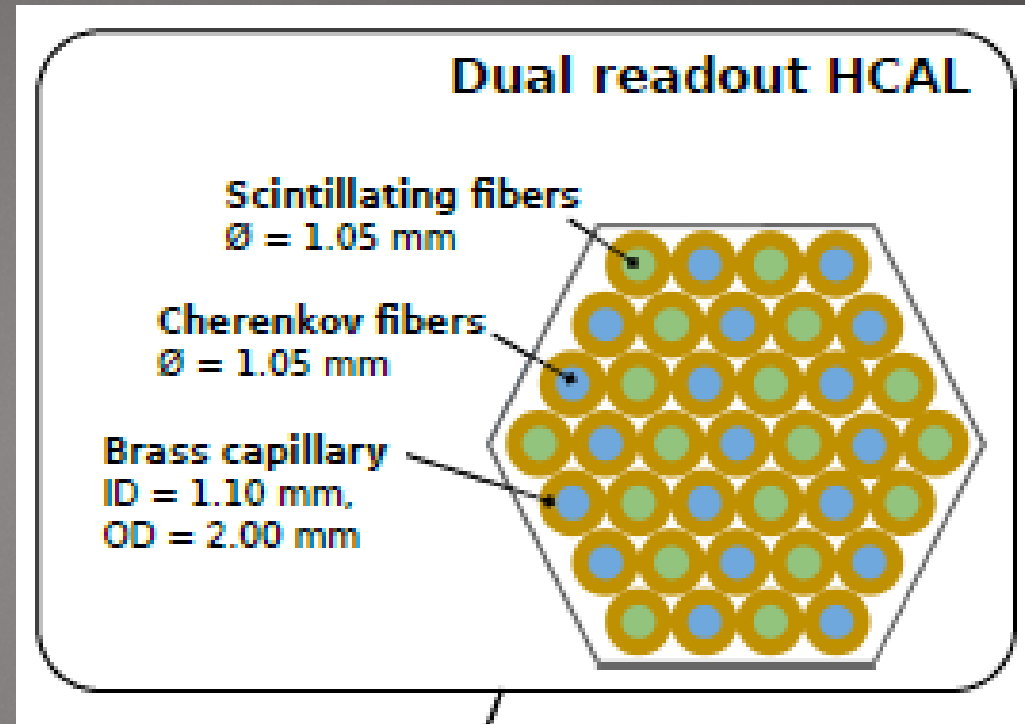
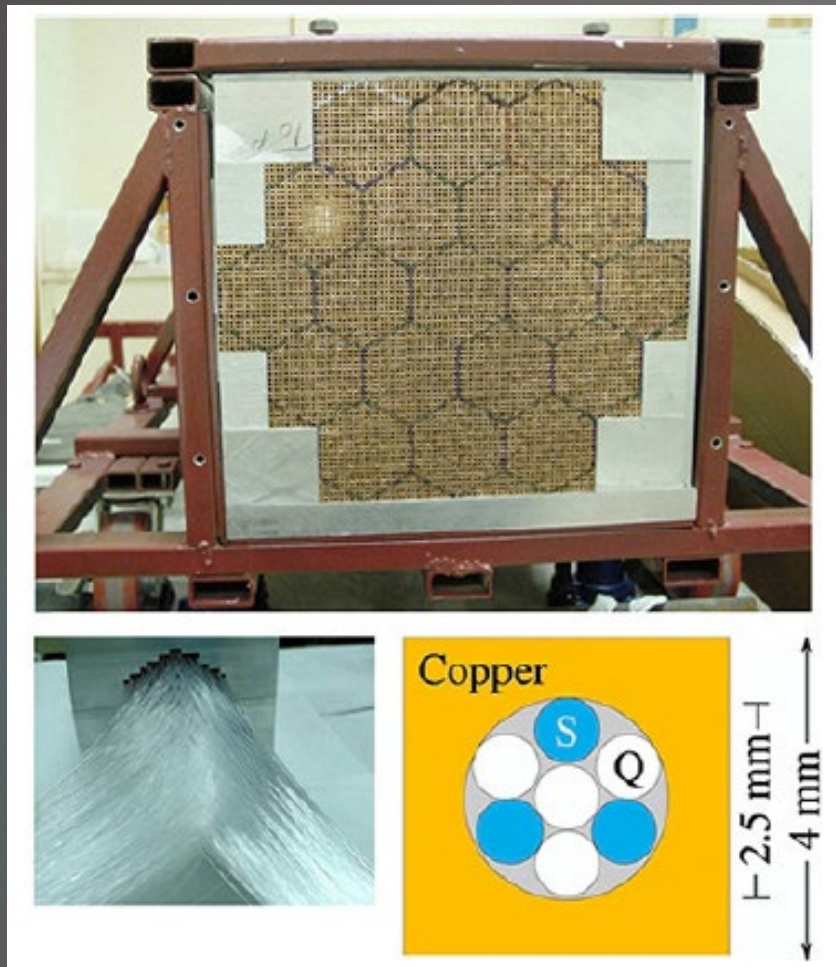
(basically need some transparent material, the higher the n the better)

But since this is only sensitive to the relativistic portion of the shower, need something else to generate signal from the entire energy deposit

- plastic scintillator (advantage of sensitivity to neutrons)
- Crystals like BGO, PbWO4



Example calorimeters

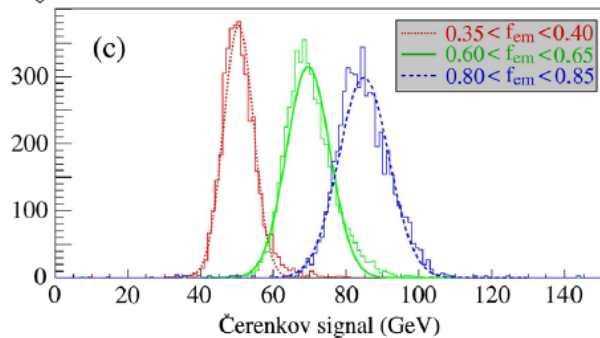
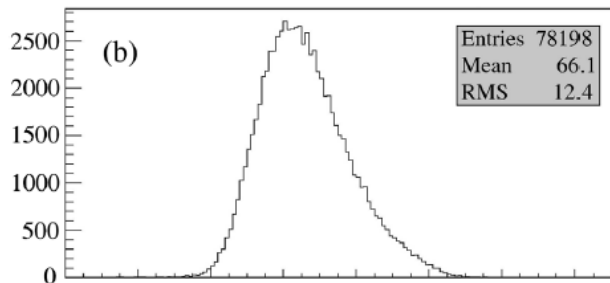
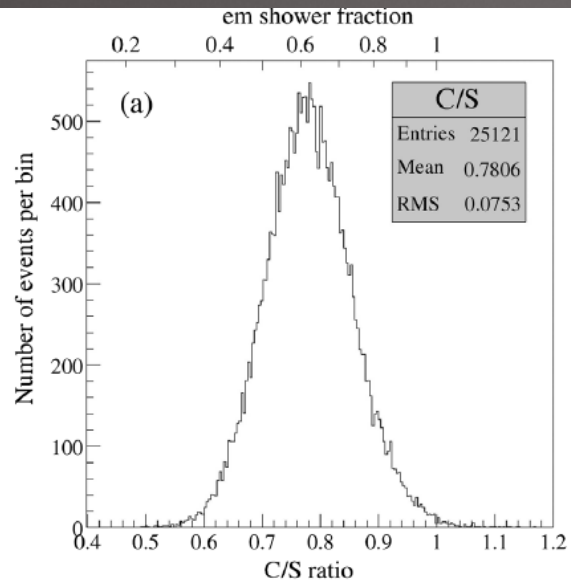


Tend to have sampling media parallel to incident particle direction to uniformly sample the longitudinal shower.

Dual-Readout Calorimetry: arXiv:1712.05494
Lee, Livan, Wigmans Rev. Mod. Phys. 90 (2018) 40
M. Lucchini et al <https://arxiv.org/abs/2008.00338>

Why it works

129



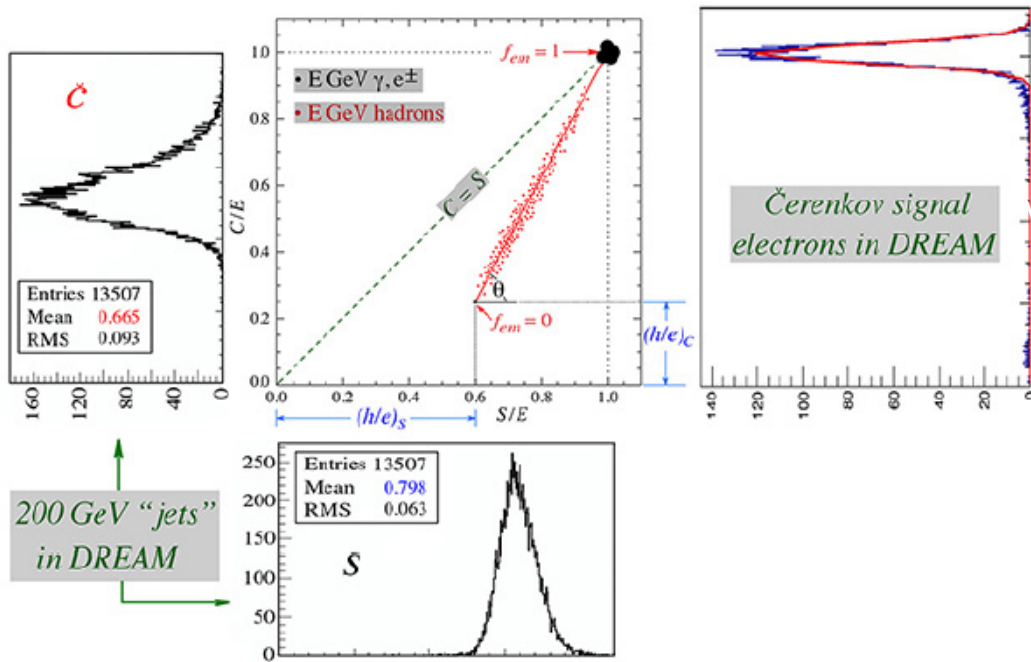
The top plot shows extracted C/S ratio.

The middle is the signal from the Cherenkov alone.

The bottom is the Cherenkov signal in bins of C/S.

Dual-readout moves the center of these individual gaussians to the same place, leading to better resolution

When you have a pure EM shower, both are calibrated to give a response of 1.
 When you have a “pure hadron” shower (no pizero production), the Cherenkov response is low but the scintillator response, while lower than before, isn’t much lower.

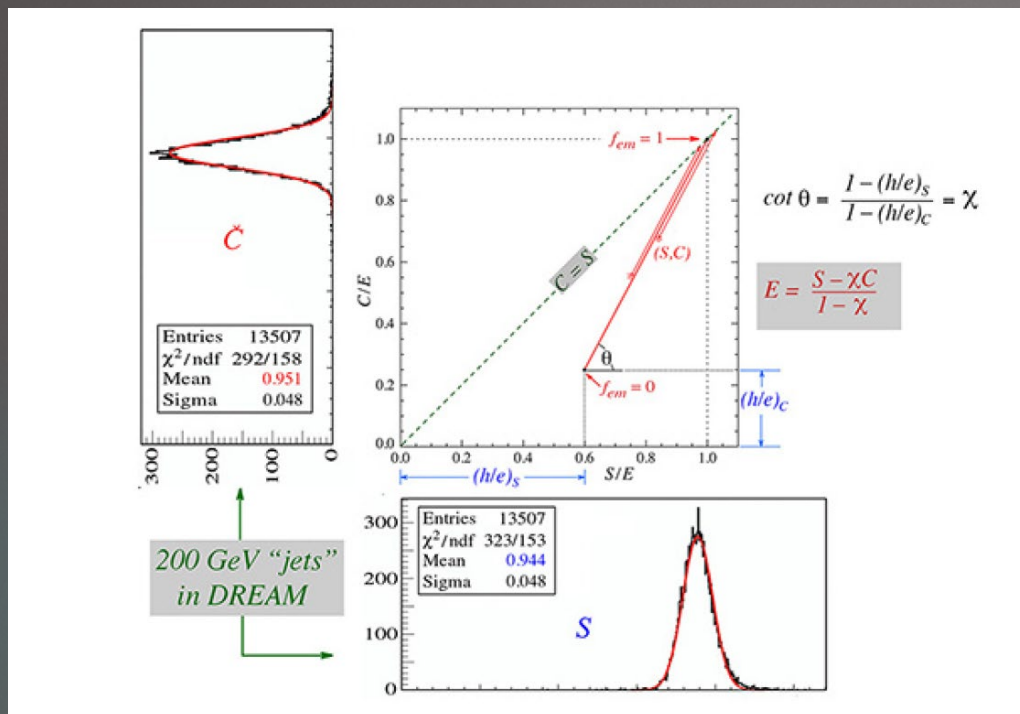


$$S = E \left[f_{em} + \frac{1}{(e/h)_S} (1 - f_{em}) \right]$$

$$C = E \left[f_{em} + \frac{1}{(e/h)_C} (1 - f_{em}) \right]$$

Two equations with two unknowns (E and f_{em}). Only two equations if (e/h)_S and (e/h)_C are different.

FIG. 8: The S – C diagram of the signals from a (generic) dual-readout calorimeter [29]. The hadron events are clustered around the straight (red) line, the electron events around the point (1,1). Experimental signal distributions measured in the scintillation and Čerenkov channels for 200 GeV “jets” with the DREAM fiber calorimeter [30] are shown as well. Also shown is a typical (Čerenkov) response function measured for electrons in DREAM.



Each point scattered along the red line is moved up until it intersects $C=S$ (note the arrows) then the projection of this onto each axis is combined.

DREAM/RD52

N. Akchurin^a, F. Bedeschi^b, A. Cardini^c, R. Carosi^b, G. Ciapetti^d, R. Ferrari^e, S. Franchino^f, M. Fraternali^f, G. Gaudio^e, J. Hauptman^g, M. Incagli^b, F. Lacava^d, L. La Rotonda^h, T. Libeiro^a, M. Livan^f, E. Meoni^h, D. Pinci^d, A. Policicchio^{h,1}, S. Popescu^a, F. Scuri^b, A. Sill^a, W. Vandelliⁱ, T. Venturelli^h, C. Voena^d, I. Volobouev^a, R. Wigmans^{a,*}

^a Texas Tech University, Lubbock, TX, USA

^b Dipartimento di Fisica, Università di Pisa and INFN Sezione di Pisa, Italy

^c Dipartimento di Fisica, Università di Cagliari and INFN Sezione di Cagliari, Italy

^d Dipartimento di Fisica, Università di Roma "La Sapienza" and INFN Sezione di Roma, Italy

^e INFN Sezione di Pavia, Italy

^f INFN Sezione di Pavia and Dipartimento di Fisica Nucleare e Teorica, Università di Pavia, Italy

^g Iowa State University, Ames, IA, USA

^h Dipartimento di Fisica, Università della Calabria and INFN Cosenza, Italy

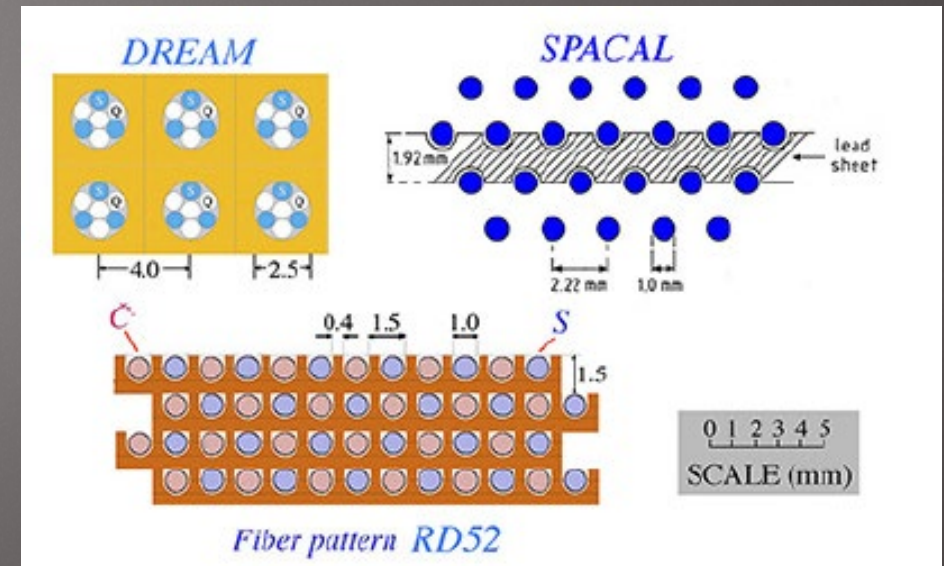
ⁱ CERN, Genève, Switzerland

Typical recent authorship list

DREAM: extruded copper rod, hollow, with 7 fibers instead (3 scintillation, rest quartz). Was a small calorimeter, and resolution was dominated by side leakage.

RD52: studied dual-readout with crystals (more on this later) and another fiber calorimeter with higher packing fraction, undoped plastic for Cherenkov. Absorber at first lead, then copper (multiple fibers in one hole isn't good, as they measure the same particles and thus are not statistically independent)

Both calorimeters really too small to do a good job with hadrons.

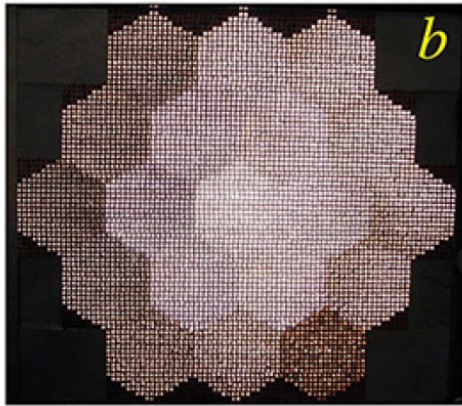


Example: DREAM calorimeter

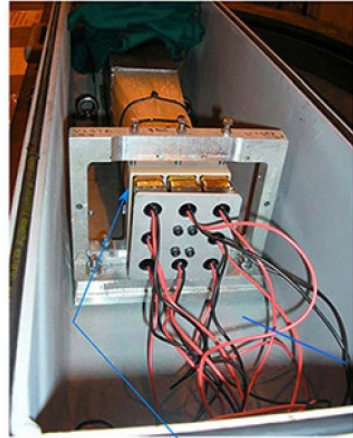
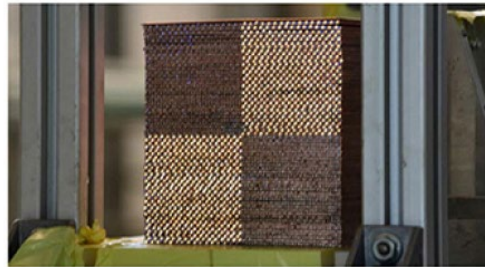
133



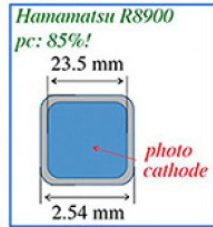
a



b



9.3 x 9.3 x 250 cm
150 kg
4 towers, 8 PMTs
2 x 2048 fibers



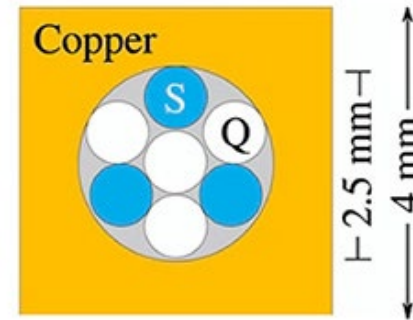
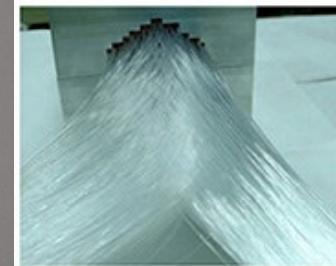
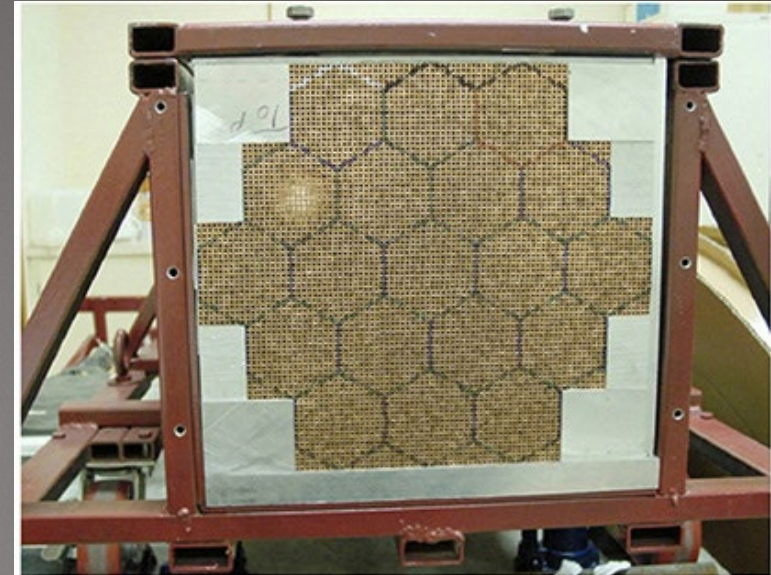
Hamamatsu R8900
pc: 85%!

23.5 mm

2.54 mm

photo cathode

FIG. 33: Front (left) and rear (right) view of one of the RD52 fiber calorimeter modules. The tower structure is made visible by shining light on two of the eight fiber bunches sticking out at the back end. See text for more details.



Copper

2.5 mm
4 mm

Separate readouts for scintillating and clear fibers (a bit expensive, but still not as many channels as PF calorimetry)

Dual Readout Calorimeter (1712.05494)

C and S signals

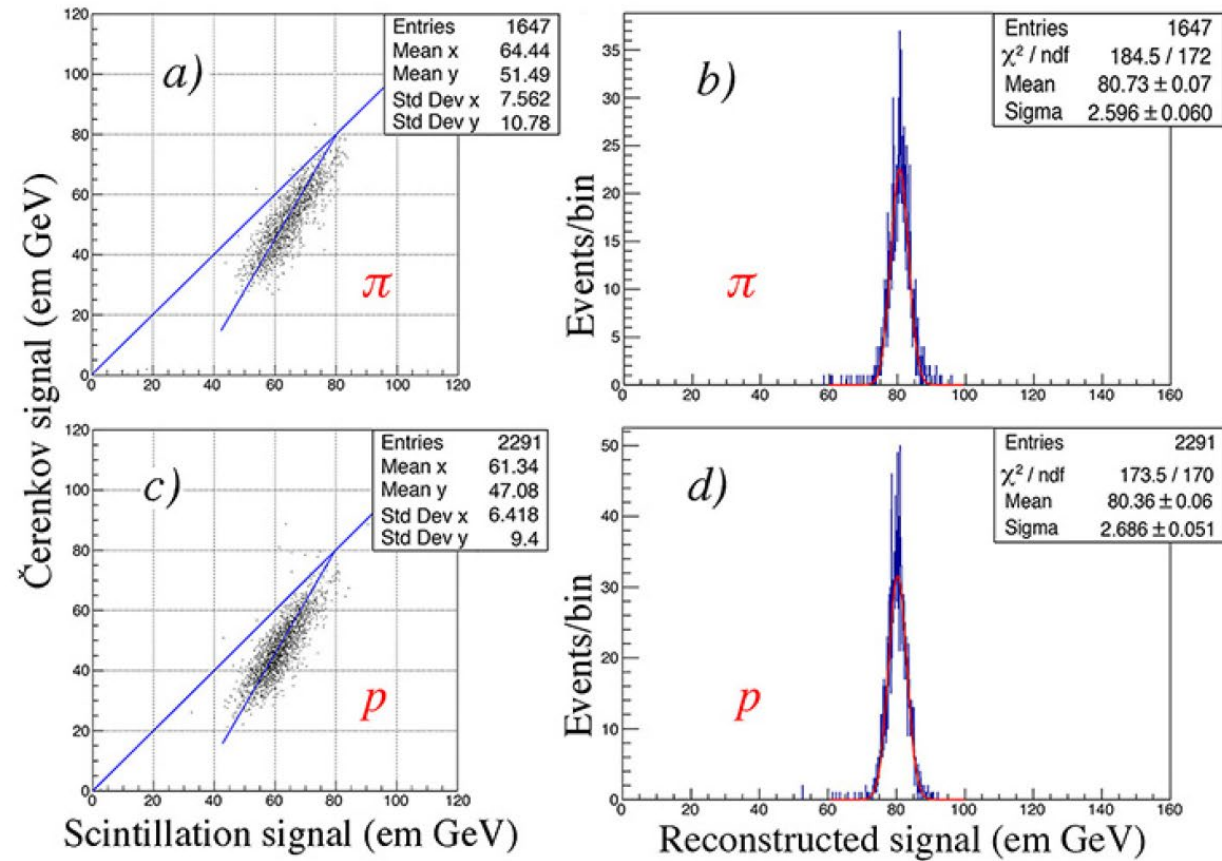


FIG. 42: Scatter plots of the Čerenkov *vs.* the scintillation signals from showers induced by 80 GeV π^+ (a) and 80 GeV protons (c) in the RD52 lead-fiber calorimeter. Projection of the rotated scatter plots on the *x* axis for the pions (b) and protons (d). The rotation procedure was identical to that used for 60 GeV π^- (Figure 12). Experimental data from [32]

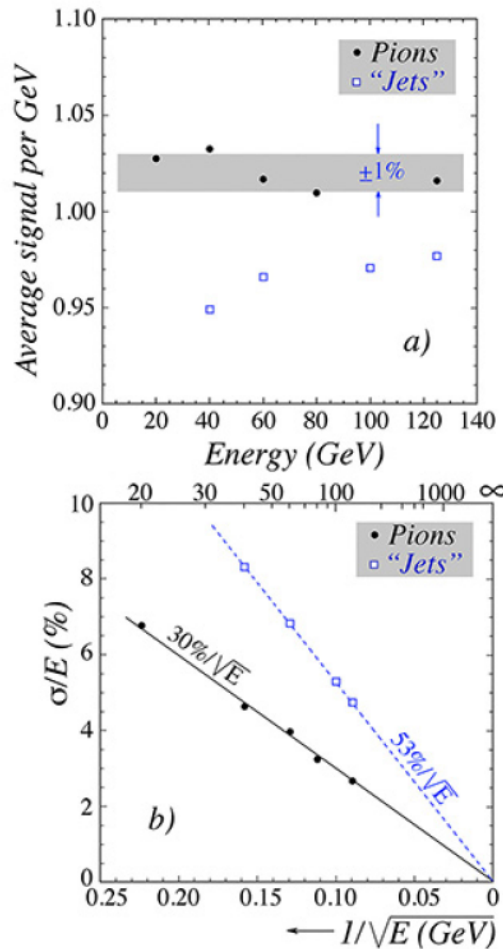


FIG. 44: The average calorimeter signal per GeV (a) and the fractional width of the signal distribution (b) as a function of energy, for single pions and multiparticle events (“jets”). Results are given for the RD52 dual-readout calorimeter signals, obtained with the rotation method [32].

Just ignore the “jets” curves. They are crap. The single pion resolution has a stochastic term of 30%, even for this small calorimeter. Pretty good!

Project fiber challenges

136

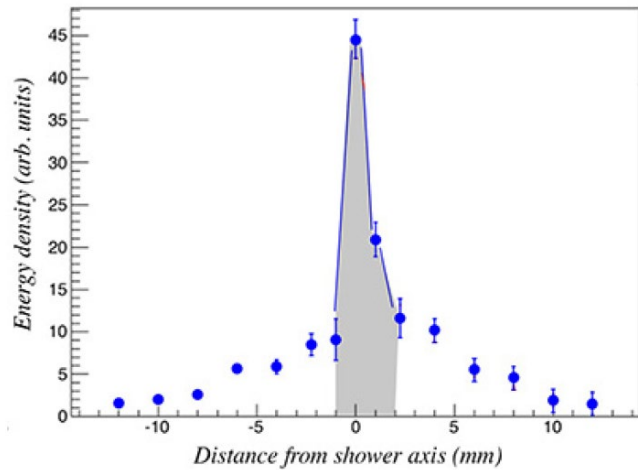


FIG. 45: The lateral profile of 100 GeV electron showers in the RD52 lead-fiber calorimeter, measured with the scintillation signals [52].

A large fraction of shower energy in a core with radius 1 mm. Because fibers are separated by 2-3 mm, response depends on impact point if fibers are projective

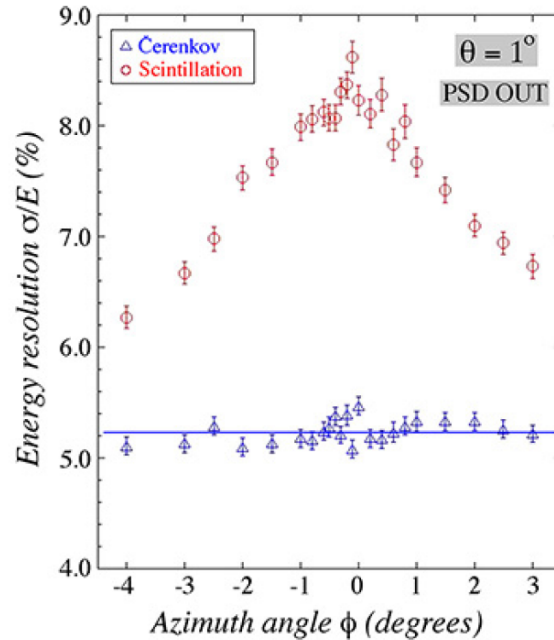


FIG. 46: The energy resolution measured for 20 GeV electrons in the scintillation and the Čerenkov channels of the RD52 copper-fiber calorimeter, as a function of the azimuth angle of incidence (ϕ) of the beam particles. The tilt angle θ was 1° [62].

Early part of shower does not contribute to Čerenkov signal since Čerenkov angle is outside of fiber aperture.

Compensation versus dual readout

137

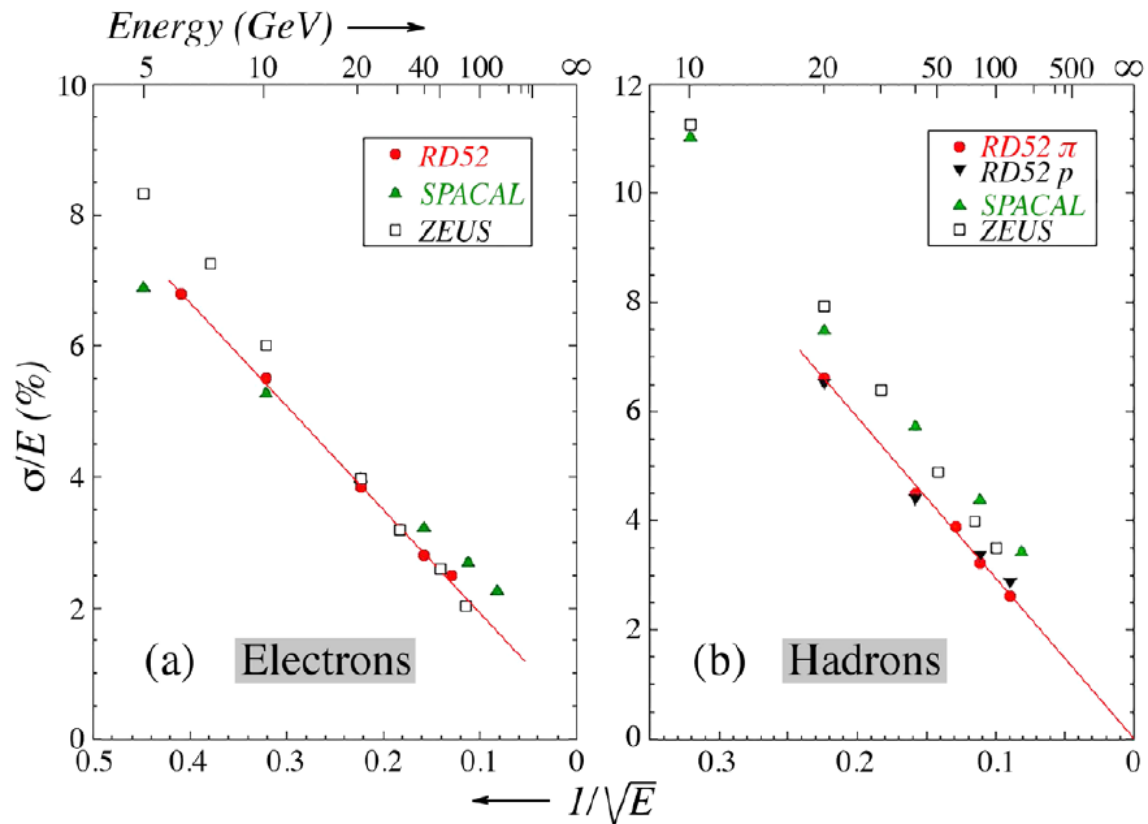
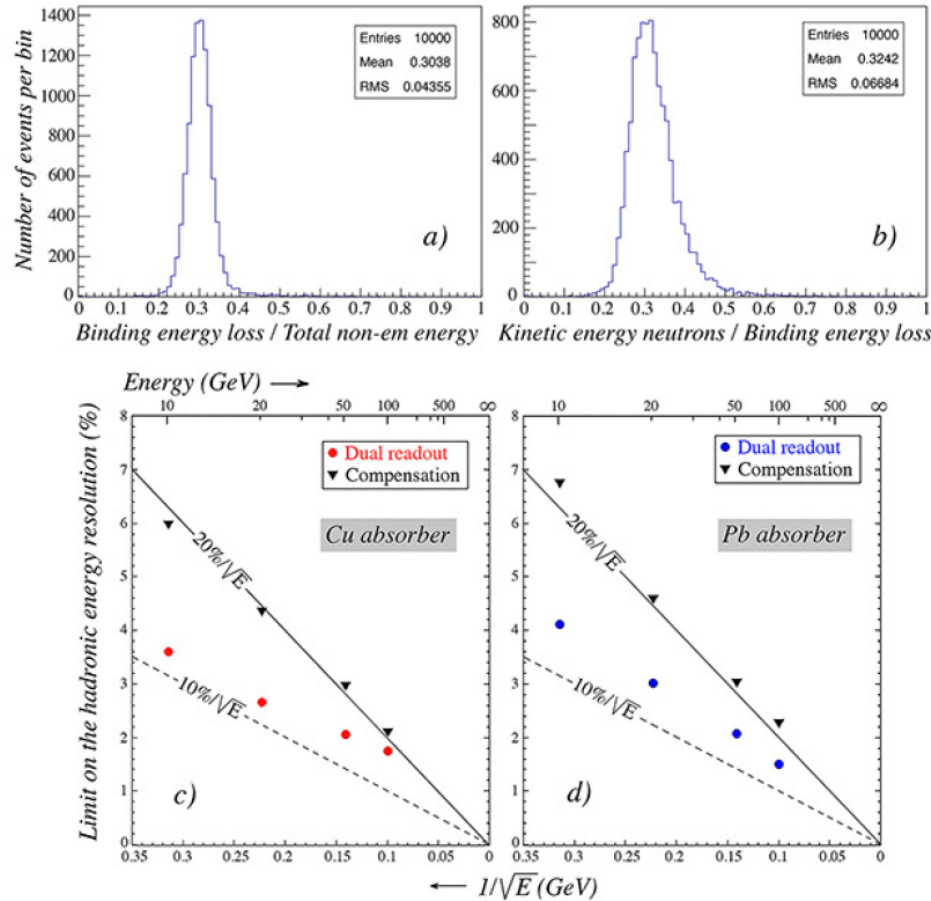


FIG. 52. Energy resolutions reported for the detection of (a) electrons and (b) hadrons by RD52 (Akchurin *et al.*, 2014b; Lee *et al.*, 2017), SPACAL (Acosta *et al.*, 1991a), and ZEUS (Behrens *et al.*, 1990). From Lee, Livan, and Wigmans, 2018.

Zeus/SPACAL are state-of-the-art compensating calorimeters.

For the RD52 calorimeter, small size leads to resolution dominated by leakage, so can be improved.

Compensation versus dual-readout



GEANT4 simulation of pure Cu or pure Pb calorimeter

Dual-readout signal (a) more highly correlated with total non-em energy than neutron energy (b)

Bottom plots show theoretical limit due to fluctuations in the binding energy loss

FIG. 53: Distributions of the ratio of the non-em energy and the nuclear binding energy loss (a) and the ratio of the total kinetic energy carried by neutrons and the nuclear binding energy loss (b) for showers generated by 50 GeV π^- in a massive block of copper. The limits on the hadronic energy resolution derived from the correlation between the nuclear binding energy losses and the parameters measured in dual-readout or compensating calorimeters, as a function of energy, as a function of the particle energy. The straight lines represent resolutions of $20\%/\sqrt{E}$ and $10\%/\sqrt{E}$, and are intended for reference purposes. Results from GEANT4 Monte Carlo simulations of pion showers developing in a massive block of copper (c) or lead (d) [29].

Dual readout benefits

139

- Not limited to high Z absorbers
- Sampling fraction can be as high as you can afford
- Shower more localized, since do not need to detect and measure the wandering neutrons
- Integration window can be short for same reason

Dual readout with crystals

140

My pet hobby (with Tully, **Lucchini**).

<https://arxiv.org/abs/2008.00338>

Pioneered by RD52 guys of course

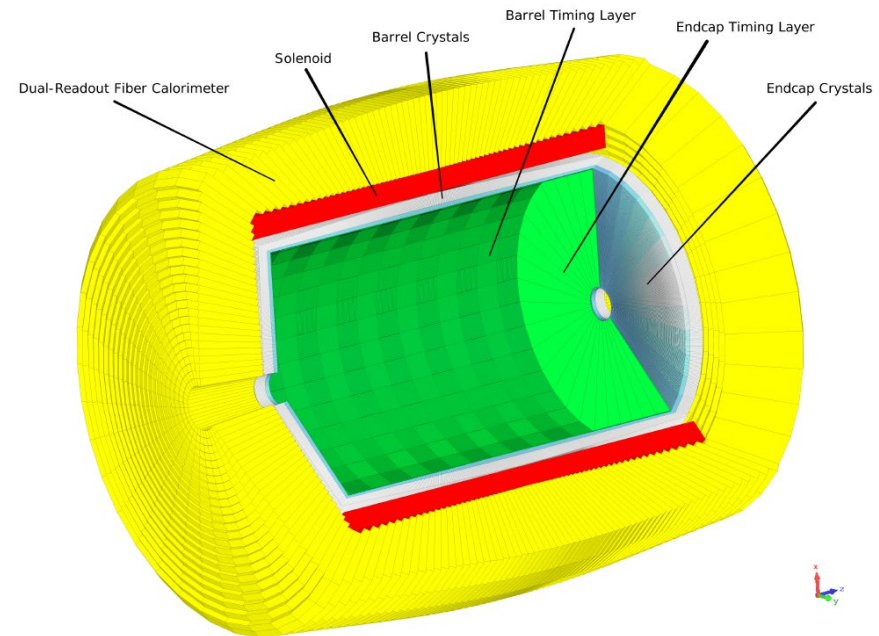


Figure 12. Implementation of the hybrid calorimeter system described in Figure 11 in a 4π detector geometry. The layers of the detector from the inner one to the outer one are: crystal timing layers T1 and T2 (green), crystal ECAL layers E1 (light blue) and E2 (white), solenoid (red), dual-readout fiber calorimeter (yellow).

Example: RD52 results

141

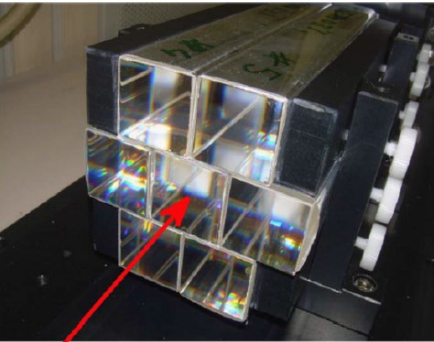


Fig. 2. The PWO matrix consisted of seven crystals with dimensions of $3 \times 3 \times 20 \text{ cm}^3$. These were arranged as shown in the figure and the beam entered the matrix in the central crystal. All crystals were individually wrapped in aluminized mylar. Both the upstream and downstream end faces were covered with filters. See text for details.

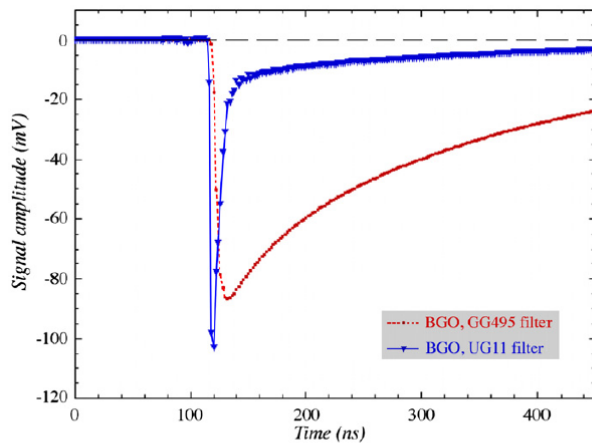


Fig. 3. The time structure of typical signals measured in a single BGO crystal, placed perpendicular to the beam line. The crystal was equipped on one side with a yellow filter, and on the other side with a UV filter, and read out with small, fast PMTs. The signals were measured with the sampling oscilloscope at a rate of 0.5 GHz, or 2.0 ns per sample.

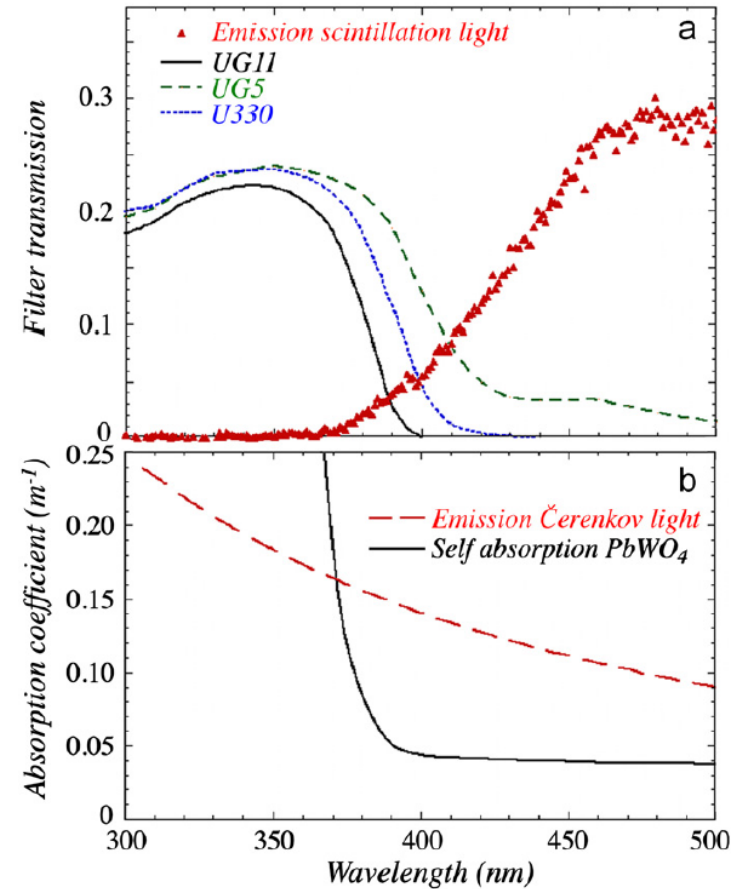


Fig. 5. Emission and absorption characteristics relevant to the PbWO_4 crystal matrix. Diagram (a) shows the emission spectrum of the scintillation light, as well as the transmission characteristics of three filters used to obtain the Čerenkov signals. In diagram (b), the Čerenkov spectrum is plotted, together with the self-absorption coefficient of the PbWO_4 crystals, as a function of the wavelength [5].

electrons

Results at this time were limited by expensive of readout. In order to have only one readout per crystal, and use timing for separation, needed to cut down the scintillation signal.

Inexpensive high efficiency extended-wavelength range photodetectors however may be a game changer

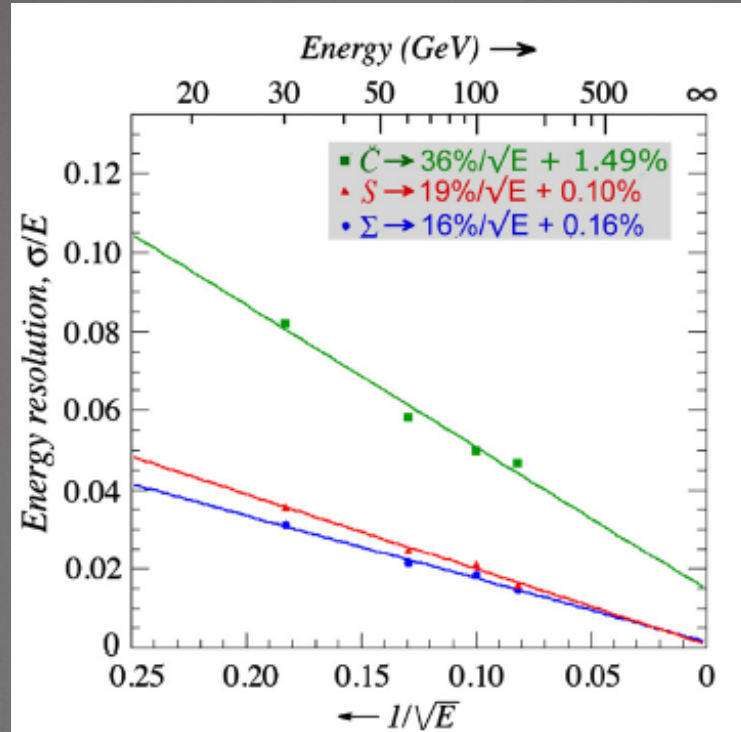


Fig. 9. The energy resolution for electrons in the BGO matrix, as a function of the energy of the showering particles. Results are given for the total charge collected by the PMTs (Σ), and for the Čerenkov (C) and scintillation (S) components of the signal. Also shown are the results of fits of the type $\sigma/E = aE^{-1/2} + b$ to the experimental data points.

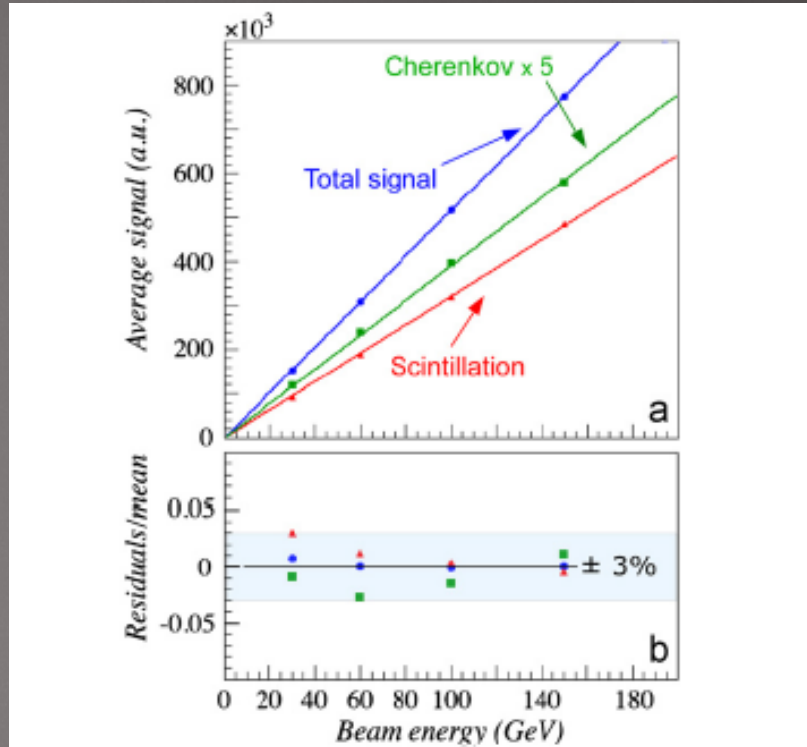


Fig. 10. Linearity of the BGO matrix for electron detection. Shown are the average total integrated signal, as well as the Čerenkov and scintillation components of that signal, as a function of energy. The results of linear fits through these data points, and the fractional residuals of these fits, are shown as well.

Future collider calorimeter?

143

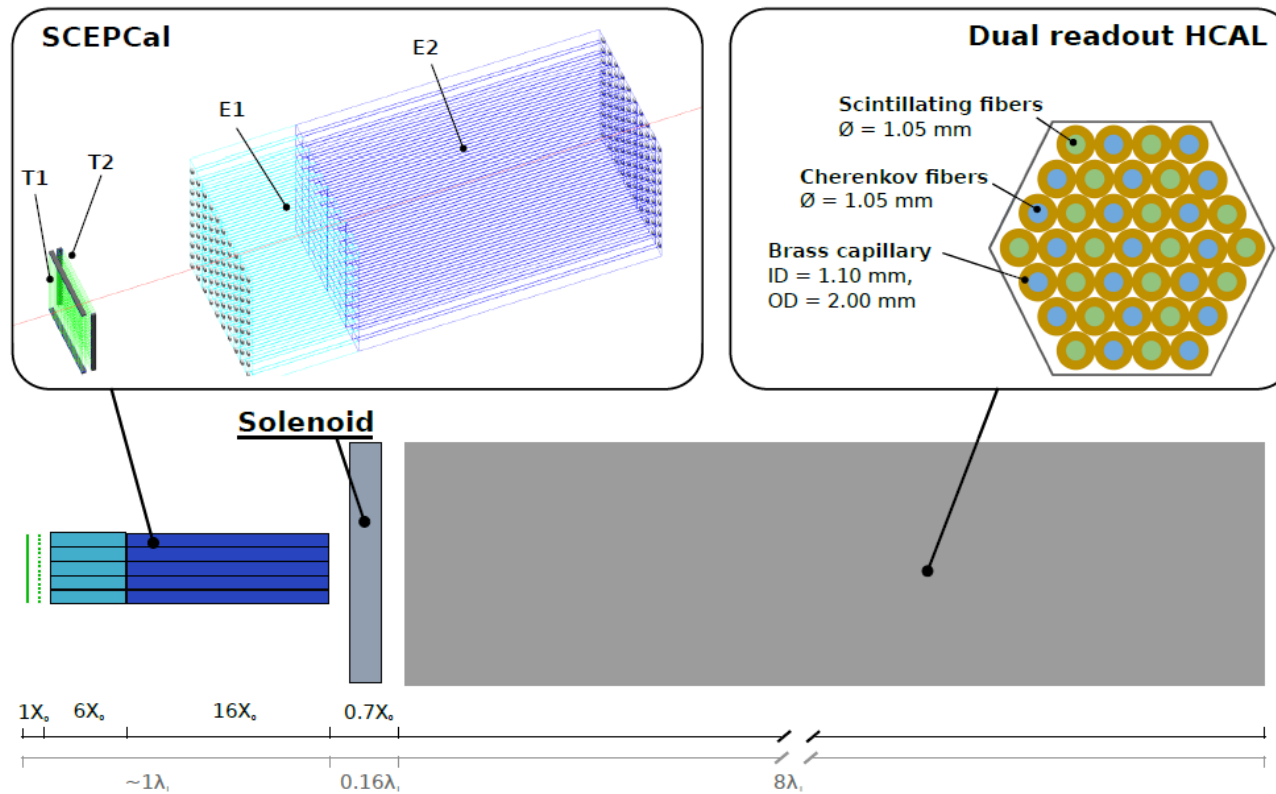


Figure 11. Overview of a hybrid segmented calorimeter layout featuring 4 front segments which exploit scintillating crystals for detection of EM showers followed by an ultrathin-bore solenoid and a hadron calorimeter based on scintillating and quartz fibers.

- One readout on E1 front
- Two readouts on E2 back, each with a wavelength filter
- RD52/IDEA style HCAL behind with dual readout

- Crystal ecal could allow state-of-the-art EM resolutions with high granularity with inexpensive sipmm readout
- Dual readout could allow state-of-the-art HAD resolutions as well
- High granularity is possible -> PFA improvements

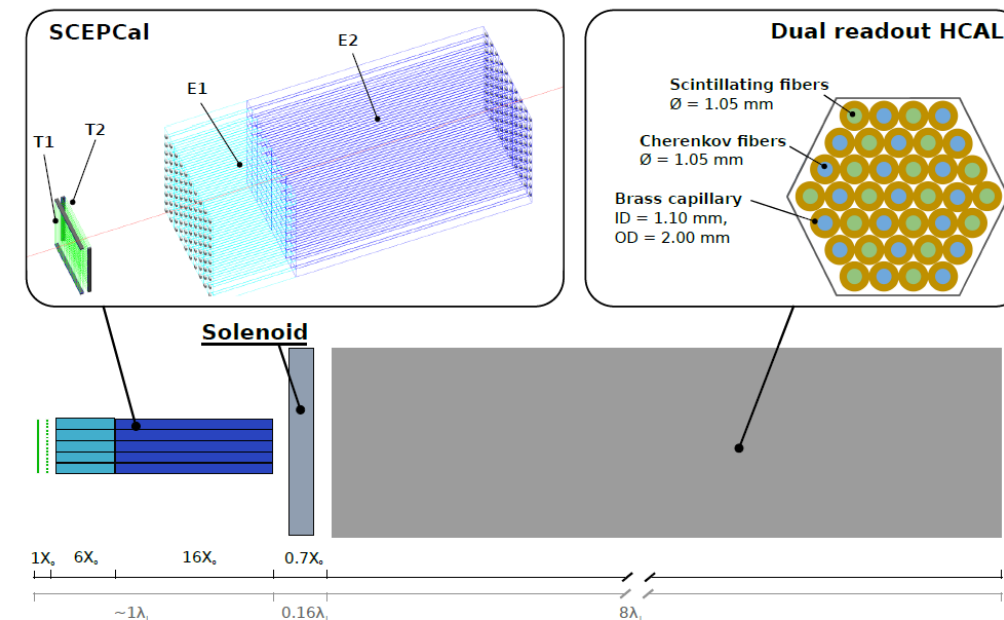


Figure 11. Overview of a hybrid segmented calorimeter layout featuring 4 front segments which exploit scintillating crystals for detection of EM showers followed by an ultrathin-bore solenoid and a hadron calorimeter based on scintillating and quartz fibers.

Separating C and S

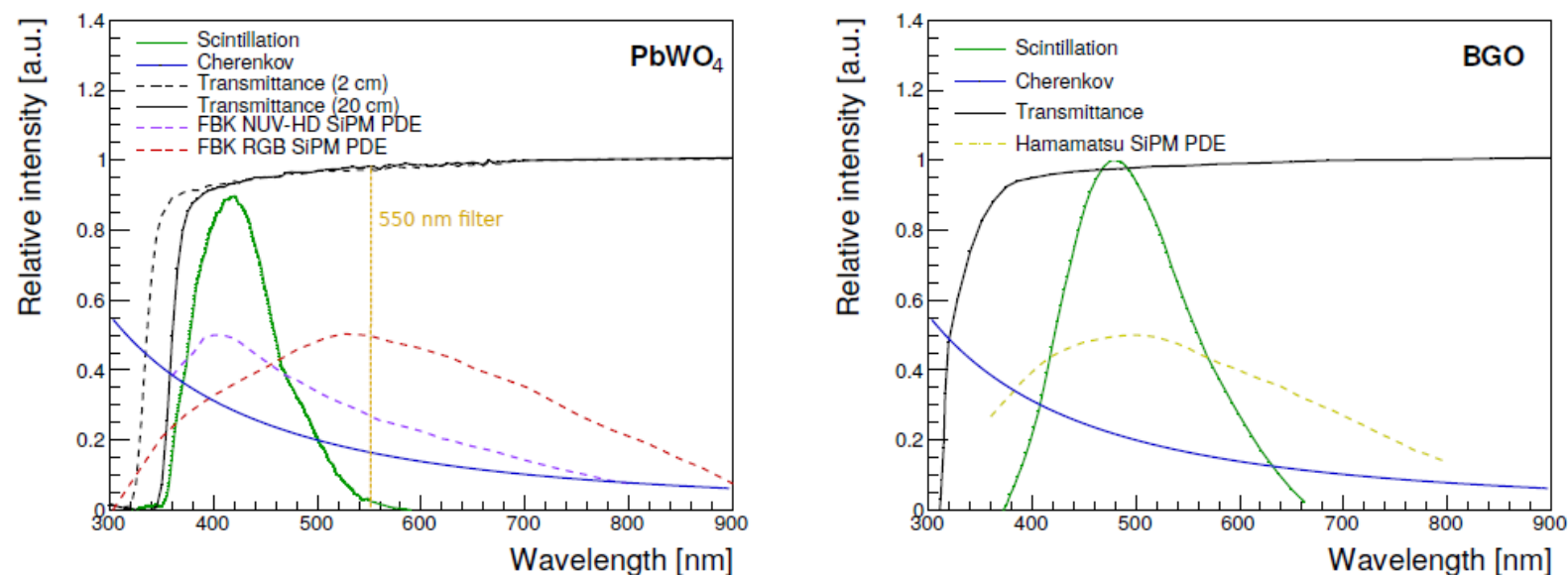


Figure 23. The transmission curves of the crystals (black) are compared with the wavelength spectrum for scintillation (green) and Cherenkov light (blue) and with the photon detection efficiency of commercially available SiPMs from FBK and Hamamatsu. A comparison of PbWO₄ (left) and BGO (right) crystals shows how different spectral regions of the Cherenkov light could be used for better separation from the scintillation component.

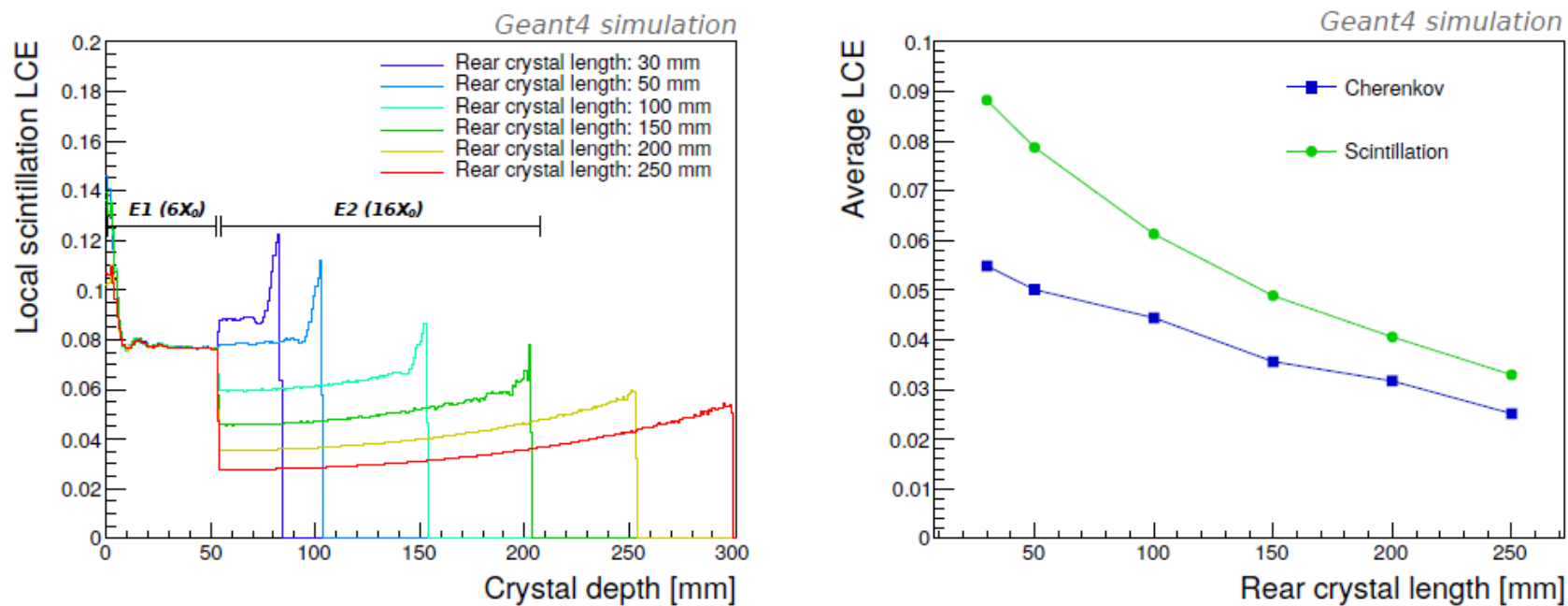


Figure 24. Left: local light collection efficiency for scintillation light along the SCEPCal for both the front and rear segments when varying the length of the rear crystal segment (E2). Right: average light collection efficiency for scintillation and Cherenkov light for the rear segment (E2) as a function of crystal length.

Excellent EM resolution

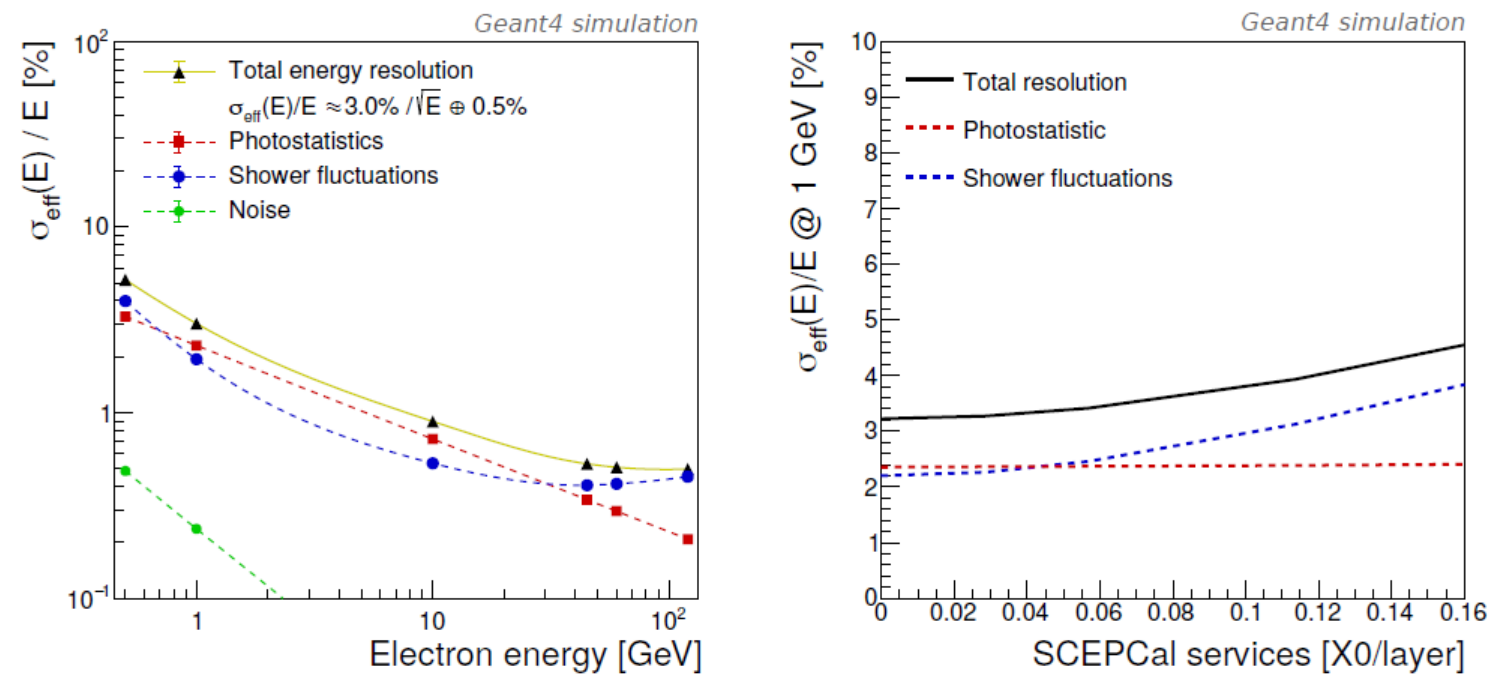


Figure 14. Left: energy resolution to electrons as a function of the electron energy with the assumption of a 2.4% contribution from photostatistics, a tracker material budget of $0.1 X_0$, and about $0.1 X_0$ of dead material between layers. Right: impact of dead material between layers on energy resolution.

Two particle separation

With high granularity,
excellent two photon
separation

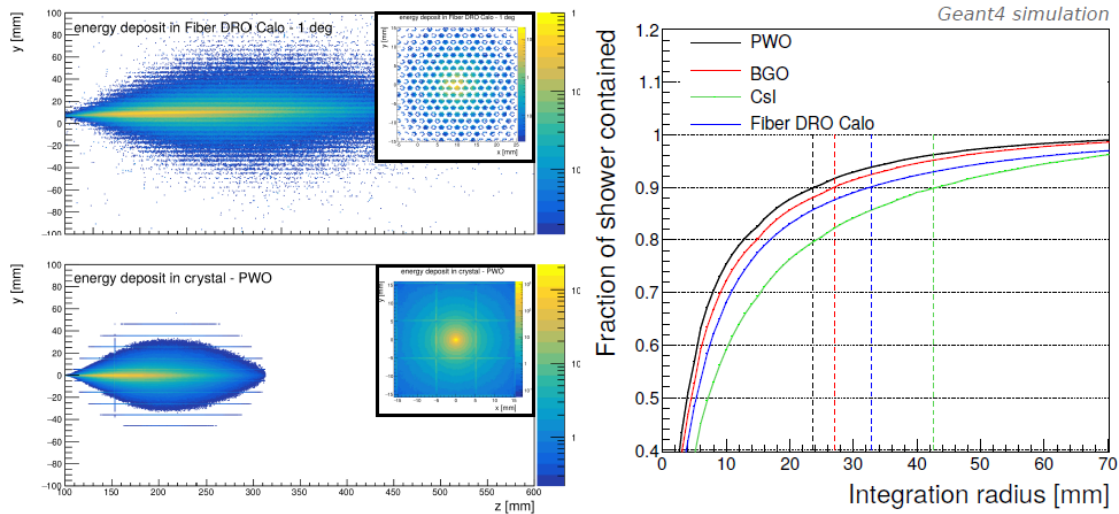


Figure 18. Left: longitudinal shower profile for 60 GeV electrons in a fiber DRO HCAL compared to that of a PbWO_4 -based SCEPCal (the inset in the plot shows the transverse shower profile). Right: comparison of Molière radii between homogeneous crystal calorimeters (PbWO_4 , BGO, CsI) and the fiber DRO HCAL.

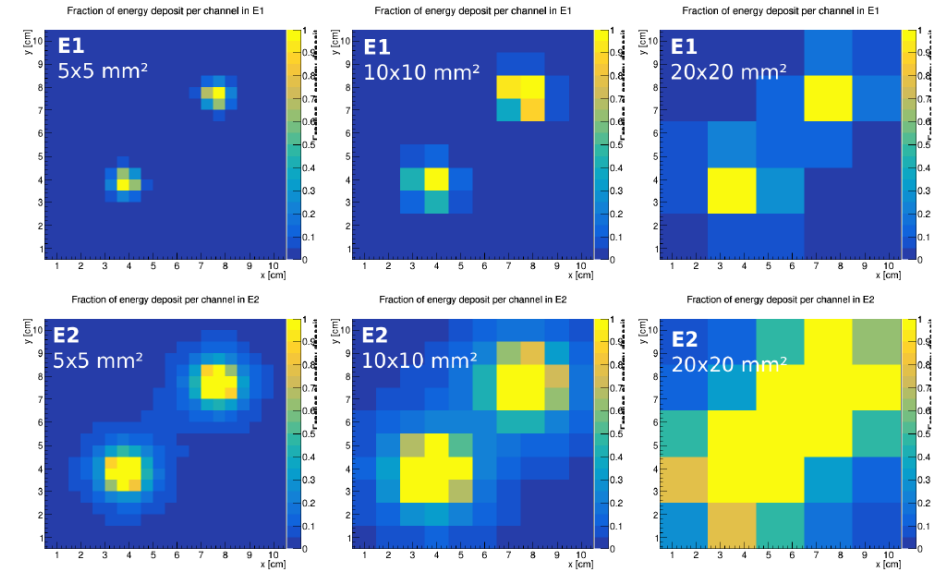


Figure 13. Transverse separation of two photons emitted with an angle of about 3 degrees, in the front and rear layer of the crystal ECAL (with PbWO_4 crystals), for different scenarios of transverse segmentation ($5 \times 5 \text{ mm}^2$, $10 \times 10 \text{ mm}^2$, $20 \times 20 \text{ mm}^2$).

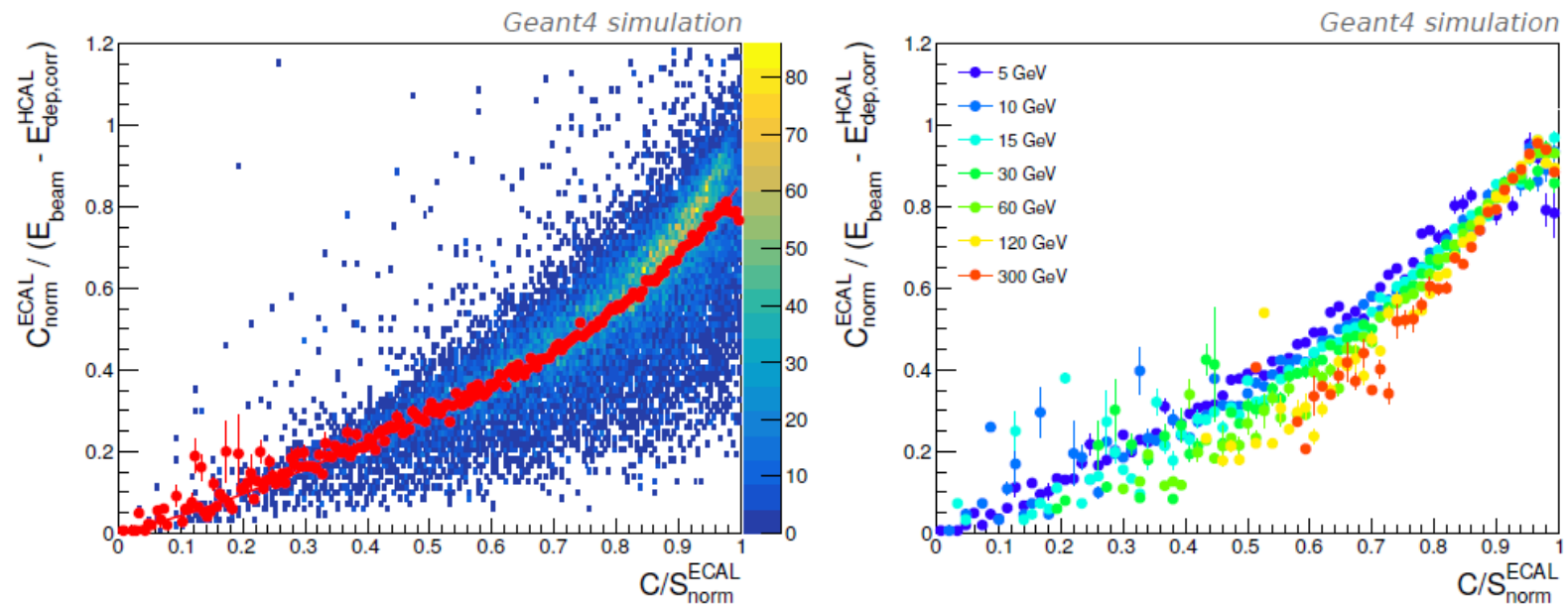


Figure 20. Left: correlation between the C signal and the C/S ratio measured in the SCEPCal for events that deposit a fraction of energy in the SCEPCal. Right: correction curve for different hadron energies.

Excellent
hadron
resolution

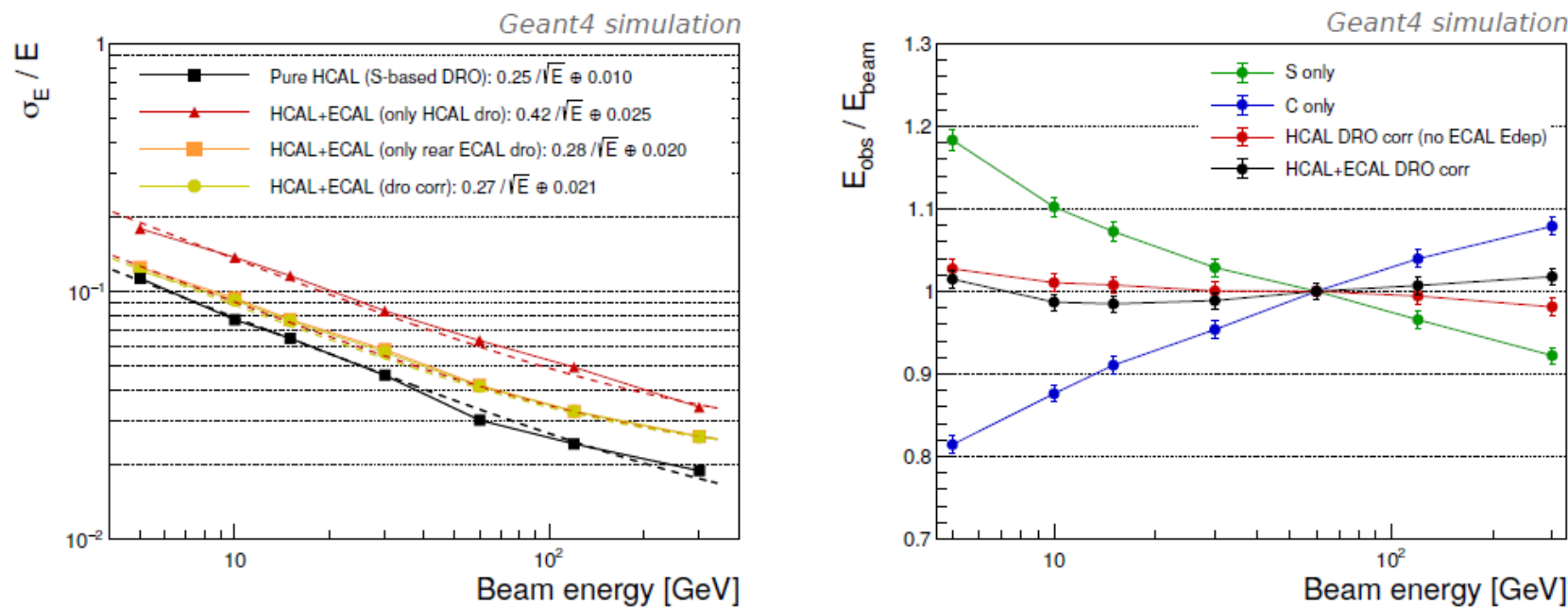


Figure 21. Response to neutral kaons in terms of energy resolution (left) and linearity (right) for a dual-readout hybrid calorimeter consisting of the SCEPCal followed by an ultrathin-bore solenoid and a dual-readout fiber HCAL.

Radiation damage

Large doses

152

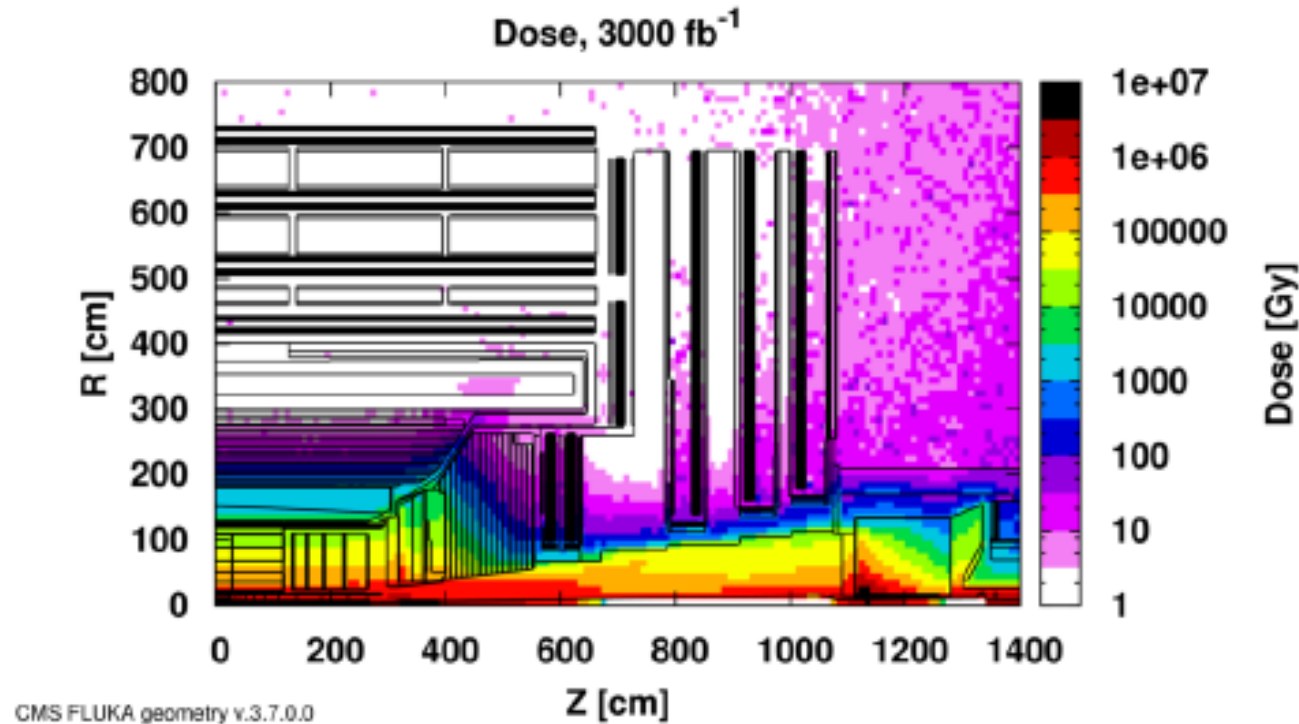
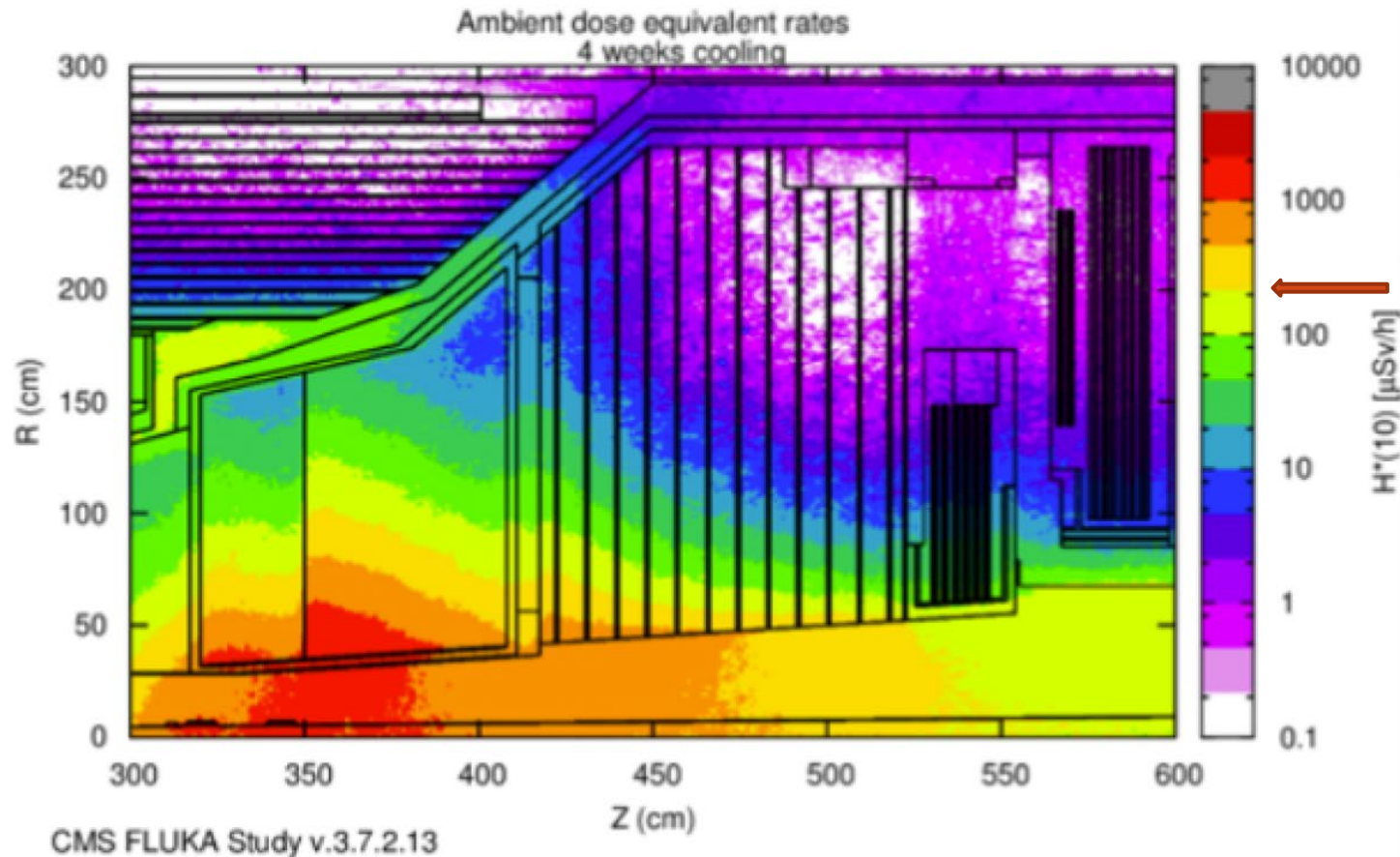


Figure 1.6: Absorbed Dose in the CMS cavern after an accumulation of 3000 fb⁻¹ delivered luminosity.

activation



Yearly dose limit of 5 rem in about 5 days work

Figure 12.6: Activation map in $\mu\text{Sv/h}$ of the HGCal at the end of exploitation after 4 weeks of cool-down.

Liquid argon

154

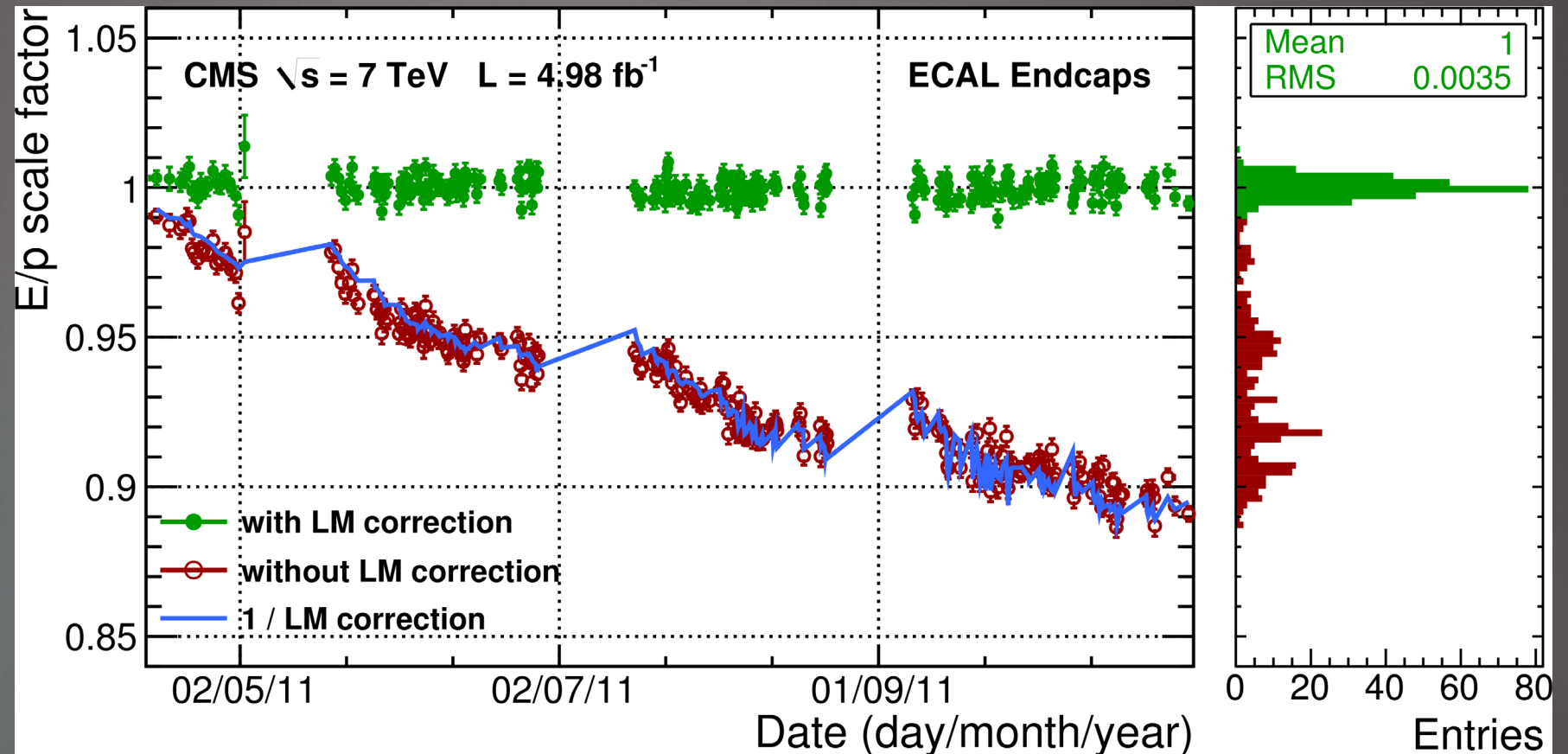
Rad hard.

Biggest danger is pollution of Argon purity due to outgassing and damage to on-detector electronics

crystals

155

And PbWO_4 is one of the most radhard crystals (LYSO is better)



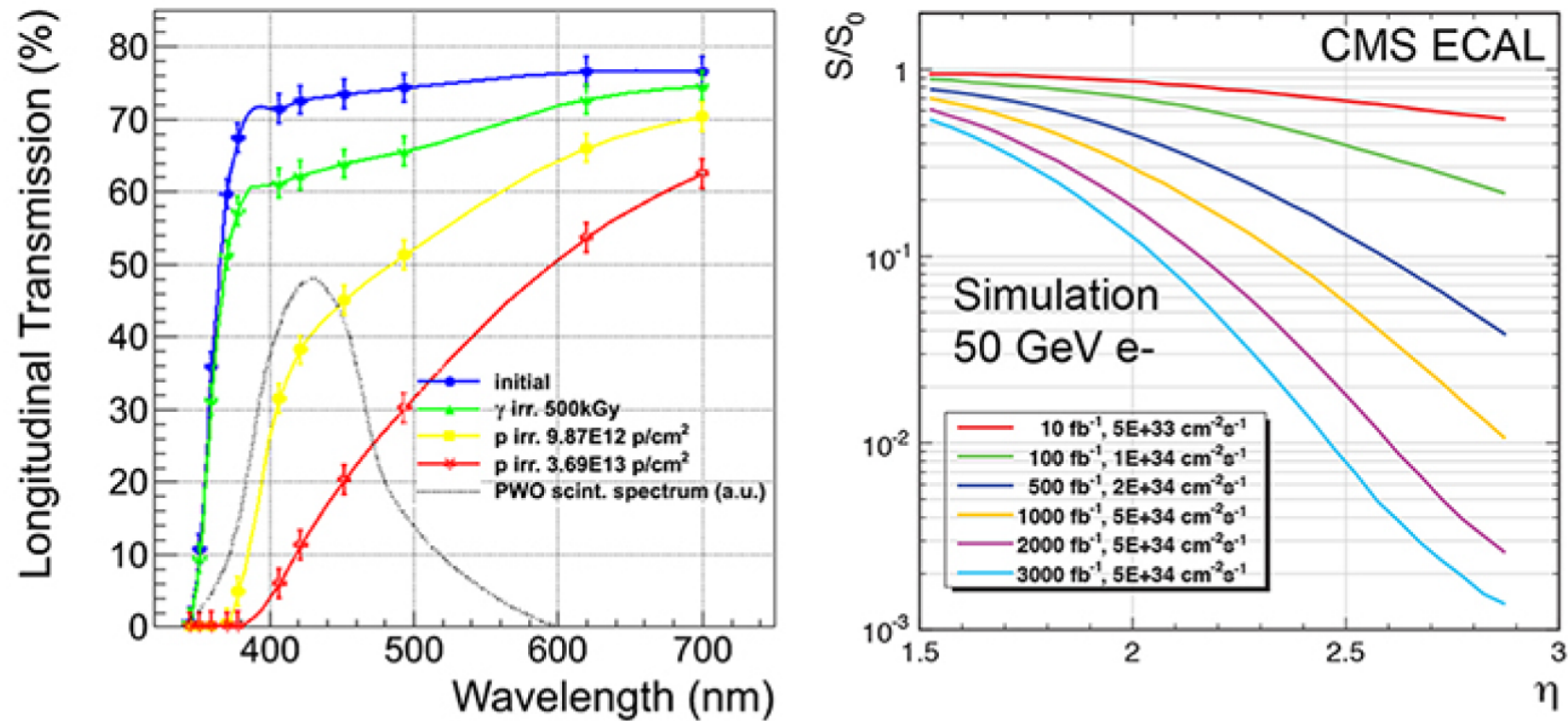
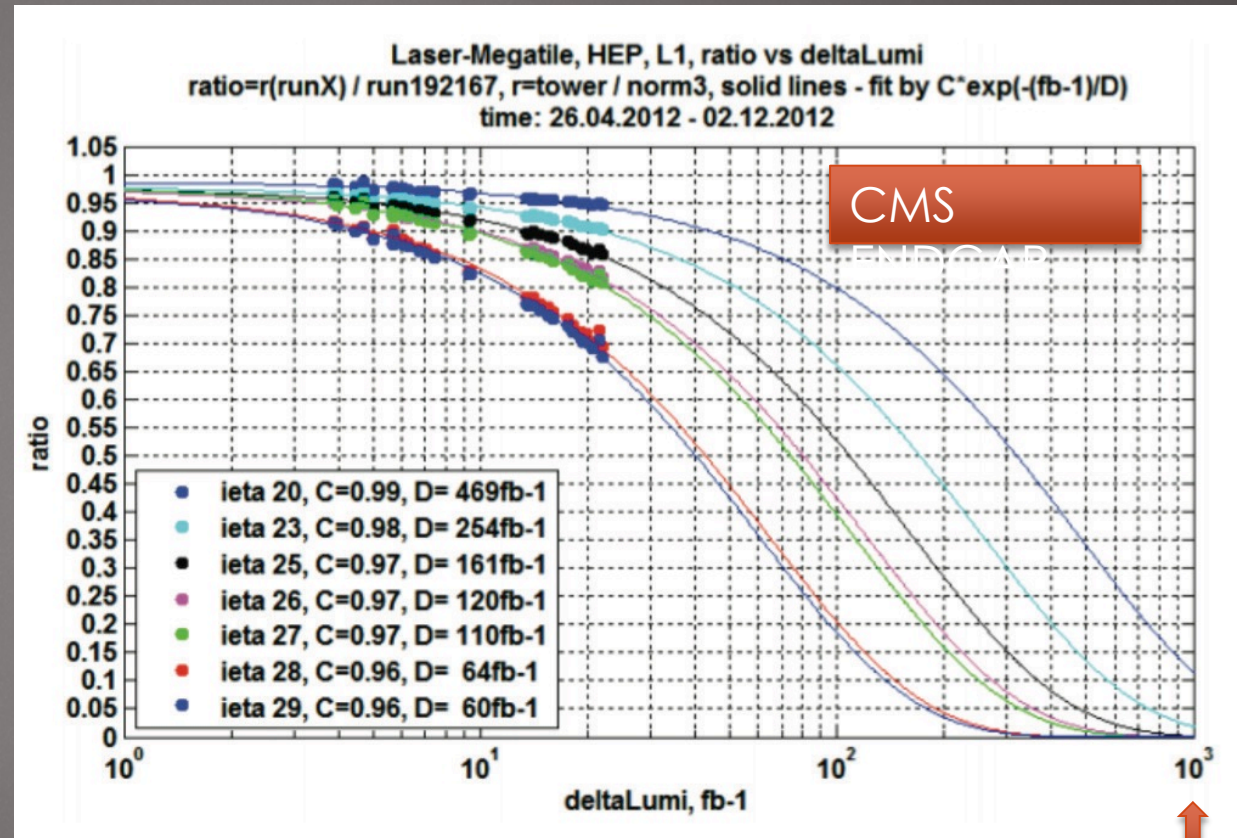


Figure 14: Effects of radiation damage on the performance of the CMS em calorimeter. The left diagram shows the light transmission in the PbWO_4 crystals after irradiation with γ s and protons. The overlaid black dotted line represents the lead tungstate light emission spectrum. The right diagram shows the (simulated) effect on the scintillation signals from 50 GeV showers in the crystals as a function of the pseudorapidity, for various values of the integrated luminosity [37].

Plastic scintillator

Data from laser injection in layers 1 and 7 of the CMS endcap calorimeter

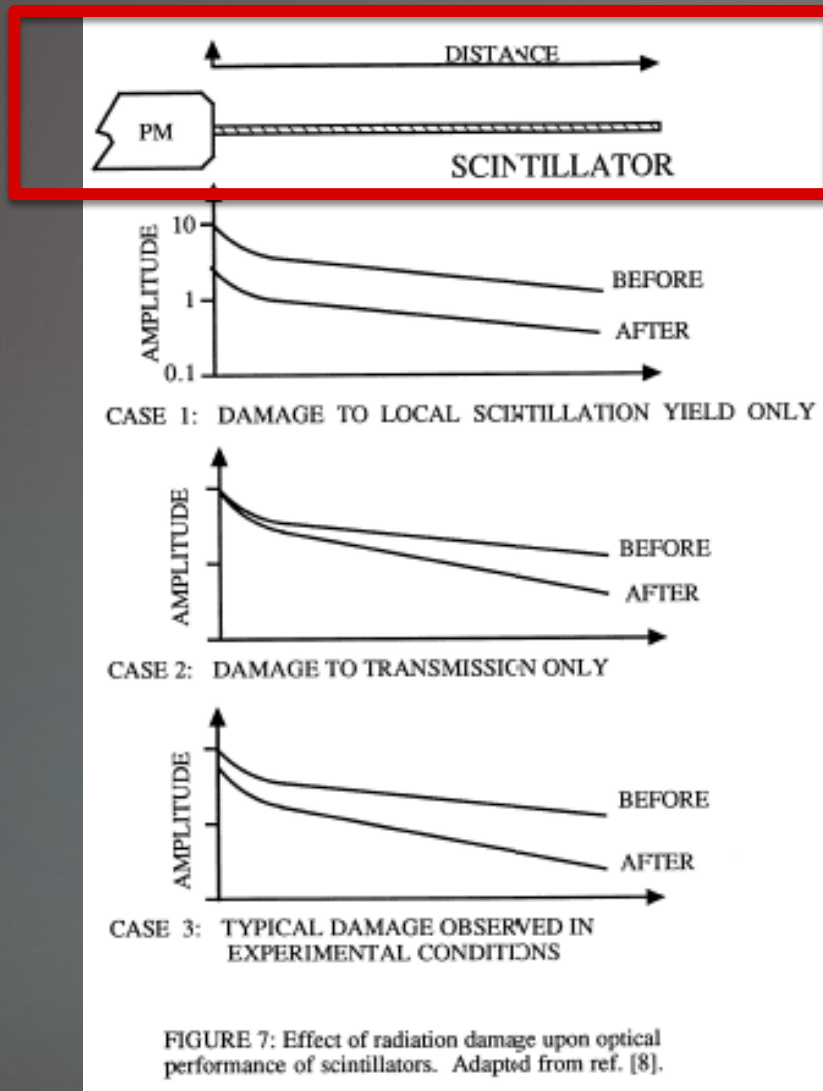
$$\frac{L}{L_0} \propto e^{-L/D}$$



1000 fb⁻¹

Radiation damage to substrate

158



Result is both

- reduction of the initial light output, due mostly to increased quenching for the primary and reduced transfer from the primary to the secondary
- Absorption of light produced by the secondary ("color centers")

Attenuation length is $1/\mu$, where μ is the number density of absorption centers) * the absorption cross section. μ is useful as it is linear in dose for doses less than a few Mrad, and has units length^{-1}

1/17/17

$$\frac{L}{L_0} \propto e^{-L/D}$$

Dose constant

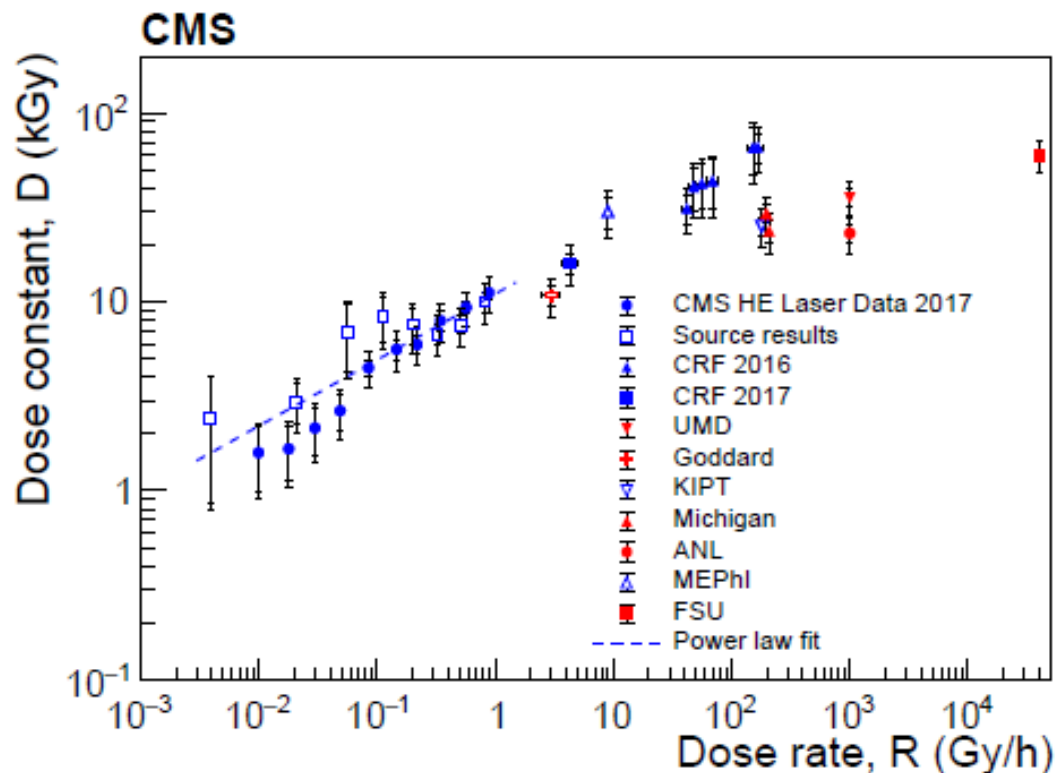


Figure 18: Values of $D(R)$ versus R for high- R data taken with gamma irradiation sources at KIPT, National Research Nuclear University MEPhI, Goddard, Michigan, ANL, and UMD, an electron beam at FSU, and in the collider environment in the CRF for SCSN-81 tiles, along with the results from the HE laser and source calibration data. The statistical uncertainties are shown as the inner bars, and the outer bars include the systematic uncertainties added in quadrature. The error bars on the irradiation data are dominated by systematic uncertainties.

Type of color centers

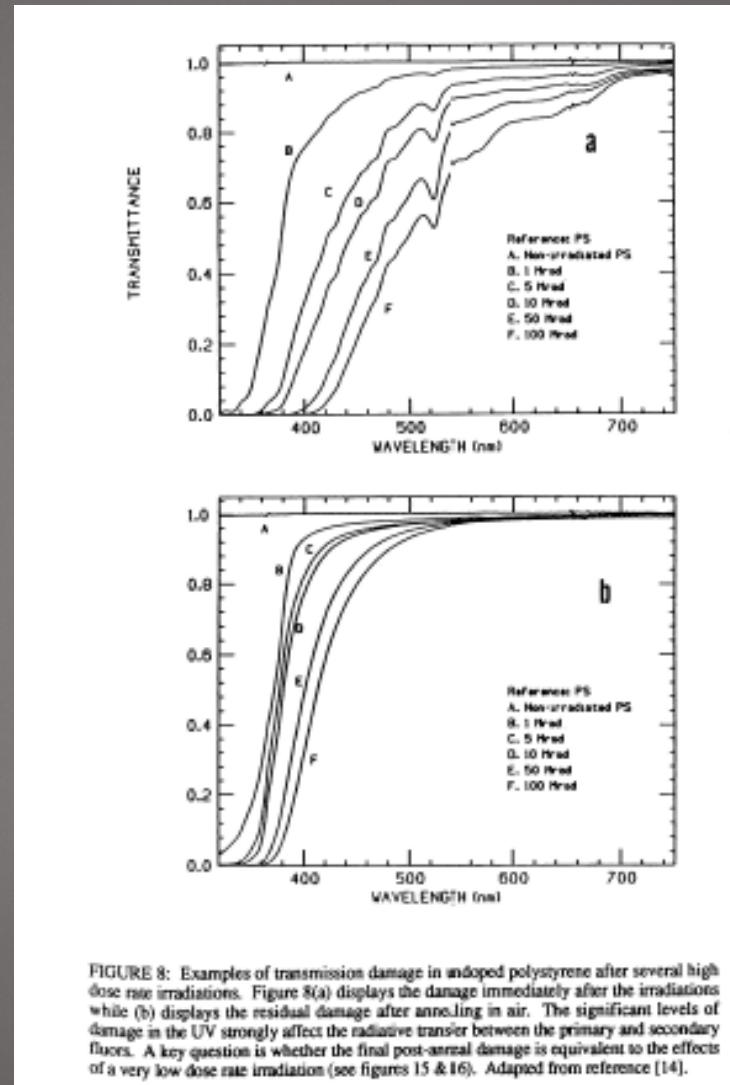
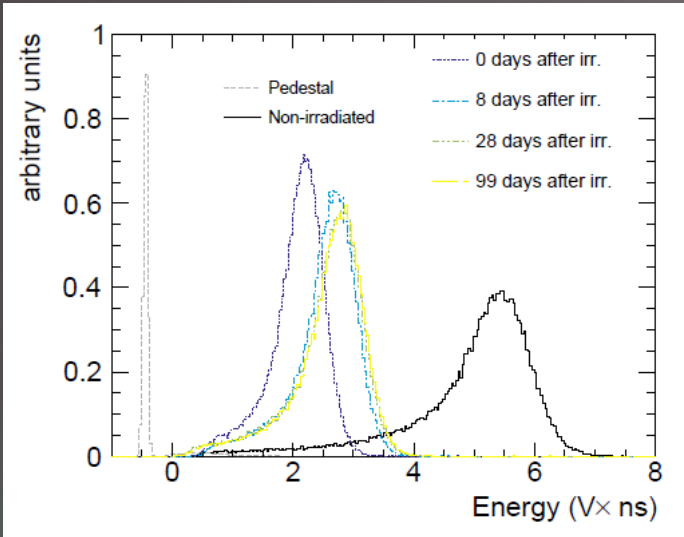


FIGURE 8: Examples of transmission damage in undoped polystyrene after several high dose rate irradiations. Figure 8(a) displays the damage immediately after the irradiations while (b) displays the residual damage after annealing in air. The significant levels of damage in the UV strongly affect the radiative transfer between the primary and secondary fluors. A key question is whether the final post-anneal damage is equivalent to the effects of a very low dose rate irradiation (see figures 15 & 16). Adapted from reference [14].

Temporary and permanent color centers in substrate that affect both transfer to the primary (depending on the primary dopant concentration) and transfer to the secondary

Table 2

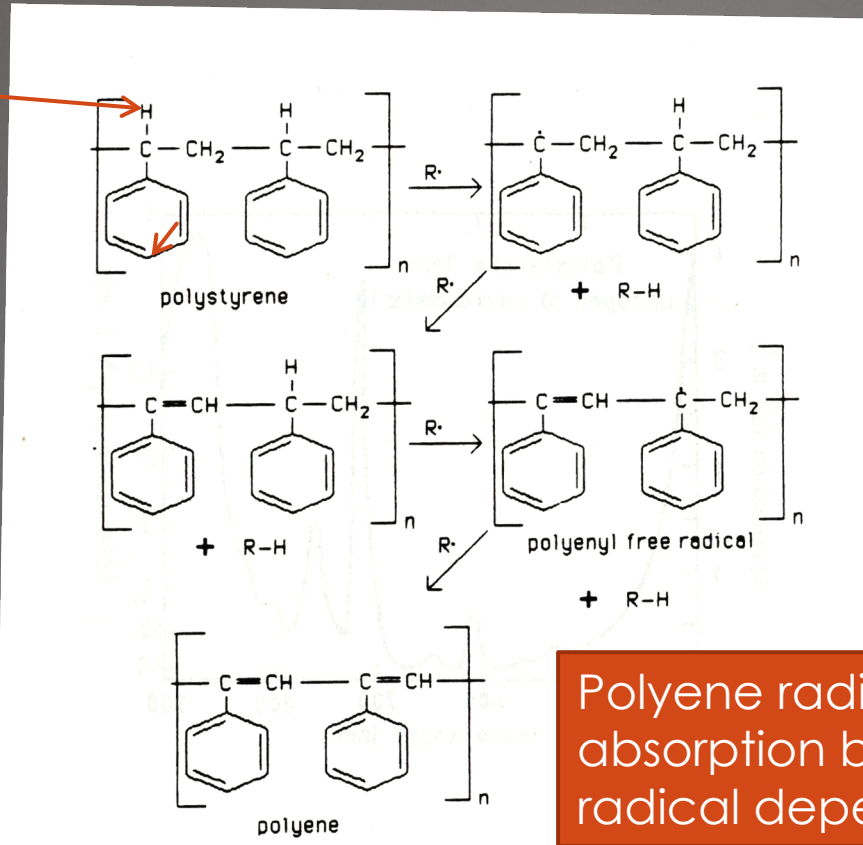
The g values for different radiation induced processes occurring in PMMA and polystyrene. Only the most probable gaseous irradiation products of PMMA (mol fraction > 10%) are given.

	g values for	
	PMMA	polystyrene
Radical production	2.4–2.5 [4,5]	0.2 [6]
Gas evolution	1.18 [7] (30.5% CO, 15.7% CO ₂ , 14.2% HCOOCH ₃ , 13.1% CH ₄ , 11.7% H ₂ ,...) [8]	0.026 [7] (100% H ₂)
Degradation	1.7–2.6 [9]	0.009 [9]
Cross-linking	0 [9]	0.034 [9]

g is the mean number of produced, destroyed, or changed per 100 eV.

Color center formation: permanent damage

Tertiary benzylic hydrogen



Polyene radical: The absorption band for this radical depends on length.

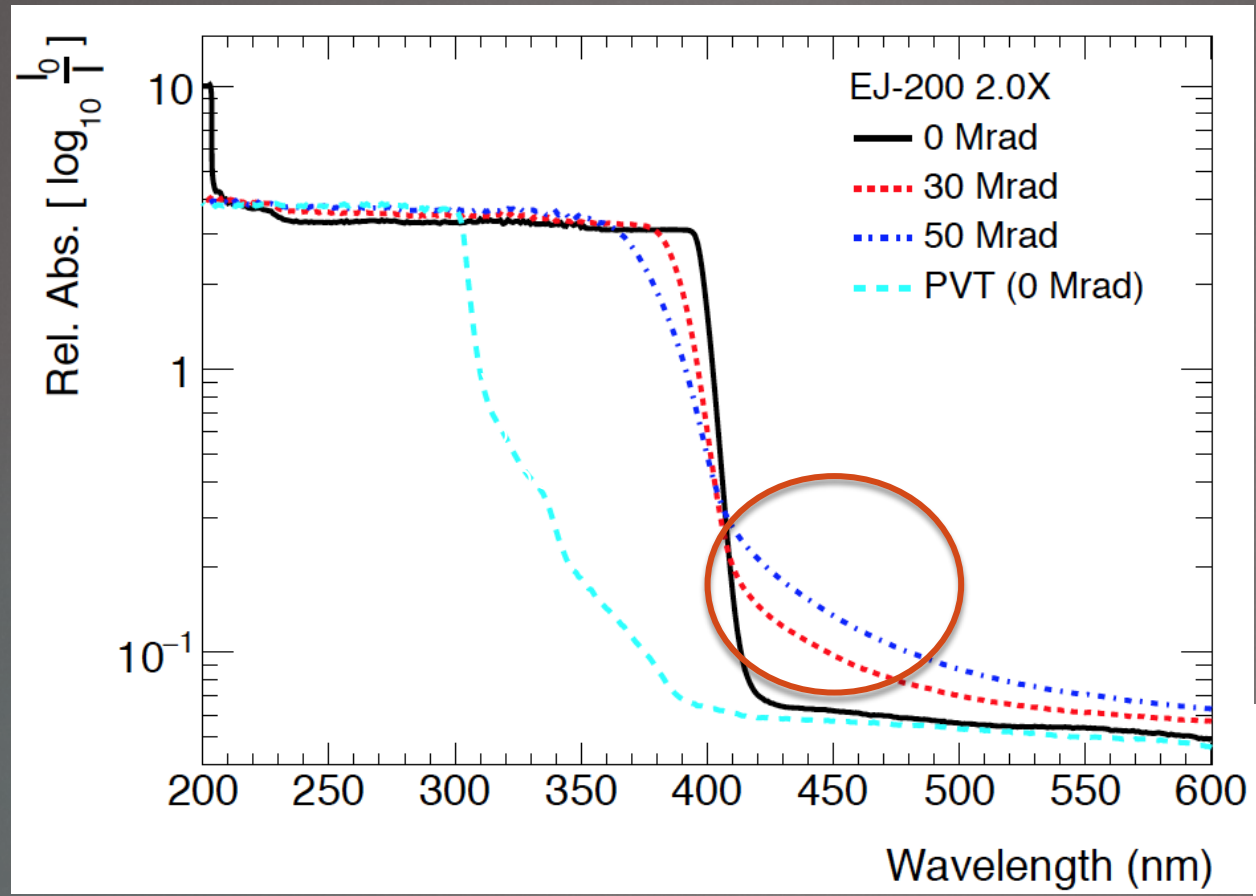
When oxygen is not present.

α -hydrogen abstraction

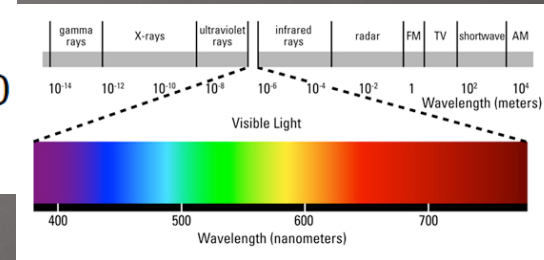
Yields double bonds and cross links

FIGURE 10: A likely candidate for the mechanism by which color centers are formed in polystyrene (and the related polyvinyltoluene). Adapted from reference [34].

Tend to absorb at short wavelengths



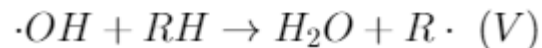
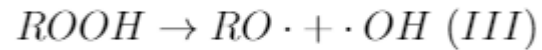
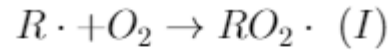
Radiation-induced permanent color centers form primarily at shorter wavelengths. Wavelengths shorter than 500 less affected



Radicals and oxygen

Radicals react rapidly with O₂, forming **peroxy radicals** RO₂ as an intermediate state.

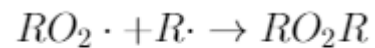
It also opens up new migration forms.



No radicals survive when O₂ is present due to the quickness of (I).

This is the process that leads to annealing in air

New terminations



Peroxide radicals do not absorb visible light.

Very reactive. Consumed faster than it can diffuse through the sample at high dose rate.

The increased migration helps limit the temporary damage, but the new terminations increases the permanent

Radiation damage to photo detectors

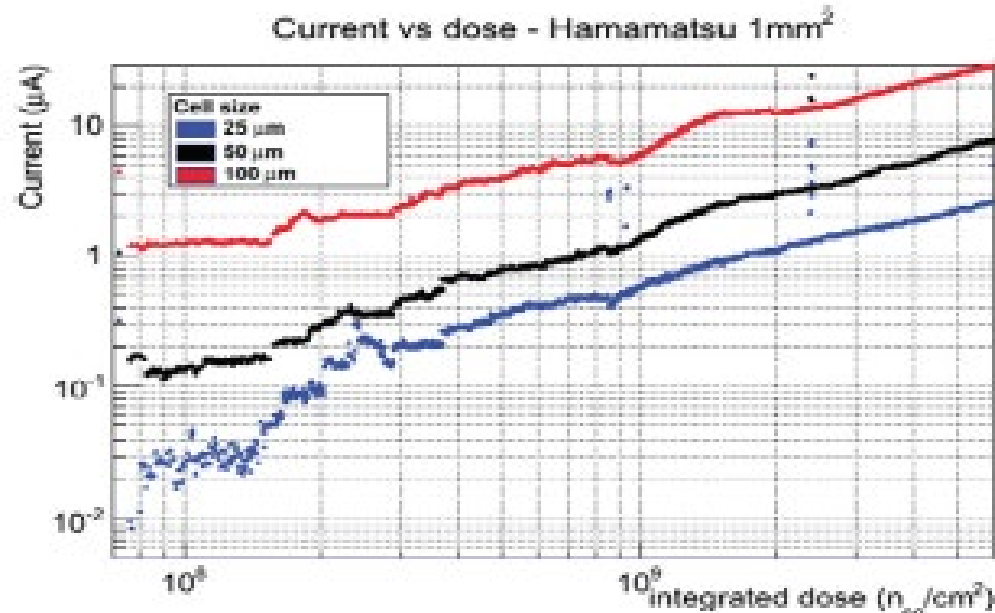


Fig. 17. Dark current vs neutron dose for 1 mm² HAMAMATSU SIPMs with different pixel size. The blue line is for the 25 μm pixel, black 50 μm and red 100 μm. From Ref. [37]. In the paper similar measurements for AdvanSiD and SensL are also reported.

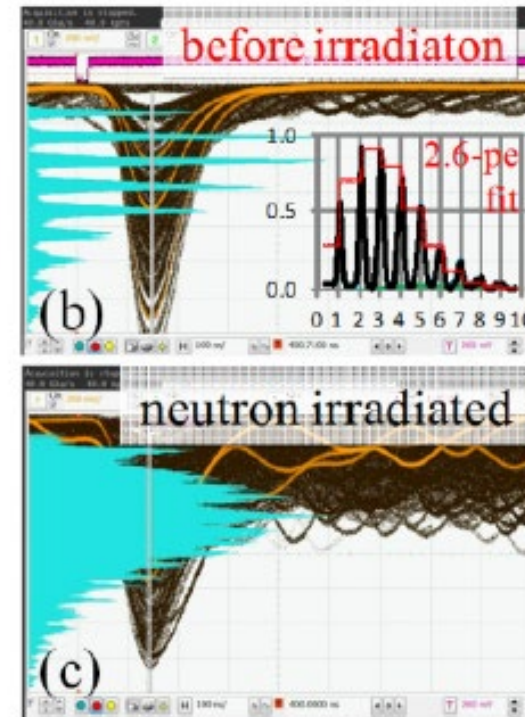


Fig. 9. Single photoelectron charge signal pulses at $V - V_{td} = 3$ V (b) before irradiation, (c) after neutron irradiation to $\Phi_{eq} = 10^9$ cm⁻². Source: From Tsang Ref. [26].

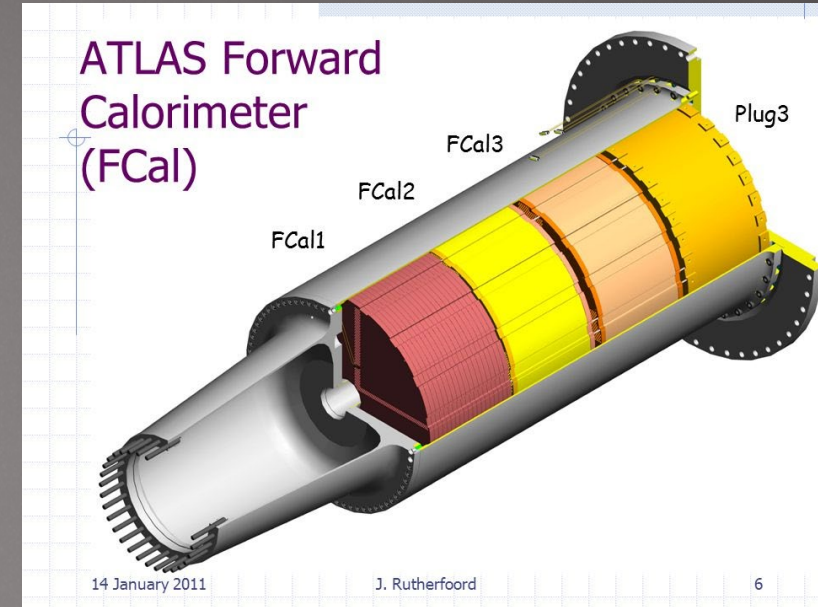
Extreme radiation $3 < \eta < 5$

CMS HF calorimeter



ATLAS forward calorimeter

Liquid argon rod/tube



Quartz is rad hard.
Only sensitive to EM portion of shower

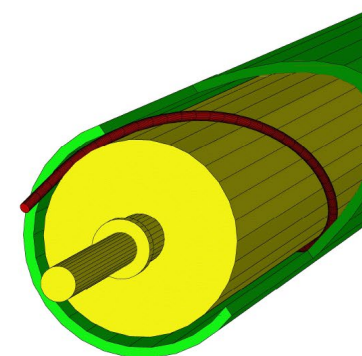


Figure 3. Cut-away drawing of an FCal electrode. Liquid argon fills the gap between the rod and tube.

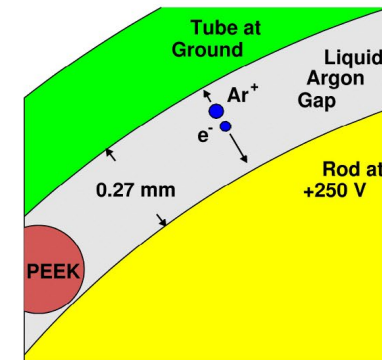


Figure 4. Close-up view of a cross-section of the FCal1 electrode gap. The insulating PEEK fiber is shown.

Detector artifacts

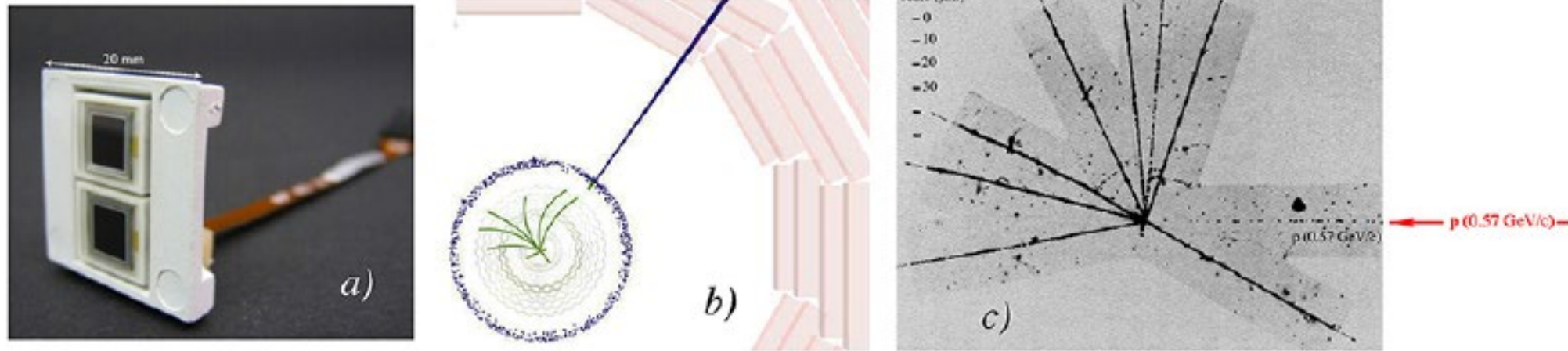


Figure 41: Photograph of two CMS APDs (active area $5 \times 5 \text{ mm}^2$) mounted in a capsule (a). CMS event display of a pp collision event, showing an isolated ECAL spike (top-right) simulating a 690 GeV transverse energy deposit (b) [84]. A nuclear reaction induced by a proton with a kinetic energy of 160 MeV in a photographic emulsion (c).



Figure 44: Three modules of the CMS forward calorimeter, which consists of 2×12 such wedges. The quartz fibers that serve as the active material in this sampling calorimeter are bunched towards a readout box, where PMTs convert the Čerenkov light signals into electric pulses.

Texas towers can also occur in thin silicon sensors

Texas towers are a problem when the sampling fraction is very low. A low energy particle loses energy per path length in a way that goes as $1/v^2$. so when they are produced in a layer, they produce anomalous signal

Calorimeter simulation

Calorimeter simulation

172

Many analyses should have a systematic uncertainty due to shower simulation, but do not

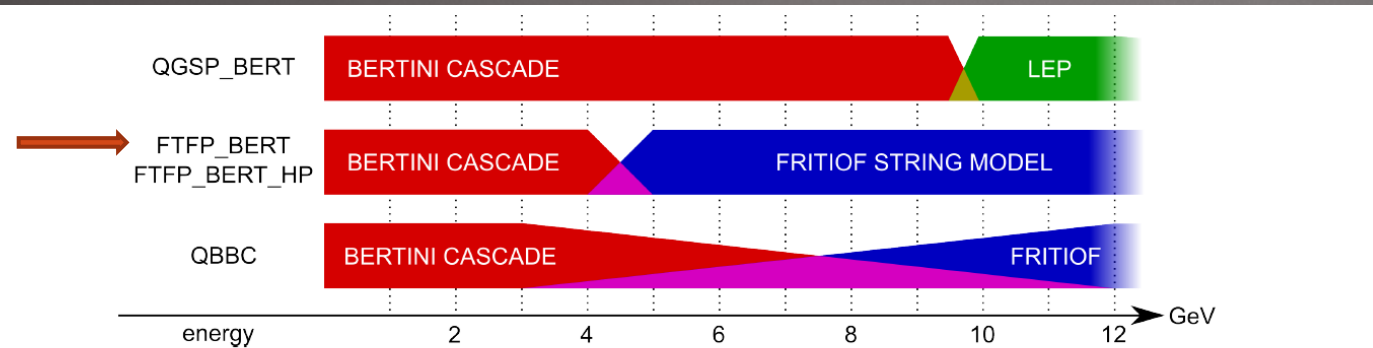


Figure 2: Model used for hadronic interactions of π^- depending on the physics list and the energy of the interacting particle for the studied energy range.

Bertini cascade model: simulates interaction of hadron with nucleus, producing secondary particles (mostly pions) which themselves collide with nucleons within the nucleus. Inside the nuclear material, the nuclear media is approximated by several concentric shells of constant nucleon density, and collisions are modelled as free. In this process, the nucleus is highly excited and evaporation models are included to de-excite the nucleus.

String models are based on diffractive scattering between a hadron and a nucleon, via momentum or pomeron exchange, resulting in excited strings that are fragmented to produce secondary particles and excited nuclei that are deexcited.

Parameterized models (LEP) are based on experimental fits to data.

Energy is only conserved on average, not on an event-by-event basis.

Since 2017 CMS used GEANT4 10.2p02 and FTFP_BERT_EMM

Geant4 hadronic models

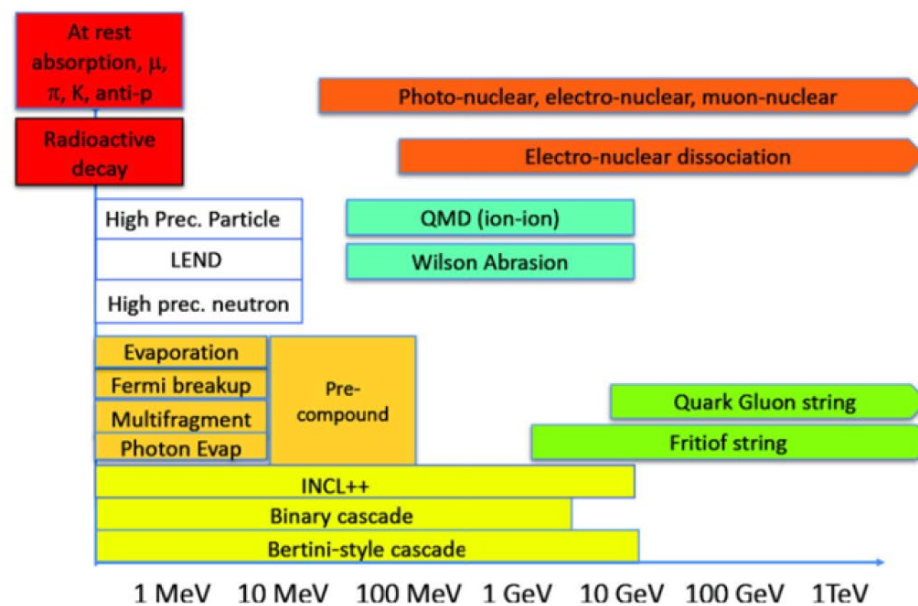
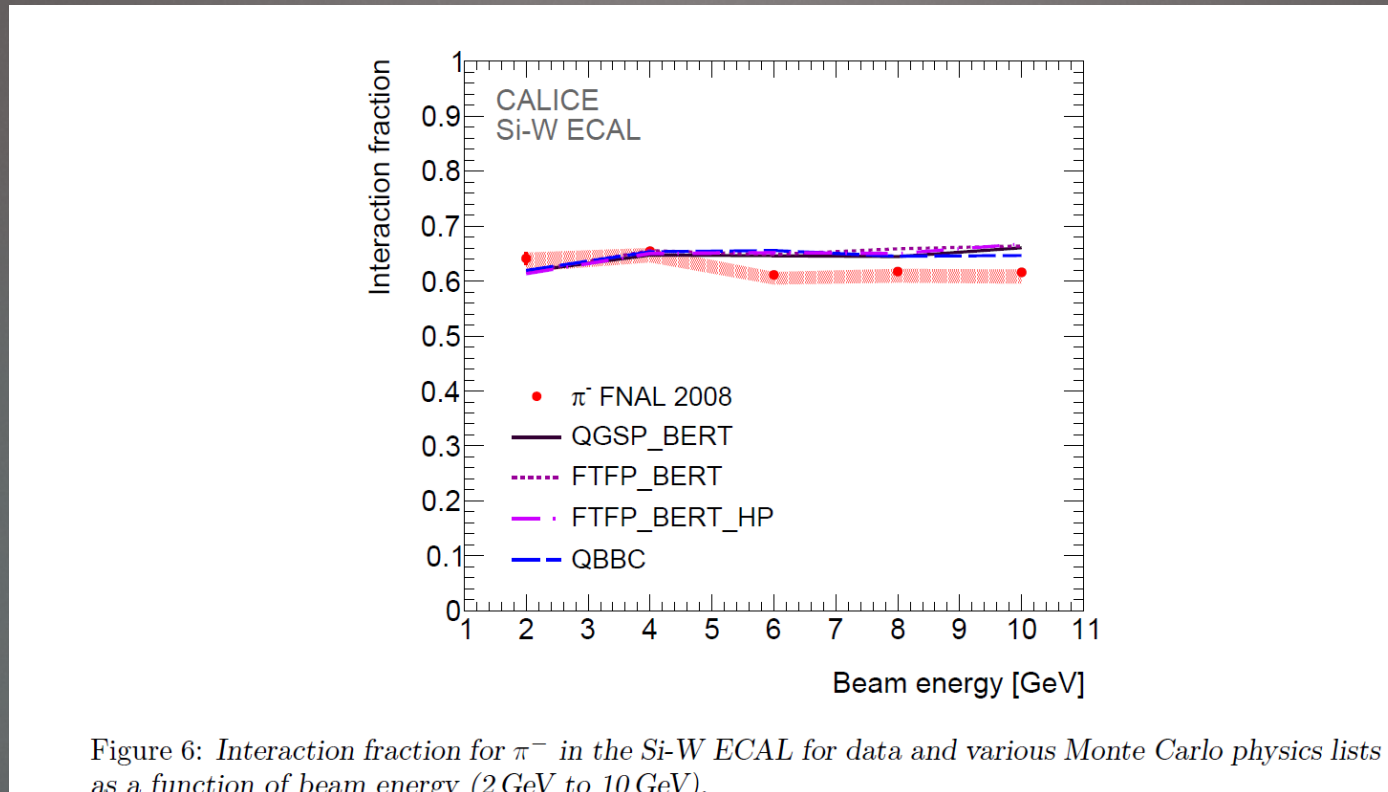


Figure 3. Geant4 10.6 schema of hadronic physics model applicability in the energy scale.

CALICE-based GEANT studies

174

Studies of individual hadronic interactions using a one λ highly segmented calorimeter. Use segmentation to find layer with an individual interaction (first in shower)



Interaction probability

Shower radial distribution

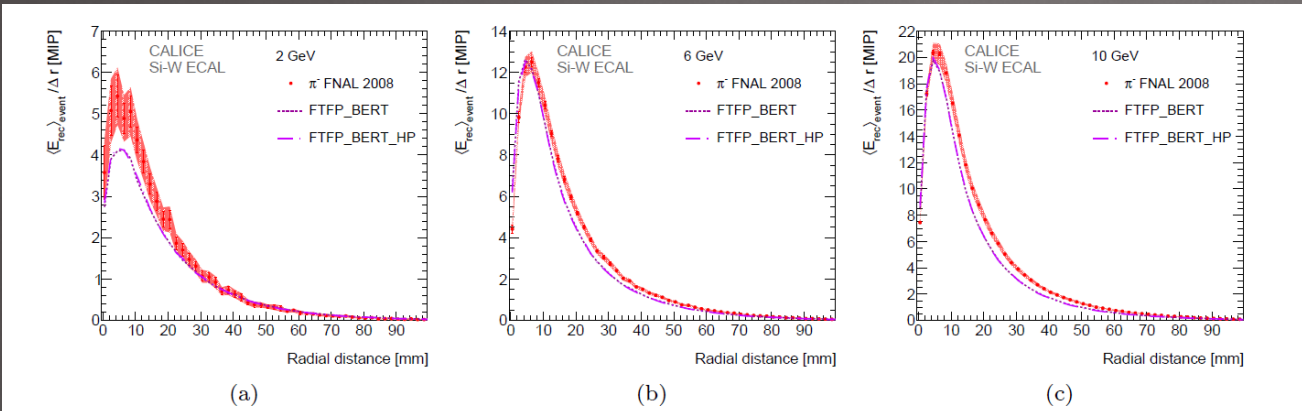


Figure 11: The radial energy profile for interacting events at 2, 6 and 10 GeV, for data and the Monte Carlo physics lists FTFP_BERT and FTFP_BERT_HP. Δr is 2 mm.

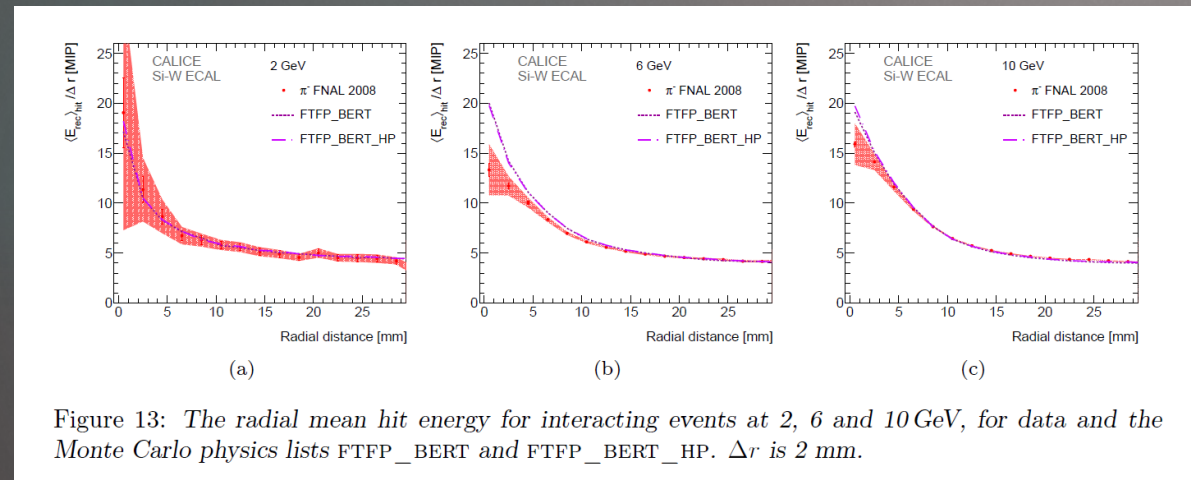


Figure 13: The radial mean hit energy for interacting events at 2, 6 and 10 GeV, for data and the Monte Carlo physics lists FTFP_BERT and FTFP_BERT_HP. Δr is 2 mm.

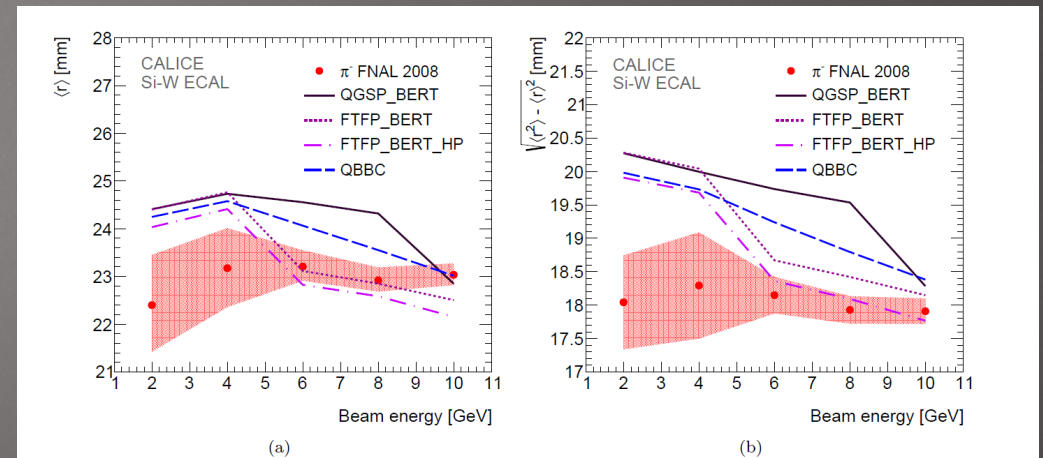


Figure 10: Mean (a) and standard deviation (b) of the radial distance of hits for interacting events as a function of beam energy (2 GeV to 10 GeV) for data and various Monte Carlo physics lists.

Shower longitudinal distribution

176

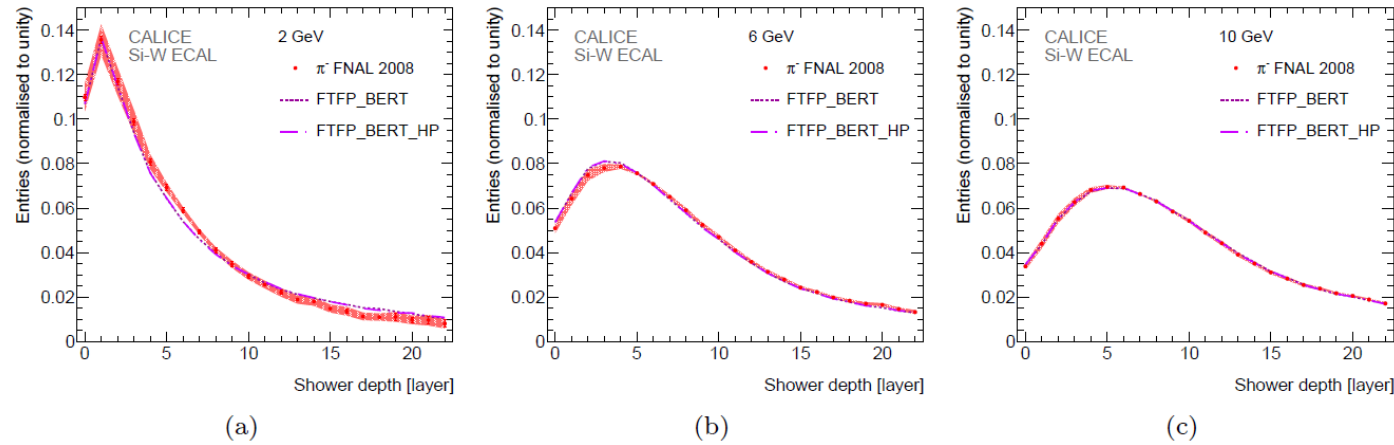


Figure 16: The longitudinal shower hit distribution for interacting events at 2, 6 and 10 GeV, for data and the Monte Carlo physics lists FTFP_BERT and FTFP_BERT_HP.

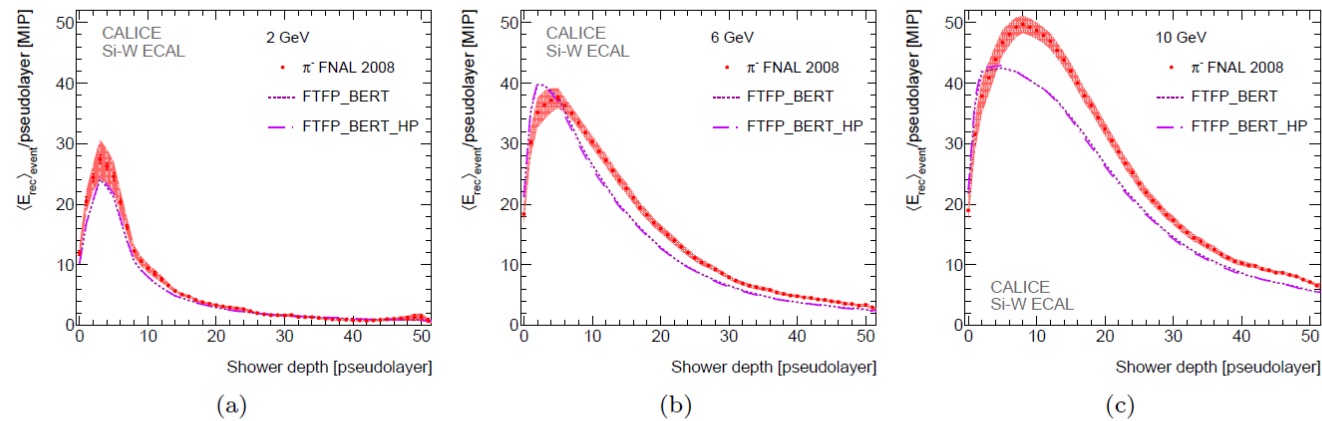
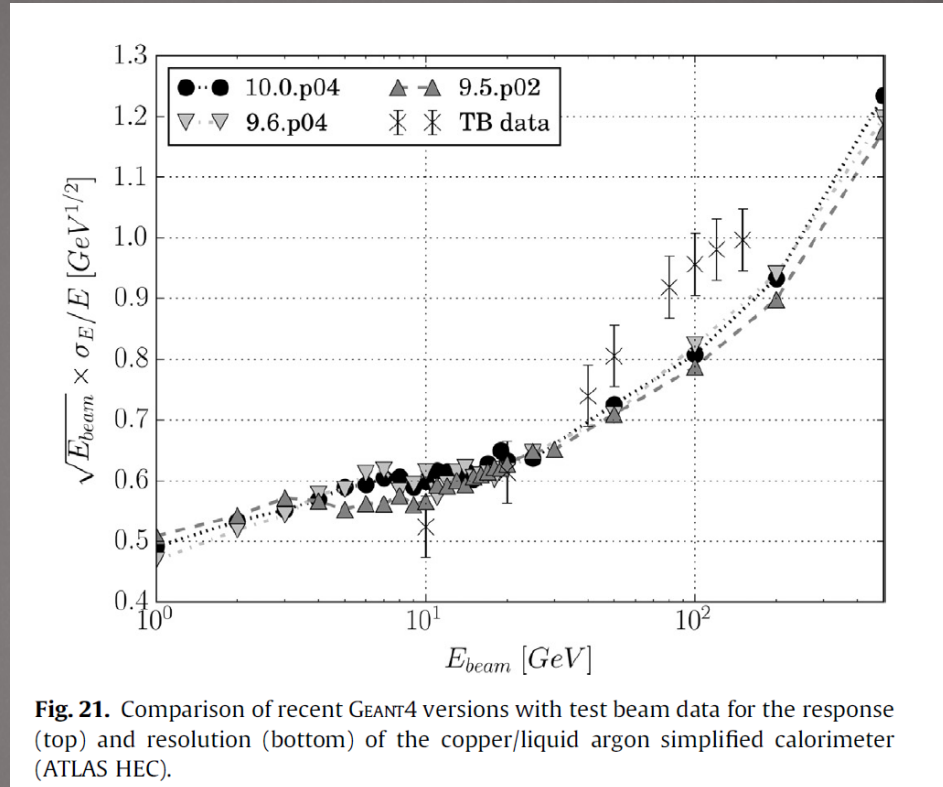


Figure 19: The longitudinal energy profile for interacting events at 2, 6 and 10 GeV, for data and the Monte Carlo physics lists FTFP_BERT and FTFP_BERT_HP.

Resolution (compared to atlas)

177



EM versus HAD CMS

178

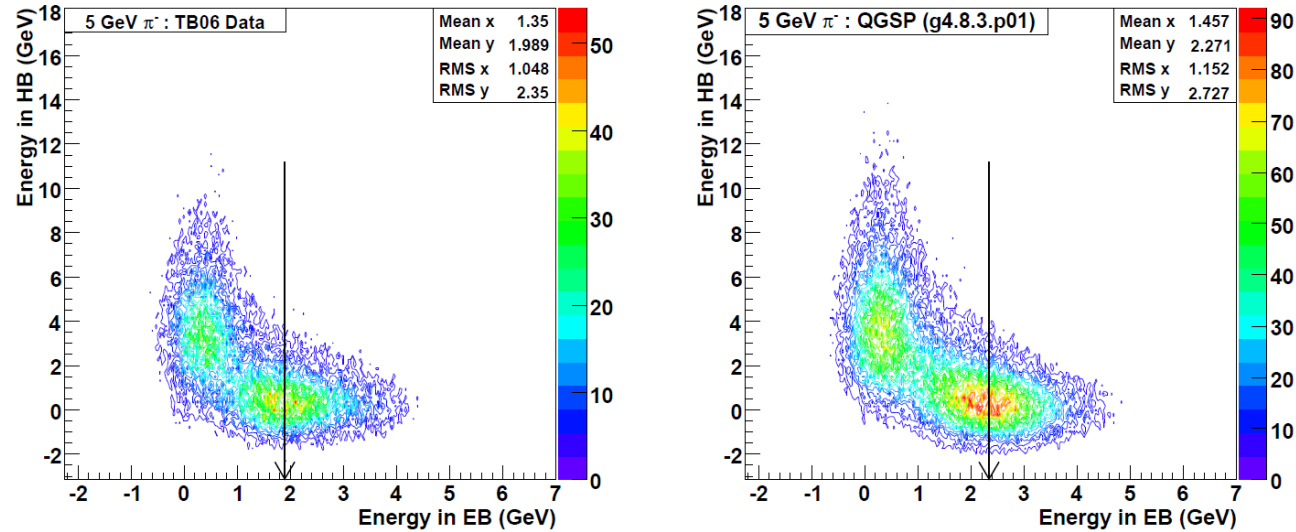


Figure 1: The measured energy in HCAL vs ECAL for 5 GeV π^- in the (a) data, (b) GEANT4 prediction using the QGSP physics list. The simulated energy in ECAL is higher than what is observed for the test beam.

Response CMS

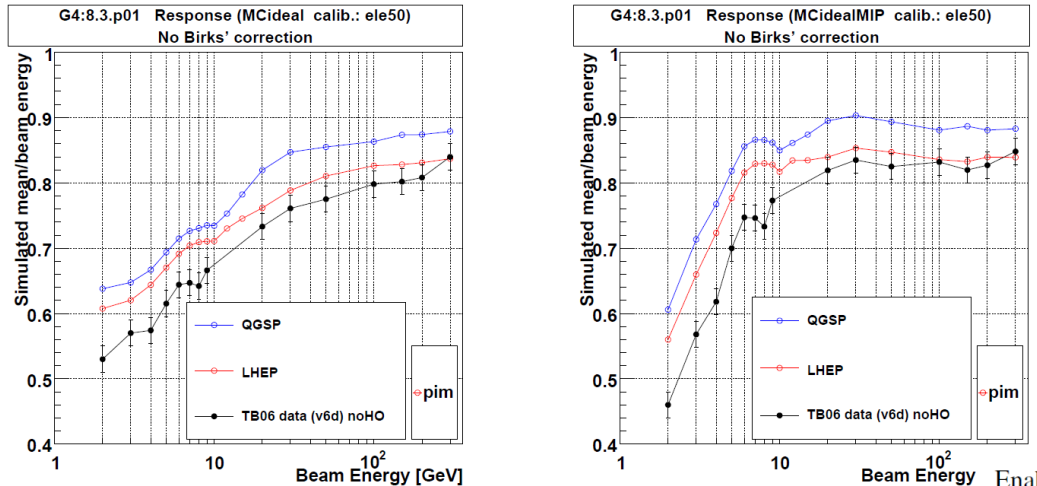


Figure 2: The mean response for a π^- beam as a function of beam momentum compared with GEANT4 using the LHEP and QGSP physics lists for (a) all interactions, (b) MIP signal simulation is not adequately describing the data.

Enabling Birks' law and using the QGSP (or QGSP_EMV) physics list results in a significant underestimation of the mean energy measurement. We recover the agreement by introducing a physics list that results in larger energy deposits at lower energies such as QGSP_BERT (or QGSP_BERT_EMV). The combination of the new physics list and Birks' law leads to a better agreement between data and simulation as shown in Figure 5 for the mean energy response.

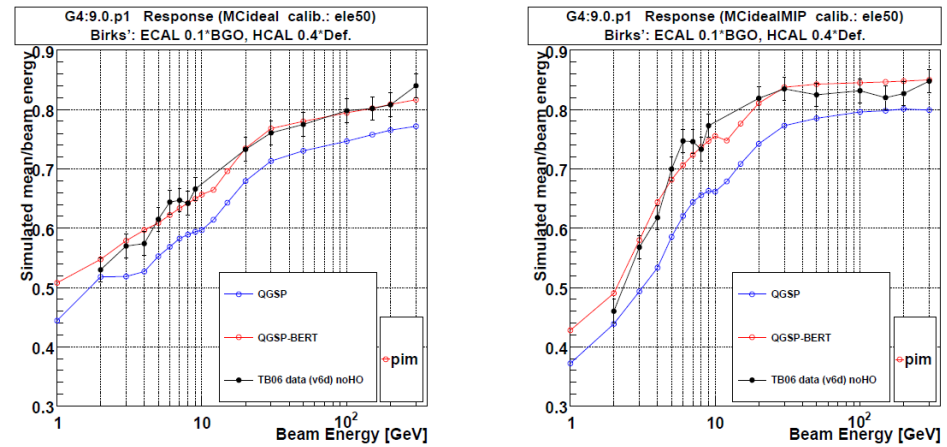


Figure 5: Mean energy response for the π^- beam in the calorimeter compared with the predictions of GEANT4 using the QGSP and QGSP_BERT physics lists for (a) all showers, (b) showers with a MIP signal in the ECAL.

GEANT

180

Have fun with a simple calorimeter in GEANT: <https://github.com/saraheno/dualtoy>

Summary

181

- Calorimeters have been a workhorse for hep experiments
- Much interesting R&D going on in hadronic calorimetry
- Much interesting R&D going on in radiation hardness

Fun times ahead for young people interested in this complex problem